frontiers | Research Topics

Radiomics-based theranostics in cancer precision medicine

Edited by
Jiansong Ji, Shenghong Ju and Wenli Cai

Published in
Frontiers in Oncology

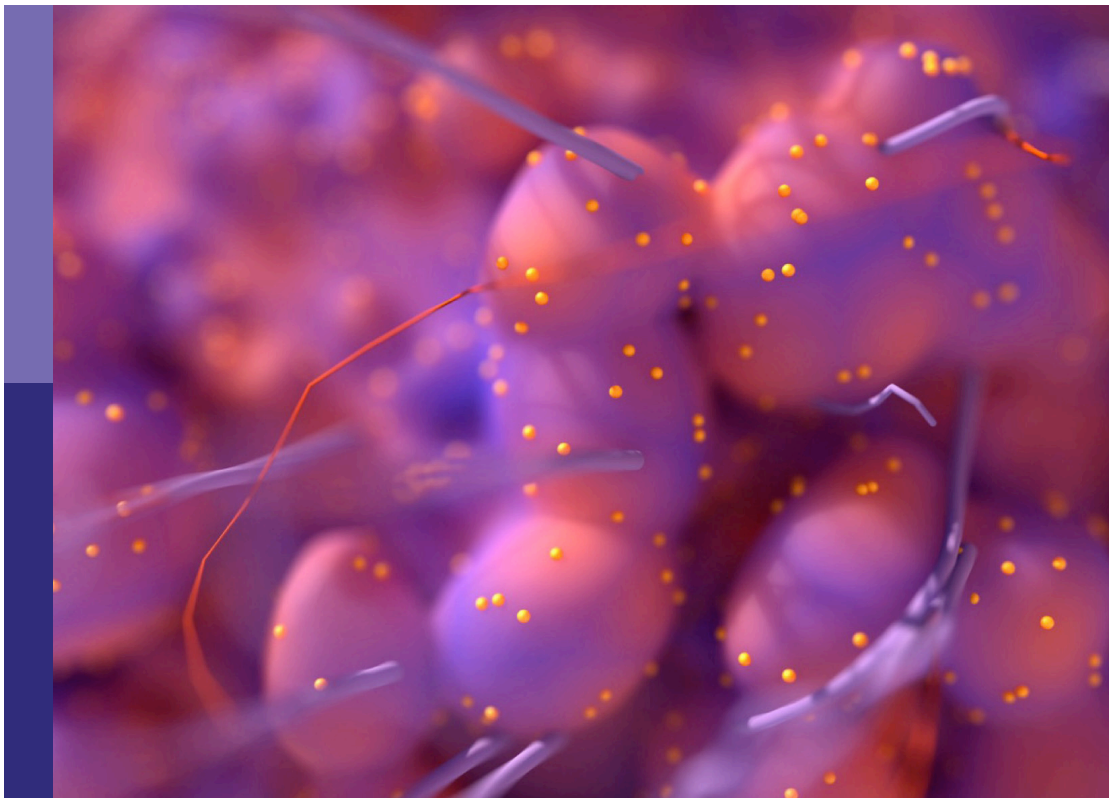

ISSN 1664-8714
ISBN 978-2-8325-3572-1
DOI 10.3389/978-2-8325-3572-1

About Frontiers

Frontiers is more than just an open access publisher of scholarly articles: it is a pioneering approach to the world of academia, radically improving the way scholarly research is managed. The grand vision of Frontiers is a world where all people have an equal opportunity to seek, share and generate knowledge. Frontiers provides immediate and permanent online open access to all its publications, but this alone is not enough to realize our grand goals.

Frontiers journal series

The Frontiers journal series is a multi-tier and interdisciplinary set of open-access, online journals, promising a paradigm shift from the current review, selection and dissemination processes in academic publishing. All Frontiers journals are driven by researchers for researchers; therefore, they constitute a service to the scholarly community. At the same time, the *Frontiers journal series* operates on a revolutionary invention, the tiered publishing system, initially addressing specific communities of scholars, and gradually climbing up to broader public understanding, thus serving the interests of the lay society, too.

Dedication to quality

Each Frontiers article is a landmark of the highest quality, thanks to genuinely collaborative interactions between authors and review editors, who include some of the world's best academicians. Research must be certified by peers before entering a stream of knowledge that may eventually reach the public - and shape society; therefore, Frontiers only applies the most rigorous and unbiased reviews. Frontiers revolutionizes research publishing by freely delivering the most outstanding research, evaluated with no bias from both the academic and social point of view. By applying the most advanced information technologies, Frontiers is catapulting scholarly publishing into a new generation.

What are Frontiers Research Topics?

Frontiers Research Topics are very popular trademarks of the *Frontiers journals series*: they are collections of at least ten articles, all centered on a particular subject. With their unique mix of varied contributions from Original Research to Review Articles, Frontiers Research Topics unify the most influential researchers, the latest key findings and historical advances in a hot research area.

Find out more on how to host your own Frontiers Research Topic or contribute to one as an author by contacting the Frontiers editorial office: frontiersin.org/about/contact

Radiomics-based theranostics in cancer precision medicine

Topic editors

Jiansong Ji — Lishui Central Hospital, China

Shenghong Ju — Southeast University, China

Wenli Cai — Massachusetts General Hospital, Harvard Medical School, United States

Citation

Ji, J., Ju, S., Cai, W., eds. (2023). *Radiomics-based theranostics in cancer precision medicine*. Lausanne: Frontiers Media SA. doi: 10.3389/978-2-8325-3572-1

Table of contents

frontiers | Frontiers in Oncology

TYPE Editorial
PUBLISHED 12 September 2023
DOI 10.3389/fonc.2023.1250079

OPEN ACCESS

EDITED AND REVIEWED BY
Zaver Bhujwalla,
Johns Hopkins University, United States

*CORRESPONDENCE
Jiansong Ji
lschrjjs@163.com

RECEIVED 29 June 2023
ACCEPTED 23 August 2023
PUBLISHED 12 September 2023

CITATION
Ji J, Ju S and Cai W (2023) Editorial: Radiomics-based theranostics in cancer precision medicine.
Front. Oncol. 13:1250079.
doi: 10.3389/fonc.2023.1250079

Editorial: Radiomics-based theranostics in cancer precision medicine

Jiansong Ji[1]*, Shenghong Ju[2] and Wenli Cai[3]

[1]Department of Radiology, Lishui Central Hospital, Lishui, China, [2]Department of Radiology, Southeast University, Nanjing, China, [3]Department of Radiology, Harvard Medical School, Boston, MA, United States

KEYWORDS

cancer, radiomics, theranostics, imaging, precision medicine

Editorial on the Research Topic
Radiomics-based theranostics in cancer precision medicine

Cancer is the second-leading cause of death worldwide and represents a large barrier to prolonging life expectancy. Cancer incidence and cancer-related mortality are rising. Lung cancer is the leading cause of cancer-related death, with approximately 1.8 million deaths worldwide (representing 18% of all cancer deaths), and breast cancer is the most commonly diagnosed cancer, with an estimated 2.3 million new cases globally in 2020 (representing 11.7% of cancer cases) (1). The management of cancer includes traditional surgery, precision/minimally invasive surgery, molecular imaging support, and, more recently, robot- or artificial intelligence (AI)-assisted surgical procedures (2). Combination therapy has been widely used to improve survival rates and reduce the side effects of treatment. Over the past few decades, cancer diagnosis and treatment strategies have been revolutionized. Medical imaging plays a pivotal role in the diagnosis and treatment of cancer because it can comprehensively assess the tumor and its environment. A wide variety of imaging modalities are used for theranostics, including optical (fluorescence or bioluminescence), nuclear (positron emission tomography [PET] or single-photon emission computerized tomography [SPECT]), ultrasound, photoacoustic, computed tomography (CT), and magnetic resonance (MR) imaging techniques.

Radiomics is an emerging tool in personalized medicine that mines features of medical images and translates high-throughput imaging features to quantitative data for predictive or prognostic purposes (3). As a bridge between medical imaging and personalized medicine, radiomics is becoming increasingly important in tumor diagnosis, treatment decisions, and prognosis prediction. Therefore, radiomics may provide quantitative and objective support for decisions surrounding cancer detection and treatment. Recently, research efforts have focused on the normalization and verification of radiomics algorithms to demonstrate their usefulness and robustness.

In this Research Topic, we focus on the most recent research on radiomics features extracted from CT, MRI, and ultrasound images to predict cancer biomarkers, treatment effectiveness, cancer progression, and cancer differential diagnoses. Through internal and external validation, one study evaluated the ability of peritumoral, intratumoral, and combined CT radiomics features to predict chemotherapy response in non-small cell lung

cancer (NSCLC). The authors concluded that noncontrast CT radiomics features from both the peri- and intratumoral regions could predict the chemotherapy response in NSCLC through machine learning models; furthermore, the 0–3 mm peritumoral region presented better performance than the peri- and intratumoral regions (Chang et al.). An accurate and reproducible model was constructed to predict the response of anti-PD-1 therapy for advanced NSCLC, which demonstrated the robustness of combining radiomics and deep learning features with machine learning methodologies (Ren et al.). A retrospective study analyzed the pretreatment CT images and clinical information of 692 patients with lung adenocarcinomas to predict their epidermal growth factor receptor (EGFR) mutation status and response to first-line tyrosine kinase inhibitors (TKIs) (Jiang et al.). For patients with small cell lung cancer (SCLC), CT-based radiomics integrated with CA125 and CA72-4 provided individualized pretreatment prediction of the response to platinum treatment (Su et al.). An accurate, rapid, and noninvasive indicator is needed to predict the efficacy of anti-angiogenic therapy in patients with advanced colorectal liver metastases (CRLMs); therefore, dynamic radiomics features from different sequences in the same patient were applied to predict treatment efficacy (Qu et al.). Considering the distinct phenotypic and biological characteristics of different pathological subtypes of lung cancer, it is important to differentiate between the pathological subtypes of NSCLC before clinical management. Nomograms combined with clinical parameters and radiomic features from pretherapy dual-energy computed tomography images presented suitable performance in distinguishing between adenocarcinoma (ADC) and squamous cell carcinoma (SCC), with an area under the curve (AUC) of 0.93 in the training set (Chen et al.). To better understand the significance of vascular endothelial growth factor (VEGF) and p53 in patients with spinal giant cell tumor of the bone (GCTB), a multiparametric model based on CT-based radiomics was constructed. The results indicated that p53 and VEGF are associated with poor prognosis in patients with spinal GCTB. Since T2-weighted imaging (T2WI) and the dynamic enhanced portal venous phase (PVP) of MRI can portray the biological characteristics of pancreatic lesions, another study verified the ability of MRI-based radiomics nomograms to evaluate lymph node metastasis (LNM) in patients with pancreatic ductal adenocarcinoma (PDAC) (Shi et al.). Ultrasound is a repeatable, cost-effective, and routinely used modality. A multicenter retrospective analysis developed an ultrasound radiomics-based nomogram to assess the prognosis of patients with nodal diffuse large B-cell lymphoma; the results demonstrated that this tool could be helpful to further individualize therapy (Deng et al.). Ultrasound radiomics has been employed in clinical practice for the management of breast cancer, with applications in lymph node status evaluation, differential diagnosis, cancer staging, neoadjuvant chemotherapy response prediction, and survival prediction (Gu and Jiang).

In conclusion, with the development of state-of-the-art AI techniques, the underlying information of oncology images can be excavated to assist clinical decision-making. This Research Topic discussed and verified the usefulness of radiomics-based prediction models. For example, CT-derived radiomics models have been established to assess treatment response, MRI-based radiomics parameters have been applied to predict lymph node metastasis, and ultrasound-based radiomics can be used to personalize breast cancer management and predict the overall survival of patients with nodal diffuse large B-cell lymphoma. Overall, radiomics features derived from medical images can translate qualitative information to quantitative data, broadening the applicability of medical images in cancer theranostics.

Author contributions

All authors listed have made a substantial, direct, and intellectual contribution to the work and approved it for publication.

Conflict of interest

The authors declare that the research was conducted in the absence of any commercial or financial relationships that could be construed as a potential conflict of interest.

Publisher's note

References

1. Sung H, Ferlay J, Siegel RL, Laversanne M, Soerjomataram I, Jemal A, et al. Global cancer statistics 2020: GLOBOCAN estimates of incidence and mortality worldwide for 36 cancers in 185 countries. *CA Cancer J Clin* (2021) 71(3):209–49. doi: 10.3322/caac.21660

2. Advancing cancer therapy. *Nat Cancer* (2021) 2(3):245–6. doi: 10.1038/s43018-021-00192-x

3. Lambin P, Leijenaar RTH, Deist TM, Peerlings J, de Jong EEC, van Timmeren J, et al. Radiomics: the bridge between medical imaging and personalized medicine. *Nat Rev Clin Oncol* (2017) 14(12):749–62. doi: 10.1038/nrclinonc.2017.141

frontiers | Frontiers in Oncology

ORIGINAL RESEARCH
published: 21 June 2022
doi: 10.3389/fonc.2022.894696

A Multiparametric Method Based on Clinical and CT-Based Radiomics to Predict the Expression of p53 and VEGF in Patients With Spinal Giant Cell Tumor of Bone

Qizheng Wang[1], Yang Zhang[2,3], Enlong Zhang[4], Xiaoying Xing[1], Yongye Chen[1], Ke Nie[3], Huishu Yuan[1], Min-Ying Su[2,5†] and Ning Lang[1*†]*

[1] Department of Radiology, Peking University Third Hospital, Beijing, China, [2] Department of Radiological Sciences, University of California Irvine, Irvine, CA, United States, [3] Department of Radiation Oncology, Robert Wood Johnson Medical School, New Brunswick, NJ, United States, [4] Department of Radiology, Peking University International Hospital, Beijing, China, [5] Department of Medical Imaging and Radiological Sciences, Kaohsiung Medical University, Kaohsiung, Taiwan

Purpose: This project aimed to assess the significance of vascular endothelial growth factor (VEGF) and p53 for predicting progression-free survival (PFS) in patients with spinal giant cell tumor of bone (GCTB) and to construct models for predicting these two biomarkers based on clinical and computer tomography (CT) radiomics to identify high-risk patients for improving treatment.

Material and Methods: A retrospective study was performed from April 2009 to January 2019. A total of 80 patients with spinal GCTB who underwent surgery in our institution were identified. VEGF and p53 expression and clinical and general imaging information were collected. Multivariate Cox regression models were used to verify the prognostic factors. The radiomics features were extracted from the regions of interest (ROIs) in preoperative CT, and then important features were selected by the SVM to build classification models, evaluated by 10-fold crossvalidation. The clinical variables were processed using the same method to build a conventional model for comparison.

Results: The immunohistochemistry of 80 patients was obtained: 49 with high-VEGF and 31 with low-VEGF, 68 with wild-type p53, and 12 with mutant p53. p53 and VEGF were independent prognostic factors affecting PFS found in multivariate Cox regression analysis. For VEGF, the Spinal Instability Neoplastic Score (SINS) was greater in the high than low groups, $p < 0.001$. For p53, SINS ($p = 0.030$) and Enneking stage ($p = 0.017$) were higher in mutant than wild-type groups. The VEGF radiomics model built using 3 features achieved an area under the curve (AUC) of 0.88, and the p53 radiomics model built using 4 features had an AUC of 0.79. The conventional model built using SINS, and the Enneking stage had a slightly lower AUC of 0.81 for VEGF and 0.72 for p53.

OPEN ACCESS

Edited by:
Shenghong Ju,
Southeast University, China

Reviewed by:
Xiao Chen,
Affiliated Hospital of Nanjing University of Chinese Medicine, China
Ning Mao,
Yantai Yuhuangding Hospital, China

***Correspondence:**
Ning Lang
langning800129@126.com
Min-Ying Su
msu@uci.edu

†These authors have contributed equally to this work

Specialty section:
This article was submitted to Cancer Imaging and Image-directed Interventions, a section of the journal Frontiers in Oncology

Received: 12 March 2022
Accepted: 19 May 2022
Published: 21 June 2022

Citation:
Wang Q, Zhang Y, Zhang E, Xing X, Chen Y, Nie K, Yuan H, Su M-Y and Lang N (2022) A Multiparametric Method Based on Clinical and CT-Based Radiomics to Predict the Expression of p53 and VEGF in Patients With Spinal Giant Cell Tumor of Bone. Front. Oncol. 12:894696. doi: 10.3389/fonc.2022.894696

Conclusion: p53 and VEGF are associated with prognosis in patients with spinal GCTB, and the radiomics analysis based on preoperative CT provides a feasible method for the evaluation of these two biomarkers, which may aid in choosing better management strategies.

Keywords: tomography, quantitative imaging, giant cell tumor of bone, immunohistochemistry, tumor suppressor protein p53, vascular endothelial growth factors

INTRODUCTION

Giant cell tumor of bone (GCTB) is one of the most common intermediate bone tumors, which occurs in young adults 20–40 years old with a high recurrence rate (20%–50%) (1) and a potential for aggressive behavior (2). Even if patients undergo the same surgical procedure and remove the tumor as completely as possible, the postoperative recurrence rate varies substantially. Many studies have suggested that this may be related to the aggressiveness of the tumor that each patient has, and thus, personalized stratified management is very important (3). For GCTB in the spine, postoperative recurrence is more common compared to GCTB in other bones, and it is also associated with a higher risk of malignant transformation (4, 5). During the surgery, it is necessary to protect the spinal cord and peripheral nerve function to minimize the postoperative complications caused by the resection damage; therefore, the tumor may not be completely resected to remain in a good quality of life (6). Given all these, it is important to characterize the aggressiveness of the spinal GCTB to choose an optimized personalized treatment. The genomics analysis and imaging may provide valuable information for treatment planning, postoperative monitoring, and prognosis assessment.

In 2020, the WHO updated the classification for primary musculoskeletal tumors, which reflects the knowledge generated from extensive research in the identification of novel gene alterations in many bone neoplasms (7). The change further emphasized that the assessment of bone tumors should be more thorough and personalized. We reviewed previous studies on prognostic-related molecular markers and found that the vascular endothelial growth factor (VEGF) and p53 mutation were two important biomarkers related to the evaluation of the biological aggressiveness of osteosarcoma and GCTB (3, 8–15). Angiogenesis occurs in numerous biological processes, which is essential for the growth of tumors and metastases. VEGF is one of the most important growth factors for the regulation of vascular development and angiogenesis (16, 17), which plays an important role in osteogenesis, bone repair, tumor cell development, and metastasis by stimulating angiogenesis (18). p53 is an important tumor suppressor gene in many carcinomas, and there are also extensive research studies for bone tumors (19). Mutation in p53 will lose this function and lead to tumorigenesis, which can also promote angiogenesis by regulating the expression of VEGF (20). For GCTB, high expression of VEGF (21–23) and mutant p53 (24–26) have been shown as risk factors for local recurrence and malignant transformation. However, the long-term follow-up studies focusing on these two biomarkers in spinal GCTB after total en bloc spondylectomy (TES), the current mainstream surgical method, were rarely reported.

The current assessment of preoperative spinal GCTB relies mainly on pathological and immunohistochemical examination of tissues taken by puncture biopsy. However, it is known that the analysis is not reliable in some cases because only a small amount of tissue in a large tumor is obtained. While this is sufficient for making a diagnosis, further characterization of molecular biomarkers may be limited by tumor heterogeneity. In addition, an invasive needle biopsy may lead to complications such as bleeding, fractures, and tumor metastasis. At present, surgeons also use some clinical scoring systems for preoperative assessment, such as the Spinal Instability Neoplastic Score (SINS) (27), the Visual Analog Scale (VAS) (28), and the Enneking stage (29). However, there is no research reporting how these scoring systems are related to the tumor biomarker status.

In recent years, "radiomics" has emerged as a widely used method to characterize diseases for molecular diagnosis, prognosis, and treatment monitoring by analyzing the spatial and temporal heterogeneity of tumors from medical images (30–35). As the full spatial extent of the tumor was considered, the computational techniques may provide a complimentary assessment of the whole tumor, thus overcoming the limitations of tissue sampling (36–38). Computed tomography (CT) is a cost-effective imaging method commonly used in the clinical examination of spinal tumors. The CT-based radiomics features may provide a new approach to reflect the heterogeneity of tumors related to the VEGF and p53 expression, which may make up for the limitations of preoperative puncture and provide supplemental information.

There are two main objectives in this study. The first aim is to evaluate the prognostic difference according to the status of VEGF and P53 using the progression-free survival (PFS) in a cohort of spinal GCTB patients with long-term follow-up. The second aim is then to build models based on preoperative CT to differentiate high vs. low VEGF and wild-type vs. mutant p53 to assist in preoperative tumor evaluation. Other information such as the clinically applied scoring system and traditional imaging evaluation results is included in the analysis, and the performance of the developed models is compared.

MATERIALS AND METHODS

Patients

The study was approved by the Medical Science Research Ethics Committee, and the written informed consent was waived. We

identified 105 consecutive patients with spinal GCTB at the orthopedics department between April 1, 2009, and January 1, 2019. The inclusion criteria were as follows (1) patients who had pathologically confirmed spinal GCTB; (2) preoperative CT was performed; and (3) the qualified postoperative pathological specimens were stored in the tissue bank.

The exclusion criteria were as follows: (1) radiotherapy, preoperative neoadjuvant chemotherapy, or other interventions for lesions were performed before CT or surgery; (2) poor image quality due to susceptibility artifacts decided by radiologists; (3) the operation method was not TES; and (4) the immunohistochemical evaluation result of H3F3A was negative (37). Finally, a total of 80 patients were included, and their clinical and CT imaging data were collected. The subject identification flowchart is shown in **Figure 1**.

Clinical and Imaging Characteristics

The clinical information for the preoperative evaluation of spinal tumors was obtained through the medical record system, including the symptom duration before surgery (months), SINS, VAS, and the Enneking stage. The instability was further defined based on the SINS into two categories: scores of 7 to 12 as indeterminate (possibly impending) instability and 13 to 18 as instability (39). The scoring methods are explained and shown in **Supplementary Part 1**.

CT Imaging

CT imaging was performed using a GE Lightspeed 64-slice spiral CT (GE Medical System, Chalfont St Giles, UK) or a Siemens Somatom Definition Flash dual-source CT (Siemens, Erlangen, Germany). The parameters were 120 kVp, 200–300 mAs; collimator width of 0.625 or 0.60 mm; pitch of 1.0; slice thickness of 2 mm; and interlayer distance of 3 mm.

For each case, 8 imaging features were determined: lesion location, position, vertebral compression, boundary, residual bone crest, "soap bubble sign", largest diameter, and CT value. These were evaluated by 3 musculoskeletal radiologists, and the consensus results were used. The location of the lesion included the cervical, thoracic, lumbar, and sacral spine. The position was classified according to whether the lesion was located in the vertebral body or vertebral arch. The boundary was classified as clear or unclear. The "soap bubble sign" was defined as the bone cortex having obvious expansive changes compared with the normal vertebra. **Figure 2** shows the axial and sagittal images from 4 cases to illustrate the evaluation of imaging features.

Evaluation of VEGF and p53 Expression

The paraffin-embedded tissue block of the patient's postoperative specimen was requested from the pathology department, and immunohistochemical staining of VEGF and p53 was performed by following the protocol (40). The expression levels of VEGF and p53 were independently evaluated by two experienced pathologists using a scoring system. The expression level of VEGF was divided into four grades according to the percentage of positively stained cells: ≤15% (grade 0), 15%–50% (grade 1), 50%–75% (grade 2), and ≥75% (grade 3). Since there were few cases of grades 0 and 3, grades 0–1 were classified into a low-VEGF group and grades 2–3 into a high-VEGF group. For p53, the tissue was considered positive when the proportion of nuclei positively stained for mutant p53 was >10%, otherwise negative. Examples of the immunohistochemical slides are illustrated in **Figure 3**.

Tumor Segmentation on CT

For each case, the range of axial CT slices containing the tumor was first determined. The ROI of the tumor was manually delineated using the Image J software (National Institute of

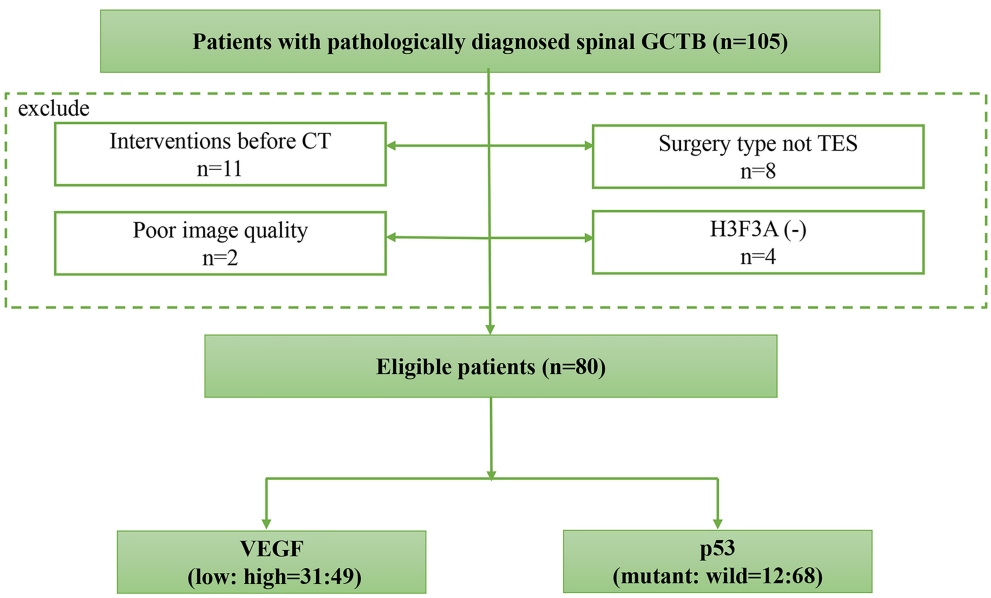

FIGURE 1 | The subject identification flowchart. A total of 80 spinal GCTB cases with VEGF and p53 immunohistochemical staining results are included.

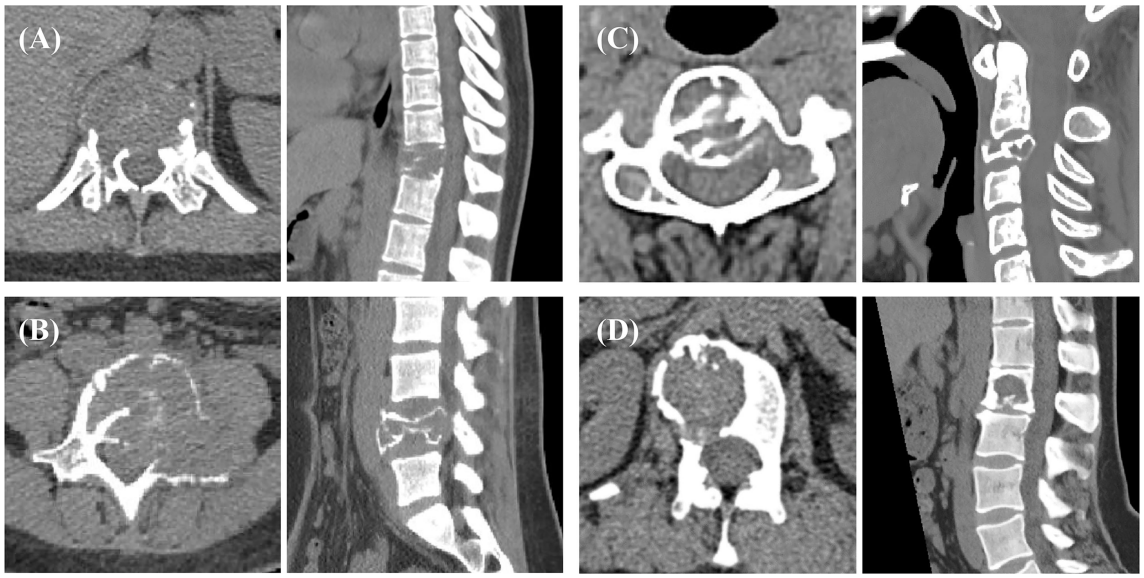

FIGURE 2 | Spinal GCTB case examples from 4 patients. The boundary of the lesion can be clearly observed on the transverse images, which are used for tumor ROI drawing. The sagittal images show vertebral compression, spinal canal compression, and spinal stability, which are used to determine additional imaging features. The biomarker results of these patients: **(A)** mutant p53 and high VEGF; **(B)** mutant p53 and low VEGF; **(C)** wild-type p53 and high VEGF; and **(D)** wild-type p53 and low VEGF. The SINS of these 4 patients were 18, 11, 11, and 7.

Health, Bethesda, USA) by a musculoskeletal radiologist (with 15 years of experience) and then validated by an experienced radiologist (with 25 years of experience in skeletal radiology). Discrepancies between the two radiologists were resolved by consensus. The two radiologists were not involved in the clinical and imaging characteristics evaluation and were blinded to other information about patients. The outlined ROIs on all imaging slices of a tumor were combined into a 3D tumor mask.

Radiomics Analysis to Build Classification Model

The radiomics analysis procedures are illustrated in **Figure 4**. The feature extraction was done using PyRadiomics, an open-source Python package platform (http://www.radiomics.io/pyradiomics.html). For each patient, a total of 107 features, including shape, first-order statistics, and texture, were extracted. The list of features and how each feature is

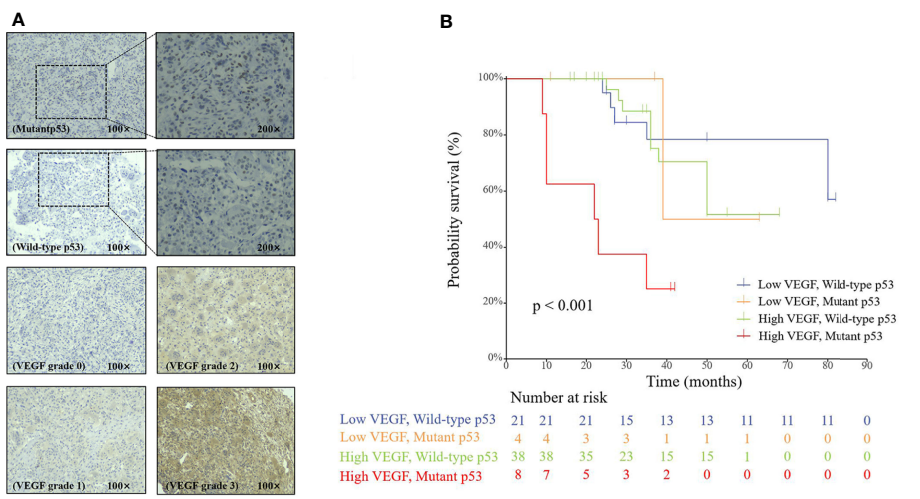

FIGURE 3 | **(A)** Immunohistochemical staining of p53 and VEGF in spinal GCTB. **(B)** The Cox proportional hazards regression analysis of the p53 and VEGF groups.

calculated is included in **Supplementary Material Part 2**. The segmented lesions on all 2D slices were rendered into a 3D space with isotropic voxel resolution for extracting the 3D texture features. Although using different quantization methods or wavelet transformation may generate many times features, they were highly correlated with the original features, so we only analyzed the original 107 features.

After the features were extracted, they were normalized to mean = 0 and standard deviation = 1. To evaluate the importance of these features in classification, the sequential feature selection process was done via the construction of multiple support vector machine (SVM) classifiers. In this process, we used SVM with a Gaussian kernel as the objective function to test the performance of models built with a subset of features. In the beginning, an empty candidate set was presented, and features were sequentially added. A 10-fold crossvalidation was applied to test the model performance. In each iteration, the training process was repeated 1,000 times to explore the robustness of each feature. After each iteration, the feature that led to the best performance was added to the candidate set. When the addition of features no longer met the criterion, the selection process stopped. Here, we used 10^{-6} as termination tolerance for the objective function value. The number of mutant p53 cases was much smaller than the wild-type p53, so we assigned different class weights according to the number of cases to address the issue of unbalanced classes. For the high vs. low VEGF, the case number was approximately equal.

The selected features were used to build the final SVM classification model with a Gaussian kernel to classify the high vs. low VEGF and wild-type vs. mutant p53 groups. The output of the model was a radiomics score (that is, a probability) for a case. The diagnostic performance was tested using 10-fold crossvalidation. Each case had only one chance to be included in the validation set. The probability of all cases in the validation set was combined to perform the receiver operating characteristic curve (ROC) analysis, and the area under the curve (AUC) was calculated.

In addition to the radiomics analysis, we also built models using the clinical characteristics and the imaging features determined by visual reading, by following a similar process for feature selection and 10-fold crossvalidation. All clinical/imaging parameters were evaluated using a random forest algorithm. Then the features with the highest significance were selected to build the classification model. Random forest algorithms were utilized *via* Bootstrap-aggregated decision trees to evaluate the importance of these features in differentiating the high vs. low VEGF and wild-type vs. mutant p53 groups. A measurement of the feature significance can be assessed as the loss of accuracy after this feature was removed. The features were sorted based on their importance scores, and then, according to the ranking, the top 1, 2, 3,… features were selected to build the diagnostic model by using logistic regression. The discrimination accuracy was evaluated by the ROC analysis using 10-fold stratified crossvalidation. This process was repeated many times using a different combination of selected imaging or clinical features (1, 2, 3,…), and the results were used to find the best model according to the highest AUC. After the features included in the best model were decided, they were used to build a final diagnostic classifier with logistic regression, and the accuracy was evaluated in the entire dataset.

Lastly, a combined logistic regression model was built by using the selected clinical/imaging variables and the radiomics scores, which were evaluated using ROC.

Statistical Analysis

For multivariate analysis of the importance of the two biomarkers for survival outcomes, we used a Cox regression model, which was performed using R 3.6.3 software (The R Foundation for Statistical Computing, Vienna, Austria) based on the patient's outcome data, including PFS and p53/VEGF expression results. PFS was defined as the time between the date of surgery and the date of confirmed disease progression or death. PFS was censored at the date of death from other causes or the date of the last follow-up visit for progression-free patients. Progression was determined by the imaging evidence of the postoperative follow-up that showed an emerging soft tissue

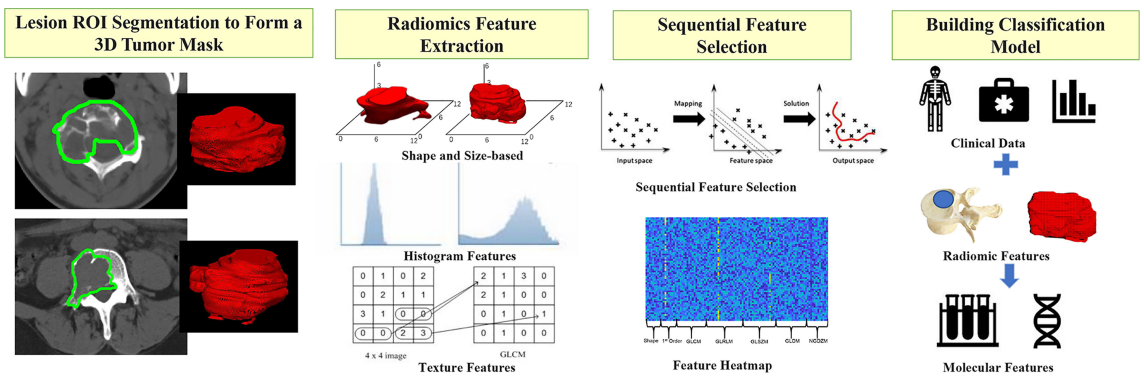

FIGURE 4 | The radiomics analysis procedures to build the classification model. Step1: The lesion ROI is outlined on each slice and then combined into a 3D tumor mask. Step 2: PyRadiomics is applied to extract 107 features, including shape, first-order statistics, and texture from each tumor mask (GLCM is an example of a feature processing). Step 3: The sequential feature selection is performed by using SVM, and finally, Step 4: The SVM algorithm is applied to build the classification model.

mass in the operation area, and pathological puncture was performed if necessary. Results were reported as hazard ratios (HR) with 95% confidence intervals (95% CI). Other statistical analyses were performed using SPSS version 18.0 (SPSS, Chicago, IL, USA). For clinical characteristics and general imaging features between different biomarker groups, the significance of each variable was tested by using the independent samples *t*-test, χ^2 test, or Mann–Whitney *U* test, depending on the data type. The ROC analysis was used to evaluate the performance of three different models, and the AUC was calculated and compared using the DeLong test. A 2-sided *p*-value of <0.05 was regarded as statistically significant.

RESULTS

Patient Characteristics

The present study included 80 patients, of whom 43.75% (35 patients) were men and 56.25% were women (45 patients). Based on the IHC results, 31 had grades 0–1 (low VEGF) and 49 had grades 2–3 (high VEGF) expression; 68 had wild-type p53 and 12 had mutant p53. The clinical and imaging characteristics of patients in different VEGF and p53 groups are listed in **Table 1**.

Multivariate Analysis of Prognostic Factors for PFS

As shown in **Figure 3**, the multivariable Cox regression analysis showed that p53 and VEGF were significantly associated with PFS ($p < 0.001$). The results showed that the mutant p53 group had a significantly poorer PFS than the wild-type group (HR: 4.231; 95% CI: 1.663–10.768; $p < 0.01$). Patients with high VEGF expression also had a worse PFS than patients with low VEGF expression (HR: 2.891; 95% CI: 1.053–7.935; $p = 0.039$). The Cox proportional risk regression model confirmed that p53 and VEGF are independent prognostic factors for spinal GCTB.

Relationship Between p53/VEGF Expression and Clinical Characteristics and General Imaging Features

The SINS score, or the dichotomized spinal stability, showed significant differences between high and low VEGF groups, all with $p < 0.001$ in univariate analysis. When using the single

TABLE 1 | Clinical and imaging characteristics in high vs. low VEGF groups and wild-type vs. mutant p53 groups.

Parameter	High VEGF (*N* = 49)	Low VEGF (*N* = 31)	*p*-value	Wild-type p53 (*N* = 68)	Mutant p53 (*N* = 12)	*p*-value
Clinical characteristics						
Age	33.3 ± 13.3	32.2 ± 10.7	0.701	32.6 ± 12.0	34.3 ± 14.0	0.694
VAS score	5.9 ± 1.6	6.4 ± 1.4	0.126	6.1 ± 1.6	6.1 ± 1.2	0.962
SINS score	12.2 ± 2.0	9.9 ± 2.0	**<0.001***	11.0 ± 2.2	12.8 ± 2.4	**0.030***
Symptom duration (months)	12.9 ± 6.8	12.6 ± 4.1	0.769	12.0 ± 4.9	17.4 ± 8.4	0.05
Intraoperative bleeding vol (ml)	1125 ± 565	574 ± 303	**<0.001***	843 ± 452	1,300 ± 854	0.095
Spinal stability			**<0.001***			**0.013***
0: Stable	24 (49.0%)	28 (90.3%)		48 (70.6%)	4 (33.3%)	
1: Unstable	25 (51.0%)	3 (9.7%)		20 (29.4%)	8 (66.7%)	
Enneking stage			0.910			**0.017***
1	31 (63.3%)	20 (64.5%)		47 (69.1%)	4 (33.3%)	
2	18 (36.7%)	11 (35.5%)		21 (30.9%)	8 (66.7%)	
Imaging characteristics						
Lesion location			0.242			0.642
Cervical	18 (36.7%)	8 (25.8%)		22 (32.4%)	4(33.3%)	
Thoracic	20 (40.8%)	13 (41.9%)		27 (39.7%)	6 (50.0%)	
Lumbar	5 (10.2%)	8 (25.8%)		11 (16.2%)	2 (16.7%)	
Sacral	6 (12.3%)	2 (6.5%)		8 (11.7%)	0 (0.0%)	
Position			0.386			0.861
Vertebral body	43 (87.8%)	25 (80.6%)		58 (85.3%)	10 (83.3%)	
Vertebral arch	6 (12.2%)	6 (19.4%)		10 (14.7%)	2 (16.7%)	
Vertebral compression			0.981			0.741
0%	15 (30.6%)	10 (32.3%)		22 (32.4%)	3 (25.0%)	
≤50%	20 (40.8%)	12 (38.7%)		26 (38.2%)	6 (50.0%)	
>50%	14 (28.6%)	9 (29.0%)		20 (29.4%)	3 (25.0%)	
Lesion boundary			0.636			**0.044***
Clear	47 (95.9%)	29 (93.5%)		66 (97.1%)	10 (83.3%)	
Unclear	2 (4.1%)	2 (6.5%)		2 (2.9%)	2 (16.7%)	
Residual bone crest			0.779			0.443
Yes	19 (38.8%)	13 (41.9%)		26 (38.2%)	6 (50.0%)	
No	30 (61.2%)	18 (58.1%)		42 (61.8%)	6 (50.0%)	
"Soap bubble-like" sign			0.815			0.292
Yes	45 (91.8%)	28 (90.3%)		63 (92.6%)	10 (83.3%)	
No	4 (8.2%)	3 (9.7%)		5 (7.4%)	2 (16.7%)	
CT Hounsfield value	48.1 ± 9.5	47.5 ± 10.0	0.795	47.8 ± 9.9	48.2 ± 8.3	0.905
Largest diameter	4.9 ± 1.7	5.3 ± 2.1	0.310	5.1 ± 1.9	4.8 ± 1.1	0.428

**p-value <0.05; VAS, Visual Analog Scale; SINS, Spinal Instability Neoplastic Score.*

parameter to construct ROC, the AUC was 0.781 (95% CI: 0.676–0.886) for the SINS score. The SINS score (or the dichotomized stability) and the Enneking stage were significantly different between patients with wild-type and mutant p53. The AUC was 0.737 (95% CI: 0.562–0.913) for the SINS score and 0.679 (95% CI: 0.511–0.847) for the Enneking stage. For the general imaging features, none was significantly different between the two VEGF groups, and only one variable, the boundary of the lesion, showed a marginal difference between wild-type and mutant p53 (p = 0.044).

Development of Radiomics, Clinical, and Combined Models

The radiomics model was built using features selected by the sequential SVM method. For high vs. low VEGF, 4 features were selected: major axis length, GLCM_contrast, GLCM_IDMN, and GLRLM_gray level variance. The best model had an AUC of 0.88 and an accuracy of 89% when using the radiomics score of 0.5 as the classification threshold. For wild-type vs. mutant p53, three features were selected: GLCM_entropy, GLDM_small dependence emphasis, and the surface-to-volume ratio. The best model had an AUC of 0.79 and an accuracy of 95%. The radiomics scores calculated from the models built for VEGF and p53 are shown in **Figure 5**. The ROC curves are shown in **Figure 6**. Abbreviations for features are shown in **Supplementary Part 3**.

The best conventional model built by considering the clinical and imaging variables yielded an AUC of 0.81 for VEGF and 0.72 for p53. The selected features, in sequence, were SINS and VAS for VEGF and SINS and Enneking stage for p53. The radiomics score and the selected clinical/imaging variables were then combined to build another model by using logistic regression. When using the radiomics score with SINS and VAS for VEGF, the achieved AUC was 0.88. When using the radiomics score with SINS and Enneking stage for p53, the achieved AUC was 0.77. The AUC for these models was not significantly different using the DeLong test. The classification sensitivity, specificity, accuracy, and AUC are summarized in **Table 2**.

DISCUSSION

There were two objectives in this study: first to evaluate the prognostic value of two tumor markers, p53 and VEGF, in the PFS of spinal GCTB, and second to build models based on the pre-perative CT radiomics features and clinical variables for the classification of the VEGF and p53 status. The Cox proportional hazards regression model confirmed the prognostic role of p53 and VEGF. The models may help to predict the biological behavior of the tumor and provide preoperative risk stratification information to aid in the selection of appropriate treatments. The analysis based on imaging of the entire tumor may help overcome the limitations of preoperative tissue sampling. Three models were built using (1) radiomics features, (2) clinical + conventional imaging variables, and (3) combined radiomics scores and selected clinical variables. The AUC of the three models for classifying high vs. low VEGF were 0.88, 0.81, and 0.88, respectively, and for wild-type vs. mutant p53 were 0.79, 0.72, and 0.77, respectively. The results support that the clinical variables and radiomics features contained in preoperative CT were related to IHC biomarkers.

In the era of precision medicine, molecular markers have been established as important diagnostic and prognostic markers in clinical decision-making (41). Our study found that high VEGF status was associated with worse postoperative survival of patients. Several studies have shown that high levels of p53/VEGF expression are associated with high recurrence rates (14, 15, 42), and therapies targeting these two biomarkers are under research or in clinical trials (13, 43–45). VEGF is one of the most important growth factors for the regulation of vascular development and angiogenesis (18). The interaction between endothelial cells and bone cells is essential for bone formation

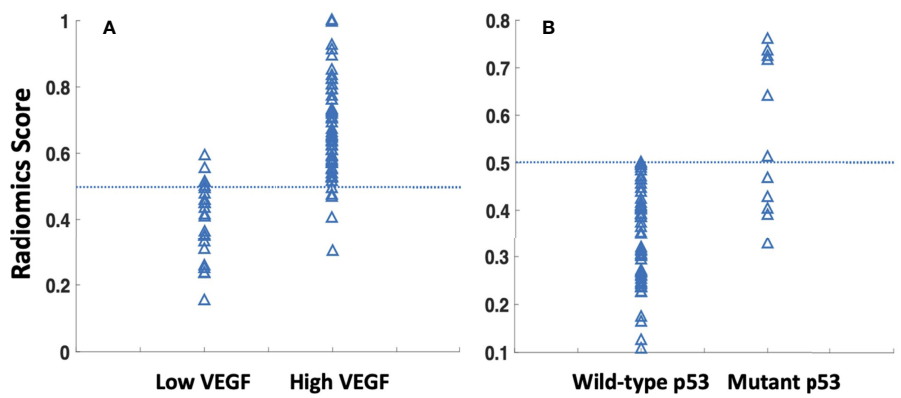

FIGURE 5 | The radiomics scores were calculated using the developed radiomics models for all cases, classified using 0.5 as the threshold. **(A)** For prediction of low vs. high VEGF groups, showing 27 true low VEGF, 4 false low VEGF, 44 true high VEGF, and 5 false high VEGF. **(B)** For wild-type vs. mutant p53 groups, showing 68 true WT-p53, 0 false WT-p53, 7 true mutant p53, and 5 false mutant p53.

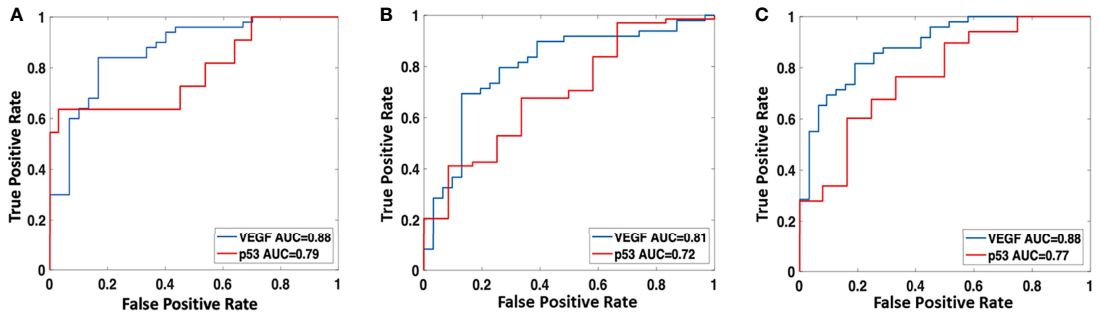

FIGURE 6 | The ROC curves were constructed by using the best models developed using **(A)** radiomics analysis; **(B)** clinical and imaging variables; and **(C)** combined radiomics scores and clinical/imaging variables.

during bone remodeling and repair (46, 47). According to this mechanism, interferon is used for the treatment of GCTB and has shown some promising efficacy (42, 43, 45). The pharmacologic treatment using interferon may provide an option for unresectable, recurring, and metastatic GCTB that failed the bisphosphonates or denosumab or could not be continued due to complications.

As for p53, mutant p53 is a well-known poor prognostic indicator for many tumors, including sarcoma (11, 12). Previous studies in GCTB have also shown that p53 is an important prognostic marker for predicting local recurrence and lung metastasis in GCTB (48–50). Yalcinkaya et al. reported a significant relationship between p53 expression and local recurrence (p = 0.022) (49). In patients with lung metastases, weakly positive staining was found in GCTB of the tibia and vertebra. However, there are currently no long-term follow-up survival studies after receiving the same surgical procedure using the TES for spinal GCTB to evaluate the specific correlation between p53 status and the prognosis of patients. Our findings provide evidence for this patient cohort through longer-term clinical follow-up. Although many of the potential therapies are at the preclinical testing stage, they may offer a new approach for osteosarcoma treatment based on p53 targeting in the future (44).

Although the IHC biomarkers are known to be important, the assessment will require high-quality tissue specimens for immunohistochemical staining. For preoperative evaluation, biopsy needle puncture may not provide a sufficient amount of tumorous tissue for analysis, and the results might also be affected by the tumor heterogeneity. As shown in our results, imaging may provide information associated with the IHC biomarkers, which can be acquired noninvasively and with a very high spatial resolution covering the entire tumor.

Several clinical variables were considered in the analysis. Among them, the intraoperative bleeding volume and the SINS score were found to be significantly different between the high VEGF and low VEGF groups. SINS was also significantly different between wild-type and mutant p53. The results showed that the spinal instability was associated with the expression of VEGF and p53 as a poor prognostic indicator. This is consistent with the role of SINS related to survival time reported in the literature (51). The amount of bleeding during surgery was greater in the high VEGF group, which was anticipated with the association between VEGF and the abundance of blood supply. The VEGF results may help the orthopedic surgeon estimate the degree of bleeding before surgery and, if necessary, to perform preoperative embolization. However, as a parameter that can only be obtained after surgery, the amount of bleeding is not included in our prediction model. We also found that the Enneking staging was significantly related to the p53 status, which was consistent with previous reports about the role of Enneking staging in planning surgery and adjuvant therapy for bone tumors and tumor-like bone lesions (52).

Imaging has always been an important examination for preoperative tumor evaluation, but most of the previous studies on GCTB focused on tumors of the extremities (53–56), which led to many findings of indicators not applicable to the spinal tumors, such as the distance between the edge of the tumor and joint surface, "paintbrush borders" sign, destruction of posterior cortical bone, and depth of local tumor cell infiltration. Although the majority of GCTB

TABLE 2 | The classification results of three models built using radiomics analysis, clinical and imaging characteristics, and the combined model (high VEGF and mutant p53 as positive).

		Sensitivity	Specificity	Accuracy	AUC
High vs. low VEGF*	Radiomics analysis	44/49 (90%)	27/31 (87%)	71/80 (89%)	0.88
	Clinical + imaging	44/49 (90%)	15/31 (48%)	64/80 (80%)	0.81
	Combined model	41/49 (84%)	27/31 (87%)	68/80 (85%)	0.88
Mutant vs. Wild-type p53	Radiomics analysis	7/12 (58%)	68/68 (100%)	75/80 (94%)	0.79
	Clinical + imaging	5/12 (42%)	61/68 (90%)	66/80 (83%)	0.72
	Combined model	7/12 (58%)	64/68 (94%)	71/80 (89%)	0.77

**VEGF, vascular endothelial growth factor. Low group includes grades 0 and 1 and high group includes grades 2 and 3.*

lesions are located in the metaphysis and epiphyses of the long tubular bones, approximately one-third of tumors are located in the axial skeleton. Our study included some features of spinal GCTB for evaluation but did not find the significance of specific imaging indicators. In this study, the unclear boundary of the lesion was the only feature related to mutant p53, which was consistent with the finding of other MRI studies showing that lesions with unclear boundaries had more aggressive biological behaviors (56, 57).

Radiomics analysis is a high-throughput method to extract a large number of features from radiographic images, which has been shown as a promising method for the diagnosis and further characterization of tumors (58). In this study, we used the SVM with Gaussian kernel for selecting important radiomics features and for building the classification models (59). The kernel in SVM works as a transformation that maps input parameters into a different feature space where the transformed data can be divided more obviously to reach a higher accuracy (60, 61). Other classification models, such as logistic regression and decision trees, work in the original feature space, so less flexible. Meanwhile, the cost function of SVM allows defining margins between different groups. This can improve the robustness of the model and avoid overfitting during the training process. For studies with a limited case number, SVM is considered the best option to balance the variance and bias of the input data (60, 61). In this study, CT imaging was analyzed because it was cost-effective and considered the most commonly used for the management of bone tumors in clinical practice.

Radiomics analysis has also been applied to predict the status of VEGF (angiogenesis) and p53 in various cancers in the literature. Wang et al. investigated the value of a radiomics model based on dynamic contrast-enhanced magnetic resonance imaging (DCE-MRI) and diffusion-weighted imaging (DWI) in estimating the isocitrate dehydrogenase 1 (IDH1) mutation and angiogenesis in gliomas, which suggested that the SVM model showed good performance for predicting the VEGF expression (validation group, AUC = 0.919) (62). Sun et al. developed a machine-learning model for predicting VEGF status in patients with diffuse gliomas, and the AUC was 74.1% in the training group and 70.2% in the validation group (63). Other studies have also applied radiomics based on different imaging techniques to predict the expression status of p53 in epithelial ovarian cancer (64), endometrial carcinoma (65), esophageal squamous cell carcinoma (66), and breast ductal carcinoma (67).

The major limitation was the small sample size identified from a retrospective clinical database. GCTB in the spine was rare, and even in our tertiary hospital specializing in bone diseases, we had to review the records over 10 years to find these cases. Also, to control for the confounding factors of different surgical methods on the progression-free survival, only patients receiving the TES were eligible for this study, which further limited the case number and the difficulty to identify an independent dataset for validation. In our analysis, we applied the 10-fold crossvalidation, so the final model has gone through rigorous validations. Another inherent limitation was the unbalanced dataset for p53 because the mutant p53 was rare. Therefore, in the analysis, we were focusing on the ROC, not the accuracy (68/80 = 85% accuracy, if assuming all cases were wild-type). In addition, some important variables were not detailed in this study, such as age, SINS, Enneking stage, etc. To further refine the description, we performed a Cox regression analysis based on these factors, which is shown in **Supplementary Part 4**. Nonetheless, we believe the results from this difficult-to-obtain dataset can contribute new knowledge to the management of spinal GCTB. The developed models can be applied to prospective patients for further validation.

In summary, our study demonstrates that VEGF and p53 are potential biomarkers for progression-free survival prediction of spinal GCTB patients. Meanwhile, we have shown that radiomics features extracted from preoperative CT imaging can be used to build models for the classification of VEGF and p53 status in spinal GCTB. The capability to predict the aggressive biological phenotype in spinal GCTB based on preoperative information may help to improve management, including choosing optimal treatment strategies and better surveillance protocols.

DATA AVAILABILITY STATEMENT

The raw data supporting the conclusions of this article will be made available by the authors, without undue reservation.

ETHICS STATEMENT

The studies involving human participants were reviewed and approved by Peking University Third Hospital Medical Science Research Ethics Committee. Written informed consent for participation was not required for this study in accordance with the national legislation and the institutional requirements.

AUTHOR CONTRIBUTIONS

Study management and guidance: NL and M-YS. Study design: NL and QW. Clinical data acquisition and analysis: QW and YZ. Imaging data acquisition and analysis: QW, EZ, and XX. Experimental studies: QW, EZ, and YC. Manuscript preparation: QW, YZ, KN, and HY. Manuscript review: NL and MS. All authors listed have made a substantial, direct, and intellectual contribution to the work and approved it for publication.

FUNDING

This study received funding from the National Natural Science Foundation of China (81971578, 81871326) and the Key Clinical Projects of the Peking University Third Hospital (BYSY2018007).

SUPPLEMENTARY MATERIAL

The Supplementary Material for this article can be found online at: https://www.frontiersin.org/articles/10.3389/fonc.2022.894696/full#supplementary-material

REFERENCES

1. Patel S, Chiu RG, Rosinski CL, Ansari D, Chaker AN, Nunna RS, et al. Incidence, Management, and Outcomes of Spinal Giant Cell Tumor of Bone in Adult Patients: A National Cancer Database Analysis. *World Neurosurg* (2020) 144:e296–305. doi: 10.1016/j.wneu.2020.08.135
2. Lin JL, Wu YH, Shi YF, Lin H, Nisar M, Meftah Z, et al. Survival and Prognosis in Malignant Giant Cell Tumor of Bone: A Population-Based Analysis From 1984 to 2013. *J Bone Oncol* (2019) 19:100260. doi: 10.1016/j.jbo.2019.100260
3. Ishihara S, Yamamoto H, Iwasaki T, Toda Y, Yamamoto T, Yoshimoto M, et al. Histological and Immunohistochemical Features and Genetic Alterations in the Malignant Progression of Giant Cell Tumor of Bone: A Possible Association With Tp53 Mutation and Loss of H3k27 Trimethylation. *Mod Pathol* (2021) 35(5):640–48. doi: 10.1038/s41379-021-00972-x
4. Charest-Morin R, Fisher CG, Varga PP, Gokaslan ZL, Rhines LD, Reynolds JJ, et al. En Bloc Resection Versus Intralesional Surgery in the Treatment of Giant Cell Tumor of the Spine. *Spine (Phila Pa 1976)* (2017) 42(18):1383–90. doi: 10.1097/BRS.0000000000002094
5. Tsukamoto S, Righi A, Mavrogenis AF, Akahane M, Honoki K, Tanaka Y, et al. Late Local Recurrence of Bone Giant Cell Tumors Associated With an Increased Risk for Malignant Transformation. *Cancers (Basel)* (2021) 13 (14):3644. doi: 10.3390/cancers13143644
6. Wang J, Du Z, Yang R, Tang X, Yan T, Guo W. Analysis of Clinical Outcome for Adolescent Patients Undergoing Conservative Nerve-Sparing Surgery Based on the Proposed Resection Classification for Sacral Giant Cell Tumor. *J Clin Neurosci* (2020) 80:23–9. doi: 10.1016/j.jocn.2020.07.057
7. Murphey MD, Kransdorf MJ. Staging and Classification of Primary Musculoskeletal Bone and Soft-Tissue Tumors According to the 2020 Who Update, From the Ajr Special Series on Cancer Staging. *AJR Am J Roentgenol* (2021) 217(5):1038–52. doi: 10.2214/AJR.21.25658
8. Watson EC, Adams RH. Biology of Bone: The Vasculature of the Skeletal System. *Cold Spring Harb Perspect Med* (2018) 8(7):a031559. doi: 10.1101/cshperspect.a031559
9. Curylova L, Ramos H, Saraiva L, Skoda J. Noncanonical Roles of P53 in Cancer Stemness and Their Implications in Sarcomas. *Cancer Lett* (2022) 525:131–45. doi: 10.1016/j.canlet.2021.10.037
10. Liu KX, Lamba N, Hwang WL, Niemierko A, DuBois SG, Haas-Kogan DA. Risk Stratification by Somatic Mutation Burden in Ewing Sarcoma. *Cancer* (2019) 125(8):1357–64. doi: 10.1002/cncr.31919
11. Synoradzki KJ, Bartnik E, Czarnecka AM, Fiedorowicz M, Firlej W, Brodziak A, et al. Tp53 in Biology and Treatment of Osteosarcoma. *Cancers (Basel)* (2021) 13(17):4284. doi: 10.3390/cancers13174284
12. Thoenen E, Curl A, Iwakuma T. Tp53 in Bone and Soft Tissue Sarcomas. *Pharmacol Ther* (2019) 202:149–64. doi: 10.1016/j.pharmthera.2019.06.010
13. Song DW, Meng T, Xu W, Hou TH, Lin ZJ, Yin HB, et al. 5-Fluoruracil Blocked Giant Cell Tumor Progression by Suppressing Osteoclastogenesis Through Nf-Kappab Signals and Blocking Angiogenesis. *Bone* (2015) 78:46–54. doi: 10.1016/j.bone.2015.04.047
14. Knowles HJ, Athanasou NA. Hypoxia-Inducible Factor Is Expressed in Giant Cell Tumour of Bone and Mediates Paracrine Effects of Hypoxia on Monocyte-Osteoclast Differentiation *Via* Induction of Vegf. *J Pathol* (2008) 215(1):56–66. doi: 10.1002/path.2319
15. Taylor RM, Kashima TG, Knowles HJ, Athanasou NA. Vegf, Flt3 Ligand, Pigf and Hgf Can Substitute for M-Csf to Induce Human Osteoclast Formation: Implications for Giant Cell Tumour Pathobiology. *Lab Invest* (2012) 92 (10):1398–406. doi: 10.1038/labinvest.2012.108
16. Ferrara N. Vascular Endothelial Growth Factor: Basic Science and Clinical Progress. *Endocr Rev* (2004) 25(4):581–611. doi: 10.1210/er.2003-0027
17. Garcia JR, Clark AY, Garcia AJ. Integrin-Specific Hydrogels Functionalized With Vegf for Vascularization and Bone Regeneration of Critical-Size Bone Defects. *J BioMed Mater Res A* (2016) 104(4):889–900. doi: 10.1002/jbm.a.35626
18. Hu K, Olsen BR. The Roles of Vascular Endothelial Growth Factor in Bone Repair and Regeneration. *Bone* (2016) 91:30–8. doi: 10.1016/j.bone.2016.06.013
19. Vogelstein B, Kinzler KW. P53 Function and Dysfunction. *Cell* (1992) 70 (4):523–6. doi: 10.1016/0092-8674(92)90421-8
20. Hainaut P, Hollstein M. P53 and Human Cancer: The First Ten Thousand Mutations. *Adv Cancer Res* (2000) 77:81–137. doi: 10.1016/s0065-230x(08)60785-x
21. Zhang J, Dong J, Yang ZZ, Ma X, Zhang JL, Li M, et al. Expression of Ezrin, Cd44, and Vegf in Giant Cell Tumor of Bone and Its Significance. *World J Surg Oncol* (2015) 13:168. doi: 10.1186/s12957-015-0579-5
22. Han YH, Gao B, Huang JH, Wang Z, Guo Z, Jie Q, et al. Expression of Cd147, Pcna, Vegf, Mmps and Their Clinical Significance in the Giant Cell Tumor of Bones. *Int J Clin Exp Patho* (2015) 8(7):8446–52.
23. Fu S, Bai R, Zhao Z, Zhang Z, Zhang G, Wang Y, et al. Overexpression of Hypoxia-Inducible Factor-1alpha and Vascular Endothelial Growth Factor in Sacral Giant Cell Tumors and the Correlation With Tumor Microvessel Density. *Exp Ther Med* (2014) 8(5):1453–8. doi: 10.3892/etm.2014.1971
24. Lujic N, Sopta J, Kovacevic R, Stevanovic V, Davidovic R. Recurrence of Giant Cell Tumour of Bone: Role of P53, Cyclin D1, Beta-Catenin and Ki67. *Int Orthop* (2016) 40(11):2393–9. doi: 10.1007/s00264-016-3292-2
25. Cheng DD, Hu T, Zhang HZ, Huang J, Yang QC. Factors Affecting the Recurrence of Giant Cell Tumor of Bone After Surgery: A Clinicopathological Study of 80 Cases From a Single Center. *Cell Physiol Biochem* (2015) 36 (5):1961–70. doi: 10.1159/000430164
26. Oda Y, Sakamoto A, Saito T, Matsuda S, Tanaka K, Iwamoto Y, et al. Secondary Malignant Giant-Cell Tumour of Bone: Molecular Abnormalities of P53 and H-Ras Gene Correlated With Malignant Transformation. *Histopathology* (2001) 39(6):629–37. doi: 10.1046/j.1365-2559.2001.01275.x
27. Fisher CG, DiPaola CP, Ryken TC, Bilsky MH, Shaffrey CI, Berven SH, et al. A Novel Classification System for Spinal Instability in Neoplastic Disease: An Evidence-Based Approach and Expert Consensus From the Spine Oncology Study Group. *Spine (Phila Pa 1976)* (2010) 35(22):E1221–9. doi: 10.1097/BRS.0b013e3181e16ae2
28. MacDowall A, Skeppholm M, Robinson Y, Olerud C. Validation of the Visual Analog Scale in the Cervical Spine. *J Neurosurg Spine* (2018) 28(3):227–35. doi: 10.3171/2017.5.SPINE1732
29. Yokogawa N, Murakami H, Demura S, Kato S, Yoshioka K, Shimizu T, et al. Total Spondylectomy for Enneking Stage Iii Giant Cell Tumor of the Mobile Spine. *Eur Spine J* (2018) 27(12):3084–91. doi: 10.1007/s00586-018-5761-3
30. Wichmann JL, Willemink MJ, De Cecco CN. Artificial Intelligence and Machine Learning in Radiology: Current State and Considerations for Routine Clinical Implementation. *Invest Radiol* (2020) 55(9):619–27. doi: 10.1097/RLI.0000000000000673
31. Bera K, Braman N, Gupta A, Velcheti V, Madabhushi A. Predicting Cancer Outcomes With Radiomics and Artificial Intelligence in Radiology. *Nat Rev Clin Oncol* (2021) 19(2):132–46. doi: 10.1038/s41571-021-00560-7
32. Limkin EJ, Sun R, Dercle L, Zacharaki EI, Robert C, Reuze S, et al. Promises and Challenges for the Implementation of Computational Medical Imaging (Radiomics) in Oncology. *Ann Oncol* (2017) 28(6):1191–206. doi: 10.1093/annonc/mdx034
33. Harding-Theobald E, Louissaint J, Maraj B, Cuaresma E, Townsend W, Mendiratta-Lala M, et al. Systematic Review: Radiomics for the Diagnosis and Prognosis of Hepatocellular Carcinoma. *Aliment Pharm Ther* (2021) 54 (7):890–901. doi: 10.1111/apt.16563
34. Guiot J, Vaidyanathan A, Deprez L, Zerka F, Danthine D, Frix AN, et al. A Review in Radiomics: Making Personalized Medicine a Reality *Via* Routine Imaging. *Med Res Rev* (2021) 42(1):426–40. doi: 10.1002/med.21846
35. Lambin P, Rios-Velazquez E, Leijenaar R, Carvalho S, van Stiphout RGPM, Granton P, et al. Radiomics: Extracting More Information From Medical Images Using Advanced Feature Analysis. *Eur J Cancer* (2012) 48(4):441–6. doi: 10.1016/j.ejca.2011.11.036
36. Veeraraghavan H, Friedman CF, DeLair DF, Nincevic J, Himoto Y, Bruni SG, et al. Machine Learning-Based Prediction of Microsatellite Instability and High Tumor Mutation Burden From Contrast-Enhanced Computed Tomography in Endometrial Cancers. *Sci Rep-Uk* (2020) 10(1):17769. doi: 10.1038/s41598-020-72475-9
37. Katsoulakis E, Yu Y, Apte AP, Leeman JE, Katabi N, Morris L, et al. Radiomic Analysis Identifies Tumor Subtypes Associated With Distinct Molecular and Microenvironmental Factors in Head and Neck Squamous Cell Carcinoma. *Oral Oncol* (2020) 110:104877. doi: 10.1016/j.oraloncology.2020.104877
38. Chen BHT, Chen ZK, Ye NR, Mambetsariev I, Fricke J, Daniel E, et al. Differentiating Peripherally-Located Small Cell Lung Cancer From Non-Small

Cell Lung Cancer Using a Ct Radiomic Approach. *Front Oncol* (2020) 10:593. doi: 10.3389/fonc.2020.00593
39. Fourney DR, Frangou EM, Ryken TC, DiPaola CP, Shaffrey CI, Berven SH, et al. Spinal Instability Neoplastic Score: An Analysis of Reliability and Validity From the Spine Oncology Study Group. *J Clin Oncol* (2011) 29 (22):3072–7. doi: 10.1200/Jco.2010.34.3897
40. Remmele W, Stegner HE. [Recommendation for Uniform Definition of an Immunoreactive Score (Irs) for Immunohistochemical Estrogen Receptor Detection (Er-Ica) in Breast Cancer Tissue]. *Pathologe* (1987) 8(3):138–40. doi: 10.1007/s00125-008-1203-9
41. Goodwin CR, Abu-Bonsrah N, Bilsky MH, Reynolds JJ, Rhines LD, Laufer I, et al. Clinical Decision Making: Integrating Advances in the Molecular Understanding of Spine Tumors. *Spine (Phila Pa 1976)* (2016) 41 Suppl 20: S171–S7. doi: 10.1097/BRS.0000000000001836
42. Gong T, Luo Y, Wang Y, Zheng C, Fang J, Min L, et al. Multiple Pulmonary Metastases of Recurrent Giant Cell Tumor of Bone With Expression of Vegfr-2 Successfully Controlled by Denosumab and Apatinib: A Case Report and Literature Review. *Cancer Manag Res* (2021) 13:4447–54. doi: 10.2147/CMAR.S312846
43. Zhu B, Li J, Xie Q, Diao L, Gai L, Yang W. Efficacy and Safety of Apatinib Monotherapy in Advanced Bone and Soft Tissue Sarcoma: An Observational Study. *Cancer Biol Ther* (2018) 19(3):198–204. doi: 10.1080/15384047.2017.1416275
44. Sanz G, Singh M, Peuget S, Selivanova G. Inhibition of P53 Inhibitors: Progress, Challenges and Perspectives. *J Mol Cell Biol* (2019) 11(7):586–99. doi: 10.1093/jmcb/mjz075
45. Li J, Zhao X, Chen L, Guo H, Lv F, Jia K, et al. Safety and Pharmacokinetics of Novel Selective Vascular Endothelial Growth Factor Receptor-2 Inhibitor Yn968d1 in Patients With Advanced Malignancies. *BMC Cancer* (2010) 10:529. doi: 10.1186/1471-2407-10-529
46. Mery B, Espenel S, Guy JB, Rancoule C, Vallard A, Aloy MT, et al. Biological Aspects of Chondrosarcoma: Leaps and Hurdles. *Crit Rev Oncol Hematol* (2018) 126:32–6. doi: 10.1016/j.critrevonc.2018.03.009
47. Boulytcheva IV, Soloviev YN, Kushlinskii NE, Mahson AN. Expression of Molecular Markers in the Tumor and Survival Prognosis in Osteosarcoma. *Bull Exp Biol Med* (2010) 150(2):237–42. doi: 10.1007/s10517-010-1114-x
48. Gong L, Liu W, Sun X, Sajdik C, Tian X, Niu X, et al. Histological and Clinical Characteristics of Malignant Giant Cell Tumor of Bone. *Virchows Arch* (2012) 460(3):327–34. doi: 10.1007/s00428-012-1198-y
49. Yalcinkaya U, Ugras N, Kabul S, Ocakoglu G, Bilgen MS. Prognostic Value of P53 Protein Expression in Giant Cell Tumor of Bone. *Pol J Pathol* (2015) 66 (4):389–96. doi: 10.5114/pjp.2015.57252
50. Chen S, Li C, Wu B, Zhang C, Liu C, Lin X, et al. Identification of Differentially Expressed Genes and Their Subpathways in Recurrent Versus Primary Bone Giant Cell Tumors. *Int J Oncol* (2014) 45(3):1133–42. doi: 10.3892/ijo.2014.2501
51. Donnellan CJ, Roser S, Maharaj MM, Davies BN, Ferch R, Hansen MA. Outcomes for Vertebrectomy for Malignancy and Correlation to the Spine Instability Neoplastic Score (Sins): A 10-Year Single-Center Perspective. *World Neurosurg* (2020) 138:e151–e9. doi: 10.1016/j.wneu.2020.02.048
52. Nogueira Drumond JM. Efficacy of the Enneking Staging System in Relation to Treating Benign Bone Tumors and Tumor-Like Bone Lesions. *Rev Bras Ortop* (2010) 45(1):46–52. doi: 10.1016/S2255-4971(15)30216-0
53. Chen L, Shi XL, Zhou ZM, Qin LD, Liu XH, Jiang L, et al. Clinical Significance of Mri and Pathological Features of Giant Cell Tumor of Bone Boundary. *Orthop Surg* (2019) 11(4):628–34. doi: 10.1111/os.12510
54. Zhou L, Zhu H, Lin S, Jin H, Zhang Z, Dong Y, et al. Computerised Tomography Features of Giant Cell Tumour of the Knee Are Associated With Local Recurrence After Extended Curettage. *Int Orthop* (2021) 46 (2):381–90. doi: 10.1007/s00264-021-05260-6
55. Parmeggiani A, Miceli M, Errani C, Facchini G. State of the Art and New Concepts in Giant Cell Tumor of Bone: Imaging Features and Tumor Characteristics. *Cancers (Basel)* (2021) 13(24):6298. doi: 10.3390/cancers13246298
56. He Y, Zhou Y, Zhang J, Yuan F, Wang J, Du L, et al. Tumor Immunohistochemistry and Preoperative Magnetic Resonance Imaging Features Predict Local Recurrence of Giant Cell Tumor of Bone Following Intralesional Curettage. *Oncol Lett* (2019) 17(2):1425–34. doi: 10.3892/ol.2018.9778
57. He Y, Wang J, Zhang J, Du L, Lu Y, Xu J, et al. Magnetic Resonance Feature of "Paintbrush Borders" Sign as a Novel Way to Predict Recurrence of Giant Cell Tumor of Bone After Curettage: A Pilot Study. *J Int Med Res* (2018) 46 (2):710–22. doi: 10.1177/0300060517720345
58. Lambin P, Rios-Velazquez E, Leijenaar R, Carvalho S, van Stiphout RG, Granton P, et al. Radiomics: Extracting More Information from Medical Images Using Advanced Feature Analysis. *Eur J Cancer* (2012) 48(4):441–6. doi: 10.1016/j.ejca.2011.11.036
59. Nasrabadi NM. Pattern Recognition and Machine Learning. *J electronic Imaging* (2007) 16(4):049901. doi: 10.1117/1.2819119
60. Drucker H, Burges CJ, Kaufman L, Smola AJ, Vapnik V. Support Vector Regression Machines. *In: Proceedings of the 9th International Conference on Neural Information Processing Systems* (1996) (Cambridge, MA, USA: MIT Press):155–61.
61. Tong S, Chang E. Support Vector Machine Active Learning for Image Retrieval. In: *Proceedings of the Ninth ACM International Conference on Multimedia*. (New York, NY, USA: Association for Computing Machinery) (2001):107–18.
62. Wang J, Hu Y, Zhou X, Bao S, Chen Y, Ge M, et al. A Radiomics Model Based on Dce-Mri and Dwi May Improve the Prediction of Estimating Idh1 Mutation and Angiogenesis in Gliomas. *Eur J Radiol* (2022) 147:110141. doi: 10.1016/j.ejrad.2021.110141
63. Sun Z, Li Y, Wang Y, Fan X, Xu K, Wang K, et al. Radiogenomic Analysis of Vascular Endothelial Growth Factor in Patients With Diffuse Gliomas. *Cancer Imaging* (2019) 19(1):68. doi: 10.1186/s40644-019-0256-y
64. Wang F, Wang Y, Zhou Y, Liu C, Liang D, Xie L, et al. Apparent Diffusion Coefficient Histogram Analysis for Assessing Tumor Staging and Detection of Lymph Node Metastasis in Epithelial Ovarian Cancer: Correlation With P53 and Ki-67 Expression. *Mol Imaging Biol* (2019) 21(4):731–9. doi: 10.1007/s11307-018-1295-7
65. Jiang X, Jia H, Zhang Z, Wei C, Wang C, Dong J. The Feasibility of Combining Adc Value With Texture Analysis of T2wi, Dwi and Ce-T1wi to Preoperatively Predict the Expression Levels of Ki-67 and P53 of Endometrial Carcinoma. *Front Oncol* (2021) 11:805545. doi: 10.3389/fonc.2021.805545
66. Wang Y, Bai G, Zhang X, Shan W, Xu L, Chen W. Correlation Analysis of Apparent Diffusion Coefficient Value and P53 and Ki-67 Expression in Esophageal Squamous Cell Carcinoma. *Magn Reson Imaging* (2020) 68:183–9. doi: 10.1016/j.mri.2020.01.011
67. Wu L, Zhao Y, Lin P, Qin H, Liu Y, Wan D, et al. Preoperative Ultrasound Radiomics Analysis for Expression of Multiple Molecular Biomarkers in Mass Type of Breast Ductal Carcinoma *in Situ*. *BMC Med Imaging* (2021) 21(1):84. doi: 10.1186/s12880-021-00610-7

Conflict of Interest: The authors declare that the research was conducted in the absence of any commercial or financial relationships that could be construed as a potential conflict of interest.

frontiers | Frontiers in Oncology

ORIGINAL RESEARCH
published: 06 July 2022
doi: 10.3389/fonc.2022.927077

Preoperative Prediction of Lymph Node Metastasis of Pancreatic Ductal Adenocarcinoma Based on a Radiomics Nomogram of Dual-Parametric MRI Imaging

Lin Shi[1†], *Ling Wang*[1†], *Cuiyun Wu*[1], *Yuguo Wei*[2], *Yang Zhang*[1] *and Junfa Chen*[1*]

[1] Cancer Center, Department of Radiology, Zhejiang Provincial People's Hospital (Affiliated People's Hospital, Hangzhou Medical College), Hangzhou, China, [2] Precision Health Institution, General Electric Healthcare, Hangzhou, China

OPEN ACCESS

Edited by:
Jiansong Ji,
Lishui Central Hospital, China

Reviewed by:
Gaofeng Shu,
Wenzhou Medical University, China
Weiqi Rong,
Chinese Academy of Medical Sciences and Peking Union Medical College, China

***Correspondence:**
Junfa Chen
cjf2002@126.com

[†]*These authors have contributed equally to this work*

Specialty section:
This article was submitted to Cancer Imaging and Image-directed Interventions, a section of the journal Frontiers in Oncology

Received: *23 April 2022*
Accepted: *06 June 2022*
Published: *06 July 2022*

Citation:
Shi L, Wang L, Wu C, Wei Y, Zhang Y and Chen J (2022) Preoperative Prediction of Lymph Node Metastasis of Pancreatic Ductal Adenocarcinoma Based on a Radiomics Nomogram of Dual-Parametric MRI Imaging. Front. Oncol. 12:927077. doi: 10.3389/fonc.2022.927077

Purpose: This study aims to uncover and validate an MRI-based radiomics nomogram for detecting lymph node metastasis (LNM) in pancreatic ductal adenocarcinoma (PDAC) patients prior to surgery.

Materials and Methods: We retrospectively collected 141 patients with pathologically confirmed PDAC who underwent preoperative T2-weighted imaging (T2WI) and portal venous phase (PVP) contrast-enhanced T1-weighted imaging (T1WI) scans between January 2017 and December 2021. The patients were randomly divided into training (n = 98) and validation (n = 43) cohorts at a ratio of 7:3. For each sequence, 1037 radiomics features were extracted and analyzed. After applying the gradient-boosting decision tree (GBDT), the key MRI radiomics features were selected. Three radiomics scores (rad-score 1 for PVP, rad-score 2 for T2WI, and rad-score 3 for T2WI combined with PVP) were calculated. Rad-score 3 and clinical independent risk factors were combined to construct a nomogram for the prediction of LNM of PDAC by multivariable logistic regression analysis. The predictive performances of the rad-scores and the nomogram were assessed by the area under the operating characteristic curve (AUC), and the clinical utility of the radiomics nomogram was assessed by decision curve analysis (DCA).

Results: Six radiomics features of T2WI, eight radiomics features of PVP and ten radiomics features of T2WI combined with PVP were found to be associated with LNM. Multivariate logistic regression analysis showed that rad-score 3 and MRI-reported LN status were independent predictors. In the training and validation cohorts, the AUCs of rad-score 1, rad-score 2 and rad-score 3 were 0.769 and 0.751, 0.807 and 0.784, and 0.834 and 0.807, respectively. The predictive value of rad-score 3 was similar to that of rad-score 1 and rad-score 2 in both the training and validation cohorts ($P > 0.05$). The radiomics nomogram constructed by rad-score 3 and MRI-reported LN status showed encouraging clinical benefit, with an AUC of 0.845 for the training cohort and 0.816 for the validation cohort.

Conclusions: The radiomics nomogram derived from the rad-score based on MRI features and MRI-reported lymph status showed outstanding performance for the preoperative prediction of LNM of PDAC.

Keywords: pancreatic ductal adenocarcinoma, magnetic resonance imaging, radiomics, lymph node metastasis, nomogram

Pancreatic cancer, as a highly malignant gastrointestinal tumor, has a five-year mortality rate close to its morbidity rate (1, 2). Pancreatic ductal adenocarcinoma (PDAC) is the predominant histological subtype, accounting for 85% of all pancreatic cancer cases (3). Schwarz et al. (4) conducted a retrospective analysis of 2787 patients who underwent surgical resection (SR) for pancreatic cancer in the United States and found that 54% of patients had lymph node metastasis (LNM), suggesting that LNM is a potential key to assess the state of the disease, as it influences the formulation of surgical procedures and patient prognosis (5). Different preoperative noninvasive examinations, including computed tomography (CT), magnetic resonance imaging (MRI) and positron emission tomography (PET), are commonly used to identify LNM of pancreatic cancer (6–11). Unfortunately, all of these technologies are still inadequate for assessing LNM status because enlarged lymph nodes are often caused by nonspecific inflammation (12). In addition, although endoscopic ultrasonography (EUS) has high sensitivity for the diagnosis of pancreatic primary lesions and LNM and sufficient histological information can be obtained from a small sample of tissue, it is an invasive method (13, 14). Its use is also limited by several other factors, such as the focal size and surrounding anatomical environment, yielding an accuracy of 41-86% for lymph node staging of pancreatic adenocarcinoma (14). Recent studies have shown that Ki-67 and serum MMP7 have the potential to predict LNM, but their sensitivities remain insufficient (15, 16).

Radiomics approaches allow for the quantitative analysis of images and can reflect heterogeneity in the region of interest (ROI), providing more information through feature analysis than can be recognized by the naked eye, making it helpful for clarifying the nature of lesions (17). T2-weighted imaging (T2WI) and the dynamic enhanced portal venous phase (PVP) of MRI can better depict the biological characteristics of pancreatic lesions and have therefore been applied to radiomics studies of pancreatic cancer (18–20), including for differential diagnosis, prognosis evaluations, and treatment response predictions. Although studies have shown that radiomics can be used for the preoperative prediction of LNM of malignant tumors (21–24), few radiomics studies based on MRI image texture analysis have been conducted for the preoperative prediction of LNM of PDAC. Therefore, this study aimed to explore whether the use of T2WI and PVP features was feasible for predicting LNM of PDAC. We sought to develop and validate a radiomics nomogram as a noninvasive and feasible approach for the preoperative detection of LNM in PDAC patients.

MATERIALS AND METHODS

Patients

This study was approved by the Ethics Committee of the Zhejiang Provincial People's Hospital, Affiliated People's Hospital of Hangzhou Medical College. The requirement for informed consent was waived due to the retrospective nature of this study. Clinical and MRI databases of patients were retrospectively reviewed to identify candidate patients who were treated between January 2017 and December 2021. The inclusion criteria were as follows: (1) patients who received radical resection and regional lymph node dissection for PDAC diagnosed by postoperative pathology and (2) patients with PDAC who underwent dynamic enhancement MRI scanning within two weeks before SR. The exclusion criteria were as follows: (1) images with artifacts that affected lesion observation; (2) patients who received any treatment for PDAC before SR, such as neoadjuvant chemoradiotherapy; and (3) patients with PDAC and other malignant tumors. Among the 141 patients who met these criteria, 58 were diagnosed with LNM. All patients were randomly divided into training (n = 98) and validation (n = 43) cohorts at a ratio of 7:3. Clinical data of the patients were collected, including sex, age, primary tumor site, the maximum diameter of the tumor, MRI tumor stage (mTs), MRI-reported lymph node status, and the levels of carbohydrate antigen 19-9 (CA19-9), carbohydrate antigen 125 (CA125) and carcinoma embryonic antigen (CEA). A positive lymph node on MRI was defined as a nodule at least 10 mm in the short-axis diameter or a nodule with a round shape, heterogeneous enhancement and low ADC value (25). The patient selection flowchart is shown in **Figure 1**.

MRI Protocol

MRI was performed with a 3.0 T Discovery MR 750 scanner (GE Healthcare, Waukesha, WI, United States). (1) The following parameters were used for fat-suppressed fast spin-echo T2-weighted imaging (T2WI): repetition time (TR)/echo time (TE), 12000/72 ms; matrix size, 320 × 320; field of view (FOV), 360 × 360 mm^2; slice thickness, 3 mm; spacing between slices, 0.6 mm; number of excitation (NEX), 2; and bandwidth, 83.3 kHz. (2) Gd-diethylenetriamine pentaacetic acid (Gd-DTPA) was injected at a dose of 0.1 mmol/kg through the median cubital vein at an injection rate of 2.0 mL/s, followed by 15 ml of saline at the same flow rate. A fat-suppressed T1-weighted three-dimensional (3D) gradient-recalled-echo sequence was used to collect dynamic enhanced images with the following parameters: TR/TE, 4.1/1.2 ms; matrix size, 260 × 240; FOV, 360 × 360 mm^2;

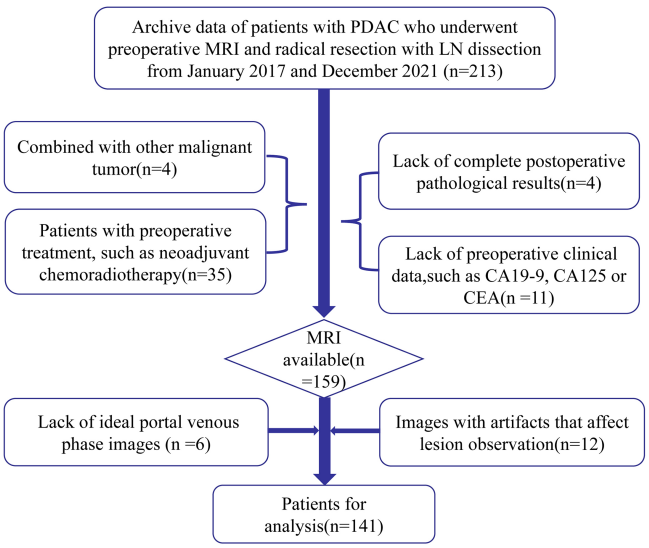

FIGURE 1 | Patient selection flowchart.

slice thickness, 3 mm; spacing between slices, 0 mm; NEX, 1; and bandwidth, 142.8 kHz. The late arterial phase (LAP), portal venous phase (PVP), and delayed phase (DP) were acquired at 25 seconds, 45 seconds, and 80 seconds. Other scanning sequence conditions not used for radiomics are not listed in this study.

Tumor Segmentation and Feature Extraction

Using ITK-SNAP software (26) (**Figure 2**), segmentation of the regions of interest (ROIs) was performed by two independent radiologists with 5 and 15 years of experience in abdominal radiology, named reader 1 and reader 2, respectively. With reference to diffusion weighted imaging (DWI) and dynamic enhanced images, 3D ROIs based on T2WI and PVP were drawn manually. Features of ROIs were extracted by PHIgo software (GE Healthcare, V1.2.0, China), which is based on pyradiomics, and complies with the image biomarker standardization initiative (IBSI) (27). Prior to this, all images underwent standardized preprocessing, including image resampling at the same resolution (1*1*1 mm^3) and dividing the gray level into grades 1-10. A total of 1037 features were obtained, including first-order features, shape features, gray level cooccurrence matrix (GLCM) features, gray level size zone matrix (GLSZM) features, gray level run length matrix (GLRLM) features, neighboring gray tone difference matrix (NGTDM) features and gray level dependence matrix (GLDM) features. The stability and reliability were evaluated using intraclass correlation coefficients (ICCs) by comparing 30 random patients' ROIs drawn by reader 1 and reader 2. Features with ICC values > 0.8 were interpreted as almost perfect and recorded.

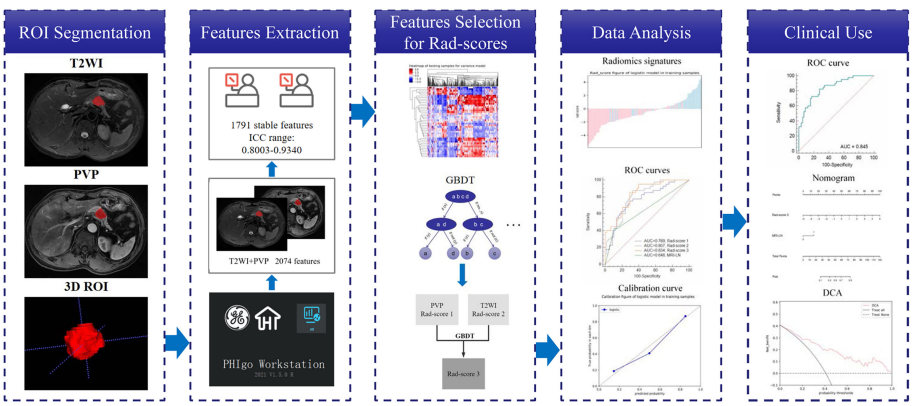

FIGURE 2 | Radiomics and model construction workflow.

Dimensionality Reduction and Radiomics Score Calculation

Dimensionality reduction for T2WI and PVP was performed using analysis of variance and the Mann–Whitney U test, Spearman's correlation, and gradient boosting decision tree (GBDT) in sequence. Combining the selected features from T2WI and PVP, GBDT was again used to select significant features. Radiomics scores (rad-score 1, rad-score 2 and rad-score 3) were calculated based on the remaining features from T2WI, PVP and T2WI combined with PVP by multivariate logistic regression.

Radiomics Nomogram Development and Evaluation

Univariate logistic regression analysis and multivariate logistic regression analysis were performed with the clinical characteristics and rad-score 3 to identify potential and independent predictors of LNM, respectively (28). Finally, a radiomics nomogram was constructed with the identified predictors of LNM. The Hosmer–Lemeshow test and calibration curves were used to assess the goodness-of-fit and calibration of the nomogram (29). The predictive performances of the clinical model, three rad-scores, and the nomogram for LNM were evaluated by receiver operator characteristic (ROC) curve analysis, and the areas under the curve (AUCs) were calculated. Decision curve analysis (DCA) was performed to determine the clinical efficiency of the nomogram.

Statistical Analysis

The data were analyzed by SPSS 22.0 (IBM Corporation), MedCalc (Version 14.10.20) and Microsoft R Open (version 3.3.1) software. Univariate analysis was used to assess the correlations between the clinical characteristics and LNM, with the chi-square test used for categorical variables and the two-sample t test used for continuous variables. Normality was assessed by the Kolmogorov–Smirnov test. The variables that followed a normal distribution are expressed as the mean ± standard deviation, and nonnormally distributed variables are expressed as the median (interquartile range). The De-Long test was used for statistical comparison of the AUCs of the models. Calibration plots and DCA were performed using the "rms" and "dca" packages in R (Microsoft R Open; version 3.3.1), respectively. All statistical tests were two-tailed, and significance was set at $P<0.05$.

RESULTS

Clinical Characteristics

There were no significant differences in any of the clinical characteristics between the training and validation cohorts (**Table 1**), and the LN positivity rate was not significantly different between the two cohorts (40.8% (40/98) vs. 41.9% (18/43), respectively; P=0.908). The only significant difference among the clinical characteristics was in the MRI-reported LNM status between patients with LNM and those with non-lymph node metastasis (nLNM) in both the training and validation cohorts ($P<0.05$) (**Table 1**).

Radiomics Signature Development and Rad-Score Calculation

The ICC values for feature extraction between reader 1 and reader 2 ranged from 0.773 to 0.934, suggesting high agreement. A total of 1791 features were proven to have high consistency (ICCs: 0.8003-0.934). For the T2WI and PVP sequences, analysis of variance and the Mann-Whitney U test identified 480 and 478 important features, respectively. Following Spearman correlation analysis, the number of important features was reduced to 14 and 19. Finally, 6 and 8 features were ultimately identified by further GBDT dimensionality reduction. The corresponding rad-scores (1 and 2) were calculated based on the retained features included in the multivariable logistic regression. After merging the 14 features and using GBDT again, 10 features were obtained to calculate rad-score 3. Various features and coefficients of rad-score 3 are shown in **Table 2**, which are all wavelet features. The three rad-scores were significantly different between LNM and nLNM patients in both the training and validation cohorts ($P<0.01$), but there was no difference between the cohorts (**Table 1**).

Rad-Score Evaluation

The ROC curve demonstrates the predictive performance of the clinical model, rad-score 1, rad-score 2, and rad-score 3, as shown in **Figure 3**. In the training and validation cohorts, the AUCs of the clinical model, rad-score 1, rad-score 2 and rad-score 3 were 0.648, 0.642; 0.769, 0.751; 0.807, 0.784 and 0.834, 0.807, respectively. The thresholds for predicting LNM using rad-score 1, rad-score 2, and rad-score 3 were -0.441, -0.696, and -0.807, respectively, in the training cohort. Although the AUC value of rad-score 3 was the largest among the rad-scores in both the training and validation cohorts, the difference was not significant. Rad-score 2 and rad-score 3 had higher predictive efficacy than the clinical model in the training cohort ($P<0.05$), while rad-score 3 showed better performance than the clinical model in the validation cohort ($P<0.05$). Detailed results are shown in **Table 3**.

Radiomics Nomogram Construction and Evaluation

The results of the univariate and multivariate logistic regression analyses are presented in **Table 4**. Univariate analysis revealed significant differences in the MRI-reported lymph node status and rad-score 3 between LNM and nLNM patients in the training cohort, and they were identified as independent predictors of LNM by multivariate logistic regression analysis. The radiomics nomogram constructed by incorporating independent predictors is shown in **Figure 4**. The Hosmer–Lemeshow test showed good calibration of the nomogram in both the training and validation cohorts ($P=0.938$ and 0.924), and the calibration curves exhibited good calibration ability (**Figure 5**). The AUC values of the nomogram for predicting LNM of PDAC in the training and validation cohorts were 0.845 [95% confidence interval (CI), 0.777-0.907] and 0.816 (95% CI,

TABLE 1 | Patients' clinical characteristics and rad-scores in the training and validation cohorts.

Characteristic	Training		*P*	Validation		*P*	*P*
	nLNM	LNM		nLNM	LNM		
Age, mean ± SD	64.9 ± 9.60	64.65 ± 9.55	0.873	65.84 ± 6.79	64.28 ± 9.11	0.523	0.833
Sex							
Female, n (%)	19 (51.4%)	39 (63.9%)	0.219	9 (69.2%)	16 (53.3%)	0.332	0.390
Male, n (%)	18 (48.6%)	22 (36.1%)		4 (30.8%)	14 (46.7%)		
Location							
Head/neck, n (%)	30 (52.6%)	28 (68.3%)	0.120	13 (56.5%)	12 (60%)	0.818	0.606
Body/tail, n (%)	27 (47.4%)	13 (31.7%)		10 (43.5%)	8 (40%)		
Size (mm), median (IQR)	33.0 (25.0, 40.0)	33.0 (25.0, 41.5)	0.876	27.0 (20.0, 37.5)	34.0 (26.5, 41.3)	0.113	0.368
CA19-9 (U/ml), median (IQR)	116.80 (55.35, 366.85)	207.05 (75.58, 853.40)	0.120	86.3 (23.5, 214.75)	271.85 (63.03, 879.38)	0.028	0.478
CA125 (U/ml), median (IQR)	17.95 (10.70, 27.33)	16.90 (9.95, 31.9)	0.680	14.5 (7.2, 19.55)	22.25 (10.65, 45.83)	0.402	0.389
CEA (μg/ml), median (IQR)	3.35 (2.08, 5.95)	4.15 (2.28, 7.73)	0.278	3.30 (2.40, 5.35)	3.90 (2.58, 5.95)	0.076	0.846
mTs							
T1-2, n (%)	40 (59.7%)	18 (58.1%)	0.878	15 (60%)	10 (55.6%)	0.771	0.240
T3-4, n (%)	27 (40.3%)	13 (41.9%)		10 (40%)	8 (44.4%)		
MRI-reported LN status							
Negative, n (%)	51 (89.5%)	24 (60.0%)	0.001	21 (84.0%)	4 (55.6%)	0.04	0.439
Positive, n (%)	6 (10.5%)	16 (40.0%)		10 (16.0%)	8 (44.4%)		
Rad-score 1, mean ± SD	-0.921 ± 1.048	0.316 ± 1.424	0.000	-0.890 ± 0.946	0.035 ± 1.134	0.008	0.713
Rad-score 2, mean ± SD	-1.268 ± 1.626	0.611 ± 2.498	0.000	-1.364 ± 1.946	0.516 ± 2.498	0.006	0.841
Rad-score 3, mean ± SD	-1.351 ± 1.439	0.693 ± 1.579	0.000	-1.932 ± 1.573	-0.463 ± 1.654	0.005	0.722

SD, standard deviation; mTs, MRI tumor stage; IQR, interquartile range; LNM, lymph node metastasis; nLNM, non-lymph node metastasis.

0.698-0.914), with AUCs of 0.828 and 0.680 for specificity and AUCs of 0.700 and 0.722 for sensitivity, respectively. ROC curves are shown in **Figure 6**. The DCA results for the validation cohort are shown in **Figure 7**. We found that the nomogram can obtain better net benefits than the "treat-all" or "treat-none" strategies under a wide probability threshold.

DISCUSSION

PDAC is a gastrointestinal tumor with extremely high malignancy and poor prognosis, which is largely attributed to difficulties in early diagnosis and the limited number of treatment options available for this disease (1). Lymph node status is the key factor in developing appropriate treatment strategies and improving the prognosis of patients (30, 31). However, traditional MRI can only make a preoperative diagnosis of LNM according to the lymph node size, morphology and signal characteristics, which can be subjective, leading to low diagnostic sensitivity (11, 12, 32). In our study, we obtained a sensitivity of 40%, similar to the literature. Moreover, logistic regression analysis showed that MRI-reported lymph node status was the only independent risk factor among all the clinical characteristics analyzed. A previous study reported that CT-reported lymph node status was the only independent risk factor, but it had relatively low predictive efficacy (AUC=0.63) (33). Although the CA19-9 level may predict the prognosis of patients with pancreatic cancer (20, 34, 35), it could not be confirmed as a risk factor for preoperative LNM in our study, which warrants further investigation.

Radiomics is an advanced method for quantitative analysis that can reveal information from microscopic features that are not easily observable by the naked eye in medical imaging (17, 36). In recent years, various studies have attempted to predict

TABLE 2 | Radiomics features selected by GBDT.

Characteristic	β	OR	95% CI
PVP_wavelet-LLH_firstorder_Minimum	0.012	1.012	0.589,1.710
PVP_wavelet-LLH_glszm_SizeZoneNonUniformity	0.231	1.260	0.685,2.316
PVP_wavelet-LHH_glcm_MaximumProbability	0.790	2.203	1.132,4.289
PVP_wavelet-HHL_glcm_ClusterTendency	-0.519	0.595	0.343,1.034
PVP_wavelet-HHH_glszm_SmallAreaEmphasis	0.791	2.205	0.256,3.872
T2WI_wavelet-LLH_firstorder_Mean	0.971	2.640	1.276,5.462
T2WI_wavelet-HLH_glcm_ClusterShade	0.921	2.513	1.152,5.484
T2WI_wavelet-HHL_glcm_Correlation	0.473	1.604	0.903,2.852
T2WI_wavelet-HHH_gldm_DependenceNonUniformityNormalized	0.542	1.719	0.958,3.086
T2WI_wavelet-LLL_firstorder_Kurtosis	-0.641	0.527	0.273,1.016

OR, odds ratio; CI, confidence interval.

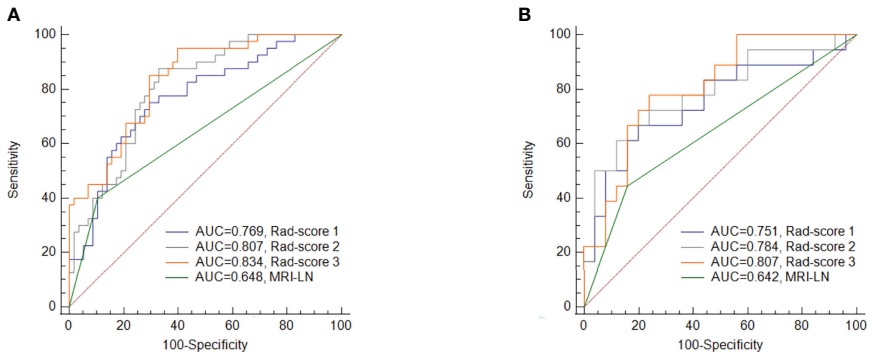

FIGURE 3 | Comparisons of the ROC curves for MRI-reported LN status and the three rad-scores in the training cohort **(A)** and validation cohort **(B)**. MRI-LN, MRI-reported LN status.

TABLE 3 | Comparison of AUCs among models.

Cohorts	Model	Rad-score 1	Rad-score 2	Rad-score 3	MRI- LN
Training	Rad-score 1	/	0.553	0.300	0.062
	Rad-score 2	0.553	/	0.654	0.011
	Rad-score 3	0.300	0.654	/	0.001
	MRI- LN	0.062	0.011	0.001	/
Validation	Rad-score 1	/	0.672	0.571	0.257
	Rad-score 2	0.672	/	0.814	0.127
	Rad-score 3	0.571	0.814	/	0.037
	MRI- LN	0.257	0.127	0.037	/

MR-LN: MRI-reported LNM status.

TABLE 4 | Univariate and multivariate logistic regression analyses of the clinical parameters and rad-scores.

Characteristic	Univariate analysis		*P*	Multivariate analysis		*P*
	OR	95% CI		OR	95% CI	
Age	0.991	0.955-1.029	0.651			
Sex	0.833	0.414-1.676	0.608			
Location	0.610	0.307-1.213	0.159			
Size	1.090	0.875-1.357	0.441			
CA19-9	1.000	1.000-1.000	0.874			
CA125	0.998	0.992-1.004	0.509			
CEA	1.001	0.999-1.003	0.535			
mTs	1.115	0.552-2.251	0.762			
MRI-reported LN status	5.153	2.219-11.966	0.000	4.251	1.309-13.808	0.016
Rad-score 3	2.471	1.756-3.477	0.000	2.448	1.571-3.814	0.000

mTs, MRI tumor stage.

LNM based on MRI radiomic analysis of primary lesions (22, 37–43). To the best of our knowledge, only one study has analyzed the predictive efficacy of radiomics based on MRI for LNM of PDAC (43), but only the arterial phase of the T1WI enhanced sequence was used. T2WI can reflect the signal intensity of the tumor tissue and its structure, and the enhanced sequence can better reflect tumor-related information such as internal heterogeneity and vascular regeneration (18–20, 24, 44). Based on the two sequences and by incorporating the independent predictor of MRI-reported lymph node status, we constructed a model with good predictive efficacy, with an AUC of 0.845 in the training cohort. This result is similar to findings reported in previous studies on multiparametric MRI-based radiomics nomograms for predicting LNM of lung adenocarcinoma, bladder cancer, and cervical cancer, with AUCs ranging from 0.820 to 0.856 in the training cohort (37–39).

We delineated a 3D ROI containing comprehensive information (45), and 1037 features were extracted, including high-order features. After dimensionality reduction, we found that rad-score 1 and rad-score 2 mainly consisted of wavelet

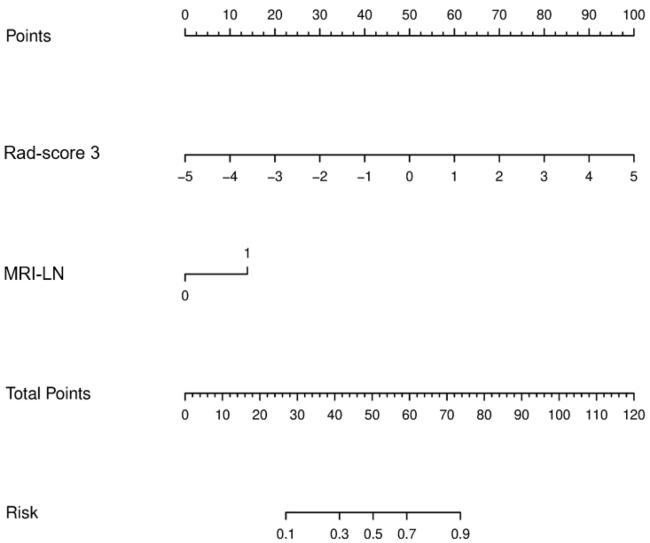

FIGURE 4 | Radiomics nomogram incorporating the MRI-reported LN status and rad-score 3. MRI-LN, MRI-reported LN status.

features (7/8, 5/6), and rad-score 3 consisted only of wavelet features, indicating that wavelet features better reflect the biological characteristics and heterogeneity of tumors. Wavelet filters can help to sharpen the image and eliminate noise (46), and the features of wavelet filters can represent the signal intensity distribution or grayscale distribution in the tissue (47). For example, among the first-order features, "LLH_firstorder_Minimum" and "LLH_firstorder_Mean" describe the minimum and mean gray intensity of the tumor region, respectively, and the difference in the grayscale intensity distribution is shown by "LLL_firstorder_Kurtosis". In addition, "LLH_glszm_SizeZoneNonUniformity" and "HHH_gldm_DependenceNonUniformityNormalized" represent the heterogeneity of the tumor tissue. "HHH_glszm_SmallAreaEmphasis" is expressed as a greater value with smaller size zones and more fine textures. This study confirmed that "MaximumProbability", "MaximumProbability" and "MaximumProbability" were the most meaningful among all the GLCM features, showing differences in the regional signal intensity distribution, gray level skewness, uniformity and linear dependency within PDAC tissues with LNM or nLNM tendency (47). The value of some of the wavelet features we obtained has also been confirmed in recent studies on LNM of rectal cancer and cervical cancer, especially the features based on T2WI (21, 24, 48). We also found that only six features from T2WI were retained—fewer than those retained from PVP (eight features). However, the former had a larger AUC score, although the difference was not statistically significant. This may be related to the higher tissue resolution provided by T2WI and greater influence of upper abdominal respiratory artifacts in dynamic enhanced scanning, which requires further studies with histopathology.

There were several limitations to this study. First, the sample size was small, so selection bias may exist. Because this was a single-center study, the application of the radiomics nomogram was limited as well; more data from multicenter and multiple

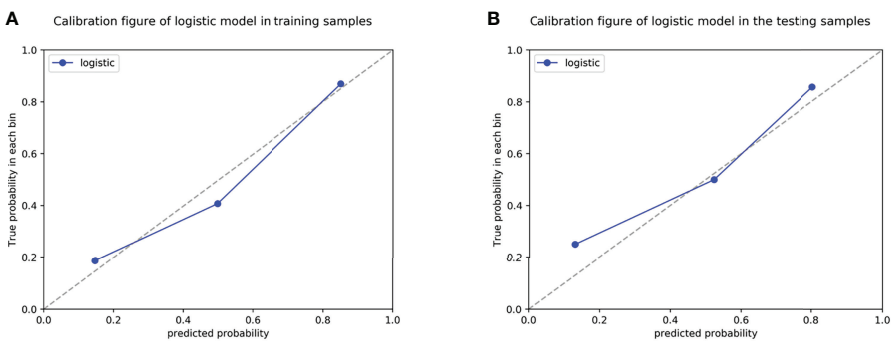

FIGURE 5 | Calibration curves of the radiomics nomogram in the training cohort **(A)** and validation cohort **(B)**.

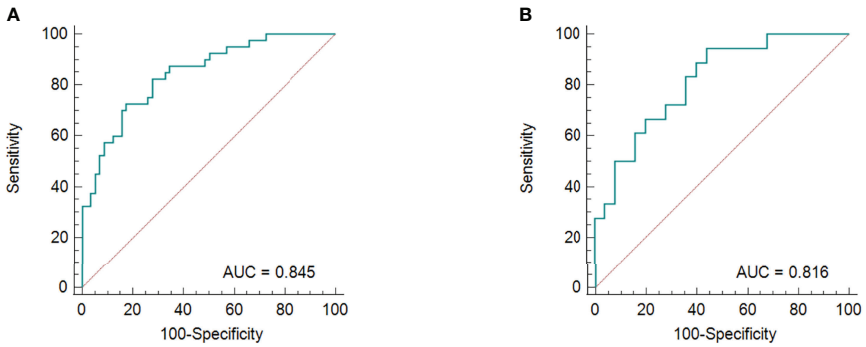

FIGURE 6 | The ROC curves for the radiomics nomogram in the training group **(A)** and validation cohort **(B)**.

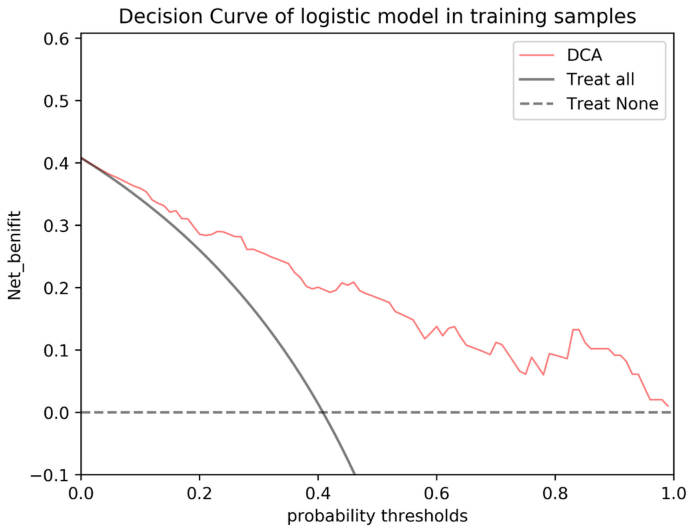

FIGURE 7 | DCA of the nomogram based on MRI-reported LN status and rad-score 3 in the validation cohort. The red line, gray line, and horizontal dotted line represent the net benefit of the nomogram, treat-all strategy, and treat-none strategy, respectively.

MRI scanners are needed to verify the accuracy and stability of our radiomics model. Second, volume effects and respiratory motion artifacts could not be completely avoided when delineating the tumor boundaries. Third, only the portal vein phase of the multiphase enhancement sequences was analyzed, analyses and comparisons of each phase could be performed to determine their predictive value in future work, DWI sequence could be studied as well.

In conclusion, the results of our study demonstrated that a radiomics nomogram based on dual-parametric MRI imaging could successfully predict LNM and nLNM of PDAC. This method shows higher specificity and sensitivity than traditional MRI can provide, allowing clinicians to be able to prepare more thoroughly before performing surgical procedures. In addition, the use of this nomogram can ultimately improve the prognosis of patients.

DATA AVAILABILITY STATEMENT

The original contributions presented in the study are included in the article/supplementary material. Further inquiries can be directed to the corresponding author.

ETHICS STATEMENT

The studies involving human participants were reviewed and approved by Zhejiang Provincial People's Hospital, Affiliated People's Hospital, Hangzhou Medical College. Written informed consent for participation was not required for this study in accordance with the national legislation and the institutional requirements.

AUTHOR CONTRIBUTIONS

JC designed the study and revised the final manuscript. LS and LW analyzed the data and wrote the first draft. GW auxiliary analyzed the data. CW and YZ performed the image acquisition and analyzed the data. All authors contributed to the article and approved the submitted version.

FUNDING

This research was supported by Zhejiang Provincial Natural Science Foundation of China (No. LGC22H180002) and Zhejiang Medical and Health Science and Technology Project (No. 2020KY406, 2021KY508).

REFERENCES

1. Rawla P, Sunkara T, Gaduputi V. Epidemiology of Pancreatic Cancer: Global Trends, Etiology and Risk Factors. *World J Oncol* (2019) 10(1):10–27. doi: 10.14740/wjon1166
2. Pereira SP, Oldfield L, Ney A, Hart PA, Keane MG, Pandol SJ, et al. Early Detection of Pancreatic Cancer. *Lancet Gastroenterol Hepatol* (2020) 5 (7):698–710. doi: 10.1016/s2468-1253(19)30416-9
3. Saad AM, Turk T, Al-Husseini MJ, Abdel-Rahman O. Trends in Pancreatic Adenocarcinoma Incidence and Mortality in the United States in the Last Four Decades; a SEER-Based Study. *BMC Cancer* (2018) 18(1):688. doi: 10.1186/s12885-018-4610-4
4. Schwarz RE, Smith DD. Extent of Lymph Node Retrieval and Pancreatic Cancer Survival: Information From a Large US Population Database. *Ann Surg Oncol* (2006) 13(9):1189–200. doi: 10.1245/s10434-006-9016-x
5. Choi SB, Han HJ, Park P, Kim WB, Song TJ, Choi SY. Systematic Review of the Clinical Significance of Lymph Node Micrometastases of Pancreatic Adenocarcinoma Following Surgical Resection. *Pancreatology* (2017) 17 (3):342–9. doi: 10.1016/j.pan.2017.03.008
6. Tseng DS, van Santvoort HC, Fegrachi S, Besselink MG, Zuithoff NP, Borel Rinkes IH, et al. Diagnostic Accuracy of CT in Assessing Extra-Regional Lymphadenopathy in Pancreatic and Peri-Ampullary Cancer: A Systematic Review and Meta-Analysis. *Surg Oncol* (2014) 23(4):229–35. doi: 10.1016/j.suronc.2014.10.005
7. Kauhanen SP, Komar G, Seppänen MP, Dean KI, Minn HR, Kajander SA, et al. A Prospective Diagnostic Accuracy Study of 18F-Fluorodeoxyglucose Positron Emission Tomography/Computed Tomography, Multidetector Row Computed Tomography, and Magnetic Resonance Imaging in Primary Diagnosis and Staging of Pancreatic Cancer. *Ann Surg* (2009) 250(6):957–63. doi: 10.1097/SLA.0b013e3181b2fafa
8. Joo I, Lee JM, Lee DH, Lee ES, Paeng JC, Lee SJ, et al. Preoperative Assessment of Pancreatic Cancer With FDG PET/MR Imaging Versus FDG PET/CT Plus Contrast-Enhanced Multidetector CT: A Prospective Preliminary Study. *Radiology* (2017) 282(1):149–59. doi: 10.1148/radiol.2016152798
9. Wang S, Shi H, Yang F, Teng X, Jiang B. The Value of (18)F-FDG PET/CT and Carbohydrate Antigen 19-9 in Predicting Lymph Node Micrometastases of Pancreatic Cancer. *Abdom Radiol (NY)* (2019) 44(12):4057–62. doi: 10.1007/s00261-019-02248-0
10. Masuda T, Dann AM, Elliott IA, Baba H, Kim S, Sedarat A, et al. A Comprehensive Assessment of Accurate Lymph Node Staging and Preoperative Detection in Resected Pancreatic Cancer. *J Gastrointest Surg* (2018) 22(2):295–302. doi: 10.1007/s11605-017-3607-7
11. Imai H, Doi R, Kanazawa H, Kamo N, Koizumi M, Masui T, et al. Preoperative Assessment of Para-Aortic Lymph Node Metastasis in Patients With Pancreatic Cancer. *Int J Clin Oncol* (2010) 15(3):294–300. doi: 10.1007/s10147-010-0066-5
12. Zhang Z, Procissi D, Li W, Kim DH, Li K, Han G, et al. High Resolution MRI for non-Invasive Mouse Lymph Node Mapping. *J Immunol Methods* (2013) 400-401:23–9. doi: 10.1016/j.jim.2013.06.013
13. Matsubayashi H, Matsui T, Yabuuchi Y, Imai K, Tanaka M, Kakushima N, et al. Endoscopic Ultrasonography Guided-Fine Needle Aspiration for the Diagnosis of Solid Pancreaticobiliary Lesions: Clinical Aspects to Improve the Diagnosis. *World J Gastroenterol* (2016) 22(2):628–40. doi: 10.3748/wjg.v22.i2.628
14. Lee YN, Moon JH, Kim HK, Choi HJ, Lee SH, Choi MH, et al. A Triple Approach for Diagnostic Assessment of Endoscopic Ultrasound-Guided Fine Needle Aspiration in Pancreatic Solid Masses and Lymph Nodes. *Dig Dis Sci* (2014) 59(9):2286–93. doi: 10.1007/s10620-014-3119-1
15. Wang SC, Parekh JR, Porembka MR, Nathan H, D'Angelica MI, DeMatteo RP, et al. A Pilot Study Evaluating Serum MMP7 as a Preoperative Prognostic Marker for Pancreatic Ductal Adenocarcinoma Patients. *J Gastrointest Surg* (2016) 20(5):899–904. doi: 10.1007/s11605-015-3057-z
16. Masui T, Sato A, Nakano K, Uchida Y, Yogo A, Anazawa T, et al. Predictive Value of the Ki67 Index for Lymph Node Metastasis of Small non-Functioning Pancreatic Neuroendocrine Neoplasms. *Surg Today* (2019) 49 (7):593–600. doi: 10.1007/s00595-019-01779-9
17. Lambin P, Rios-Velazquez E, Leijenaar R, Carvalho S, van Stiphout RG, Granton P, et al. Radiomics: Extracting More Information From Medical Images Using Advanced Feature Analysis. *Eur J Cancer* (2012) 48(4):441–6. doi: 10.1016/j.ejca.2011.11.036
18. Jeon SK, Lee JM, Joo I, Lee ES, Park HJ, Jang JY, et al. Nonhypervascular Pancreatic Neuroendocrine Tumors: Differential Diagnosis From Pancreatic Ductal Adenocarcinomas at MR Imaging-Retrospective Cross-Sectional Study. *Radiology* (2017) 284(1):77–87. doi: 10.1148/radiol.2016160586
19. Eresen A, Yang J, Shangguan J, Li Y, Hu S, Sun C, et al. MRI Radiomics for Early Prediction of Response to Vaccine Therapy in a Transgenic Mouse Model of Pancreatic Ductal Adenocarcinoma. *J Transl Med* (2020) 18(1):61. doi: 10.1186/s12967-020-02246-7
20. Tang TY, Li X, Zhang Q, Guo CX, Zhang XZ, Lao MY, et al. Development of a Novel Multiparametric MRI Radiomic Nomogram for Preoperative Evaluation of Early Recurrence in Resectable Pancreatic Cancer. *J Magn Reson Imaging* (2020) 52(1):231–45. doi: 10.1002/jmri.27024
21. Li C, Yin J. Radiomics Based on T2-Weighted Imaging and Apparent Diffusion Coefficient Images for Preoperative Evaluation of Lymph Node Metastasis in Rectal Cancer Patients. *Front Oncol* (2021) 11:671354. doi: 10.3389/fonc.2021.671354
22. Zhang K, Zhang Y, Fang X, Fang M, Shi B, Dong J, et al. Nomograms of Combining Apparent Diffusion Coefficient Value and Radiomics for Preoperative Risk Evaluation in Endometrial Carcinoma. *Front Oncol* (2021) 11:705456. doi: 10.3389/fonc.2021.705456
23. Calabrese A, Santucci D, Landi R, Beomonte Zobel B, Faiella E, de Felice C. Radiomics MRI for Lymph Node Status Prediction in Breast Cancer Patients: The State of Art. *J Cancer Res Clin Oncol* (2021) 147(6):1587–97. doi: 10.1007/s00432-021-03606-6
24. Deng X, Liu M, Sun J, Li M, Liu D, Li L, et al. Feasibility of MRI-Based Radiomics Features for Predicting Lymph Node Metastases and VEGF Expression in Cervical Cancer. *Eur J Radiol* (2021) 134:109429. doi: 10.1016/j.ejrad.2020.109429
25. Lee JH, Han SS, Hong EK, Cho HJ, Joo J, Park EY, et al. Predicting Lymph Node Metastasis in Pancreatobiliary Cancer With Magnetic Resonance Imaging: A Prospective Analysis. *Eur J Radiol* (2019) 116:1–7. doi: 10.1016/j.ejrad.2019.04.007
26. Yushkevich PA, Piven J, Hazlett HC, Smith RG, Ho S, Gee JC, et al. User-Guided 3D Active Contour Segmentation of Anatomical Structures: Significantly Improved Efficiency and Reliability. *Neuroimage* (2006) 31 (3):1116–28. doi: 10.1016/j.neuroimage.2006.01.015
27. Zwanenburg A, Vallières M, Abdalah MA, Aerts H, Andrearczyk V, Apte A, et al. The Image Biomarker Standardization Initiative: Standardized Quantitative Radiomics for High-Throughput Image-Based Phenotyping. *Radiology* (2020) 295(2):328–38. doi: 10.1148/radiol.2020191145
28. Yang L, Liu D, Fang X, Wang Z, Xing Y, Ma L, et al. Rectal Cancer: Can T2WI Histogram of the Primary Tumor Help Predict the Existence of Lymph Node Metastasis? *Eur Radiol* (2019) 29(12):6469–76. doi: 10.1007/s00330-019-06328-z
29. Vickers AJ, Cronin AM, Elkin EB, Gonen M. Extensions to Decision Curve Analysis, a Novel Method for Evaluating Diagnostic Tests, Prediction Models and Molecular Markers. *BMC Med Inform Decis Mak* (2008) 8:53. doi: 10.1186/1472-6947-8-53

30. Strobel O, Hinz U, Gluth A, Hank T, Hackert T, Bergmann F, et al. Pancreatic Adenocarcinoma: Number of Positive Nodes Allows to Distinguish Several N Categories. *Ann Surg* (2015) 261(5):961–9. doi: 10.1097/sla.0000000000000814
31. Hoshikawa M, Ogata S, Nishikawa M, Kimura A, Einama T, Noro T, et al. Pathomorphological Features of Metastatic Lymph Nodes as Predictors of Postoperative Prognosis in Pancreatic Cancer. *Med (Baltimore)* (2019) 98(5): e14369. doi: 10.1097/md.0000000000014369
32. Loch FN, Asbach P, Haas M, Seeliger H, Beyer K, Schineis C, et al. Accuracy of Various Criteria for Lymph Node Staging in Ductal Adenocarcinoma of the Pancreatic Head by Computed Tomography and Magnetic Resonance Imaging. *World J Surg Oncol* (2020) 18(1):213. doi: 10.1186/s12957-020-01951-3
33. Liang X, Cai W, Liu X, Jin M, Ruan L, Yan S. A Radiomics Model That Predicts Lymph Node Status in Pancreatic Cancer to Guide Clinical Decision Making: A Retrospective Study. *J Cancer* (2021) 12(20):6050–7. doi: 10.7150/jca.61101
34. Azizian A, Rühlmann F, Krause T, Bernhardt M, Jo P, König A, et al. CA19-9 for Detecting Recurrence of Pancreatic Cancer. *Sci Rep* (2020) 10(1):1332. doi: 10.1038/s41598-020-57930-x
35. Ye C, Sadula A, Ren S, Guo X, Yuan M, Yuan C, et al. The Prognostic Value of CA19-9 Response After Neoadjuvant Therapy in Patients With Pancreatic Cancer: A Systematic Review and Pooled Analysis. *Cancer Chemother Pharmacol* (2020) 86(6):731–40. doi: 10.1007/s00280-020-04165-2
36. Liu Z, Wang S, Dong D, Wei J, Fang C, Zhou X, et al. The Applications of Radiomics in Precision Diagnosis and Treatment of Oncology: Opportunities and Challenges. *Theranostics* (2019) 9(5):1303–22. doi: 10.7150/thno.30309
37. Ran J, Cao R, Cai J, Yu T, Zhao D, Wang Z. Development and Validation of a Nomogram for Preoperative Prediction of Lymph Node Metastasis in Lung Adenocarcinoma Based on Radiomics Signature and Deep Learning Signature. *Front Oncol* (2021) 11:585942. doi: 10.3389/fonc.2021.585942
38. Liu X, Liang X, Ruan L, Yan S. A Clinical-Radiomics Nomogram for Preoperative Prediction of Lymph Node Metastasis in Gallbladder Cancer. *Front Oncol* (2021) 11:633852. doi: 10.3389/fonc.2021.633852
39. Xiao M, Ma F, Li Y, Li Y, Li M, Zhang G, et al. Multiparametric MRI-Based Radiomics Nomogram for Predicting Lymph Node Metastasis in Early-Stage Cervical Cancer. *J Magn Reson Imaging* (2020) 52(3):885–96. doi: 10.1002/jmri.27101
40. Yu Y, He Z, Ouyang J, Tan Y, Chen Y, Gu Y, et al. Magnetic Resonance Imaging Radiomics Predicts Preoperative Axillary Lymph Node Metastasis to Support Surgical Decisions and is Associated With Tumor Microenvironment in Invasive Breast Cancer: A Machine Learning, Multicenter Study. *EBioMedicine* (2021) 69:103460. doi: 10.1016/j.ebiom.2021.103460
41. Yang YS, Feng F, Qiu YJ, Zheng GH, Ge YQ, Wang YT. High-Resolution MRI-Based Radiomics Analysis to Predict Lymph Node Metastasis and Tumor Deposits Respectively in Rectal Cancer. *Abdom Radiol (NY)* (2021) 46(3):873–84. doi: 10.1007/s00261-020-02733-x
42. Wang F, Tan R, Feng K, Hu J, Zhuang Z, Wang C, et al. Magnetic Resonance Imaging-Based Radiomics Features Associated With Depth of Invasion Predicted Lymph Node Metastasis and Prognosis in Tongue Cancer. *J Magn Reson Imaging* (2021) 56(1):196–209. doi: 10.1002/jmri.28019
43. Shi Z, Ma C, Huang X, Cao D. Magnetic Resonance Imaging Radiomics-Based Nomogram From Primary Tumor for Pretreatment Prediction of Peripancreatic Lymph Node Metastasis in Pancreatic Ductal Adenocarcinoma: A Multicenter Study. *J Magn Reson Imaging* (2022) 55(3):823–39. doi: 10.1002/jmri.28048
44. Nie K, Shi L, Chen Q, Hu X, Jabbour SK, Yue N, et al. Rectal Cancer: Assessment of Neoadjuvant Chemoradiation Outcome Based on Radiomics of Multiparametric MRI. *Clin Cancer Res* (2016) 22(21):5256–64. doi: 10.1158/1078-0432.Ccr-15-2997
45. Ng F, Kozarski R, Ganeshan B, Goh V. Assessment of Tumor Heterogeneity by CT Texture Analysis: Can the Largest Cross-Sectional Area be Used as an Alternative to Whole Tumor Analysis? *Eur J Radiol* (2013) 82(2):342–8. doi: 10.1016/j.ejrad.2012.10.023
46. Qian Z, Li Y, Wang Y, Li L, Li R, Wang K, et al. Differentiation of Glioblastoma From Solitary Brain Metastases Using Radiomic Machine-Learning Classifiers. *Cancer Lett* (2019) 451:128–35. doi: 10.1016/j.canlet.2019.02.054
47. Van Griethuysen JJM, Fedorov A, Parmar C, Hosny A, Aucoin N, Narayan V, et al. Computational Radiomics System to Decode the Radiographic Phenotype. *Cancer Res* (2017) 77(21):e104–e7. doi: 10.1158/0008-5472.Can-17-0339
48. Ma X, Shen F, Jia Y, Xia Y, Li Q, Lu J. MRI-Based Radiomics of Rectal Cancer: Preoperative Assessment of the Pathological Features. *BMC Med Imaging* (2019) 19(1):86. doi: 10.1186/s12880-019-0392-7

Conflict of Interest: Author YW was employed by General Electric Healthcare.

The remaining authors declare that the research was conducted in the absence of any commercial or financial relationships that could be construed as a potential conflict of interest.

Publisher's Note: All claims expressed in this article are solely those of the authors and do not necessarily represent those of their affiliated organizations, or those of the publisher, the editors and the reviewers. Any product that may be evaluated in this article, or claim that may be made by its manufacturer, is not guaranteed or endorsed by the publisher.

frontiers | Frontiers in Oncology

TYPE Original Research
PUBLISHED 05 August 2022
DOI 10.3389/fonc.2022.952749

OPEN ACCESS

EDITED BY
Jiansong Ji,
Lishui Central Hospital, China

REVIEWED BY
Pei Pei Pang,
GE Healthcare, China
Minjiang Chen,
Lishui Central Hospital, China

*CORRESPONDENCE
Nan He
henan_union@hust.edu.cn
Qianna Jin
jinqianna@hust.edu.cn

†These authors have contributed equally to this work and share first authorship

SPECIALTY SECTION
This article was submitted to Cancer Imaging and Image-directed Interventions, a section of the journal Frontiers in Oncology

RECEIVED 25 May 2022
ACCEPTED 04 July 2022
PUBLISHED 05 August 2022

CITATION
Ren Q, Xiong F, Zhu P, Chang X, Wang G, He N and Jin Q (2022) Assessing the robustness of radiomics/deep learning approach in the identification of efficacy of anti–PD-1 treatment in advanced or metastatic non-small cell lung carcinoma patients.
Front. Oncol. 12:952749.
doi: 10.3389/fonc.2022.952749

Assessing the robustness of radiomics/deep learning approach in the identification of efficacy of anti–PD-1 treatment in advanced or metastatic non-small cell lung carcinoma patients

Qianqian Ren[1,2†], Fu Xiong[1,2†], Peng Zhu[3†], Xiaona Chang[4], Guobin Wang[5], Nan He[6*] and Qianna Jin[1,2*]

[1]Department of Radiology, Union Hospital, Tongji Medical College, Huazhong University of Science and Technology, Wuhan, China, [2]Hubei Province Key Laboratory of Molecular Imaging, Tongji Medical College, Huazhong University of Science and Technology, Wuhan, China, [3]Department of Hepatobiliary Surgery, Wuhan No.1 Hospital, Wuhan, China, [4]Department of Pathology, Union Hospital, Tongji Medical College, Huazhong University of Science and Technology, Wuhan, China, [5]Department of Gastrointestinal Surgery, Union Hospital, Tongji Medical College, Huazhong University of Science and Technology, Wuhan, China, [6]Cancer Center, Department of Gastrointestinal Surgery, Union Hospital, Tongji Medical College, Huazhong University of Science and Technology, Wuhan, China

Administration of anti–PD-1 is now a standard therapy in advanced non-small cell lung carcinoma (NSCLC) patients. The clinical application of biomarkers reflecting tumor immune microenvironment is hurdled by the invasiveness of obtaining tissues despite its importance in immunotherapy. This study aimed to develop a robust and non-invasive radiomics/deep learning machine biomarker for predicting the response to immunotherapy in NSCLC patients. Radiomics/deep learning features were exacted from computed tomography (CT) images of NSCLC patients treated with Nivolumab or Pembrolizumab. The robustness of radiomics/deep learning features was assessed against various perturbations, then robust features were selected based on the Intraclass Correlation Coefficient (ICC). Radiomics/deep learning machine-learning classifiers were constructed by combining seven feature exactors, 13 feature selection methods, and 12 classifiers. The optimal model was selected using the mean area under the curve (AUC) and relative standard deviation (RSD). The consistency of image features against various perturbations was high (the range of median ICC: 0.78–0.97), but the consistency was poor in test–retest testing (the range of median ICC: 0.42–0.67). The optimal model, InceptionV3_RELF_Nearest Neighbors classifiers, had the highest prediction efficacy (AUC: 0.96 and RSD: 0.50) for anti–PD-1/PD-L1 treatment. Accuracy (ACC), sensitivity, specificity, precision, and F1 score were 95.24%, 95.00%,

95.50%, 91.67%, and 95.30%, respectively. For successful model robustification, tailoring perturbations for robustness testing to the target dataset is key. Robust radiomics/deep learning features, when paired with machine-learning methodologies, will work on the exactness and the repeatability of anticipating immunotherapy adequacy.

KEYWORDS

NSCLC, radiomics, deep learning, robustness, immunotherapy

Introduction

The introduction of programmed death 1 receptor (PD-1)/programmed death ligand 1 (PD-L1) blocking antibodies and targeted agents have substantially changed the therapeutic strategies for advanced lung cancer. In the setting of pre-treated patients with advanced non-small cell lung carcinoma (NSCLC), Nivolumab and Pembrolizumab monotherapy showed significantly better overall survival (OS), compared with traditional chemotherapy (1–3). Several predictive biomarkers based on cellular phenotypes, immunohistochemical, mutational tests, and expression-based approaches have been proposed to predict response to immune checkpoint inhibition. However, the predictive power of these methods was far from perfect. For example, only 44.8% of PD-L1–positive NSCLCs were responsive to Pembrolizumab in a first-line setting (4). Furthermore, it is difficult to identify the current status of immune profiles from an archival sample due to the dynamical evolution of the immune-escape mechanism during anti-cancer treatment (5, 6). Therefore, non-invasive methods, understanding the dynamics of the tumors in clinical practice, and assessing the immune landscape of tumors are critical.

Radiomics/deep learning (DL) image features are becoming a promising non-invasive method to obtain quantitative measurements for tumor classification and assessment for therapy response in oncological research (7–9). An imaging biomarker should be reproducible, robust, and accurate. However, image features are susceptible to several factors, such as imaging protocol variability, different vendors, image reconstruction processes, inter-rater tumor segmentation variability, patient motion artifact, overall image quality, and tumor phenotype (10–13). Ideally, only features that are robust to these variations would be incorporated into a predictive model for good generalizability (14).

We hypothesized that the combination of machine learning (ML) technologies and high-dimensional radiomics/DL features would facilitate the prediction of immunotherapy efficacy. Therefore, we investigated the robustness of radiomics/DL features against different perturbations and then determined the optimal model by combining feature extractors, feature selectors, and ML classifiers.

Materials and methods

Whuh (Wuhan Union Hospital) data

The medical records of patients with advanced NSCLC who had received Nivolumab (3 mg/kg every 2 weeks) or Pembrolizumab (200 mg every 3 weeks) monotherapy between January 2019 and January 2021 were retrospectively reviewed at Union Hospital, Tongji Medical College, Huazhong University of Science and Technology. Treatments were provided until disease progression, intolerable side effects, or consent to the withdrawal. The retrospective study was approved by the Ethics Committee of Union Hospital, which also waived the written informed consent, because the data were analyzed anonymously.

Patient inclusion criteria were (1) pathologically confirmed NSCLC, (2) enhanced computed tomography (CT) performed fewer than 15 days before treatment, and (3) availability of clinical data. The exclusion criteria were (1) missing or low-

Abbreviations: ICC, Intraclass Correlation Coefficient; NSCLC, non-small cell lung carcinoma; AUC, area under the curve; RSD, relative standard deviation in percentile; PD-1, programmed death 1 receptor; PD-L1, programmed death ligand 1; OS, overall survival; RR, response rates; imRECIST, Immune-Modified Response Evaluation Criteria In Solid Tumors; ROIs, the tumor regions of interest; GLCM, gray-level co-occurrence matrix; GLSZM, gray-level size zone matrix; GLRLM, gray-level run-length matrix; NGTDM, neighborhood gray-tone difference matrix; GLDM, gray-level dependence matrix; CHSQ, chi-square score; RELF, ReliefF; MIM, mutual information maximization; FSCR, Fischer Score; MIFS, mutual information feature selection; GINI, Gini index; ICAP, interaction capping; JMI, joint mutual information; CIFE, conditional infomax feature extraction; CMIM, conditional mutual information maximization; DISR, double input symmetric relevance; MRMR, minimum redundancy maximum relevance; TSCR, t-test score; QDA, quadratic discriminant analysis; SVC, Support Vector Classifiers; RBF, radial basis function; ACC, accuracy; DL, deep learning.

quality treatment CT, (2) suffering from other tumor diseases at the same time, (3) combining other treatments while using immunotherapy, (4) Patients with no measurable lesion by Immune-Modified Response Evaluation Criteria In Solid Tumors (imRECIST) or no available response evaluation (15). Tumor response to Nivolumab or Pembrolizumab monotherapy was objectively assessed by experienced radiologists (QQ. R, QN. J) using imRECIST in the third month. The details regarding the response assessment were described in the supplemental. The data pertaining to demographics, smoking history, histology type, TNM stage, and molecular testing and the number of prior lines of therapy were extracted from electronic medical records (Table 1).

TABLE 1 Demographic and clinical characteristics of patient populations.

Characteristic	Responsive to Immunotherapy (n=124)	Unresponsive to Immunotherapy (n=33)	*p*
Age (mean±SD [years])	59.69±8.19	58.42±8.89	
Gender			0.336
Male	103	25	
Female	21	8	
Smoking History			0.140
Yes	89	19	
No	35	14	
HistoType			0.108
A	85	19	
S	36	10	
U	2	3	
AS	1	1	
Clinical Stage			0.378
IIIB	25	9	
IV	99	24	
The expression of EGFR			0.267
Positive	16	1	
Negative	28	8	
Unknown	80	24	
The expression of ALK			0.556
Positive	1	1	
Negative	35	8	
Unknown	88	24	
The level of PD-Ll			0.235
High	36	6	
Low	20	9	
Unknown	68	18	
Chemotherapy			0.194
1 course	21	10	
2 courses	43	8	
3 courses	60	15	

U, undifferentiated large cell carcinoma; A, adenocarcinoma; S, squamous cell carcinoma; AS, adenosquamous carcinoma.

Test–retest cohorts

The test–retest cohort with 31 NSCLC patients was available from the Cancer Imaging Archive (16, 17). Images in the test–retest cohort using the same scanner and acquisition protocol were acquired every 15 min. Informed consent was waived.

Computed tomography acquisition and segmentation

CT scans were acquired using a multi-slice spiral CT system (Philips Healthcare, General Electric Health Care, and Siemens Healthcare) with a tube voltage of 100–120 kVp, slice thickness (spacing) of 1–5mm, and in-plane resolution of 0.75 mm × 0.75 mm. All scans were acquired using the facilities' CT chest protocol and standard image reconstruction.

Pre-processing and tumor segmentation

The tumor regions of interest (ROIs), which corresponded to the biggest target lesion, were manually performed using three-dimensional Slicer software, which was based on a consensus reached by two experienced radiologists (one with 5 years of experience, another with 10 years of experience). For those cases with a blurred edge around the lesion, the maximum range was drawn and regarded as the border. Large vessels, adjacent organs, and air cavities were excluded. On contrast-enhanced CT, difficult-to-identify lesions were labeled with reference to the corresponding nuclear positron emission tomography (PET) image (some patients had PET scans) or with the permission of two physicians. The two readers repeated the same procedures 2 weeks later and any disagreement was resolved through consultation.

Feature extraction

To be consistent with DL features, three consecutive slices with the maximum cross-sectional area of the tumor lesion were selected. Radiomic feature calculations were automatically done using the PyRadiomics package implemented in Python (18). Radiomics features with or without wavelet filtration included three groups: (1) first-order statistics, (2) shape features, and (3) second-order features: gray-level co-occurrence matrix (GLCM), gray-level size zone matrix (GLSZM), gray-level run-length

matrix (GLRLM), neighborhood gray-tone difference matrix (NGTDM), and gray-level dependence matrix (GLDM) features (18).

ImageNet, which has numerous object categories and manually annotated training photos, was used to pre-train InceptionResnetV2, InceptionV3, Resnet50, VGG16, VGG19, and Xception (19). The six pre-trained CNNs were used as an arbitrary feature extractor while executing DL feature extraction, allowing the input picture to propagate forward, halting at the penultimate layer, and using the outputs of that layer as our features. We used global max pooling to extract the feature map's maximum value before converting it to its original value.

Image normalization

An image interpolation procedure was needed to standardize the images after CT image acquisition and segmentation. The image brightness was adjusted through the adaptive window level. The histogram equalization method was applied to CT images to get better visualization. The size of the three axial slices was adjusted to 224 mm × 224 mm, consistent with the input layer size of the pre-trained CNN models. The Gaussian filter was used to remove noise in images since CT images were mainly affected by quantum noise, which would be caused by the variability of the electron density of tissue voxels, and represented by random Gaussian process statistics (20).

Robust features for test–retest imaging and image perturbations

We tested feature robustness against various perturbations in Whuh data, then feature robustness was verified in the test–retest cohort.

According to the imaging guidelines (21) and the radiologist's visual inspection, we defined the expected perturbations in a multicenter setting.

(1) Axial slice spacing (S): CT images were reconstructed contiguously at 1, 2, 3, and 5 mm section thicknesses.

(2) Rotation (R): The depicted tumor rotation would be affected by the patient's position. Therefore, we generated a set angle θ [−30°, −15°, 15° 30°] and rotated the image, and segmented tumor in the axial (x, y) plane.

(3) ROI variation (Seg): The depicted tumor edge might be affected by the patient's respiratory motion artifact and the variability of intra- and inter-observer ROI segmentation. Therefore, ROI enlargement and shrinking were considered (enlargement and shrinking were shown in Figure 1) (14, 22).

Robust features evaluation: ICC (2,1) for each feature was calculated and only those that reach the cutoff (ICC > 0.75) for all tested perturbations were entered following the feature selection and modeling process. Raw feature vectors were further standardized by being centered to the mean and scaled to unit variance. Features with zero median absolute deviation (MAD), regarded as nonpredictive features, were further removed.

Feature selectors and machine learning methods

The feature selection methods included chi-square score (CHSQ), ReliefF(RELF), mutual information maximization (MIM), Fischer Score (FSCR), mutual information feature selection (MIFS), Gini index (GINI), interaction capping (ICAP), joint mutual information (JMI), conditional infomax feature extraction (CIFE), conditional mutual information maximization (CMIM), double input symmetric relevance (DISR), minimum redundancy maximum relevance (MRMR), and test score (TSCR).

The 12 ML classifiers included logistic regression, k-nearest neighbors, quadratic discriminant analysis (QDA), Support Vector Classifiers (SVCs) with linear and radial basis function (RBF) kernels, XGBoost, multilayer perceptrons, Gaussian processes, decision trees, naive Bayes, random forests, and AdaBoost. These classifiers were all imported from a Python (version 3.6.4) ML library named scikit-learn (version 19.0) (23). Further details about the feature selection methods were in Supplementary S2, and the parameter settings and tuning range of ML classifiers were detailed in the Supplementary Materials.

Machine learning and model performance evaluation

Seven feature extractors, 13 feature selectors, and 12 classifiers were combined, then 1,092 (7 × 13 × 12 = 1092) ML models were generated. The nomenclature of each model combined the feature exactor, the names of the feature selector, and the classification method. For example, Rnest50_ RELF _ nearest neighbors was a model trained by a k-nearest neighbors classifier with features selected by the ReliefF and extracted from Rnest50.

Each of the 1,092 models was trained during the 10-fold stratified cross-validation using the StratifiedKFold iterator in scikit-learn, which is a variation of kfold cross-validation that ensured each set contained approximately the same percentage of samples of each target class as the whole training dataset.

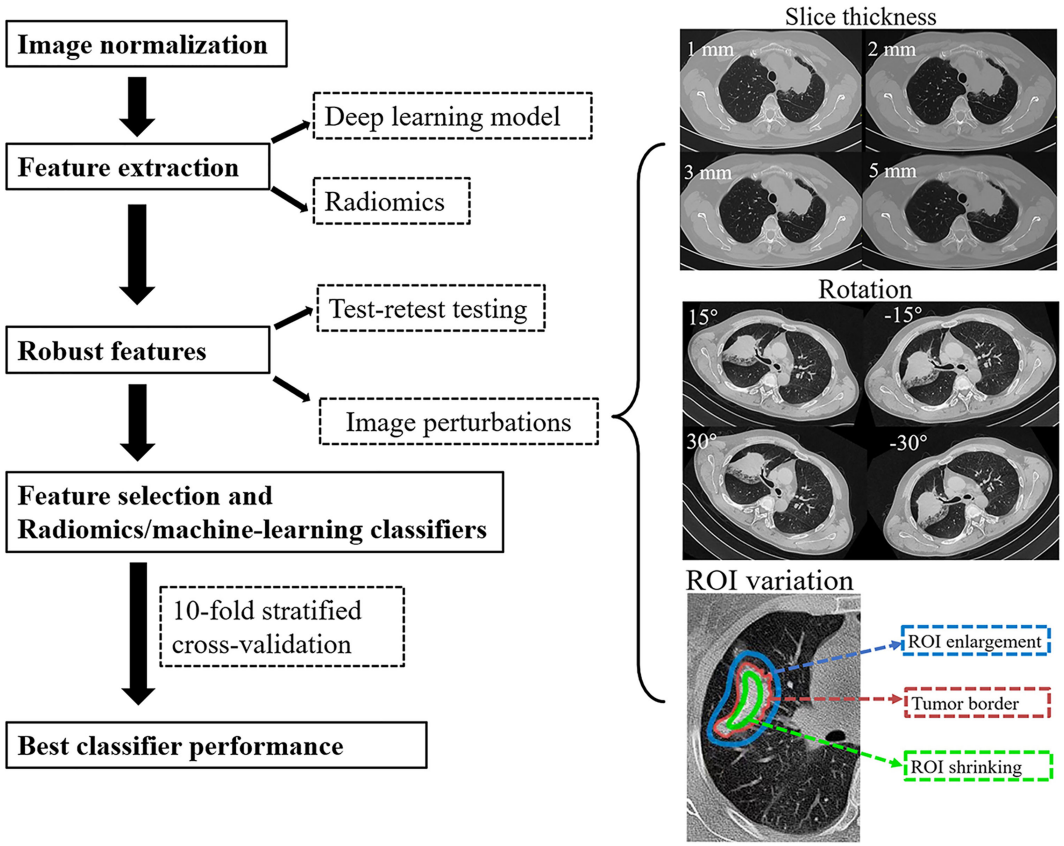

FIGURE 1
The study flowchart. After pre-processing and tumor segmentation, the images were artificially perturbed. Robust features were evaluated by machine learning (ML) models.

Synthetic minority over-sampling technique was adopted to handle the imbalanced data.

The best performing model was selected based on AUC and relative standard deviation (RSD). RSD was defined as the ratio between the standard deviation and mean of the 10-fold cross-validated AUC values: RSD = (sdAUC/mean AUC) ×100. The lower the RSD value, the higher the stability of the predicting model. The model with the highest AUC value and the lowest RSD was considered the best performing model. The performance of the best performing model was further measured by accuracy (ACC), sensitivity, specificity, F1 score, and precision.

Statistical analysis

Continuous variables were presented by using median with mean + SD and the statistic difference was compared by Wilcoxon signed-rank test. For differences in categorical variables, Fisher's exact test was adopted, and the results were shown as the number of events followed by relative frequencies (%). A two-sided $p < 0.05$ was used as the criterion to indicate a statistically significant difference.

Results

The study flowchart was presented in Figure 1.

Patient characteristics

Of 157 patients with advanced NSCLC (128 men, 29 women), 109 patients underwent nivolumab monotherapy and 48 underwent pembrolizumab monotherapy during the study period. The median age was 59 (range: 29–78) years. One hundred four (66%) were diagnosed as having adenocarcinoma, 46 (29.3%) were squamous cell carcinoma, five (3.2%) were undifferentiated large cell carcinoma, and two (1.3%) were adenosquamous carcinoma. Mutations in epidermal growth factor receptors were present in 17 patients (10.8%). Thirty-one patients (19.7%) had received one course of

chemotherapy, 51 patients (32.5%) had received two courses, and 75 patients (47.8%) had received three or more courses. The expression of PD-L1 was abundant (tumor proportion score [TPS] ≥ 50%) in 42 patients (26.8%), at low levels (1% ≤ TPS < 50%) in 29 patients (18.5%), and unknown in the remaining 86 (54.8%). According to Response Evaluation Criteria in Solid Tumors, version 1.1, after anti–PD-1 immunotherapy, 65 patients (41.4%) had a partial response, 59 patients (37.6%) had stable disease, and 33 patients (21.0%) had progressive disease (Table 1).

Feature robustness

One hundred seven original features and 744 wavelet features were extracted concerning radiomics features. Radiomics features included 14 shape parameters, 162 first-order parameters, 216 GLCM parameters, 144 GLRLM parameters, 144 GLSZM parameters, 126 GLDM features, and 45 NGTDM parameters. The number of features for DL models was InceptionResNetV2 1536, InceptionV3 2048, Xception 2048, and Resnet50 2048, VGG16 512 and VGG19 512. The representative feature heatmaps of features generated from InceptionV3 were presented in Figure 2.

In DL and radiomics features, ICCs ranging from 0.80 to 0.90 demonstrated favorable feature reproducibility for S (axial slice spacing). The features from InceptionResnetV2 and InceptionV3 were robust against R(rotation) but have a lower agreement if the ROI changed. For features from Resnet50 and Xception, robustness against S and Seg (ROI variation) were comparable. The features from VGG16 and VGG19 were robust against Seg but had a lower ICC for R. Radiomics features were robust against each perturbation, especially against Seg. The percentage of robust features against all perturbations for each feature extractor was presented in Figure 3 (The performance of each feature extractor against each image perturbation was reported in Supplementary Table 1 with median and the interquartile range (IQR)). The number of robust features for different ICC threshold settings was reported in the Supplementary Material Figure 1.

Compared with the consistency test for various perturbations, the repeatability in the test–retest group was much worse. The ICC of the best radiomic features in the above robustness testing was 0.6 in the test–retest group. The performance of each feature extractor regarding the test_retesting images was reported in Supplementary Table 2 with median and IQR.

We then reduced the number of features by removing features with zero MAD across the two cohorts. With the ICC threshold set to 0.75, the numbers of features remaining after robustness testing were radiomics 233, InceptionResNetV2 25, InceptionV3 74, Resnet50 109, VGG16 30, VGG19 73, and Xception 50. These features were first screened by the 13 feature selectors mentioned, and then the best combination

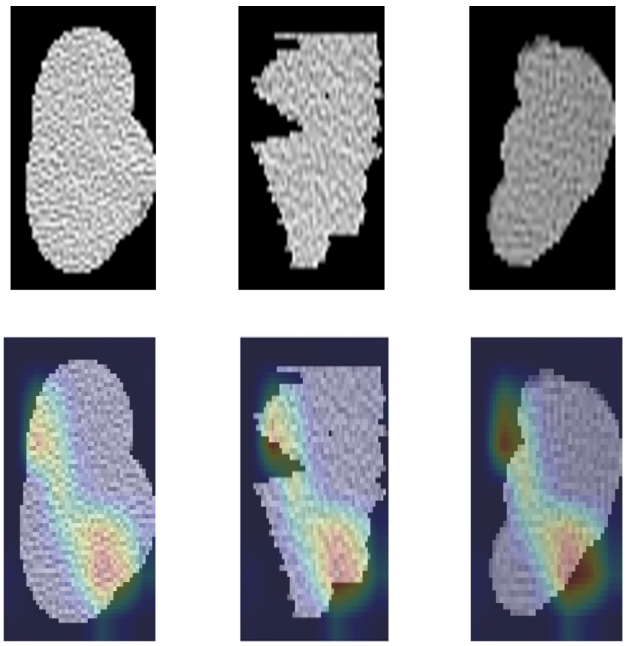

FIGURE 2
The heatmap of features generated from InceptionV3 for representative patients.

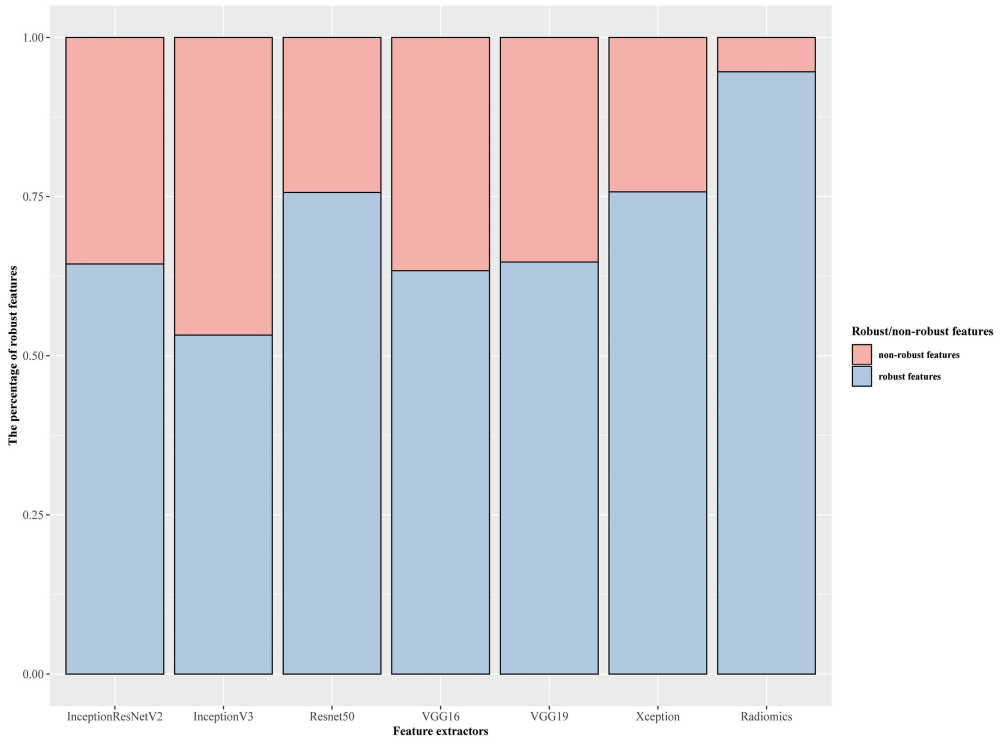

FIGURE 3
Overall percentage of robust features against image perturbations.

was further screened by the wrapper feature selection method based on the recursive feature addition algorithm.

Feature selection and machine learning models

The optimal model InceptionV3_RELF_ Nearest Neighbors was selected with the AUC value 0.96 and RSD 0.50 among the 1,092 machine-learning models (list of all feature selectors were in Supplementary Table 3, and the parameter settings and tuning range of ML methods were presented in Supplementary Material). Analysis of the confusion matrix-related classification metrics of InceptionV3_RELF_ Nearest Neighbors showed that the ACC, sensitivity, specificity, precision, and F1 score were 95.24%, 95.00%, 95.50%, 91.67%, and 95.30%, respectively. The illustration of the 10-fold cross-validated AUC for InceptionV3 features was presented in Figure 4A. Interestingly, the radiomics models had equal performance. The AUC value of Radiomics_CIFE_Nearest Neighbors, Radiomics_CIFE_QDA, Radiomics_CMIM_Nearest Neighbors, and Radiomics_CMIM_Multilayer Perceptron) was 0.96 in each model, and the RSD was 0.61, 0.67, 0.61, and 0.67. The heatmap of the 10-fold cross-validated AUC concerning radiomics features were presented in Figure 4B. Regarding the ML classifiers, the Nearest Neighbors classification outperformed other classifications, with the median AUC 0.79 (IQR 0.75–0.85). Supplementary Figure 2 reported the mean AUC of the Nearest Neighbors classification.

Discussion

In this study, by utilizing quantitative image analysis to extract features in conjunction with a ML classifier, we constructed accurate and reproducible models to predict immunotherapy response for advanced NSCLC. Importantly, these efficient models were obtained using cross-validation, and the inputs of the models were robust.

PD-L1 immunohistochemistry (IHC) expression, tumor mutation burden, and tumor-infiltrating lymphocytes have been suggested to predict the response to immunotherapy (24, 25). However, tissue-based biomarkers rely on individual tumor samples from accessible lesions in clinic practice and may not truly reflect the complexity of inter-tumoral heterogeneity. Furthermore, it is difficult to determine the current status of immune profiles from archival samples, as immune-escape mechanisms evolve dynamically during anti-cancer treatment (5, 6).

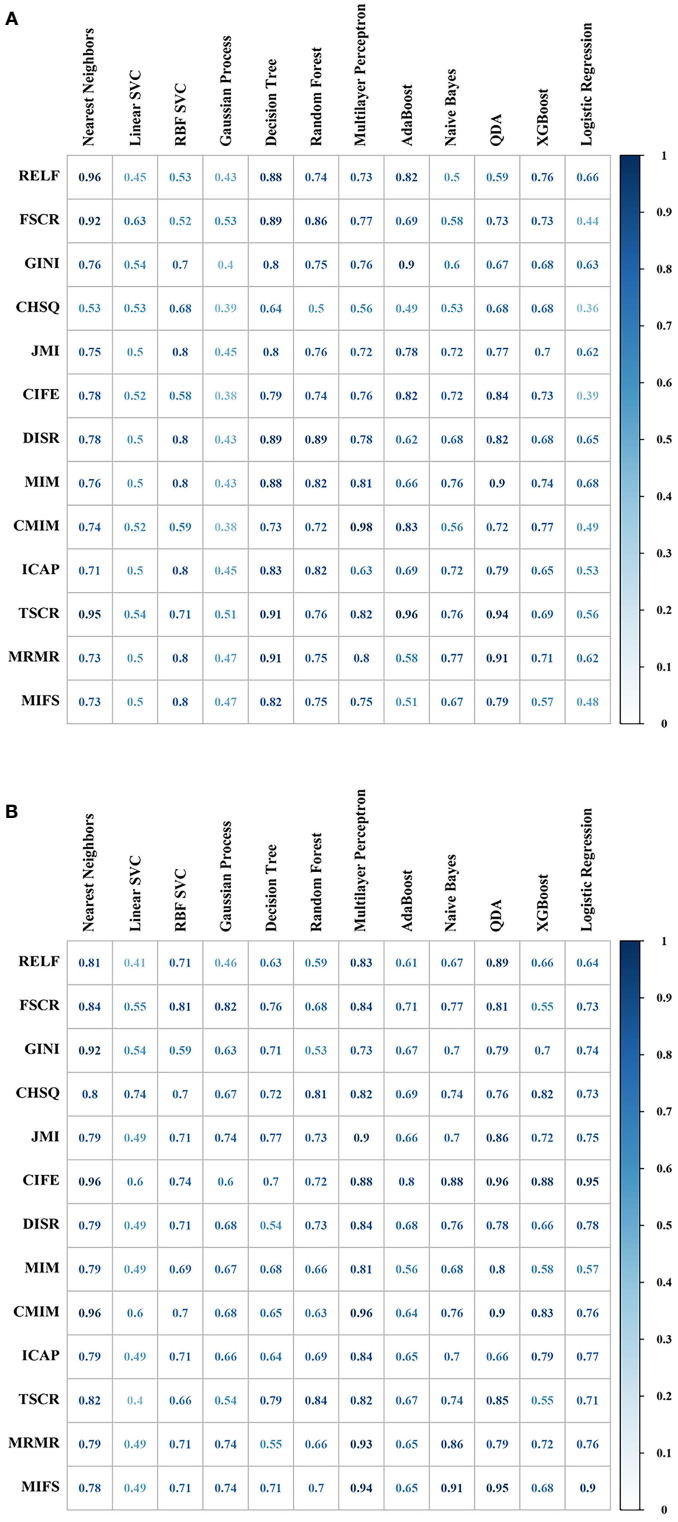

FIGURE 4
The predictive performance (area under the curve, AUC) of different combinations of feature selection methods (rows) and classification algorithms (columns) were presented in the heatmap. **(A)** Cross-validated AUC values of 156 models with InceptionV3 features. **(B)** Cross-validated AUC values of 156 models with radiomics features.

The main idea of DL is to employ a deep neural network, which provides a unique set of novel tools to improve NSCLC detection (26), characterization (27), survival prediction, and treatment outcome (28). However, compared with statistical ML models, DL models typically required a much larger amount of data to train for optimal results. To overcome the limitations of small datasets, transfer learning patterns (29) facilitate DL models as powerful extractors of useful feature sets.

Radiomic features have been used to predict the benefit of adjuvant chemotherapy, disease risk in early stage lung cancer (30), treatment response to concurrent chemoradiation in locally advanced lung cancer (31), and response to immune checkpoint inhibition in advanced NSCLC (32, 33). Most studies focused on the AUC of predictive models on a given dataset without considering the robustness of imaging features.

Our model is reliable and reproducible, because it uses robust features following the standardization of the model's input images and can be applied to CT data of various institutions. This model can minimize possible differences between different medical centers, inspection machines, and image reconstruction methods.

The evaluation of the robustness feature is based on the assumption that test–retest images and perturbations do not have consistent bias. We tested the robustness of features against perturbations, such as slice thickness spacing(S), rotation(R), and ROI variation (Seg). Both DL and radiomic features show excellent robustness to S perturbation and have a modest performance to Seg perturbation. The Seg perturbation captured the range of variability that occurred with human inter-observer variability and patient respiratory motion artifact. It is better to underestimate rather than overestimate the ROI when segmenting.

Several major limitations remained in the present study. First, our data were relatively small, and baseline characteristics maybe not in accordance with the population-based dataset. For example, the objective response rate was higher than in the previous study (34, 35). Thirty-two patients chose immunotherapy, because they could not tolerate chemotherapy toxicity rather than disease progression, which partly explained the high efficiency. Second, three consecutive slices of the tumor were sampled for the analysis, and volumetric assessments were not performed. In a previous study, data from a single slice were found to be sufficient for this type of analysis (36). Third, whether our algorithm model for predicting immunotherapy response can be applied to cancer types other than NSCLC is another potential research question to be solved. Fourth, our model lacks external verification. Compared with the DL model, the characteristic stability of radiomics model was higher; however, the prediction capabilities of the DL and radiomics model were comparable. Which model is better requires further verification. Fifth, the factors involved with image features, such as histogram equalization approaches, noise removal methods, and image reconstruction methods, require more in-depth study. Sixth, more study is required to determine whether transfer learning may take the role of the specifically created model for NSCLC due to the heterogeneity between the source and destination databases. In addition, PD-L1 expression data were unavailable for a majority of patients in our cohort. The correlation between PD-L1 expression, which was a clinically validated biomarker of benefit from PD1/PD-L1 blockade, and the instructed model, was not involved in our study.

To the best of our knowledge, this is the first work assessing the robustness of image features in CT imaging of NSCLC patients. In addition, we perform a comparative analysis to select the best machine-learning methods with favorable predictive AUC and stability. Inception V3_RELF_Nearest Neighbors classifiers provided a robust, non-invasive way to identify NSCLC patients who may benefit from immunotherapy. We believe that combining machine-learning methods and radiomics/DL features will improve the AUC in predicting immunotherapy efficacy.

Data availability statement

The raw data supporting the conclusions of this article will be made available by the authors, without undue reservation.

Ethics statement

The studies involving human participants were reviewed and approved by the Ethics Committee of Union Hospital. Written informed consent for participation was not required for this study in accordance with the national legislation and the institutional requirements.

Author contributions

The study was designed by NH, QJ, and QR with the help of the others. QR, PZ, FX, XC, NH, and QJ analyzed and interpreted the data. QR developed a model. QR, QJ, FX, and PZ performed the main computational works. NH, XC, and GW collected surgical data and supported transcriptome analyses. QR, FX, PZ, XC, NH, and QJ collected and analyzed the clinical data. QR, FX, PZ, and QJ performed image analysis and interpretation. GW and NH acquired funding for this study. QR, FX, PZ, NH, and QJ mainly wrote the manuscript, and all authors edited the manuscript. All authors contributed to the article and approved the submitted version.

Funding

This study was supported by the National Natural Science Foundation of China (No. 82172755) and Wuhan Knowledge Innovation Special (Item Number: 2022020801020532).

Conflict of interest

The authors declare that the research was conducted in the absence of any commercial or financial relationships that could be construed as a potential conflict of interest.

Publisher's note

All claims expressed in this article are solely those of the authors and do not necessarily represent those of their affiliated organizations, or those of the publisher, the editors and the reviewers. Any product that may be evaluated in this article, or claim that may be made by its manufacturer, is not guaranteed or endorsed by the publisher.

Supplementary material

The Supplementary Material for this article can be found online at: https://www.frontiersin.org/articles/10.3389/fonc.2022.952749/full#supplementary-material

References

1. Borghaei H, Gettinger S, Vokes EE, Chow LQM, Burgio MA, de Castro Carpeno J, et al. Five-year outcomes from the randomized, phase III trials CheckMate 017 and 057: Nivolumab versus docetaxel in previously treated non-Small-Cell lung cancer. *J Clin Oncol* (2021) 39:723–33. doi: 10.1200/JCO.20.01605

2. Herbst RS, Baas P, Kim D-W, Felip E, Pérez-Gracia JL, Han J-Y, et al. Pembrolizumab versus docetaxel for previously treated, PD-L1-positive, advanced non-small-cell lung cancer (KEYNOTE-010): a randomised controlled trial. *Lancet* (2016) 387:1540–50. doi: 10.1016/s0140-6736(15)01281-7

3. Rittmeyer A, Barlesi F, Waterkamp D, Park K, Ciardiello F, von Pawel J, et al. Atezolizumab versus docetaxel in patients with previously treated non-small-cell lung cancer (OAK): a phase 3, open-label, multicentre randomised controlled trial. *Lancet* (2017) 389:255–65. doi: 10.1016/s0140-6736(16)32517-x

4. Garon EB, Rizvi NA, Hui R, Leighl N, Balmanoukian AS, Eder JP, et al. Pembrolizumab for the treatment of non-small-cell lung cancer. *N Engl J Med* (2015) 372:2018–28. doi: 10.1056/NEJMoa1501824

5. Mansfield AS, Aubry MC, Moser JC, Harrington SM, Dronca RS, Park SS, et al. Temporal and spatial discordance of programmed cell death-ligand 1 expression and lymphocyte tumor infiltration between paired primary lesions and brain metastases in lung cancer. *Ann Oncol* (2016) 27:1953–8. doi: 10.1093/annonc/mdw289

6. Santos R, Ursu O, Gaulton A, Bento AP, Donadi RS, Bologa CG, et al. A comprehensive map of molecular drug targets. *Nat Rev Drug Discovery* (2017) 16:19–34. doi: 10.1038/nrd.2016.230

7. Gillies RJ, Kinahan PE, Hricak H. Radiomics: Images are more than pictures, they are data. *Radiology* (2016) 278:563–77. doi: 10.1148/radiol.2015151169

8. Lambin P, Rios-Velazquez E, Leijenaar R, Carvalho S, van Stiphout RG, Granton P, et al. Radiomics: extracting more information from medical images using advanced feature analysis. *Eur J Cancer* (2012) 48:441–6. doi: 10.1016/j.ejca.2011.11.036

9. Limkin EJ, Sun R, Dercle L, Zacharaki EI, Robert C, Reuze S, et al. Promises and challenges for the implementation of computational medical imaging (radiomics) in oncology. *Ann Oncol* (2017) 28:1191–206. doi: 10.1093/annonc/mdx034

10. van Timmeren JE, Leijenaar RTH, van Elmpt W, Wang J, Zhang Z, Dekker A, et al. Test-retest data for radiomics feature stability analysis: Generalizable or study-specific? *Tomography* (2016) 2:361–5. doi: 10.18383/j.tom.2016.00208

11. Stonnington CM, Tan G, Kloppel S, Chu C, Draganski B, Jack CRJr., et al. Interpreting scan data acquired from multiple scanners: a study with alzheimer's disease. *Neuroimage* (2008) 39:1180–5. doi: 10.1016/j.neuroimage.2007.09.066

12. Saha A, Yu X, Sahoo D, Mazurowski MA. Effects of MRI scanner parameters on breast cancer radiomics. *Expert Syst Appl* (2017) 87:384–91. doi: 10.1016/j.eswa.2017.06.029

13. Mackin D, Fave X, Zhang L, Fried D, Yang J, Taylor B, et al. Measuring computed tomography scanner variability of radiomics features. *Invest Radiol* (2015) 50:757–65. doi: 10.1097/RLI.0000000000000180

14. Zwanenburg A, Leger S, Agolli L, Pilz K, Troost EGC, Richter C, et al. Assessing robustness of radiomic features by image perturbation. *Sci Rep* (2019) 9:614. doi: 10.1038/s41598-018-36938-4

15. Hodi FS, Ballinger M, Lyons B, Soria JC, Nishino M, Tabernero J, et al. Immune-modified response evaluation criteria in solid tumors (imRECIST): Refining guidelines to assess the clinical benefit of cancer immunotherapy. *J Clin Oncol* (2018) 36:850–8. doi: 10.1200/JCO.2017.75.1644

16. Zhao B, James LP, Moskowitz CS, Guo P, Ginsberg MS, Lefkowitz RA, et al. Evaluating variability in tumor measurements from same-day repeat CT scans of patients with non-small cell lung cancer. *Radiology* (2009) 252:263–72. doi: 10.1148/radiol.2522081593

17. Clark K, Vendt B, Smith K, Freymann J, Kirby J, Koppel P, et al. The cancer imaging archive (TCIA): maintaining and operating a public information repository. *J Digit Imaging* (2013) 26:1045–57. doi: 10.1007/s10278-013-9622-7

18. van Griethuysen JJM, Fedorov A, Parmar C, Hosny A, Aucoin N, Narayan V, et al. Computational radiomics system to decode the radiographic phenotype. *Cancer Res* (2017) 77:e104–7. doi: 10.1158/0008-5472.CAN-17-0339

19. Sainath TN, Kingsbury B, Saon G, Soltau H, Mohamed AR, Dahl G, et al. Deep convolutional neural networks for large-scale speech tasks. *Neural Networks Off J Int Neural Network Soc* (2015) 64:39–48. doi: 10.1016/j.neunet.2014.08.005

20. Koyuncu H, Ceylan R. Elimination of white Gaussian noise in arterial phase CT images to bring adrenal tumours into the forefront. *Comput Med Imaging Graph* (2018) 65:46–57. doi: 10.1016/j.compmedimag.2017.05.004

21. Zwanenburg A, Vallieres M, Abdalah MA, Aerts H, Andrearczyk V, Apte A, et al. The image biomarker standardization initiative: Standardized quantitative radiomics for high-throughput image-based phenotyping. *Radiology* (2020) 295:328–38. doi: 10.1148/radiol.2020191145

22. Baiocco S, Sah BR, Mallia A, Kelly-Morland C, Neji R, Stirling JJ, et al. Exploratory radiomic features from integrated (18)F-fluorodeoxyglucose positron emission tomography/magnetic resonance imaging are associated with contemporaneous metastases in oesophageal/gastroesophageal cancer. *Eur J Nucl Med Mol Imaging* (2019) 46:1478–84. doi: 10.1007/s00259-019-04306-7

23. Abraham A, Pedregosa F, Eickenberg M, Gervais P, Mueller A, Kossaifi J, et al. Machine learning for neuroimaging with scikit-learn. *Front Neuroinform* (2014) 8:14. doi: 10.3389/fninf.2014.00014

24. Tumeh PC, Harview CL, Yearley JH, Shintaku IP, Taylor EJ, Robert L, et al. PD-1 blockade induces responses by inhibiting adaptive immune resistance. *Nature* (2014) 515:568–71. doi: 10.1038/nature13954

25. Hellmann MD, Ciuleanu TE, Pluzanski A, Lee JS, Otterson GA, Audigier-Valette C, et al. Nivolumab plus ipilimumab in lung cancer with a high tumor mutational burden. *N Engl J Med* (2018) 378:2093–104. doi: 10.1056/NEJMoa1801946

26. Gu D, Liu G, Xue Z. On the performance of lung nodule detection, segmentation and classification. *Comput Med Imaging Graph* (2021) 89:101886. doi: 10.1016/j.compmedimag.2021.101886

27. Coudray N, Ocampo PS, Sakellaropoulos T, Narula N, Snuderl M, Fenyo D, et al. Classification and mutation prediction from non-small cell lung cancer histopathology images using deep learning. *Nat Med* (2018) 24:1559–67. doi: 10.1038/s41591-018-0177-5

28. Arbour KC, Luu AT, Luo J, Rizvi H, Plodkowski AJ, Sakhi M, et al. Deep learning to estimate RECIST in patients with NSCLC treated with PD-1 blockade. *Cancer Discovery* (2021) 11:59–67. doi: 10.1158/2159-8290.CD-20-0419

29. Shin HC, Roth HR, Gao M, Lu L, Xu Z, Nogues I, et al. Deep convolutional neural networks for computer-aided detection: CNN architectures, dataset

characteristics and transfer learning. *IEEE Trans Med Imaging* (2016) 35:1285–98. doi: 10.1109/TMI.2016.2528162

30. Vaidya P, Bera K, Gupta A, Wang X, Corredor G, Fu P, et al. CT derived radiomic score for predicting the added benefit of adjuvant chemotherapy following surgery in stage I, II resectable non-small cell lung cancer: a retrospective multicohort study for outcome prediction. *Lancet Digital Health* (2020) 2:e116–28. doi: 10.1016/s2589-7500(20)30002-9

31. Khorrami M, Jain P, Bera K, Alilou M, Thawani R, Patil P, et al. Predicting pathologic response to neoadjuvant chemoradiation in resectable stage III non-small cell lung cancer patients using computed tomography radiomic features. *Lung Cancer* (2019) 135:1–9. doi: 10.1016/j.lungcan.2019.06.020

32. Khorrami M, Prasanna P, Gupta A, Patil P, Velu PD, Thawani R, et al. Changes in CT radiomic features associated with lymphocyte distribution predict overall survival and response to immunotherapy in non-small cell lung cancer. *Cancer Immunol Res* (2020) 8:108–19. doi: 10.1158/2326-6066.CIR-19-0476

33. Trebeschi S, Drago SG, Birkbak NJ, Kurilova I, Calin AM, Delli Pizzi A, et al. Predicting response to cancer immunotherapy using noninvasive radiomic biomarkers. *Ann Oncol* (2019) 30:998–1004. doi: 10.1093/annonc/mdz108

34. Mok TSK, Wu Y-L, Kudaba I, Kowalski DM, Cho BC, Turna HZ, et al. Pembrolizumab versus chemotherapy for previously untreated, PD-L1-expressing, locally advanced or metastatic non-small-cell lung cancer (KEYNOTE-042): a randomised, open-label, controlled, phase 3 trial. *Lancet* (2019) 393:1819–30. doi: 10.1016/s0140-6736(18)32409-7

35. Reck M, Rodriguez-Abreu D, Robinson AG, Hui R, Csoszi T, Fulop A, et al. Updated analysis of KEYNOTE-024: Pembrolizumab versus platinum-based chemotherapy for advanced non-Small-Cell lung cancer with PD-L1 tumor proportion score of 50% or greater. *J Clin Oncol* (2019) 37:537–46. doi: 10.1200/JCO.18.00149

36. Ng F, Kozarski R, Ganeshan B, Goh V. Assessment of tumor heterogeneity by CT texture analysis: can the largest cross-sectional area be used as an alternative to whole tumor analysis? *Eur J Radiol* (2013) 82:342–8. doi: 10.1016/j.ejrad.2012.10.023

frontiers | Frontiers in Oncology

TYPE Original Research
PUBLISHED 08 August 2022
DOI 10.3389/fonc.2022.915835

OPEN ACCESS

EDITED BY
Shenghong Ju,
Southeast University, China

REVIEWED BY
Marta Zerunian,
Sapienza University of Rome, Italy
Lihua Chen,
Wuxi Taihu Hospital, China

*CORRESPONDENCE
Shouliang Qi
qisl@bmie.neu.edu.cn

SPECIALTY SECTION
This article was submitted to Cancer Imaging and Image-directed Interventions, a section of the journal Frontiers in Oncology

RECEIVED 08 April 2022
ACCEPTED 18 July 2022
PUBLISHED 08 August 2022

CITATION
Chang R, Qi S, Zuo Y, Yue Y, Zhang X, Guan Y and Qian W (2022) Predicting chemotherapy response in non-small-cell lung cancer *via* computed tomography radiomic features: Peritumoral, intratumoral, or combined?
Front. Oncol. 12:915835.
doi: 10.3389/fonc.2022.915835

Predicting chemotherapy response in non-small-cell lung cancer *via* computed tomography radiomic features: Peritumoral, intratumoral, or combined?

Runsheng Chang[1], Shouliang Qi[1,2]*, Yifan Zuo[1], Yong Yue[3], Xiaoye Zhang[4], Yubao Guan[5] and Wei Qian[1]

[1]College of Medicine and Biological Information Engineering, Northeastern University, Shenyang, China, [2]Key Laboratory of Intelligent Computing in Medical Image, Ministry of Education, Northeastern University, Shenyang, China, [3]Department of Radiology, Shengjing Hospital of China Medical University, Shenyang, China, [4]Department of Oncology, Shengjing Hospital of China Medical University, Shenyang, China, [5]Department of Radiology, The Fifth Affiliated Hospital of Guangzhou Medical University, Guangzhou, China

Purpose: This study aims to evaluate the ability of peritumoral, intratumoral, or combined computed tomography (CT) radiomic features to predict chemotherapy response in non-small cell lung cancer (NSCLC).

Methods: After excluding subjects with incomplete data or other types of treatments, 272 (Dataset 1) and 43 (Dataset 2, external validation) NSCLC patients who were only treated with chemotherapy as the first-line treatment were enrolled between 2015 and 2019. All patients were divided into response and nonresponse based on the response evaluation criteria in solid tumors, version 1.1. By using 3D slicer and morphological operations in python, the intra- and peritumoral regions of lung tumors were segmented from pre-treatment CT images (unenhanced) and confirmed by two experienced radiologists. Then radiomic features (the first order, texture, shape, et al.) were extracted from the above regions of interest. The models were trained and tested in Dataset 1 and further validated in Dataset 2. The performance of models was compared using the area under curve (AUC), confusion matrix, accuracy, precision, recall, and F1-score.

Results: The radiomic model using features from the peritumoral region of 0–3 mm outperformed that using features from 3–6, 6–9, 9–12 mm peritumoral region, and intratumoral region (AUC: 0.95 versus 0.87, 0.86, 0.85, and 0.88). By the fusion of features from 0–3 and 3–6 mm peritumoral regions, the logistic regression model achieved the best performance, with an AUC of 0.97. This model achieved an AUC of 0.85 in the external cohort. Moreover, among the 20 selected features, seven features differed significantly between the two groups ($p < 0.05$).

Conclusions: CT radiomic features from both the peri- and intratumoral regions can predict chemotherapy response in NSCLC using machine learning models. Combined features from two peritumoral regions yielded better predictions.

KEYWORDS

non-small cell lung cancer, Computed Tomography (CT), chemotherapy response, radiomics, peritumoral features, area under curve

Introduction

Lung cancer remains the leading cause of cancer-related deaths, with a 2-year relative survival rate of 36% (1). Histologically, non-small cell lung cancer (NSCLC) is the most common type of lung cancer, and locally advanced NSCLC patients comprise approximately 30% of newly diagnosed patients (2–4). Clinically, patients received surgery, chemotherapy, radiation, or targeted drug therapies as the first-line treatment according to related clinical guidelines. As the standard first-line treatment of advanced-stage NSCLC patients with no specific gene mutations, chemotherapy has been and will still be a cornerstone in the near future (5). However, owing to the heterogeneity of tumors, different patients may have extremely different therapeutic effects on chemotherapy, and the adverse reaction may even have a significant impact on the survival rate of NSCLC patients (6–10).

Radiomic features, extracted from computed tomography (CT) images, can quantitatively express crucial information regarding the physiology of the entire tumor, including the intra-tumor and its surroundings (11–13). Owing to the spatially and temporally heterogeneous nature of tumors, these features can quantify the phenotypic differences from a high-dimensional space that cannot be distinguished by the naked eye. Therefore, these features and the resulting radiomic models are of important guiding significance for precision oncology and can improve decision support in prognosis and therapeutic response prediction at a low cost (14, 15).

Recently, many studies have begun investigating the role of radiomics features of the surrounding area of the lesion (peritumoral region) in disease screening, prediction of treatment response, and prognosis. The microenvironment and habitat surrounding the tumor may play an extremely important role in predicting prognosis. Many studies have found that the pathogenesis and progression of lung cancer are closely related to tumor-infiltrating lymphocytes and tumor-associated macrophages all over the tumor microenvironment (Maeda et al) (16–18). Algohary *et al.* studied 231 prostate cancer patients and extracted radiomic features from the intra- and peri-tumoral region of interest (ROI) to distinguish prostate cancer risk categories as defined by the D'Amico Risk Classification System, with an area under the receiver operating characteristic curve (AUC) of 0.84 (19). Shan *et al.* constructed a model based on peritumoral radiomic signatures from CT images of 156 patients to predict the early recurrence of hepatocellular carcinoma after curative treatment and obtained an AUC of 0.80 (20).

Many radiomics studies have also been applied to the treatment of NSCLC. Khorrami *et al.* collected 125 NSCLC patients to identify the role of radiomics texture features from regions both within and outside the nodule in predicting response to chemotherapy and overall survival; they obtained an AUC of 0.82 (21). Braman *et al.* analyzed intra- and peritumoral regions of 117 patients with breast cancer to predict pathological complete response to neoadjuvant chemotherapy and obtained an AUC of 0.78 (22).

However, the ability of peritumoral, intratumoral, or combined CT radiomic features to predict chemotherapy response in NSCLC has not been well studied. In this study, we established different CT radiomic models using features from different peritumoral, intratumoral, or combined regions and evaluated their performance in predicting chemotherapy response in NSCLC.

Materials and methods

Patient characteristics

This study was approved by the ethics committee of Shengjing Hospital of China Medical University and the Fifth Affiliated Hospital of Guangzhou Medical University, and the requirement for informed consent was waived because this was a retrospective study. A total of 605 patients with NSCLC were enrolled between 2015 and 2019 at Shengjing Hospital of China Medical University. Of these 605 patients, 272 NSCLC patients who were treated with chemotherapy alone as first-line treatment were included in this study (Dataset 1).

Supplemental Figure S1 shows the two steps of the exclusion criteria. Using the same criteria, 43 patients from the Fifth Affiliated Hospital of Guangzhou Medical University were selected and used as the external validation cohort (Dataset 2).

The clinical characteristics of the patients are presented in Table 1. Pathologic stage was characterized according to the seventh edition of the American Joint Committee on Cancer TNM staging system. For each patient, non-contrast CT images were acquired before and after chemotherapy. The parameters used for CT image acquisition are listed in Supplemental Table S1.

According to the response evaluation criteria in solid tumors (RECIST, version 1.1) (23), clinical responses were categorized into four parts by comparing CT images collected before and after chemotherapy: (I) complete response (CR): all target lesions disappeared; (II) partial response (PR): the target lesions decreased by at least 30% in the sum of the diameters; (III) progressive disease (PD): the target lesions increased by at least 20% in the sum of the diameters; (IV) stable disease (SD): neither sufficient shrinkage to qualify for PR nor sufficient increase to qualify for PD. The interval between CT scans before and after chemotherapy was 4.56 ± 1.41 and 3.87 ± 2.04 treatment courses in response and nonresponse groups (each treatment course takes three weeks) of Dataset 1. The interval was 3.87± 1.58 and 3.24± 1.06 treatment courses in the two groups of Dataset 2.

In this study, clinical response was defined as "response" and "nonresponse" based on the radiologist's evaluation *via* RECIST and clinical manifestations. The response group included patients with CR and PR, while the non-response group included patients with PD and SD.

Overview of the study procedure

Figure 1 shows a brief procedure of this study. First, the 272 NSCLC patients (148 responses and 124 nonresponses) were randomly divided into a training cohort of 189 patients (105 responses and 84 nonresponses) and an independent test cohort of 83 patients (44 responses and 39 nonresponses). Second, all lesions were segmented from the pre-treatment CT images, and then the peritumoral regions (0–3 mm, 3–6 mm, 6–9 mm, and 9–12 mm) around the lesion. Third, radiomics features were extracted from the segmented regions, and discriminative features were selected. Finally, different models were trained using radiomic features, validated, and compared.

Segmentation of intra- and peritumoral regions

First, to eliminate interference factors, all pre-treatment CT images of the NSCLC patients were interpolated into voxels of 1×1×1 mm. Thereafter, intratumoral regions were semi-automatically segmented from these CT images by two radiologists with more than 15 years of experience using 3D Slicer software (24). By adding seed points and applying the fast marching method, the lesions could be quickly segmented automatically. If necessary, the errors were corrected by radiologists manually. To compare the segmentation by the two radiologists, the Dice coefficient and over– and under–lesion segmentation errors were calculated.

Next, four morphological dilation operations were applied with the number of pixels of 3, 6, 9, and 12, respectively. These

TABLE 1 Clinical characteristics of NSCLC patients.

Characteristics		Dataset 1			Dataset 2		
		Response group	Non response group	*p*-value	Response group	Non response group	*p*-value
No. of patients		148	124	–	24	19	–
Gender	Male	81	69	3.843[a]	22	15	4.987[a]
	Female	67	55		2	4	
Age, median (SD), y		63.76 (11.30)	64.86 (10.65)	0.453[b]	66.42 (9.86)	62.36 (14.58)	0.629[b]
Smoking status	Ever	50	69	1.021[a]	17	12	1.235[a]
	Never	98	55		7	7	
Histological type	Adenocarcinoma	121	101	2.241[a]	13	11	3.244[a]
	Squamous cell carcinoma	27	23		11	8	
TNM Stage	II	22	16	1.232[a]	1	2	2.065[a]
	III	118	103	0.863[a]	20	15	0.983[a]
	IV	8	5	1.528[a]	3	2	1.024[a]
Courses, median (SD)		4.56 ± 1.41	3.87 ± 2.04	0.002[b]	3.87± 1.58	3.24± 1.06	0.688[a]

[a]p value of Chi-square test; [b]p value of two-sample t-test.
SD, standard deviation; TNM, tumor node metastasis classification.

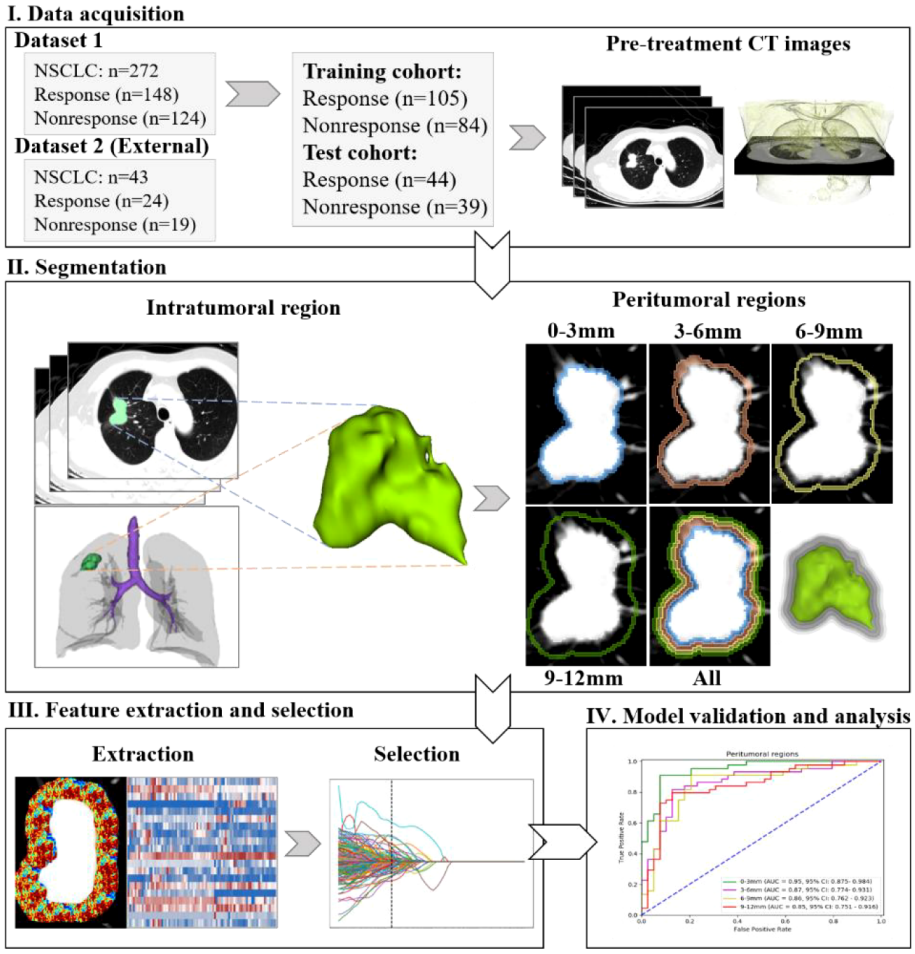

FIGURE 1
Overview of the whole study procedure.

operations were based on a 3D morphology algorithm in the skimage package (https://scikit-image.org). After subtraction, four peritumoral regions of 0–3 mm, 3–6 mm, 6–9 mm, and 9–12 mm were obtained. Supplemental Figure S2 shows the details of these regions.

Radiomic features extraction and selection

First, an open-source PyRadiomics Python package was applied to extract 1688 radiomic features from each segmented region. To establish a reference standard for radiomics analysis, PyRadiomics provides an open-source platform for easy and reproducible radiomic feature extraction (25). The original CT images and derived 19 categories of images (LoG with five sigma levels, one level of wavelet decompositions yielding eight derived images and images derived using square, square root, logarithm, exponential, gradient, and local binary pattern filters) were utilized to extract the features. 1896 radiomics features including the first order (380), shape-based (16), gray-level co-occurrence matrix (480), gray level run length matrix (320), gray level size zone matrix (320), neighboring gray tone difference matrix (100), and gray level dependence matrix (280) were obtained. After removing the unusable ones, 1688 features were retained.

Next, for each intra- or peritumoral region, 20 discriminative radiomics features were selected using the least absolute shrinkage and selection operator (LASSO) algorithm. The LASSO algorithm adds a penalty term (λ) to the loss function (optimization target); therefore, λ is considered in the process of training and solving parameters. As shown in Supplemental Figure S3, with an increase in λ, the mean square error decreases gradually to the lowest point. This point corresponds to the optimal parameter of λ. Meanwhile,

the coefficient of the less influential feature will decrease to 0, and finally, only the most important features are retained (26). At the optimal λ, features with non-zero coefficients will be retained and ranked by the absolute value of the coefficient. To decrease the overfitting risk and avoid the dimensionality curse, only the top 20 features are finally selected as the discriminative features according to the rule of thumb that each feature corresponds to 10 samples in a binary classifier (27).

Model construction, validation, and comparison

To clarify the performance of models using features from different peri- and intratumoral regions, four groups of comparative experiments were conducted.

I. To investigate features from which peritumoral regions perform best, the four models corresponding to 0–3 mm, 3–6 mm, 6–9 mm, and 9–12 mm are compared.
II. To investigate whether the fusion of peritumoral features and images improves the performance, models using the feature and image fusion of 0–3 mm and 3–6 mm were compared (28–30).
III. To consider whether peritumoral features outperform intratumoral features, a model using features from the intratumoral region was studied.
IV. To explore whether the fusion of peri- and intratumoral features and images improves the performance, the models using the feature and image fusion of intratumoral and 0–3 mm peritumoral regions were compared.

Feature fusion implies that 1688 features from each region are combined into 3376 features, and the top 20 features are selected according to the same method described previously. Image fusion implies that the two regions are combined, 1688 features are extracted, and the top 20 are maintained in the same way.

Different models were constructed using three representative machine-learning classifiers: random forest (RF), support vector machine (SVM), and logistic regression (LR). Each optimal hyper-parameter of the models was calculated using a grid search algorithm and 10-fold cross-validation. This implies that every grid of hyper-parameters is evaluated by the average of 10-fold cross-validation, and a combination of optimal hyper-parameters is obtained after traversing all grids. The model with optimal hyper-parameters was retrained using all training data (n=189), and then the generated model was evaluated in an independent test cohort (n=83). The aim of dividing Dataset 1 into a training cohort and a test cohort is to obtain the optimal hyper-parameters in machine-learning classifiers and simultaneously avoid information leakage. Dataset 2 was used as an external validation cohort to know the generalizability of the model developed in Dataset 2. The two datasets were collected from different hospitals and by different CT scanners.

Specifically, we used a grid search with cross-validation (GridSearchCV) to traverse the hyper-parameters within a certain range and with a specific interval. In SVM, the kernel parameter was set as "linear" or radial basis function ("rbf"); the parameter C was set as 0.001, 0.01, 0.1, 1, 10, 100 or 1000; the gamma parameter was set as 0.0001, 0.001, 0.005, 0.01, 0.1, 0.5, 1, 3, 5, 10 or 100. In RF, n_estimators parameter ranged from 20 to 2000 with an interval of 10, max_features parameter was set as 2 or 3, min_sample_leaf ranged from 1 to 50 with an interval of 1 and ranged from 100 to 500 with an interval of 50. In LR, the C parameter was set as 0.001, 0.01, 0.1, 1, 10, or 100; the penalty item was set as L1 or L2.

Model evaluation and statistical analysis

For each model, the performance was evaluated by the area under the receiver operating characteristic curve (AUC) with 95% confidence interval (CI), confusion matrix, accuracy, precision, recall, and F1-score. The cut-off was determined using Youden's index and the shortest distance from the coordinate (0, 1) on the ROC curve.

A two-sample t-test was used to compare the age and number of treatment courses between the response and non-response groups. The chi-square test was used to compare the gender, histological type, and smoking status of the two groups. The ROC curves of the different models were compared using the Delong test. If $p<0.05$, a significant difference was considered to be statistically significant.

Results

Performance of features from different peritumoral regions

In the independent test cohort, the predictive performance of the three machine-learning models in each peritumoral region is shown in Figure 2. It was found that among the three machine learning classifiers, the LR model presented the highest AUC and performed best in every peritumoral region (Figure 2A). The ROC curve and confusion matrix of LR models using features from four peritumoral regions are summarized in Figures 2B, C, respectively. The AUC of 0–3, 3–6, 6–9, and 9–12 mm peritumoral regions were 0.95, 0.87, 0.86, and 0.85,

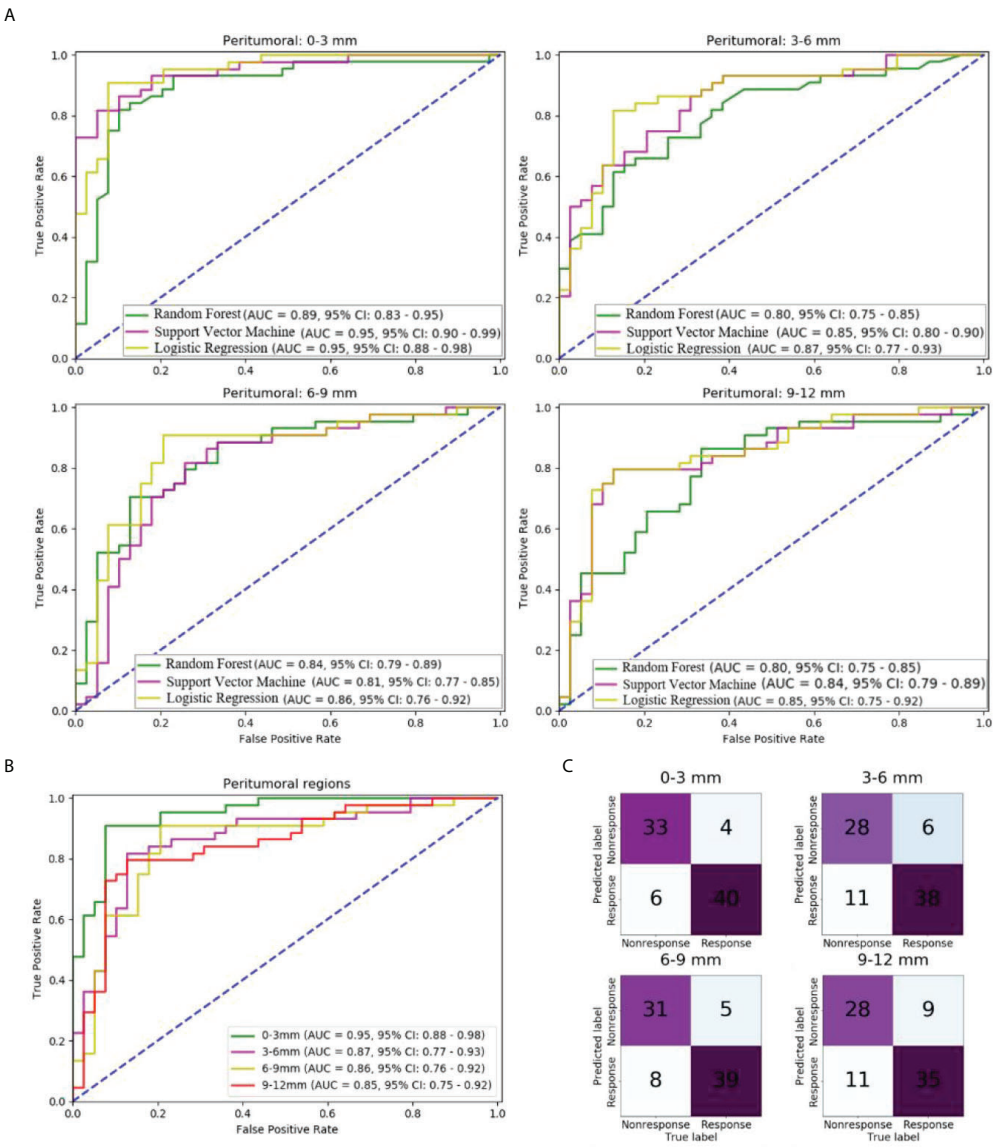

FIGURE 2
Comparison of models using different peritumoral regions in the independent test cohort: **(A)** ROC curves of models using different peritumoral regions and machine learning methods; **(B)** ROC curve of models using different peritumoral regions and logistic regression; **(C)** Confusion matrix of models using different peritumoral regions and logistic regression.

respectively. The peritumoral region of 0–3 mm had the highest AUC.

The other performance measures are listed in Table 2. For the 0–3 mm peritumoral region, the accuracy, precision, recall, and F1-score were 87.9%, 0.89, 0.85, and 0.87, respectively, while the cut-off value was 0.83. For the 3–6 mm peritumoral region, the measures were 79.5%, 0.82, 0.72, and 0.77, while the cut-off value was 0.69. For the 6–9 mm peritumoral region, the measures were 84.3%, 0.86, 0.80, and 0.83, while the cut-off value was 0.70. For the 9–12 mm peritumoral region, the measures were 75.9%, 0.76, 0.72, and 0.74, respectively, while the cut-off value was 0.67.

Performance of different methods of fusing peritumoral regions

In the independent test cohort, the predictive performance of models using the feature and image fusion of 0–3 mm and 3–6 mm peritumoral regions were compared

TABLE 2 Predictive performance of different regions in the independent test cohort.

ROI	AUC	Accuracy	Precision	Recall	F-score
0-3 mm	0.95	87.9%	0.89	0.85	0.87
3-6 mm	0.87	79.5%	0.82	0.72	0.77
6-9 mm	0.86	84.3%	0.86	0.80	0.83
9-12 mm	0.85	75.9%	0.76	0.72	0.74
Image fusion (0–3 and 3–6 mm)	0.89	80.7%	0.85	0.72	0.78
Feature fusion (0–3 and 3–6 mm)	0.97	92.7%	0.922	0.92	0.92
Intratumoral region	0.88	81.9%	0.85	0.74	0.80
Image fusion (Intra and 0–3 mm)	0.88	81.9%	0.82	0.80	0.81
Feature fusion (Intra and 0–3 mm)	0.92	91.5%	0.94	0.87	0.91

ROI, region of interest; AUC, area under the curve.

(Figure 3). As shown in Figure 3A, the LR model outperformed the SVM and RF models in both feature fusion and image fusion. For the LR model, the feature fusion and image fusion were compared using the ROC curve and confusion matrix (Figures 3B, C). The AUC of feature fusion of 0–3 and 3–6 mm peritumoral regions was 0.97, higher than that of image fusion (AUC of 0.89). The LR model using feature fusion of 0–3 and 3–6 mm peritumoral regions can correctly predict 36 of 39 nonresponse patients and 41 of 44 response patients.

The other performance measures of these two models are listed in Table 2. The model of feature fusion achieved an accuracy of 92.7%, precision of 0.92, recall of 0.92, an F1-score of 0.92, and a cut-off value of 0.88. For the image fusion model, the four measures were 80.7%, 0.85, 0.72, and 0.78, respectively, while the cut-off value was 0.69.

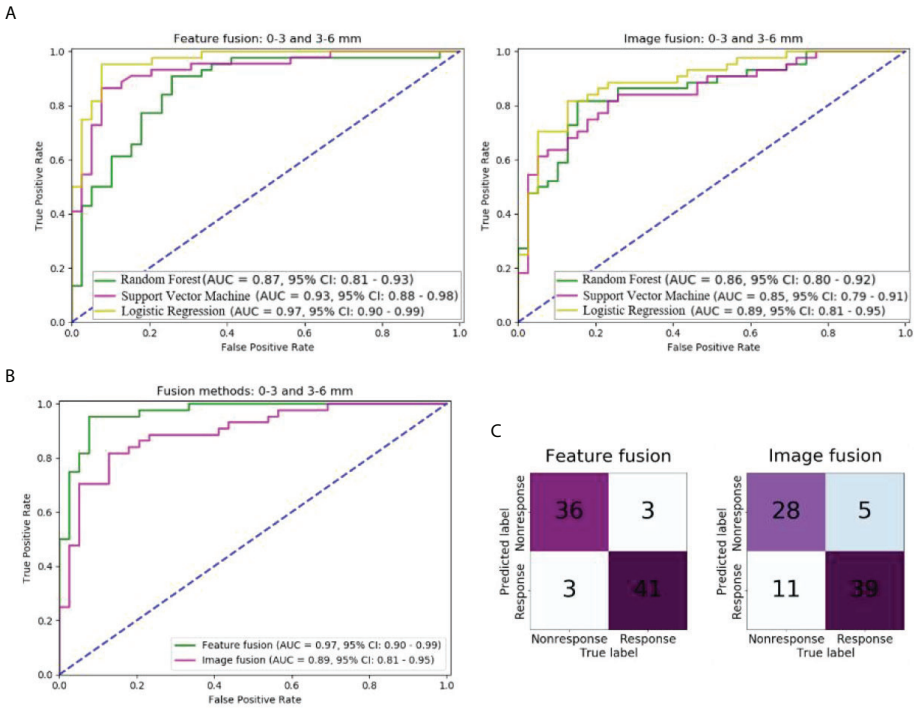

FIGURE 3
Comparison of models with different fusion methods of 0–3 and 3–6 mm peritumoral regions in the independent test cohort: **(A)** ROC curves of models of two fusion methods and three machine learning methods; **(B)** ROC curves of models of two fusion methods and logistic regression; **(C)** Confusion matrix of models of two fusion methods and logistic regression.

Performance of intratumoral region

The ROC curve and confusion matrix of models using CT radiomic features from the intratumoral region are shown in Supplemental Figure S4. Among the three models, the LR model performed the best, with an AUC of 0.88. In the independent test cohort, 29 of 39 non-response patients and 39 of 44 response patients were correctly predicted by the LR model. The cut-off value was 0.71, and the accuracy, precision, recall, and F-score were 81.9%, 0.85, 0.74, and 0.80, respectively (Table 2).

Performance of different methods of fusing intra and peritumoral regions

Supplemental Figure S5 shows the performance of radiomic models using different methods of fusing intra and 0–3 mm peritumoral regions. Similar to the previous results, the LR model outperformed the SVM and RF models for both fusion methods (image and feature) (Supplemental Figure S5A); the AUC was 0.88 for the LR model using the image fusion method and it was 0.92 using the feature fusion (Supplemental Figures S5B, C). Feature fusion yields better performance than image fusion. For the LR model using the image fusion method, the accuracy, precision, recall, and F-score were 81.9%, 0.82, 0.80, 0.81, and 0.67, respectively, while the cut-off value was 0.83. For the LR model using the image method, it was 91.5%, 0.94, 0.87, and 0.91, while the cut-off value was 0.83.

The p values in the Delong test of ROC curves of nine different models are shown in Figure 4. The AUC of the LR model using the 0–3 mm peritumoral region was significantly higher than that of the three models using the 3–6, 6–9, and 9–12 mm peritumoral regions and that of the model using the intratumoral region (Delong test, $p<0.05$). Feature fusion of 0–3 and 3–6 mm peritumoral regions produced an AUC significantly higher than that in the six cases of 3–6, 6–9, and 9–12 mm peritumoral regions, intratumoral regions, image fusion of 0–3 and 3–6 mm peritumoral regions, and image fusion of intratumoral and 0–3 mm peritumoral regions (Delong test, $p<0.05$). Although the AUC of the model using feature fusion of 0–3 and 3–6 mm peritumoral regions was higher than that of the other two cases of 0–3 mm peritumoral region and feature fusion of intratumoral and 0–3 mm peritumoral regions, no significant difference was observed (Delong test, $p>0.05$).

Radiomic features over traditional clinical features

Supplemental Figure S6 shows the performance of models with radiomics features and clinical features (gender, age, histological type, TNM stage, smoking status and the number of treatment courses). The AUC of the model with only clinical features was 0.55. While using both radiomics and clinical features, the model achieved an AUC of 0.96, even lower than that only using radiomic features (0.97). It demonstrates that clinical features had no improvement in predicting chemotherapy in this research.

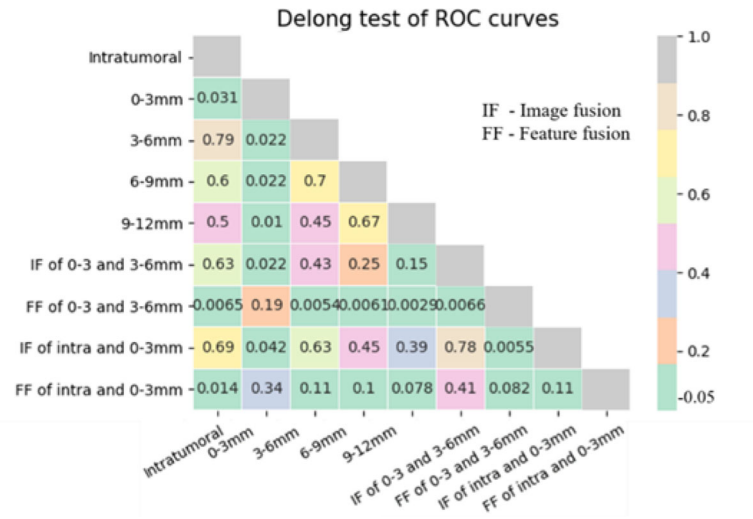

FIGURE 4
p values of Delong test between ROC curves of different models.

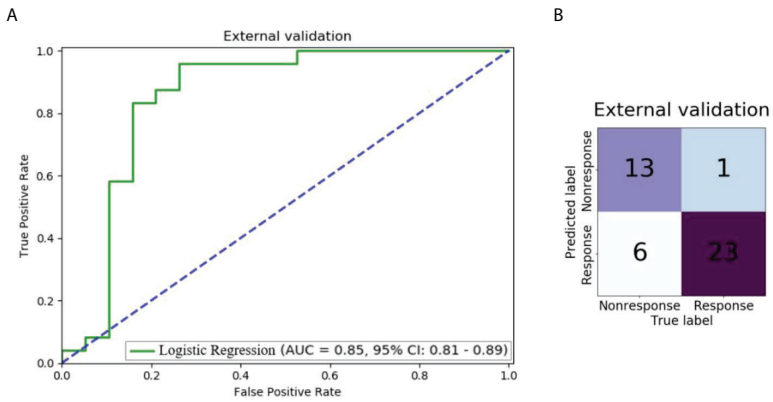

FIGURE 5
Performance of the model using 0-3 and 3-6 peri-tumoral features in the external validation dataset: **(A)** ROC curve; **(B)** Confusion matrix.

Performance in the external validation dataset

Figure 5 shows the performance of the model using 0-3 and 3-6 peri-tumoral features in the external validation dataset. The AUC was 0.85 (95% CI: 0.81-0.89) and 13 of 19 non-response patients and 23 of 24 response patients were correctly predicted by the LR model.

Segmentation agreement and characteristics of radiomic features

For the segmentation agreement by two radiologists, the Dice coefficient is 0.85 ± 0.06, and the over- and under-segmentation errors of segmented tumor volume are 0.22 ± 0.14, 0.28 ± 0.03, respectively.

Feature fusion of 0–3 and 3–6 mm peritumoral regions had the highest AUC in all nine cases. In this case, the 20 discriminative radiomic features (13 from 0–3 mm, 7 from 3–6 mm) included five first-order features, one shape feature, and 14 texture features. Seven radiomic features were significantly different between the response and nonresponse groups [two features with $p<0.001$(★★) and five features with $p<0.05$(★)]. Figure 6 shows the unsupervised hierarchal clustering of radiomic features in the training set, where the x-axis represents the training cohort of patients (n = 189) and the y-axis represents the 20 radiomic features.

Discussions

In this study, the ability of peritumoral, intratumoral, or combined CT radiomic features to predict chemotherapy response in NSCLC was evaluated. It was found that the radiomic model using features from 0–3 mm peritumoral region outperforms that using features from 3–6 mm, 6–9 mm, 9–12 mm peritumoral region, and intratumoral region, with the highest AUC of 0.95. By fusing features from 0–3 mm and 3–6 mm peritumoral regions, the AUC can be further 0.97. Two over-represented features in the response group indicated higher heterogeneity of NSCLC tumors.

Is the peritumoral region predictive?

Our results demonstrated that CT radiomic features from peritumor regions are predictive of chemotherapy response in NSCLC. The prognosis of lung cancer is not only reflected in the lesion but also the surrounding normal tissues; thus, the microbial environment also has great predictive potential for the response to clinical treatment (31). The microenvironment of the peritumoral region of breast malignancy is related to aggressiveness (22). The capillaries and various cells around the tumor border might be more active than those inside the tumor; thus, their immune response to cancer and response to the prognosis, such as chemotherapy, is probably more severe. Algohary *et al.* studied the density of stromal macrophages, epithelial cells, and lymphocytes in the peritumoral region and found it to be related to metastasis of prostate cancer risk.[19] Matsumura et al. collected 1069 resected NSCLC patients with lymphatic permeation located in intra-, peritumoral, or absent to determine the survival impact, and found that lymphatic canals present in peritumoral regions have a significantly higher overall survival rate than the other two groups (32).

Which peritumoral region is optimal?

Similar to the recommended negative surgical margin in the clinic, the different ranges of the peritumoral region contribute

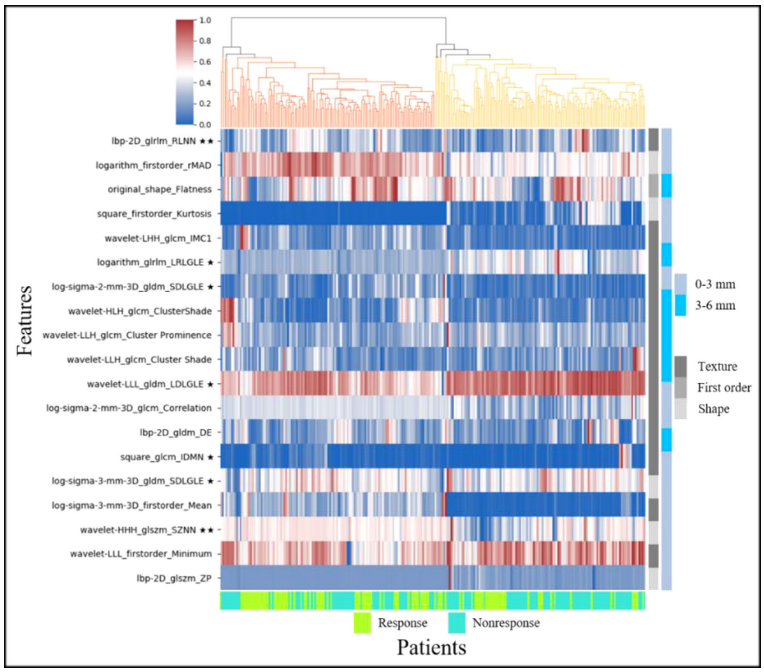

FIGURE 6
Heat map and dendrogram of the top 20 radiomic features in response and nonresponse groups of the training set (★ indicates $p < 0.05$, ★★ indicates $p < 0.001$).

significantly to the prediction of prognostic response. We have found that the features from the 0–3 mm peritumoral region are more predictive of the chemotherapy response of NSCLC than those from 3–6 mm, 6–9 mm, and 9–12 mm peritumoral regions. Some previous studies have indicated that the region beyond 15 mm around the lung tumor lesion has no contribution to predicting the recurrence or remission (21, 33). Beig *et al.* showed that low and middle frequencies of Gabor filters had a higher response at 5 mm around the adenocarcinomas lesion (23). Braman *et al.* found that features from the 2.5–5.0 mm region surrounding the breast tumor are predictive of the pathological complete response to neoadjuvant chemotherapy (22). Algohary *et al.* have found that Haralick from 3–6 and 6–9 mm peritumoral rings and CoLlAGe texture features from 6–9 mm ring were over- and under-expressed, respectively, in high-risk prostate cancer lesions (19).

Is the peritumoral region superior to the intratumoral region?

Our study has shown that the peritumoral region is superior to the intratumoral region in predicting chemotherapy response in NSCLC. A growing number of studies have proven that the tissues and microenvironment around the tumor can provide unique effects on radiomic analysis, sometimes exceeding the intratumoral region (34). Braman *et al.* analyzed the tumor and its surroundings of breast cancer and found that the peritumoral region performed better in estimating the response to HER2-targeted neoadjuvant therapy (35).

Does the combination of regions improve prediction?

In this study, we investigated models using different methods of fusing two peritumoral regions. The model using feature fusion of 0–3 and 3–6 mm peritumoral regions achieves an AUC of 0.97, which is higher than that of the model using the 0–3 mm peritumoral region (0.95), although there was no significant difference (Delong test, $p=0.19$). The feature fusion of the 0–3 mm peritumoral region and intratumoral region even decrease the AUC from 0.95 (only using features from 0–3 peritumoral region) to 0.92. However, Jiang *et al.* have reported that a combination of intra- and peritumoral features of gastric cancer can improve the prediction of chemotherapy response (36). Chen *et al.* also found that incorporating peritumoral radiomic analysis of hepatocellular cancer with intratumoral features can improve the immunoscore estimation of hepatocellular cancer (37). Hu *et al.* have shown that the combination of intra- and peritumoral

features can improve the performance in estimating pathological complete response after neoadjuvant chemoradiation in patients with oesophagal squamous cell carcinoma (38). Therefore, we thought that whether the combination of regions improves prediction might depend on two aspects: discriminative and supplementary. If the features from different regions are both discriminative and supplementary, the combination will improve the prediction. Otherwise, the results of the combination are uncertain.

Moreover, we found that feature fusion was better than image fusion for prediction. This might be because each feature extraction method might have an upper limit of capability. After the combination of images from different regions, the 1688 extracted features are representative of the entire region. However, the feature fusion method combines features extracted from two regions into a set of 3376 features and then uses feature selection methods to obtain the discriminative features. Therefore, complementary features from two different regions can remain. This might be the reason why most previous studies have adopted feature fusion methods (36–38).

Does higher heterogeneity in the peritumoral region correspond to response?

In the response group, run length non-uniformity normalized (RLNN) and size zone nonuniformity normalized (SZNN) features were overrepresented (i.e., higher than that in the nonresponse group). The RLNN measures the similarity of run lengths throughout the image, with a lower value indicating greater homogeneity among run lengths in the image. SZNN measures the variability of size zone volumes throughout the image, with a lower value indicating greater homogeneity among the zone size volumes in the image.

One constructive finding of this research is that in the peritumoral region of NSCLC lesions, the response group had higher heterogeneity than the nonresponse group. Specifically, SZNN and RLNN were overrepresented. This finding provides further evidence that the heterogeneity of the microenvironment in both the tumor and the area around the tumor is predictive of the prognosis of lung cancer. This heterogeneity might be reflective of genomic and genetic heterogeneity and be reflected in pretreatment CT images (6, 39, 40). Some findings have shown that tumor heterogeneity is a predictor of survival in patients with NSCLC (6, 41).

Limitations and further works

There are some limitations to this study. First, the sample size was small. This made the extensive stratified analysis unfeasible, such as investigating the difference between adenocarcinoma and squamous cell carcinoma. Second, the segmentation of intra-and peritumoral regions is semi-automatic, and some features might be dependent on segmentation results. Automatic segmentation by deep learning and extraction of features from the bounding box may address this problem (42). Third, only machine learning methods are employed. Deep learning can be utilized as a powerful end-to-end solution or classifier (43–46).

Conclusion

Non-contrast CT radiomic features from both the peri- and intratumoral regions can predict chemotherapy response in NSCLC *via* machine learning models. The 0–3 mm peritumoral region presented better performance than the peri- and intratumoral regions. The combined features from the two peritumoral regions may further improve the prediction. With the further evaluation of generalizability, the developed model and identified features may help improve the management of patients with NSCLC in precision medicine.

Data availability statement

The datasets presented in this article are not readily available because they must be approved by the Ethics Committee of Shengjing Hospital of Chinese Medical University and the Fifth Affiliated Hospital of Guangzhou Medical University. Requests to access the datasets should be directed to Shouliang Qi, qisl@bmie.neu.edu.cn.

Ethics statement

The studies involving human participants were reviewed and approved by the Ethics Committee of Shengjing Hospital of China Medical University and the Fifth Affiliated Hospital of Guangzhou Medical University. Written informed consent for participation was not required for this study in accordance with the national legislation and the institutional requirements.

Author contributions

RC performed experiments and analyzed the data. SQ, YZ, and WQ proposed the idea, made discussions, and composed the manuscript together with RC. YY, XZ, and YG collected and analyzed the data. JS directed the algorithm development and

analyzed the data. All authors have read and approved the final manuscript.

Funding

This work was partly supported by the National Natural Science Foundation of China (82072008), Liaoning Natural Science Foundation (2011-YGJC-21), Key R&D Program Guidance Projects in Liaoning Province (2019JH8/10300051), and the Fundamental Research Funds for the Central Universities (N2119010, N2224001-10).

Acknowledgments

Some subjects in Dataset 1 (n=250) have been previously used in Chang R, Qi S, Yue Y, Zhang X, Song J and Qian W (2021) Predictive Radiomic Models for the Chemotherapy Response in NonSmall-Cell Lung Cancer based on Computerized-Tomography Images. Front. Oncol. 11:646190. doi: 10.3389/fonc.2021.646190.

Conflict of interest

The authors declare that the research was conducted in the absence of any commercial or financial relationships that could be construed as a potential conflict of interest.

Publisher's note

Supplementary material

The Supplementary Material for this article can be found online at: https://www.frontiersin.org/articles/10.3389/fonc.2022.915835/full#supplementary-material

References

1. Siegel RL, Miller KD, Fuchs HE, Jemal A. Cancer statistics, 2021. *CA Cancer J Clin* (2021) 71(1):7–33. doi: 10.3322/caac.21654

2. Dou TH, Coroller TP, van Griethuysen JJM, Mak RH, Aerts HJWL. Peritumoral radiomics features predict distant metastasis in locally advanced NSCLC. *PloS One* (2018) 13(11):e0206108. doi: 10.1371/journal.pone.0206108

3. Rossi A, Di Maio M. Platinum-based chemotherapy in advanced non-small-cell lung cancer: optimal number of treatment cycles. *Expert Rev Anticancer Ther* (2016) 16(6):653–60. doi: 10.1586/14737140.2016.1170596

4. Duma N, Santana-Davila R, Molina JR. Non-small cell lung cancer: epidemiology, screening, diagnosis, and treatment. *Mayo Clin Proc* (2019) 94(8):1623–40. doi: 10.1016/j.mayocp.2019.01.013

5. Pirker R. Chemotherapy remains a cornerstone in the treatment of non-small cell lung cancer. *Curr Opin Oncol* (2020) 32(1):63–7. doi: 10.1097/CCO.0000000000000592

6. Win T, Miles KA, Janes SM, Ganeshan B, Shastry M, Endozo R, et al. Tumor heterogeneity and permeability as measured on the CT component of PET/CT predict survival in patients with non-small cell lung cancer. *Clin Cancer Res* (2013) 19(13):3591–9. doi: 10.1158/1078-0432.CCR-12-1307

7. Junttila MR, de Sauvage FJ. Influence of tumour micro-environment heterogeneity on therapeutic response. *Nature* (2013) 501(7467):346–54. doi: 10.1038/nature12626

8. O'Connor JP, Rose CJ, Waterton JC, Carano RA, Parker GJ, Jackson A. Imaging intratumor heterogeneity: role in therapy response, resistance, and clinical outcome. *Clin Cancer Res* (2015) 21(2):249–57. doi: 10.1158/1078-0432.CCR-14-0990

9. Bashir U, Siddique MM, Mclean E, Goh V, Cook GJ. Imaging heterogeneity in lung cancer: techniques, applications, and challenges. *AJR Am J Roentgenol* (2016) 207(3):534–43. doi: 10.2214/AJR.15.15864

10. O'Connor JPB. Cancer heterogeneity and imaging. *Semin Cell Dev Biol* (2017) 64:48–57. doi: 10.1016/j.semcdb.2016.10.001

11. Lambin P, Rios-Velazquez E, Leijenaar R, Carvalho S, van Stiphout RG, Granton P, et al. Radiomics: extracting more information from medical images using advanced feature analysis. *Eur J Cancer* (2012) 48(4):441–6. doi: 10.1016/j.ejca.2011.11.036

12. Kumar V, Gu Y, Basu S, Berglund A, Eschrich SA, Schabath MB, et al. Radiomics: the process and the challenges. *Magn Reson Imaging* (2012) 30(9):1234–48. doi: 10.1016/j.mri.2012.06.010

13. Mayerhoefer ME, Materka A, Langs G, Häggström I, Szczypiński P, Gibbs P, et al. Introduction to radiomics. *J Nucl Med* (2020) 61(4):488–95. doi: 10.2967/jnumed.118.222893

14. Aerts HJ, Velazquez ER, Leijenaar RT, Parmar C, Grossmann P, Carvalho S, et al. Decoding tumour phenotype by noninvasive imaging using a quantitative radiomics approach. *Nat Commun* (2014) 5:4006. doi: 10.1038/ncomms5006

15. Parmar C, Grossmann P, Bussink J, Lambin P, Aerts HJWL. Machine learning methods for quantitative radiomic biomarkers. *Sci Rep* (2015) 5:13087. doi: 10.1038/srep13087

16. Maeda R, Yoshida J, Ishii G, Hishida T, Nishimura M, Nagai K. Prognostic impact of intratumoral vascular invasion in non-small cell lung cancer patients. *Thorax* (2010) 65(12):1092–8. doi: 10.1136/thx.2010.141861

17. Gabor S, Renner H, Popper H, Anegg U, Sankin O, Matzi V, et al. Invasion of blood vessels as significant prognostic factor in radically resected T1-3N0M0 non-small-cell lung cancer. *Eur J Cardiothorac Surg* (2004) 25(3):439–42. doi: 10.1016/j.ejcts.2003.11.033

18. Morita R, Sato K, Nakano M, Miura H, Odaka H, Nobori K, et al. Endothelial progenitor cells are associated with response to chemotherapy in human non-small-cell lung cancer. *J Cancer Res Clin Oncol* (2011) 137(12):1849–57. doi: 10.1007/s00432-011-1043-8

19. Algohary A, Shiradkar R, Pahwa S, Purysko A, Verma S, Moses D, et al. Combination of peri-tumoral and intra-tumoral radiomic features on bi-parametric mri accurately stratifies prostate cancer risk: a multi-site study. *Cancers (Basel)* (2020) 12(8):2200. doi: 10.3390/cancers12082200

20. Shan QY, Hu HT, Feng ST, Peng ZP, Chen SL, Zhou Q, et al. CT-based peritumoral radiomics signatures to predict early recurrence in hepatocellular carcinoma after curative tumor resection or ablation. *Cancer Imaging* (2019) 19(1):11. doi: 10.1186/s40644-019-0197-5

21. Khorrami M, Khunger M, Zagouras A, Patil P, Thawani R, Bera K, et al. Combination of peri- and intratumoral radiomic features on baseline ct scans predicts response to chemotherapy in lung adenocarcinoma. *Radiol Artif Intell* (2019) 1(2):e180012. doi: 10.1148/ryai.2019180012

22. Braman NM, Etesami M, Prasanna P, Dubchuk C, Gilmore H, Tiwari P, et al. Intratumoral and peritumoral radiomics for the pretreatment prediction of pathological complete response to neoadjuvant chemotherapy based on breast DCE-MRI. *Breast Cancer Res* (2017) 19(1):57. doi: 10.1186/s13058-017-0846-1

23. Eisenhauer EA, Therasse P, Bogaerts J, Schwartz LH, Sargent D, Ford R, et al. New response evaluation criteria in solid tumours: revised RECIST guideline (version 1. *1) Eur J Cancer* (2009) 45(2):228–47. doi: 10.1016/j.ejca.2008.10.026

24. Fedorov A, Beichel R, Kalpathy-Cramer J, Finet J, Fillion-Robin JC, Pujol S, et al. 3D slicer as an image computing platform for 432 the quantitative imaging network. *Magn Reson Imaging* (2012) 30(9):1323–41. doi: 10.1016/j.mri.2012.05.001

25. van Griethuysen J, Fedorov A, Parmar C, Hosny A, Aucoin N, Narayan V, et al. Computational radiomics system to decode 435 the radiographic phenotype. *Cancer Res* (2017) 77(21):e104–7. doi: 10.1158/0008-5472.CAN-43617-0339

26. Tibshirani R. Regression shrinkage and selection *via* the lasso: a retrospective. *J R Stat Soc Ser B Stat Methodol* (2011) 73:273–82. doi: 10.1111/j.1467-9868.2011.00771.x

27. Gillies RJ, Kinahan PE, Hricak H. Radiomics: images are more than pictures, they are data. *Radiology* (2016) 278(2):563–77. doi: 10.1148/radiol.2015151169

28. Antropova N, Huynh BQ, Giger ML. A deep feature fusion methodology for breast cancer diagnosis demonstrated on three imaging modality datasets. *Med Phys* (2017) 44(10):5162–71. doi: 10.1002/mp.12453

29. Avanzo M, Stancanello J, El Naqa I. Beyond imaging: the promise of radiomics. *Phys Med* (2017) 38:122–39. doi: 10.1016/j.ejmp.2017.05.071

30. Hatt M, Le Rest CC, Tixier F, Badic B, Schick U, Visvikis D. Radiomics: data are also images. *J Nucl Med* (2019) 60(Supplement 2):38S–44S. doi: 10.2967/jnumed.118.220582

31. Joyce JA, Pollard JW. Microenvironmental regulation of metastasis. *Nat Rev Cancer* (2009) 9(4):239–52. doi: 10.1038/nrc2618

32. Matsumura Y, Hishida T, Shimada Y, Ishii G, Aokage K, Yoshida J, et al. Impact of extratumoral lymphatic permeation on postoperative survival of non-small-cell lung cancer patients. *J Thorac Oncol* (2014) 9(3):337–44. doi: 10.1097/JTO.0000000000000073

33. Mohiuddin K, Haneuse S, Sofer T, Gill R, Jaklitsch MT, Colson YL, et al. Relationship between margin distance and local recurrence among patients undergoing wedge resection for small (≤2 cm) non-small cell lung cancer. *J Thorac Cardiovasc Surg* (2014) 147(4):1169–77. doi: 10.1016/j.jtcvs.2013.11.056

34. Wu J, Li B, Sun X, Cao G, Rubin DL, Napel S, et al. Heterogeneous enhancement patterns of tumor-adjacent parenchyma at MR imaging are associated with dysregulated signaling pathways and poor survival in breast cancer. *Radiology* (2017) 285(2):401–13. doi: 10.1148/radiol.2017162823

35. Braman N, Prasanna P, Whitney J, Singh S, Beig N, Etesami M, et al. Association of peritumoral radiomics with tumor biology and pathologic response to preoperative targeted therapy for her2 (erbb2)-positive breast cancer. *JAMA Netw Open* (2019) 2(4):e192561. doi: 10.1001/jamanetworkopen.2019.2561

36. Jiang Y, Wang H, Wu J, Chen C, Yuan Q, Huang W, et al. Noninvasive imaging evaluation of tumor immune microenvironment to predictoutcomes in gastric cancer. *Ann Oncol* (2020) 31(6):760–8. doi: 10.1016/j.annonc.2020.03.295

37. Chen S, Feng S, Wei J, Liu F, Li B, Li X, et al. Pretreatment prediction of immunoscore in hepatocellular cancer: a radiomicsbased clinical model based on gd-EOB-DTPA-enhanced MRI imaging. *Eur Radiol* (2019) 29(8):4177–87. doi: 10.1007/s00330-018-5986-x

38. Hu Y, Xie C, Yang H, Ho J, Wen J, Han L, et al. Assessment of intratumoral and peritumoral computed tomography radiomics for predicting pathological complete response to neoadjuvant chemoradiation in patients with esophageal squamous cell carcinoma. *JAMA Netw Open* (2020) 3(9):e2015927. doi: 10.1001/jamanetworkopen.2020.15927

39. Gerlinger M, Rowan AJ, Horswell S, Math M, Larkin J, Endesfelder D, et al. Intratumor heterogeneity and branched evolution revealed by multiregion sequencing [published correction appears in n engl J med. *N Engl J Med* (2012) 366(10):883–92. doi: 10.1056/NEJMoa1113205

40. Burrell RA, Swanton C. Tumour heterogeneity and the evolution of polyclonal drug resistance. *Mol Oncol* (2014) 8(6):1095–111. doi: 10.1016/j.molonc.2014.06.005

41. Oikonomou A, Khalvati F, Tyrrell PN, Haider MA, Tarique U, Jimenez-Juan L, et al. Radiomics analysis at PET/CT contributes to prognosis of recurrence and survival in lung cancer treated with stereotactic body radiotherapy. *Sci Rep* (2018) 8(1):4003. doi: 10.1038/s41598-018-22357-y

42. Chang R, Qi S, Yue Y, Zhang X, Song J, Qian W. Predictive radiomic models for the chemotherapy response in non-small-cell lung cancer based on computerized-tomography images. *Front Oncol* (2021) 11:646190. doi: 10.3389/fonc.2021.646190

43. Liu Z, Wang S, Dong D, Wei J, Fang C, Zhou X, et al. The applications of radiomics in precision diagnosis and treatment of oncology: opportunities and challenges. *Theranostics* (2019) 9(5):1303–22. doi: 10.7150/thno.30309

44. Ardila D, Kiraly AP, Bharadwaj S, Choi B, Reicher JJ, Peng L, et al. End-to-end lung cancer screening with three-dimensional deep learning on low-dose chest computed tomography. *Nat Med* (2019) 25:954–61. doi: 10.1038/s41591-019-0447-x

45. Dong D, Fang MJ, Tang L, Shan XH, Gao JB, Giganti F, et al. Deep learning radiomic nomogram can predict the number of lymph node metastasis in locally advanced gastric cancer: an international multicenter study. *Ann Oncol* (2020) 31(7):912–20. doi: 10.1016/j.annonc.2020.04.003

46. Zhang B, Qi S, Pan X, Li C, Yao Y, Qian W, et al. Deep cnn model using ct radiomics feature mapping recognizes egfr gene mutation status of lung adenocarcinoma. *Front Oncol* (2021) 10:598721. doi: 10.3389/fonc.2020.598721

frontiers | Frontiers in Oncology

TYPE Original Research
PUBLISHED 16 August 2022
DOI 10.3389/fonc.2022.985284

OPEN ACCESS

EDITED BY
Jiansong Ji,
Lishui Central Hospital, China

REVIEWED BY
Fu Xiong,
Huazhong University of Science and Technology, China
Chunli Kong,
Lishui Central Hospital, China

*CORRESPONDENCE
Lin Wu
wulin-calf@yeah.net

†These authors have contributed equally to this work and share first authorship

SPECIALTY SECTION
This article was submitted to Cancer Imaging and Image-directed Interventions, a section of the journal Frontiers in Oncology

RECEIVED 03 July 2022
ACCEPTED 25 July 2022
PUBLISHED 16 August 2022

CITATION
Jiang M, Yang P, Li J, Peng W, Pu X, Chen B, Li J, Wang J and Wu L (2022) Computed tomography-based radiomics quantification predicts epidermal growth factor receptor mutation status and efficacy of first-line targeted therapy in lung adenocarcinoma.
Front. Oncol. 12:985284.
doi: 10.3389/fonc.2022.985284

Computed tomography-based radiomics quantification predicts epidermal growth factor receptor mutation status and efficacy of first-line targeted therapy in lung adenocarcinoma

Meilin Jiang[1†], Pei Yang[2,3†], Jing Li[4†], Wenying Peng[5], Xingxiang Pu[1], Bolin Chen[1], Jia Li[1], Jingyi Wang[1] and Lin Wu[1*]

[1]The Second Department of Thoracic Oncology, Hunan Cancer Hospital, The Affiliated Cancer Hospital of Xiangya School of Medicine, Central South University, Changsha, China, [2]The General Surgery Department of Xiangya Hospital Affiliated to Central South University, Changsha, China, [3]The National Clinical Research Center for Geriatric Disorders of Xiangya Hospital Affiliated to Central South University, Changsha, China, [4]Medical Oncology, Hunan Cancer Hospital, The Affiliated Cancer Hospital of Xiangya School of Medicine, Central South University, Changsha, China, [5]The Second Department of Oncology, Yunnan Cancer Hospital, The Third Affiliated Hospital of Kunming Medical University, Yunnan Cancer Center, Kunming, China

Background: Biomarkers that predict the efficacy of first-line tyrosine kinase inhibitors (TKIs) are pivotal in epidermal growth factor receptor (EGFR) mutant advanced lung adenocarcinoma. Imaging-based biomarkers have attracted much attention in anticancer therapy. This study aims to use the machine learning method to distinguish EGFR mutation status and further explores the predictive role of EGFR mutation-related radiomics features in response to first-line TKIs.

Methods: We retrospectively analyzed pretreatment CT images and clinical information from a cohort of lung adenocarcinomas. We entered the top-ranked features into a support vector machine (SVM) classifier to establish a radiomics signature that predicted EGFR mutation status. Furthermore, we identified the best response-related features based on EGFR mutant-related features in first-line TKI therapy patients. Then we test and validate the predictive effect of the best response-related features for progression-free survival (PFS).

Results: Six hundred ninety-two patients were enrolled in building radiomics signatures. The 13 top-ranked features were input into an SVM classifier to establish the radiomics signature of the training cohort (n = 514), and the predictive score of the radiomics signature was assessed on an independent validation group with 178 patients and obtained an area under the curve (AUC) of 74.13%, an F1 score of 68.29%, a specificity of 79.55%, an accuracy of 70.79%,

and a sensitivity of 62.22%. More importantly, the skewness-Low (≤0.882) or 10th percentile-Low group (≤21.132) had a superior partial response (PR) rate than the skewness-High or 10th percentile-High group ($p < 0.01$). Higher skewness (hazard ratio (HR) = 1.722, $p = 0.001$) was also found to be significantly associated with worse PFS.

Conclusions: The radiomics signature can be used to predict EGFR mutation status. Skewness may contribute to the stratification of disease progression in lung cancer patients treated with first-line TKIs.

KEYWORDS

lung adenocarcinoma, computed tomography, radiomic response biomarker, epidermal growth factor receptor mutation status, machine learning

Introduction

Lung cancer is the most prevalent cancer worldwide, causing the highest cancer-related death rate of all malignancies (1). Adenocarcinoma comprises 80% of non-small cell lung cancer (NSCLC), and epidermal growth factor receptor (EGFR) mutations mostly appear in this subtype (2, 3). With the discovery and development of tyrosine kinase inhibitors (TKIs), the clinical treatment strategy for advanced activating EGFR mutation lung adenocarcinoma has evolved into a personalized approach (4, 5). Based on the National Comprehensive Cancer Network (NCCN) and Chinese Society of Clinical Oncology (CSCO) guidelines, EGFR TKIs have been approved as first-line standard therapy for driver mutation-positive metastatic adenocarcinoma based on studies that have shown better survival than chemotherapy (3, 6–9).

Nowadays, the individual diagnosis and treatment of EGFR-mutant lung adenocarcinoma depend on invasive biopsy testing. However, low DNA quality and testing methods can limit the reliability of results and sequencing applications (10–14). Furthermore, the EGFR mutation result was only determined by a part of tumor tissue, ignoring the heterogeneity of the entire tumor, which might be the reason for the inconsistent treatment outcome. When patients preliminarily elect for EGFR-TKI therapy only based on EGFR mutation, their response will not last long and varies so markedly after treatment (4, 9, 15). In sum, it is crucial and urgent to use the whole picture of the tumor to predict the potential resistance or the likelihood of rapid progression comprehensively before patients receive EGFR TKIs.

Radiomics is a non-invasive and high-throughput image assessment approach based on medical imaging (16, 17). A correlation between radiomics features and underlying intertumoral heterogeneity of lung cancer has been observed (18–26). Furthermore, molecular images have been used to identify patients with different therapeutic outcomes of EGFR-TKI therapy (27–30). Tian et al. built a signature to discriminate lung cancer patients with rapid and slow progression to EGFR-TKI therapy using the least absolute shrinkage and selection operator (LASSO) Cox regression model based on two-direction imaging data. Cook et al. found the association between features and survival by Cox regression analyses. However, compared to the predictive model that was made of an 'unknown process', oncologists tend to identify some specific image features and link them to the medical explanation.

Hence, our study aimed to locate some specific image features that were highly related to the survival outcome and could be linked to clinical practice. We proposed a radiomics signature based on all three computed tomography (CT) image dimensions for predicting EGFR mutation status. We further explored in-depth the relevance between EGFR mutation-related features and risk stratification of progression-free survival (PFS) in EGFR mutant advanced adenocarcinoma.

Materials and methods

Patients

The institutional research board of Hunan Cancer Hospital (Changsha, China) approved this retrospective study. A total of 1,219 lung adenocarcinoma patients at Hunan Cancer Hospital were initially collected between July 2013 and September 2019. Patients were included in this research based on the following inclusion criteria: 1) pathologically confirmed primary pulmonary adenocarcinoma in our institute, 2) there are measurable target lesions under the Response Evaluation Criteria in Solid Tumors version 1.1 (RECIST v 1.1), 3) next-

generation sequencing-proven EGFR mutational status by tumor tissue sample, and 4) available patient characteristic clinical data. Finally, 692 patients were included in our study. Furthermore, clinical data were collected, including therapy protocol, response evaluation, and follow-up material. In the process of building the predictive radiomics signature, patients confirmed between 1 July 2013 and 1 May 2018 were enrolled in a training cohort, and those confirmed between 1 June 2018 and 1 September 2019 were enrolled in a test cohort (Figure 1).

Response assessment routinely took place 4–6 weeks after treatment completion by diagnostic CT scans and laboratory tests according to the RECIST v 1.1. PFS is the study endpoint

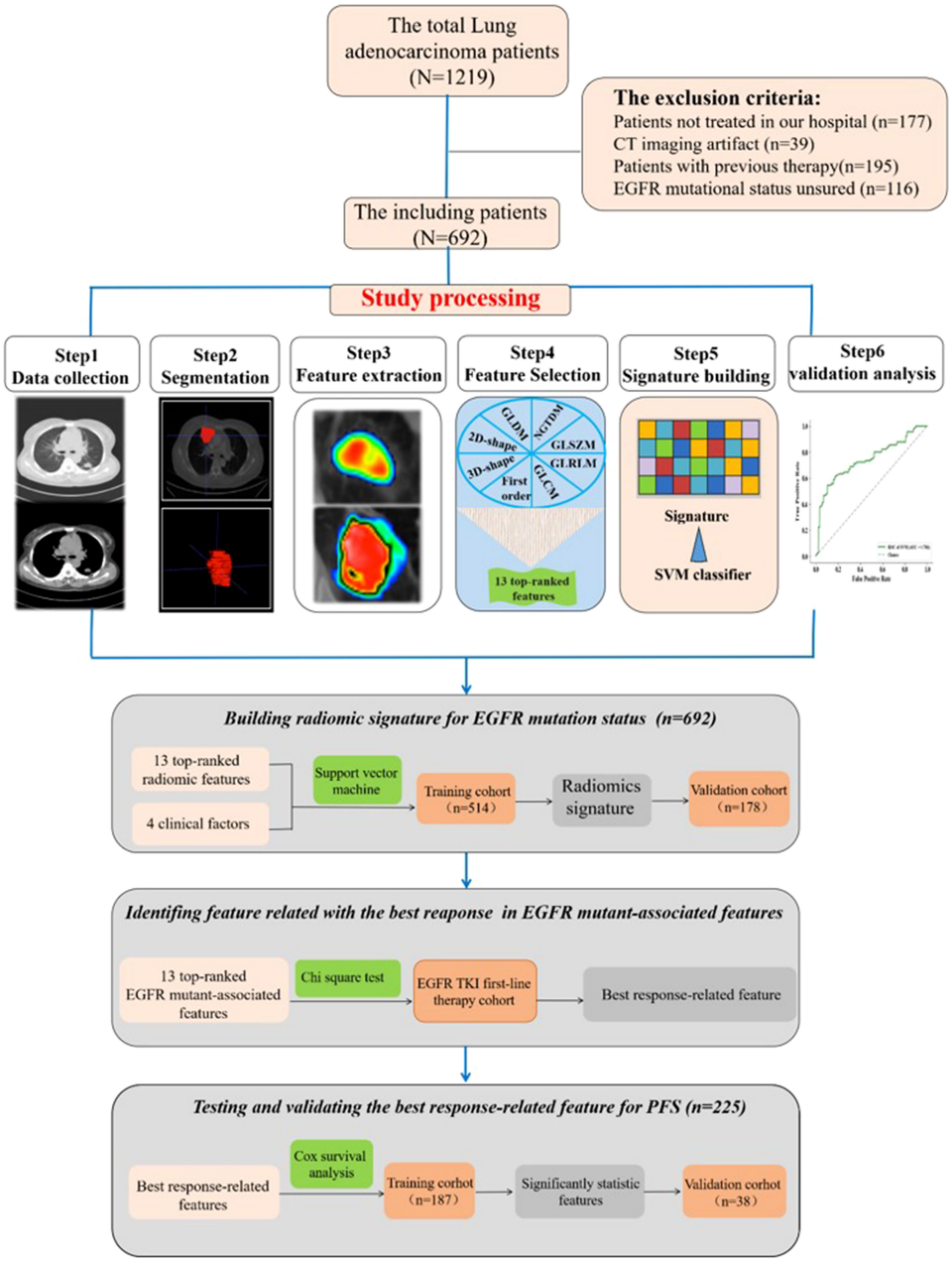

FIGURE 1
Images show study processing of radiomics. Computed tomography (CT) data were retrospectively collected. Region of interest was manually segmented in axial view by a clinical doctor using imaging biomarker explorer software. Eight categories of radiomics features were extracted from region of interest (ROI) in CT images and next, the top 13 features to train support vector machine classifier and validate it on independent set (n = 178). Experiment 1 is for developing radiomics signature for epidermal growth factor receptor (EGFR) mutational status in lung adenocarcinoma. Experiment 2 is for analyzing the relationship between progression-free survival and the top 13 features.

considered the time from the initiation of therapy to confirmation of progression or death.

CT scanning protocol

All thoracic CT examinations were performed at Hunan Cancer Hospital. CT images of all patients were acquired on CT-on-rails (Brilliance CT 16, Hunan Tumor Hospital, Changsha) with the following parameters: a 5.0-mm slice thickness reconstruction, 313-mA tube current, and 120-kV peak voltage.

Tumor imaging segmentation and feature extraction

In this study, all nodules were identified by a radiologist with more than 10 years of experience, and the clinician manually annotated the regions of interest (ROIs) on axial view piece by piece using imaging biomarker explorer (IBEX) software (31, 32). In the end, each ROI of the subject was reviewed by a radiologist. Imaging features were extracted by the PyRadiomics toolbox (33), which is an open-source python software package. To mine rich radiomics, each original image was processed by eight image filters. 1) Wavelet filter: yields eight decompositions per level (all possible combinations of applying either a high- or low-pass filter in each of the three dimensions). 2) Laplacian of Gaussian filter: edge enhancement filter, emphasizes areas of gray-level change, where sigma defines how coarse the emphasized texture should be. A low sigma emphasis on fine textures (change over a short distance), where a high sigma value emphasizes coarse textures (gray-level change over a large distance). 3) Square: takes the square of the image intensities and linearly scales them back to the original range. 4) SquareRoot: takes the square root of the absolute image intensities and scales them back to the original range. 5) Logarithm: takes the logarithm of the absolute intensity + 1. 6) Exponential: takes the exponential, where filtered intensity is e^(absolute intensity). 7) Gradient: returns the magnitude of the local gradient. 8) Local Binary Pattern: computes the Local Binary Pattern in a by-slice operation (two-dimensional (2D)) and three-dimensional (3D) using spherical harmonics (34). Then, the features were quantified by the following eight categories of imaging features: 1) first-order statistics with 19 features, 2) 3D shape-based with 16 features, 3) 2D shape-based with 10 features, 4) gray-level co-occurrence matrix (GLCM) with 24 features, 5) gray-level run length matrix (GLRLM) with 16 features, 6) gray-level size zone matrix (GLSZM) with 16 features, 7) neighboring gray-tone difference matrix (NGTDM) with five features, and 8) gray-level dependence matrix (GLDM) with 14 features. In the end, 2,153 quantitative radiological features from each ROI were obtained.

Feature selection and signature building

The Mann–Whitney statistical test (13) was first conducted to distinguish the redundant features. Each feature with a p-value >0.05 was redundant and eliminated. After redundant features were removed, the residual parameters were normalized by the z-score method, which is widely used in machine learning. Then, the feature where the variance is equal to zero was removed again. To further decrease the dimension, the minimum redundancy maximum relevance (mRMR) method was used to determine the most remarkable radiomics features.

Finally, the top-ranked radiomics features were entered into a support vector machine (SVM) classifier to establish a radiomics signature that predicts EGFR mutation status. The parameters of the classifier were optimized by a grid searching technology on the training cohort using 10-fold cross-validation. The radiomics signature with the best accuracy was confirmed. Previous studies have shown that clinical features are associated with the outcome of lymph node metastasis (35). In this study, we found a radiomics signature based on the top-ranked features and then added critical clinical features to explore the predictive score of EGFR mutation status.

Evaluation of radiomics signature

The performance of the radiomics signature in predicting EGFR mutation status was estimated by the area under the curve (AUC) of the receiver operating characteristic (ROC) curve. In addition, accuracy, sensitivity, specificity, and an F1 score were also used to measure the signature.

Statistical analysis

Statistical analysis was performed with SPSS version 22. The independent-samples t-test was used to evaluate the difference in median age between the EGFR-positive and EGFR-negative groups. The chi-square test was used for statistical analysis of gender, tumor stage, smoking history, family history, and tumor position. In the EGFR mutational advanced patients, the cutoff points of statistically significant features were defined by the AUC value of the ROC curve. Survival analysis included patients with disease progression treated with first-line EGFR TKIs. Based on the cutoff points, the chi-square test was used to identify the relationship between radiomics features and the best response. Cox regression analysis was used to explore the predictive

capability of the best response-related features for PFS. Parameters with a *p*-value <0.1 in univariate analysis were selected in multivariate Cox proportional hazards regression analysis. The results were presented as hazard ratio (HR) and 95% CI. The reported statistical remarkable levels were all two-sided, and *p*-values <0.05 were significant.

Results

Patient characteristics

The clinicopathologic features of patients are shown in Table 1. In all patients, 355 patients with confirmed EGFR-positive type were enrolled, while 337 patients were EGFR wild type. Most patients were diagnosed with inoperable stage III or IV disease (677/692, 97.8%), and 50.4% of 692 patients were former or active smokers (Table 1). Patient characteristics including age, gender, and smoking history were demonstrated to be different between EGFR-positive and EGFR-negative type cohorts, which is consistent with a previous clinical study (Table 1).

Two hundred twenty-five patients with EGFR mutation who experienced disease progression following first-line TKI therapy were included in the efficacy analysis presented in Table 2. The median follow-up time was 1 year (range, 0.7–37.7 months). In the training and validation cohorts (187 and 38 cases, respectively), the results showed no significant difference in PFS (median PFS: training cohort, 12 months; validation cohort, 11.8 months; Mann–Whitney, $p = 0.304$). Moreover, there were also no significant differences ($p > 0.05$) regarding age, gender, smoking history, family history, tumor stage, and position between the two cohorts (Table 2).

TABLE 1 Clinical characteristics of all patients included in the study.

Factors	Training cohort		*p*-Value	Validation cohort		*p*-Value
	EGFR-wild	EGFR-mutant		EGFR-wild	EGFR-mutant	
Subject (*N*)	514			178		
Age (years)	57 ± 9	55 ± 4	<0.001[b]	57 ± 11	59 ± 9	<0.001[b]
Gender			<0.001[b]			<0.001[b]
Male	171	136		76	40	
Female	78	129	12	50		
Smoking history			<0.001[b]			<0.001[b]
Yes	158	95		67	29	
No	91	170	21	61		
Family history			0.417			0.565
Yes	31	26		11	15	
No	218	239	77	75		
TNM stage[a]			0.717			0.076
I	2	2		0	1	
II	5	3	2	0		
III	42	38	11	4		
IV	200	222	75	85		
Tumor position			0.853			0.116
RUL	81	87		18	27	
RML	20	27	12	16		
RLL	45	52	14	16		
LUL	66	63	17	18		
LLL	37	36	27	13		
EGFR mutation type	0	265		0	90	
Wild type	249	0		88	0	
Exon 19 deletion	0	167	0	58		
Exon 21 insertion	0	89	0	31		
Other types	0	9	0	1		

EGFR, epidermal growth factor receptor; RUL, right upper lung; RML, right middle lung; RLL, right lower lung; LUL, left upper lung; LLL, left lower lung.
[a]Based on American Joint Committee on Cancer (AJCC) 8th edition.
[b]Only statistically significant ($p < 0.05$) results are reported for analysis.

TABLE 2 Clinical characteristics of patients included in treatment response analysis.

Factors	Training cohort N (%)	Validation cohort N (%)	*p*-Value
Subject(*N*)	187 (100)	38 (100)	
Age(years)			0.114
Median	55	57	
Range	29–80	37–75	
Gender			0.707
Male	80 (42.8)	15 (39.5)	
Female	107 (57.2)	23 (60.5)	
Smoking history			0.894
Yes	57 (30.5)	12 (31.6)	
No	130 (69.5)	26 (68.4)	
Family history			0.469
Yes	19 (10.2)	6 (15.8)	
No	168 (89.8)	32 (84.2)	
TNM stage[a]			0.083
III	19 (10.2)	0 (0)	
IV	168 (89.8)	38 (100)	
Tumor position			0.466
RUL	57 (30.5)	9 (23.7)	
RML	17 (9.1)	9 (23.7)	
RLL	33 (17.7)	9 (23.7)	
LUL	53 (28.3)	7 (18.4)	
LLL	27 (14.4)	4 (10.5)	
EGFR-TKI therapy			0.718
Gefitinib	66	13	
Erlotinib	62	15	
Icotinib	59	10	
Median PFS (months)	12	11.8	0.304

PFS, progression-free survival; RUL, right upper lung; RML, right middle lung; RLL, right lower lung; LUL, left upper lung; LLL, left lower lung; EGFR, epidermal growth factor receptor; TKI, tyrosine kinase inhibitor.
[a]Based on American Joint Committee on Cancer (AJCC) 8th edition.

Building and validating the predictive radiomics signature for epidermal growth factor receptor mutation status

The feature with a *p*-value >0.05 was excluded using the Mann–Whitney statistical test. Thus, the number of radiomics features was reduced from 2,153 to 1,545. Then, 13 normalized features with variance equal to zero were removed. The residual 1,532 features were sorted using mRMR algorithm to pick the 13 top-ranked features (34), including six (skewness, minimum, kurtosis, variance, minimum, and 10th percentile) in the Firstorder features that describe the distribution of voxel intensities within the image region defined by the mask through commonly used and basic metrics, one (SumSquares) in the gray-level co-occurrence matrix features that describe the second-order joint probability function of an image region constrained by the mask and is defined, three (SizeZoneNonUniformity, HighGrayLevelZoneEmphasis, and ZoneVariance) in the gray-level size zone matrix features that quantify the number of connected voxels sharing the same gray-level intensity in an image, and three (LargeDependence HighGrayLevelEmphasis, LargeDependenceHighGrayLevel Emphasis, and DependenceEntropy) in the gray-level dependence matrix features that quantify the number of connected voxels within distance, which are dependent on the center voxel in an image. Then, the top-ranked features and four clinical features (age, gender, smoking, and tumor family history) were input into the SVM classifier to establish a radiomics signature that predicts EGFR mutation status in the training group (n = 514). The predictive score of the radiomics signature was assessed on an independent validation group with 178 patients and obtained an AUC of 74.13%, an F1 score of 68.29%, a specificity of 79.55%, an accuracy of 70.79%, and a sensitivity of 62.22% (Figure 2).

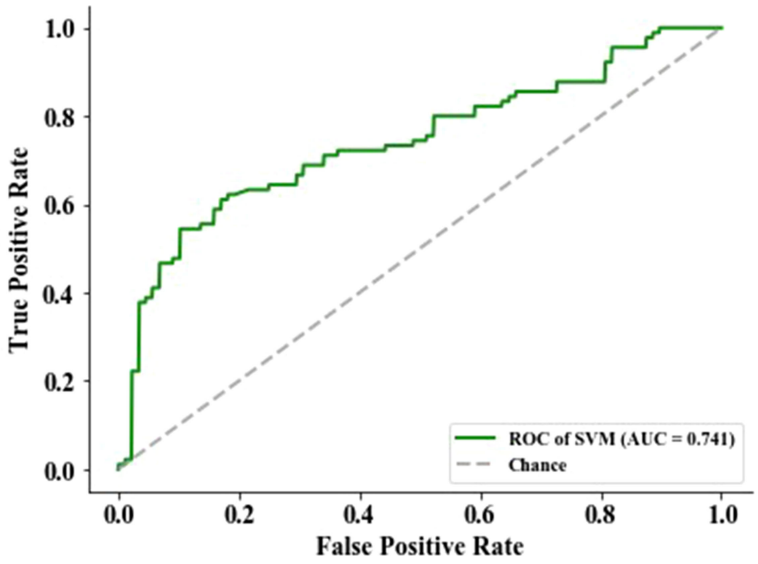

FIGURE 2
The performance of epidermal growth factor receptor (EGFR) status-related radiomics signature was evaluated by the area under the curve (AUC) of the receiver operating characteristic (ROC) curve.

Identification of the best response-related features based on 13 epidermal growth factor receptor mutant-associated features in epidermal growth factor receptor tyrosine kinase inhibitor therapy patients

To identify the imaging biomarkers candidates for the best response of EGFR TKI first-line treatment, the 13 top-rank radiomics features associated with EGFR mutation were further used to explore by logistic analysis. The two features that significantly negatively correlated with the best response were skewness (p = 0.004) and 10th percentile (p = 0.002) (Table S1). Skewness and 10th percentile were divided into two groups based on predicting the best response. ROC curve was applied to confirm the optimal cutoff points of significant features. For skewness and 10th percentile, the AUC values were 0.832 (p = 0.004, Youden's index = 0.614) and 0.653 (p = 0.002, Youden's index =0.289), respectively. The best cutoff points of skewness and 10th percentile, as confirmed by the AUC value, were 0.882 and 21.132, respectively.

Among the results from skewness, the skewness-L (≤0.882) group had a superior partial response (PR) rate than had the skewness-H (>0.882) group (89/117, 76.1% *vs* 27/108, 25.0%, HR = 9.536, 95% CI: 5.189–17.52, p < 0.0001) (Figure 3, Table S2). For the 10th percentile, the SD/PD rate was inferior in the 10th percentile-H group (>21.132) than in the 10th percentile-L group (≤21.132) (76/130, 58.5% *vs* 33/95, 34.7%, HR = 2.644, 95% CI: 1.529–4.574, p = 0.0005) (Figure 3, Table S2). In conclusion, we suggest that skewness and 10th percentile may be better predictive markers for differentiating response to first-line EGFR TKIs.

Testing the correlation between the best response-associated features and progression-free survival

To explore whether advanced lung cancer patients with a good curative outcome can be distinct, we tested the defined cutoff points of the skewness of first-orders (≤0.882 versus >0.882) and the 10th percentile of first-orders (≤21.132 versus >21.132) in the training cohort (n = 187). Univariate analysis revealed that the skewness > 0.882 (p = 0.001) and the 10th percentile > 21.132 (p = 0.015) before treatment were associated with a significantly worse PFS. We then carried out a multivariate Cox proportional regression analysis containing these covariates to ensure independent factors. The relationship between two features and PFS was obvious in multivariate analysis; for the skewness, HR = 1.722, 95% CI: 1.261–2.352, p = 0.001 (Figure 4A, Table 3); for the 10th percentile, HR = 1.466, 95% CI: 1.085–1.981, p = 0.013 (Figure 4B, Table 3). Therefore, the skewness and 10th percentile of first-order features at baseline level could be used to predict the efficacy in EGFR-mutant advanced lung adenocarcinoma following standard first-line EGFR-TKI therapy.

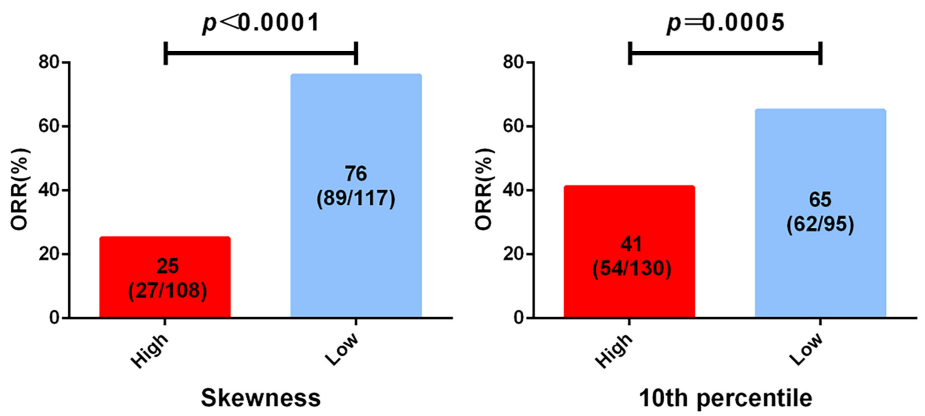

FIGURE 3
Analysis of epidermal growth factor receptor (EGFR) mutation-associated features from computed tomography (CT) imaging before treatment and the best clinical response to tyrosine kinase inhibitor (TKI) first-line therapy. All patients were divided into two groups according to the cutoff of skewness and 10th percentile.

Validation of the predictive effect of skewness and 10th percentile features for progression-free survival

Next, we intended to validate the clinical effect of the skewness and 10th percentile of first-order features in the validation cohort (n = 38). Here, we used the aforesaid cutoff value in the training group: high skewness value (>0.882) versus low (≤0.882) and high 10th percentile value (>21.132) versus low (≤21.132). The correlation between the skewness of first-order and PFS is consistent with the training cohort (Figure 4C, Table 3). Probably due to the limited number of samples, we did not observe a statistical difference between the 10th percentile of first-order before treatment and PFS in the validation cohort (Table 3). However, the skewness of first-order is an effective biomarker that could better indicate the response of first-line EGFR-TKI therapy.

Discussion

Therapeutic opportunities for EGFR mutant lung adenocarcinoma patients have radically changed because of the application of EGFR-TKI therapy. The response varies markedly, and more objective markers are needed to identify patients best suited for certain targeted therapies (4, 9, 15). EGFR mutation types are a well-studied biomarker of response to TKI therapy (6, 7, 36–41). Next-generation sequencing of tissue samples is the standard technique of EGFR status detection. Nevertheless, a biopsy is an invasive procedure of locating tissue that ignores organizational heterogeneity of tumor and microenvironment where distinct bioactive molecules can drive tumor development and progression.

Radiomics is a non-invasive technology that collects routine clinical medical images to assess the tumor phenotype (16, 17). Previous studies used clinical and radiomics models to predict EGFR mutation status (13, 14, 21–26). The radiomics features combined with the clinical factors had a greater prediction effect (13, 14, 22). For example, Aerts et al. found that homogeneity, inverse variance, sum entropy, short-run emphasis, maximum diameter, and tumor volume radiomics features had important roles in discriminating EGFR mutant status in lung adenocarcinoma (14). These features belong to GLCM, GLRLM, and shape features that reveal that EGFR mutation is more likely to be heterogeneous. Similarly, Ye et al., in a single group association study of lung adenocarcinomas, showed that CT imaging characteristics including bubble-like lucency and homogeneous enhancement were remarkably independent predictive factors for EGFR-activating mutation (22). The deep learning model also revealed that the deep learning features such as circle or arch shapes and horizontal and diagonal edges had a significant correlation between high-dimensional CT image characteristics and EGFR genotype (26). Based on previous research progress, we carried out new research for further exploration in this study, and we confirmed a radiomics signature by the SVM classifier combined with four clinical factors to forecast EGFR status in advanced lung adenocarcinoma using preoperative three-dimensional CT images. The radiomics signature showed strong predictive performance in the test group (AUC, 0.7413; specificity, 79.55%; accuracy, 70.79%). We found 13 radiological features that were remarkably associated with EGFR mutations; the first-order category had six features such as skewness, minimum, kurtosis, variance, and 10th percentile, which describes the distribution of voxel intensities within the image region defined by the mask through commonly used and basic

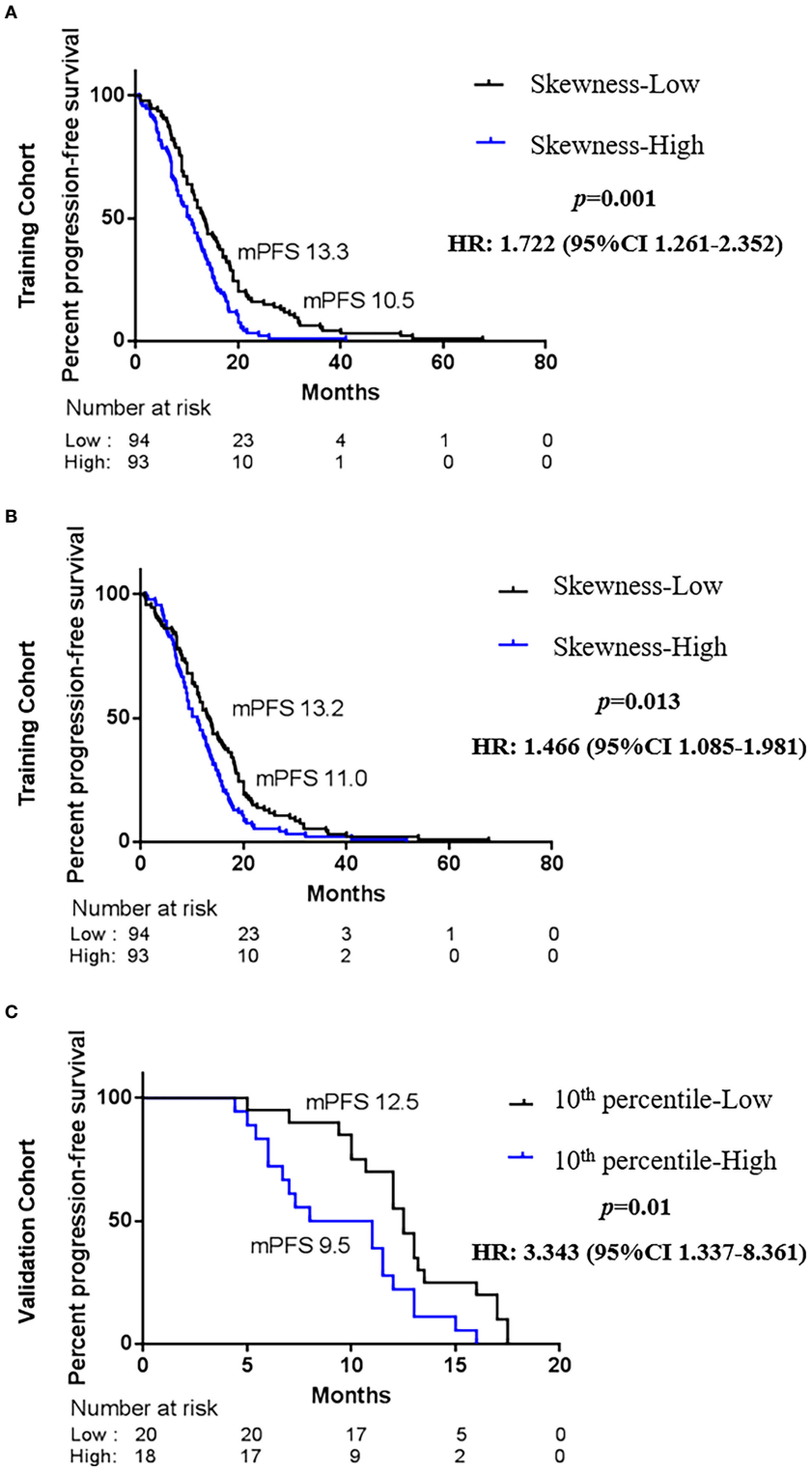

FIGURE 4
Kaplan–Maier survival curves of progression-free survival under biomarker-defined subgroups. In the tyrosine kinase inhibitor (TKI) therapy training cohort, **(A)** stratification by the skewness of first-order category (low ≤ 0.882 versus high > 0.882); **(B)** stratification by the 10th percentile of first-order category (low ≤ 21.132 versus high > 21.132). In the TKI therapy validation cohort, **(C)** stratification by the skewness of first-order category (low ≤ 0.882 versus high > 0.882). *p*-Values are calculated with multivariate Cox models adjusted by age, gender, smoking history, family history, TNM stage, and tumor position.

TABLE 3 Multivariate analysis of the categorization of two features and PFS.

Factors	Categorization	Training cohort (*N*=187)		Validation cohort (*N*=38)	
		HR (95% CI)	*p*-Value	HR (95% CI)	*p*-Value
Age	Continuous	0.992 (0.976–1.009)	0.368	1.015 (0.976–1.055)	0.461
Gender	Female *vs* male	1.181 (0.751–1.856)	0.471	0.719 (0.154–3.360)	0.675
Smoking history	No *vs* yes	0.994 (0.609–1.621)	0.98	0.822 (0.180–3.744)	0.8
Family history	No *vs* yes	1.246 (0.764–2.031)	0.378	1.019 (0.357–2.907)	0.972
TNM stage[a]	III *vs* IV	0.854 (0.517–1.413)	0.54	0	0
Tumor position	RUL *vs* RML *vs* RLL *vs* LUL *vs* LLL	0.980 (0.887–1.083)	0.695	0.879 (0.671–1.153)	0.352
Skewness	≤Cutoff1[c] *vs* >cutoff1[c]	1.722 (1.261–2.352)	0.001[b]	3.343 (1.337–8.361)	0.01[b]
Age	Male *vs* female	0.995 (0.979–1.012)	0.579	0.998 (0.961–1.036)	0.905
Gender	Continuous	1.154 (0.740–1.800)	0.528	1.694 (0.425–6.748)	0.455
Smoking history	0 or 1 *vs* 2	0.870 (0.534–1.416)	0.575	0.437 (0.109–1.751)	0.243
Family history	No *vs* yes	1.128 (0.694–1.833)	0.628	0.638 (0.237–1.718)	0.374
TNM stage[a]	First *vs* second	0.682 (0.418–1.111)	0.124	0	0
Tumor position	RUL *vs* RML *vs* RLL *vs* LUL *vs* LLL	0.996 (0.902–1.101)	0.943	1.013 (0.798–1.285)	0.919
10th percentile	≤Cutoff2[c] *vs* >cut0ff2[c]	1.466 (1.085–1.981)	0.013[b]	1.122 (0.492–2.561)	0.784

PFS, progression-free survival; EGFR, epidermal growth factor receptor; TKI, tyrosine kinase inhibitor; RUL, right upper lung; RML, right middle lung; RLL, right lower lung; LUL, left upper lung; LLL, left lower lung; HR, hazard ratio; CI, confidence interval.
[a]Based on American Joint Committee on Cancer (AJCC) 8th edition.
[b]Only statistically significant ($p < 0.05$) results are reported for analysis.
[c]Cutoff1 = 0.882; Cutoff2 = 21.132.

metrics (34). The GLSZM and GLDM categories had three features each. The GLSZM is defined as the gray-level zone quantization of connected voxel numbers that share the same gray-level intensity in an image, while GLDM quantifies gray-level dependencies defined as the number of connected voxels within a distance that are dependent on the center voxel in an image. Together, the representation of these features indicates tumor heterogeneous related to EGFR mutation phenotype, which provides an alternative non-invasive way easily to forecast EGFR status in routine CT diagnosis and supply a good supplement to biopsy in real clinical practice.

Radiomics markers that can predict the efficacy of first-line EGFR-TKI therapy are now more needed; we also have found two CT features for progression risk stratification to first-line EGFR-TKI remedy in advanced lung adenocarcinoma. The skewness and 10th percentile of first-order features included in ROI preprocessed by gradient and exponential filter, respectively, were significantly negatively correlated with the best response and PFS of EGFR TKI therapy. Few studies used radiomics to explore the response of targeted therapy. For example, Jie Tian et al. extracted features from two-directional CT images and used the LASSO Cox regression analysis to select 12 CT features for discriminating between patients with rapid and slow progression to EGFR TKI therapy. The 12 CT features are part of GLCM, GLRLM, and first-order features (30). However, our study retrospectively obtained more comprehensive data of the tumors in 3D from CT images and was the first to further explore the relationship between EGFR mutation-related features and the response of EGFR TKI therapy in advanced lung adenocarcinoma. To date, several studies have found the first-order features with response and prognosis of EGFR TKI therapy, including energy, standard deviation, uniformity, and entropy (26, 30), but we are the first to find the predictive value of other first-order features for the best response and PFS. The skewness feature assesses the asymmetry of the distribution of values about the mean value, while the 10th percentile represents the first 10% proportion of voxels with positive order of susceptibility. The two features indicated the whole tumor heterogeneity and the asymmetry distribution of tumor parenchyma, which corresponds to the inhomogeneity of gross findings in CT images checked by the radiologist. It could explain why radiomics characteristics reveal treatment outcomes, while further work is needed to explore the potential mechanisms of the above features and predict the efficacy of lung cancer.

There are several limitations that could not be ignored. First, this was a retrospective study and CT images were acquired with 5-mm slice thicknesses, which is indeed used in hospitals. Although we may ignore some tumor information, our results are certainly closer to practice. Second, given that this was a single-center study, the study lacks an external validation group of patients, which is a key component of radiological analyses, and required validation in a larger patient population study. Third, our investigation only concentrated on EGFR mutation status. The interrelationship among radiomics features, EGFR, and other driver mutations (i.e., ROS-1, ALK, and c-Met) is unknown but could be studied in future research. Nonetheless, the study still had significant positive results. Further assessment

of two indicators could be contained together with other predictive biomarkers in the evaluation of lung and other solid tumor patients who are candidates for treatment efficacy.

Data availability statement

The raw data supporting the conclusions of this article will be made available by the authors, without undue reservation.

Ethics statement

Ethical review and approval was not required for the study of human participants in accordance with the local legislation and institutional requirements. Written informed consent from the patients/participants was not required to participate in this study in accordance with the national legislation and the institutional requirements.

Author contributions

Conception and design: LW, MJ, PY, and JiL. Acquisition of data (acquired and managed patients): MJ, PY, JiL, WP, XP, BC, JaL, and JW. Analysis and interpretation of data: MJ and PY. Writing, review, and/or revision of the manuscript: MJ, PY, and JiL. LW designed and supervised the study. All authors contributed to the article and approved the submitted version.

Funding

This work was supported by the Hunan Provincial Natural Science Foundation of China (No. 2021JJ30430), Wu Jieping Medical Foundation (No. 320.6750.19088-11) and the Research Foundation of Chinese Sociaty of Clinical Oncology (No. Y-2019Genecast-024 and No. Y-HR2019-0464) to LW. This work was supported by the National Cancer Center (NCC2017A17) to PY.

Acknowledgments

We thank all patients, family, nurses, and doctors for their contribution to this study.

Conflict of interest

The authors declare that the research was conducted in the absence of any commercial or financial relationships that could be construed as a potential conflict of interest.

Publisher's note

Supplementary material

The Supplementary Material for this article can be found online at: https://www.frontiersin.org/articles/10.3389/fonc.2022.985284/full#supplementary-material

References

1. Siegel RL, Miller KD, Jemal A. Cancer statistics. *CA Cancer J Clin* (2018) 68:7–30. doi: 10.3322/caac.21442

2. Alamgeer M, Ganju V, Watkins DN. Novel therapeutic targets in non-small cell lung cancer. *Curr Opin Pharmacol* (2013) 13:394–401. doi: 10.1016/j.coph.2013.03.010

3. Savas P, Hughes B, Solomon B. Targeted therapy in lung cancer: IPASS and beyond, keeping abreast of the explosion of targeted therapies for lung cancer. *J Thorac Dis* (2013) 5 Suppl 5:S579–92. doi: 10.3978/j.issn.2072-1439.2013.08.52

4. Chan BA, Hughes BG. Targeted therapy for non-small cell lung cancer: current standards and the promise of the future. *Transl Lung Cancer Res* (2015) 4 (1):36–54. doi: 10.3978/j.issn.2218-6751.2014.05.01

5. Gadgeel SM. Personalized therapy of non-small cell lung cancer (NSCLC). *Adv Exp Med Biol* (2016) 890:203–22. doi: 10.1007/978-3-319-24932-2_11

6. Mok TS, Wu YL, Thongprasert S, Yang CH, Chu DT, Saijo N, et al. Gefitinib or carboplatin-paclitaxel in pulmonary adenocarcinoma. *N Engl J Med* (2009) 361 (10):947–57. doi: 10.1056/NEJMoa0810699

7. Gao G, Ren S, Li A, Xu J, Xu Q, Su C, et al. Epidermal growth factor receptor-tyrosine kinase inhibitor therapy is effective as first-line treatment of advanced non-small-cell lung cancer with mutated EGFR: A meta-analysis from six phase III randomized controlled trials. *Int J Cancer* (2012) 131(5):E822–9. doi: 10.1002/ijc.27396

8. Li T, Kung HJ, Mack PC, Gandara DR. Genotyping and genomic profiling of non-small-cell lung cancer: implications for current and future therapies. *J Clin Oncol* (2013) 31(8):039–1049. doi: 10.1200/JCO.2012.45.3753

9. Chong CR, Janne PA. The quest to overcome resistance to EGFR-targeted therapies in cancer. *Nat Med* (2013) 19(11):1389–400. doi: 10.1038/nm.3388

10. Bedard PL, Hansen AR, Ratain MJ, Siu LL. Tumour heterogeneity in the clinic. *Nature* (2013) 501(7467):355–64. doi: 10.1038/nature12627

11. Swanton C. Intratumor heterogeneity: evolution through space and time. *Cancer Res* (2012) 72(19):4875–82. doi: 10.1158/0008-5472.CAN-12-2217

12. Taniguchi K, Okami J, Kodama K, Higashiyama M, Kato K. Intratumor heterogeneity of epidermal growth factor receptor mutations in lung cancer and its correlation to the response to gefitinib. *Cancer Sci* (2008) 99(5):929–35. doi: 10.1111/j.1349-7006.2008.00782.x

13. Girard N, Sima CS, Jackman DM, Sequist LV, Chen H, Yang JC, et al. Nomogram to predict the presence of EGFR activating mutation in lung adenocarcinoma. *Eur Respir J* (2012) 39(2):366–72. doi: 10.1183/09031936.00010111

14. Rios Velazquez E, Parmar C, Liu Y, Coroller TP, Cruz G, Stringfield O, et al. Somatic mutations drive distinct imaging phenotypes in lung cancer. *Cancer Res* (2017) 77(14):3922–30. doi: 10.1158/0008-5472.CAN-17-0122

15. Yu HA, Arcila ME, Rekhtman N, Sima CS, Zakowski MF, Pao W, et al. Analysis of tumor specimens at the time of acquired resistance to EGFR-TKI therapy in 155 patients with EGFR-mutant lung cancers. *Clin Cancer Res* (2013) 19(8):2240–7. doi: 10.1158/1078-0432.CCR-12-2246

16. Gillies RJ, Kinahan PE, Hricak H. Radiomics: Images are more than pictures, they are data. *Radiology* (2016) 278(2):563–77. doi: 10.1148/radiol.2015151169

17. Lambin P, Leijenaar RTH, Deist TM, Peerlings J, de Jong EEC, van Timmeren J, et al. Radiomics: the bridge between medical imaging and personalized medicine. *Nat Rev Clin Oncol* (2017) 14:749–62. doi: 10.1038/nrclinonc.2017.141

18. Gevaert O, Xu J, Hoang CD, Leung AN, Xu Y, Quon A, et al. Non-small cell lung cancer: identifying prognostic imaging biomarkers by leveraging public gene expression microarray data-methods and preliminary results. *Radiology* (2012) 264:387–96. doi: 10.1148/radiol.12111607

19. Aerts HJ WL, Velazquez ER, Leijenaar RTH, Parmar C, Grossmann P. Decoding tumour phenotype by non-invasive imaging using a quantitative radiomics approach. *Nat Commun* (2014) 5:4006. doi: 10.1038/ncomms5006

20. Zhou M, Leung A, Echegaray S, Gentles A, Shrager JB, Jensen KC, et al. Non-small cell lung cancer radiogenomics map identifies relationships between molecular and imaging phenotypes with prognostic implications. *Radiology* (2018) 286:307–15. doi: 10.1148/radiol.2017161845

21. Sugano M, Shimizu K, Nakano T, Kakegawa S, Miyamae Y, Kaira K, et al. Correlation between computed tomography findings and epidermal growth factor receptor and KRAS gene mutations in patients with pulmonary adenocarcinoma. *Oncol Rep* (2011) 26(5):1205–11. doi: 10.3892/or.2011.1412

22. Liu Y, Kim J, Qu F, Liu S, Wang H, Balagurunathan Y, et al. CT features associated with epidermal growth factor receptor mutation status in patients with lung adenocarcinoma. *Radiology* (2016) 280(1):271–80. doi: 10.1148/radiol.2016151455

23. Lee HJ, Kim YT, Kang CH, Zhao B, Tan Y, Schwartz LH, et al. Epidermal growth factor receptor mutation in lung adenocarcinomas: relationship with CT characteristics and histologic subtypes. *Radiology* (2013) 268(1):254–64. doi: 10.1148/radiol.13112553

24. Zhou JY, Zheng J, Yu ZF, Xiao WB, Zhao J, Sun K. Comparative analysis of clinicoradiologic characteristics of lung adenocarcinomas with ALK rearrangements or EGFR mutations. *Eur Radiol* (2015) 25(5):1257–66. doi: 10.1007/s00330-014-3516-z

25. Rizzo S, Petrella F, Buscarino V, De Maria F, Raimondi S, Barberis M, et al. CT radiogenomic characterization of EGFR, K-RAS, and ALK mutations in non-small cell lung cancer. *Eur Radiol* (2016) 26(1):32–42. doi: 10.1007/s00330-015-3814-0

26. Wang S, Shi J, Ye Z, Dong D, Yu D, Zhou M, et al. Predicting EGFR mutation status in lung adenocarcinoma on computed tomography image using deep learning. *Eur Respir J* (2019) 53(3):1800986 doi: 10.1183/13993003.00986-2018

27. Dingemans AC, de Langen AJ, van den Boogaart V, Marcus JT, Backes WH, Scholtens HTGM, et al. First-line erlotinib and bevacizumab in patients with locally advanced and/or metastatic non-small-cell lung cancer: A phase II study including molecular imaging. *Ann Oncol* (2011) 22:559–66. doi: 10.1093/annonc/mdq391

28. Nishino M, Dahlberg SE, Cardarella S, Jackman DM, Rabin MS, Hatabu H. Tumor volume decrease at 8 weeks is associated with longer survival in EGFR-mutant advanced non-small-cell lung cancer patients treated with EGFR TKI. *J Thorac Oncol* (2013) 8:1059–68. doi: 10.1097/JTO.0b013e318294c909

29. Dai D, Li XF, Wang J, Liu JJ, Zhu YJ, Zhang Y. Predictive efficacy of 11 c-PD153035 PET imaging for EGFR-tyrosine kinase inhibitor sensitivity in non-small cell lung cancer patients. *Int J Cancer* (2016) 138:1003–12. doi: 10.1002/ijc.29832

30. Song J, Shi J, Dong D, Fang M, Zhong W, Wang K, et al. A new approach to predict progression-free survival in stage IV EGFR-mutant NSCLC patients with EGFR-TKI therapy. *Clin Cancer Res* (2018) 24(15):3583–92. doi: 10.1158/1078-0432.CCR-17-2507

31. Perez NP, Guevara Lopez MA, Silva A, Ramos I. Improving the Mann-Whitney statistical test for feature selection: an approach in breast cancer diagnosis on mammography. *Artif Intell Med* (2015) 63(1):19–31. doi: 10.1016/j.artmed.2014.12.004

32. Zhang L, Fried DV, Fave XJ, Hunter LA, Yang J, Court LE. IBEX: an open infrastructure software platform to facilitate collaborative work in radiomics. *Med Phys* (2015) 42(3):1341–53. doi: 10.1118/1.4908210

33. van Griethuysen JJM, Fedorov A, Parmar C, Hosny A, Aucoin N, Narayan V, et al. Computational radiomics system to decode the radiographic phenotype. *Cancer Res* (2017) 77(21):e104–7. doi: 10.1158/0008-5472.CAN-17-0339

34. Zwanenburg A, Vallières M, Abdalah MA, Aerts HJWL, Andrearczyk V, Apte A, et al. The image biomarker standardization initiative: Standardized quantitative radiomics for high-throughput image-based phenotyping. *Radiology* (2020) 295(2):328–38. doi: 10.1148/radiol.2020191145

35. Wang X, Zhao X, Li Q, Xia W, Peng Z, Zhang R, et al. Can peritumoral radiomics increase the efficiency of the prediction for lymph node metastasis in clinical stage T1 lung adenocarcinoma on CT. *Eur Radiol* (2019) 29(11):6049–58. doi: 10.1007/s00330-019-06084-0

36. Shepherd FA, Rodrigues Pereira J, Ciuleanu T, Tan EH, Hirsh V, Thongprasert S, et al. Erlotinib in previously treated non-small-cell lung cancer. *N Engl J Med* (2005) 353(2):123–32. doi: 10.1056/NEJMoa050753

37. Sequist LV, Yang JCH, Yamamoto N, O'Byrne K, Hirsh V, Mok T. Phase III study of afatinib or cisplatin plus pemetrexed in patients with metastatic lung adenocarcinoma with EGFR mutations. *J Clin Oncol* (2013) 31(27):3327–34. doi: 10.1200/JCO.2012.44.2806

38. Mok TS, Wu YL, Ahn MJ, Garassino MC, Kim HR, Ramalingam SS. Osimertinib or platinum-pemetrexed in EGFR T790M-positive lung cancer. *N Engl J Med* (2017) 376(7):629–40. doi: 10.1056/NEJMoa1612674

39. Zhang Y, Sun Y, Pan Y, Li C, Shen L, Li Y, et al. Frequency of driver mutations in lung adenocarcinoma from female never-smokers varies with histologic subtypes and age at diagnosis. *Clin Cancer Res* (2012) 18(7):1947–53. doi: 10.1158/1078-0432.CCR-11-2511

40. Song Z, Zhu H, Guo Z, Wu W, Sun W, Zhang Y. Correlation of EGFR mutation and predominant histologic subtype according to the new lung adenocarcinoma classification in Chinese patients. *Med Oncol* (2013) 30(3):645. doi: 10.1007/s12032-013-0645-1

41. Jia Y, Yun CH, Park E, Ercan D, Manuia M, Juarez J. Overcoming EGFR (T790M) and EGFR(C797S) resistance with mutant-selective allosteric inhibitors. *Nature* (2016) 534:129–32. doi: 10.1038/nature17960

frontiers | Frontiers in Oncology

TYPE Mini Review
PUBLISHED 17 August 2022
DOI 10.3389/fonc.2022.963612

OPEN ACCESS

EDITED BY
Jiansong Ji,
Lishui Central Hospital, China

REVIEWED BY
Zhiming Li,
The Affiliated Hospital of Qingdao University, China
Yangyang Zhu,
Lanzhou University, China

*CORRESPONDENCE
Tian'an Jiang
tiananjiang@zju.edu.cn

SPECIALTY SECTION
This article was submitted to Cancer Imaging and Image-directed Interventions, a section of the journal Frontiers in Oncology

RECEIVED 07 June 2022
ACCEPTED 01 August 2022
PUBLISHED 17 August 2022

CITATION
Gu J and Jiang T (2022) Ultrasound radiomics in personalized breast management: Current status and future prospects.
Front. Oncol. 12:963612.
doi: 10.3389/fonc.2022.963612

Ultrasound radiomics in personalized breast management: Current status and future prospects

Jionghui Gu[1,2,3] and Tian'an Jiang[1,2,3]*

[1]Department of Ultrasound, The First Affiliated Hospital, College of Medicine, Zhejiang University, Hangzhou, China, [2]Key Laboratory of Pulsed Power Translational Medicine of Zhejiang Province, Hangzhou, China, [3]Zhejiang University Cancer Center, Hangzhou, China

Breast cancer is the most common cancer in women worldwide. Providing accurate and efficient diagnosis, risk stratification and timely adjustment of treatment strategies are essential steps in achieving precision medicine before, during and after treatment. Radiomics provides image information that cannot be recognized by the naked eye through deep mining of medical images. Several studies have shown that radiomics, as a second reader of medical images, can assist physicians not only in the detection and diagnosis of breast lesions but also in the assessment of risk stratification and prediction of treatment response. Recently, more and more studies have focused on the application of ultrasound radiomics in breast management. We summarized recent research advances in ultrasound radiomics for the diagnosis of benign and malignant breast lesions, prediction of molecular subtype, assessment of lymph node status, prediction of neoadjuvant chemotherapy response, and prediction of survival. In addition, we discuss the current challenges and future prospects of ultrasound radiomics.

KEYWORDS

ultrasound, radiomics, breast, personalized medicine, artificial intelligence

Introduction

Breast cancer (BC) has become the most commonly diagnosed malignancy among women worldwide, with approximately 2.3 millions new cases diagnosed and 680,000 deaths in 2020, which indicates that effective clinical strategies are urgently needed to manage BC patients (1). With the increasing advocacy of precision medicine, it is important to perform accurate and efficient diagnosis, risk stratification, and timely adjustment of treatment strategies before, during, and after treatment. Breast ultrasound (US) is one of the most important imaging technology and is used in clinical practice, which aims to monitor neoadjuvant chemotherapy (NAC) treatment and characterize

breast lesions and axillary lymph nodes (2, 3). Various new US imaging techniques and quantitative analysis methods have been proposed, including US elastography and contrast-enhanced ultrasound (CEUS), to improve the sensitivity of conventional US and increase the accuracy of monitoring and prognostic prediction (4). However, it is difficult for radiologists to perform a comprehensive analysis of tumors with the information obtained by looking at various ultrasound images (5, 6). Radiologists face great challenges in achieving stable and reliable interpretation and efficacy prediction of such multi-modal US images.

New opportunities have emerged with the advent of radiomics, a technique for extracting high-throughput quantitative features from medical images In recent years, radiomics based on X-ray, US, magnetic resonance imaging (MRI) and positron emission tomography-computed tomography (PET-CT) has proved to be useful for extracting a large number of image features that cannot be observed with the naked eye (7–10). In some tasks, it matches or exceeds human perception (11, 12). Ultrasound has the characteristics of large data size, multiple data types, and frequent examination, which makes ultrasound radiomics uniquely advantageous in clinical applications. Therefore, the application of ultrasound radiomics in BC is being explored positively.

In this review, we aimed to briefly introduce ultrasound radiomics and summarize its potential clinical applications in the diagnosis of benign and malignant breast lesions, prediction of molecular staging, assessment of lymph node status, prediction of NAC response, and the prediction of survival. Moreover, we discuss the current challenges of ultrasound radiomics and how it can be more quickly applied to clinical practice, and then to achieve precise personalized medical management for BC patients based on US images and clinicopathological information.

Workflows of radiomics

Radiomics is an effective combination of big data analysis technology and medical images, which utilizes a large number of data characterization algorithms based on artificial intelligence to extract high-throughput quantitative image features from massive medical images and build a data information bank (13, 14). Then, radiomics performs deep learning analysis and information mining from these quantified image features and link them with clinical macroscopic information and pathological and/or genetic microscopic information, which holds potential in disease detection, diagnosis, prognosis, and treatment (13). At present, radiomics strategies mainly include two methods (13, 15). One is the classic approach based on extracting pre-designed (also referred to as hand-crafted or engineered) features using conventional machine learning (ML) (Figure 1). The other is the recently developed approach based on deep learning (DL), it can autonomously learn and extract complex and abstract features related to disease from a large number of medical images by constructing a multi-layer neural network, without any prior design (Figure 1).

The radiomics process based on engineered features can be divided into five steps: 1) Medical image acquisition, which can be various types of medical images, such as X-ray, computed tomography (CT), MRI, PET-CT, US, or even images of H&E-stained biopsy sections. 2) Region of interest (ROI) segmentation, which is to extract only the information related to the lesion. The current segmentation of ROI mainly includes manual segmentation, semi-automatic segmentation and automatic segmentation. Different segmentation algorithms have their applicable scope and conditions. There is no universal segmentation algorithm with high recognition yet. 3) Feature extraction: Radiomics features are extracted from ROI, including signal intensity, shape, size, and first-order, second-order and higher-order texture features. 4) Feature selection: Although radiomics extracts many features, some features are spurious and redundant for a specific task. Therefore, it is necessary to select features with good repeatability, high stability and independence according to feature selection methods, which is conducive to the construction of robust models. At present, the main methods include least absolute shrinkage and selection operator (LASSO), recursive feature elimination, principal component analysis, and max-relevance and min-redundancy, etc. 5) Model building and validation: This mainly refers to model building and testing independent samples, which can be done by a variety of methods, from statistics to advanced machine learning strategies. The common methods include linear regression, logistic regression, support vector machine, random forest, Cox regression, artificial neural network and so on.

In recent years, with the exponential increase of GPU computing power and the development of medical big data, DL has become one of the most popular analysis methods in radiomics (16). DL-based radiomics (DLR) is an end-to-end model that does not require human involvement. The feature extraction and analysis parts of DLR are coupled. While hand-crafted feature-based radiomics requires pre-determination along with expert knowledge, DLR does not require the preparation of pre-defined features, which reduces the subjectivity and uncertainty of hand-crafted feature design and selection.

Radiomics in the ultrasound

Compared with other imaging techniques, US has the advantages of simple, no radiation and real-time, and is one of

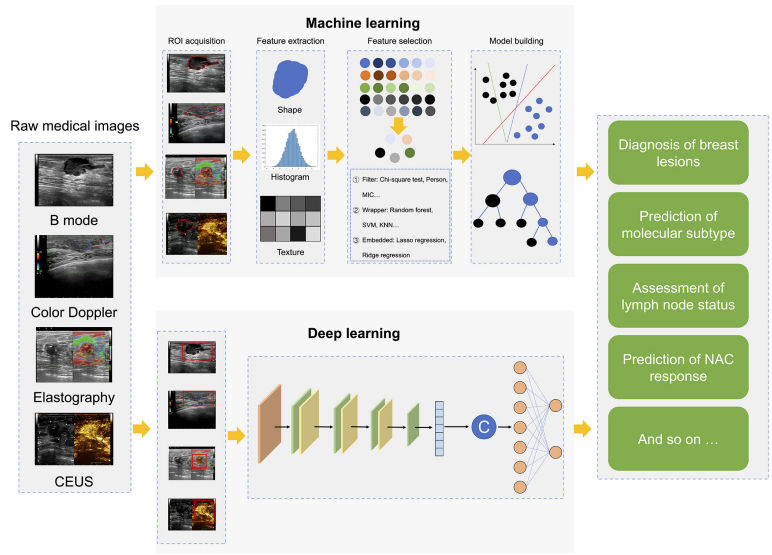

FIGURE 1
Radiomics workflows based on hand-crafted features or deep learning. CEUS, contrast-enhanced ultrasound; ROI, region of interest; MIC, mutual information and maximal information coefficient; SVM, support vector machine; KNN, k nearest neighbor; NAC, neoadjuvant chemotherapy.

the most important methods for monitoring breast lesions. In recent years, with the continuous development of ultrasound instruments, various new ultrasound techniques such as color doppler imaging, contrast-enhanced ultrasound (CEUS) and US elastography have also been used as complementary techniques for breast examination. Radiologists' demand for efficient and objective assessment of US images in routine clinical work is increasing, and AI-assisted ultrasound image analysis has attracted attention.

The traditional radiomics based on feature engineering requires manual segmentation of target regions and manual definition of features on images. However, it is difficult to perform manual segmentation of US images due to low resolution and vague boundary definition. Additionally, the repeatability of US examinations is easily affected by different operators, patients and instruments. Therefore, the application of machine learning based on feature engineering in US image analysis has certain limitations. However, the DLR approach supports a simple end-to-end training or learning process that can create a fully automated workflow. Moreover, deep learning networks can learn specific features from the data itself. Therefore, DLR can better enable the analytical processing of US images and improve the dependence of US images on various operators, patients and machines. DLR is expected to achieve robust and scalable ultrasound radiomics models to assist in disease detection, diagnosis, prognosis, and treatment.

Ultrasound radiomics in the breast diagnosis

Although ultrasonography is the one of most common imaging technique used to detect and distinguish benign and malignant breast lesions, it is difficult to accurately and stably identify some lesions with the naked eye. Recently, many studies have explored the potential of ultrasound radiomics to aid in the detection and differentiation of lesions (9, 17–20) (Table 1).

Earlier, Fujioka et al. (24) began to use the DLR model based on US images to identify benign and malignant breast lesions. This study confirmed that the DLR model had equal or better diagnostic performance compared to radiologists on a test dataset with 120 breast lesions (AUC = 0.913 *vs* 0.728-0.845, p = 0.01-0.14). Subsequently, several studies have shown that ultrasound radiomics based on 2D-US images has good performance in identifying benign from malignant breast lesion, with AUCs ranging from 0.817-0.943 (9, 17–19). Additionally, studies have shown that the classification performance of the AI model may be affected by adjusting the ROI as different inputs of the model. Dong et al. (25) proposed that the performance of the DLR model with coarse ROI is slightly better than the DLR model with fine ROI. Therefore, we can conclude that peripheral tissue is also an important factor in the classification of breast lesions.

TABLE 1 Summary of ultrasound radiomics studies in breast diagnosis.

Study	Task	Data size	Imaging data	Radiomics results
Fleury et al. (17) 2020	benign vs malignant	207 lesions	2D-US	AUC: 0.817
Li et al. (18) 2021	benign vs malignant	256 lesions	2D-US	AUC: 0.943
Romeo et al. (9) 2021	benign vs malignant	201 lesions	2D-US	AUC: 0.820
Shen et al. (21) 2021	benign vs malignant	143203	2D-US + Color Doppler	AUC: 0.962
Fujioka et al. (22) 2020	benign vs malignant	377 lesions	SWE-US	AUC: 0.898
Ciritsis et al. (20) 2019	Task A: BI-RADS 2 vs BI-RADS 3-5; Task B: BI-RADS 2-3 vs BI-RADS 4-5	582 lesions	2D-US + radiological report	ACC: 0.930 for task A; ACC: 0.953 for task B
Mango et al. (19) 2020	benign vs malignant	900 lesions	2D-US	AUC: 0.870
Moustafa et al. (23) 2020	benign vs malignant	159 lesions	2D-US + Color Doppler	AUC: 0.958
Fujioka et al. (24) 2019	benign vs malignant	360 lesions	2D-US	AUC: 0.913
Dong et al. (25) 2021	benign vs malignant	367 lesions	2D-US	AUC: 0.899 with coarse ROIs AUC: 0.869 with fine ROIs
Qian et al. (26) 2021	benign vs malignant	873 lesions	2D-US + Color Doppler + elastography	AUC: 0.922 (2D-US + Color Doppler) AUC: 0.955 (2D-US + Color Doppler + elastography)
Zhang et al. (27) 2021	benign vs malignant	1311 lesions	2D-US	AUC: 0.846 PPV:9.3% for BI-RADS 4A
Chen et al. (28) 2021	benign vs malignant	221 lesions	CEUS	ACC: 0.863
Jiang et al. (29) 2021	benign vs malignant	401 lesions	2D-US + SWE	AUC: 0.920
Zhang et al. (30) 2019	benign vs malignant	227 lesions	2D-US + SWE	AUC: 0.961
Misra et al. (31) 2022	benign vs malignant	85 lesions	2D-US + SE	ACC: 0.900
Zhang et al. (32)2020	benign vs malignant	291 lesions	2D-US + SWE	ACC: 1.000

US: ultrasound, SWE: shear wave elastography, SE: strain elastography, AUC: area under the curve, ACC: accuracy, PPV: positive predictive value

Since breast ultrasonography has a high rate of false positives (FP), how to reduce the rate of FP with artificial intelligence (AI) has attracted extensive attention by researchers. Chen et al. (21) established an AI model with 288,767 US examinations in a retrospective study and demonstrated that with the assistance of AI, radiologists reduced the FP rate by 37.3% and unnecessary biopsies by 27.8% without sacrificing sensitivity. And several other studies have also confirmed this finding (33, 34). Recent studies have challenged the use of ultrasound radiomics for specific breast lesions that are difficult to diagnose in clinical practice, particularly for BI-RADS 4A lesions. Niu et al. (35) analyzed 206 patients with a US score of BI-RADS 4A and concluded that AI can reveal more subtle differences associated with benign-malignant differentiation in BI-RADS 4A lesions compared to the naked eye. Thus, with the morphological and textural information provided by AI, physicians can make more accurate judgments about such atypical lesions. In addition, a study by Zhang et al. (27) confirmed a positive predictive value was 9.3% when using the AI model to analyze BI-RADS 4A lesions. Although this result was not significant, it was superior to radiologists.

Studies have shown that radiomic features extracted from multimodal US images can improve the ability of lesion diagnosis. A recent study by Zhan et al. (30) showed that dual-mode image features from 2D and shear wave elastography (SWE) achieved accurate differentiation for malignant and benign breast tumors with an AUC of 0.961, which employed a framework for feature learning and classification with the deep polynomial network. Several studies have further confirmed the superior performance of ultrasound radiomics based on bimodal US images in classifying over quantitative elastography parameters (22, 29, 31, 32, 36, 37). As known, the blood supply characteristics of breast masses are important features to determine the malignancy of the lesion. Moustafa et al. (23) extracted radiomics features from 2D-US and color doppler images, respectively, to establish DLR models to help determine the possibility of malignant. CEUS can provide more detailed blood supply characteristics, which can be used to establish an AI model for the differential diagnosis of breast cancer (28). The interpretability and clinical applicability of the DLR model have always been two major challenges in the field of AI. Notably, an interpretable and clinically applicable DLR system was recently proposed and validated by Qian et al. (26). The study used 10,815 and 912 multi-modal (B mode, color doppler and elastography) multi-view (transverse and longitudinal) breast US images for training and prospective testing, respectively, and had an AUC of 0.955 finally. Such a clinically applicable AI

system may be incorporated into future breast cancer US screening, as well as workflows that support ancillary or secondary readings.

Ultrasound radiomics in the evaluation of molecular subtype

BC is a highly heterogeneous tumor, and the molecular expression status is one of the key factors indicating the prognosis and guiding the choice of treatment options. At present, molecular subtypes of BC are mainly determined by genetic or immunohistochemistry analysis. However, there are false negatives for biopsy results of individual tissues. The ultrasound radiomics is based on the assumption that microstructural discrepancies in different molecular subtypes of breast cancer result in different gray-scale patterns, margins, or any other features on US images that can be identified by AI models. Currently, researchers are attempting to use ultrasound imaging histology to non-invasively and comprehensively analyze the molecular status of the entire tumor tissue to provide personalized management for BC patients (Table 2).

Studies have shown that ultrasound radiomics is expected to be a new imaging label for identifying molecular subtypes (HER2 +, triple-negative, Luminal A and Luminal B) of BC patients because of its good performance (38, 39). In addition, Jiang et al. (38) confirmed that the DLR model could distinguish the luminal type and non-luminal type satisfactorily with AUCs of 0.87 and 0.83 in two independent test cohort. However, Wu et al. (40) extracted quantitative radiomics features of tumors in raw US images and showed a general performance in predicting molecular biomarker expression. The radiomics models showed predictive performance with AUC greater than 0.7 in the test cohort, and the AUCs are 0.84, 0.78, 0.74, 0.86, 0.78, and 0.74 for ER, PR, HER2, Ki67, p16, and p53, respectively. The treatment of triple-negative BC has been a challenge due to the absence of effective drugs for specific molecular targets. Whereas the expression of ki67 is a prognostic indicator and p53 is considered a tumor suppressor. Cui et a.l (41) and Li et al. (42) found that ultrasound radiomics models enabled preoperative classification of ki67 and p53 status. Furthermore, it is noteworthy that recent studies have shown that ultrasound radiomics features are not only a potential imaging biomarker for disease-free survival risk stratification, but also can predict the risk of postoperative recurrence in patients with triple-negative BC (43, 44). At present, the ultrasound radiomics in predicting molecular subtype and survival recurrence of BC needs further research.

Ultrasound radiomics in the assessment of lymph node status

Accurate identification of axillary lymph node (ALN) status is important in determining tumor stage, developing appropriate axillary treatment plans, and predicting prognosis for BC patients with or without NAC treatment (2, 3). Sentinel lymph node (SLN) biopsy and axillary lymph node dissection (ALND) are two main methods for determining ALN status. It is worth mentioning that there are varying degrees of complications with both sentinel lymph node dissection and ALND (45, 46). Thus, the development of noninvasive biomarkers to identify ALN status is of great significance for the accurate management of BC patients. At present, researchers are challenging the radiomics approach based on primary breast tumors on US images in predicting the status of ALN and SLN (Table 3).

The majority of the earliest studies using ultrasound radiomics to predict lymph node status were based on 2D grayscale US images. Several studies have confirmed that DLR combined with clinicopathological features has a satisfactory

TABLE 2 Summary of ultrasound radiomics studies in classifying breast cancer subtypes.

Study	Task	Data size	Imaging data	Radiomics results
Jiang et al. (38) 2021	assessment of four breast cancer molecular subtypes: luminal A, luminal B, HER2+, triple-negative	2120 lesions	2D-US	ACC: form 0.8007 to 0.9702 for the test cohort A; and 0.8794 to 0.9883 for the test cohort B for each sub-category
Guo et al. (39) 2018	distinguish between HR+/HER2- and triple-negative	215 lesions	2D-US	AUC: 0.760
Wu et al. (40) 2021	predicting the expression of ER, PR, HER2, Ki67, P16, and P53	116 lesions	2D-US	AUC: ER (0.940 and 0.840), PR (0.900 and 0.780), HER2 (0.940 and 0.740), Ki67 (0.950 and 0.860), P16 (0.960 and 0.780), and P53 (0.95 and 0.74) in training and test cohort, respectively.
Cui et al. (41) 2021	predicting the expression of Ki67 and P53	263 lesions	2D-US	AUC: 0.780 for Ki67; 0.710 for P53
Li et al. (42) 2021	predicting the expression of Ki67 and HER2	252 lesions	2D-US	AUC: 0.680 for Ki67; 0.651 for HER2

US, ultrasound; HER2, human epidermal growth factor receptor 2; HR, hormone receptor; ER, estrogen receptor; PR, progesterone receptor; AUC, area under the curve; ACC, accuracy.

TABLE 3 Summary of ultrasound radiomics studies in predicting axillary lymph node status.

Study	Task	Data size	Imaging data	Radiomics results
Lee et al. (47) 2021	Predicting ALN metastasis	496 patients	2D-US	AUC: 0.810
Qiu et al. (48) 2020	Predicting ALN metastasis	196 patients	2D-US	AUC: 0.759
Zhou et al. (49) 2021	Predicting ALN metastasis	192 patients	2D-US	AUC: 0.650
Yu et al. (50) 2019	Predicting ALN metastasis	426 patients	2D-US	AUC: 0.810
Guo et al. (51) 2020	Predicting SLN metastasis and NSLN metastasis	937 patients	2D-US	AUC: 0.848 for SLN metastasis; AUC: 0.812 for NSLN metastasis
Lee et al. (52) 2021	Predicting ALN metastasis	153 patients	2D-US	AUC: 0.805
Sun et al. (53) 2020	Predicting ALN metastasis	479 patients	2D-US	AUC: 0.950
Jiang et al. (54)2021	Predicting ALN burden	433 patients	2D-US+SWE	C-index: 0.817 for N0 and N+(≥ 1) C-index: 0.810 for N+(1-2) and N+(≥ 3)
Zheng et al. (55) 2020	Predicting ALN metastasis	584 patients	2D-US+SWE	AUC: 0.905
Gao et al. (56) 2021	Predicting ALN burden	343 patients	2D-US	AUC: 0.733 for N+(<3) and N+(≥ 3)

US, ultrasound; SWE, shear wave elastography; ALN, axillary lymph node; SLN, sentinel lymph node; NSLN, non-sentinel lymph node; AUC, area under the curve

performance in predicting ALN metastasis, with an AUC between 0.75 and 0.85 (47–50). Guo et al. (51) proposed a DLR ultrasonography (DLRU) model for comprehensive evaluation of SLN and non-sentinel lymph node (NSLN) status. And DLRU achieved a sensitivity of 98.4% in identifying SLN+ and 98.4%in identifying NLSN+. In addition, Lee et al. (52) innovatively explored the performance of peritumoral region combined with tumor region in predicting lymph node metastasis (LNM) with method of ultrasound radiomics. They found that DLR model with 3mm thick peritumoral tissue tumor area had the best predictive performance, achieving an accuracy of 81.05% (124/153). Therefore, combining tumor and peri-tumor tissues contributes to the prediction of LNM, which is consistent with the results of previous study (53). SWE is an elastographic technique that integrates B-mode US with a color-coded map to allow better characterization of breast lesions. Jiang et al. (54) developed and validated a nomogram containing radiomics features of SWE for assessing the risk level of LNM in early BC, then the result confirmed that ultrasound radiomics model showed good predictive power for LNM risk staging in early-stage BC patients, which can provide incremental information for decision making. Moreover, recent studies have shown that clinical characteristics combined with DLR model based on multimodal US images (B mode and SWE) can provide a noninvasive and practical tool for preoperative prediction of ALN status, and achieve an AUC of 0.905 in the test cohort (55). Compared with the DLR model based on grayscale US images alone, the performance of the DLR model based on multimodal US images for tumor load of ALN achieved a significant improvement (56). As clinical practice proposes greater demands on precision treatment, studies with larger data size and more multimodal fusion are needed to confirm the validity of the DLR model.

Ultrasound radiomics in the prediction of NAC response

NAC has become one of the most important treatment methods for BC patients. Normally, if the efficacy of NAC is unresponsive or unsatisfactory, further treatment should be changed accordingly. Therefore, early discontinuation of ineffective treatment or adjustment of treatment strategy is essential to avoid unnecessary toxicities and optimize overall benefits. However, owing to the heterogeneity and complexity of the tumor, individual responses of BC patients to NAC exhibit vast differences and tumors and axillary response to NAC are not parallel (57–60). Histopathological examination of surgical specimens is the gold standard for evaluating response and can only be performed after NAC treatment. Accurate assessment and prediction of response are of particular significance for the precise management of breast cancer patients who underwent NAC. Although MRI is currently the most important method for assessing NAC response (61–63), it still cannot predict pathologic complete response (PCR) with sufficient accuracy (64). MRI is not suitable for frequent monitoring during NAC treatment due to its high cost and time-consuming. Ultrasound is the most suitable examination method to be used repeatedly in the process of NAC. Several studies have shown that DLR based on US images has good performance in predicting the efficacy of NAC for BC patients (Table 4).

Quiaoit et al. (65) attempted to explore the performance of quantitative ultrasound radiomics in monitoring the response to NAC on a dataset of 59 patients, and the results were generally consistent with those of other previous studies (66, 67, 71). The usefulness of quantitative ultrasound radiomics for NAC response assessment remained relatively limited. Recently, the emergence of DLR has greatly enhanced the image analysis capabilities of radiomics, which relies on deep neural network

TABLE 4 Summary of ultrasound radiomics studies in predicting response of NAC.

Study	Task	Data size	Imaging data	Radiomics results
Quiaoit et al. (65) 2020	Predicting the response to NAC before surgery	59 patients	2D-US	AUC: 0.870
DiCenzo et al. (66) 2020	Predicting the response to NAC before treatment	82 patients	2D-US	ACC: 0.870
Sannachi et al. (67) 2019	Predicting the response to NAC	100 patients	2D-US	ACC: 0.780 at 1 week after the start of treatment ACC: 0.900 at 4 weeks after the start of treatment ACC: 0.920 at 8 week after the start of treatment
Jiang et al. (68) 2021	Predicting the response to NAC before surgery	592 patients	2D-US	AUC: 0.940
Byra et al. (69) 2021	Predicting the response to NAC	38 patients	2D-US	AUC: 0.844 (Pre NAC) AUC: 0.827 (after first course of NAC) AUC: 0.828 (after second course of NAC)
Gu et al. (70) 2021	Predicting the response to NAC	168 patients	2D-US	AUC: 0.812 (after second course of NAC) AUC: 0.937 (after fourth course of NAC)

NAC: neoadjuvant chemotherapy; US, ultrasound; AUC, area under the curve; ACC, accuracy.

and data-driven learning to achieve automatic feature extraction and is promising in US images analysis. Jiang et al. (68) proposed an integrated ultrasound radiomics model based on a multicenter dataset of 592 individuals that combined deep learning and machine learning to predict PCR to NAC for BC patients. The deep learning radiomics nomogram model achieved an AUC of 0.94 in the validation cohort, with a significant improvement in predictive accuracy compared to two radiologists ($p < 0.01$). In addition to assessing the tumor status of patients at the end of NAC, predicting response early in NAC appears critical for early treatment change and avoiding unnecessary treatment. Byra et al. (69) and Gu et al. (70) proposed the Siamese convolutional neural network for predicting response at an early stage of NAC and achieved accurate and personalized prediction. Gu et al. also developed a deep learning radiomics pipeline using cascading models constructed at different courses of NAC treatment. Although, various studies have confirmed that the ultrasound radiomics can provide physicians with a valid and feasible tool to predict the response to NAC and determine further personalized treatment protocols. However, no large clinical trial has yet shown that ultrasound radiomics predictions can fully determine whether a patient should be discontinued from NAC. Clinicians must consider treatment strategies in combination with various resources and patients' demands.

Ultrasound radiomics and personalized management of BC

The personalized treatment plan for BC patients includes the timing and specific implementation of surgery, the timing and protocol of radiotherapy and chemotherapy, and other treatment strategies, all of which require comprehensive consideration of molecular subtypes, lymph node status, the efficacy of neoadjuvant therapy and other factors. However, BC is a heterogeneous disease with a high degree of diversity in biochemistry, histopathology and morphology, all of which affect treatment and clinical outcomes. In addition, most gold standards need to be obtained after surgery. Therefore, preoperative noninvasive assessment and prediction is the most important clinical issue in the realization of personalized management of BC patients, which has not been addressed by imaging methods at present. Ultrasound radiomics aims to extract a large number of high-throughput features to obtain more useful information about tissue lesions and treatment response information for personalized medicine. The solution by ultrasound radiomics is highly expected.

Future challenges

Ultrasound radiomics transforms medical images into high-dimensional quantitative data, which help physicians understand the characteristics of tumor phenotypes (including the macroscopic phenotype of the tumor, and the cellular and molecular characteristics of the tumor tissue), and achieved impressive results in both diagnosis and prediction (13, 72). In addition, ultrasound radiomics, as a complement to biopsy analysis, can simultaneously assess the tumor microenvironment, characterize tumor spatial heterogeneity, and assess disease progression longitudinally with the advantage of non-invasive. However, it is still a long way to transfer ultrasound radiomics from scientific research to clinical practice, given some of the current limitations and challenges. First, ultrasound with handheld technology lacks reproducibility compared to other techniques such as mammography or MRI. Compared with radiomics based on ML, DLR can overcome this drawback to a certain extent. However, most of the previous studies were small sample single-center retrospective studies, which leads to the robustness of ultrasound radiomics models is not stable enough. Future internationalized multi-center data with larger sample sizes are needed to validate and improve the robustness of the models. In addition, due to the differences in

imaging acquisition and the diversity of reconstruction algorithms, an exhaustive data management and coordination process is needed to obtain multi-center data. Second, there is a lack of effective methods to fuse multi-modal US data (such as B mode, color doppler, CEUS, and elastography) to perform a multi-scale and all-around assessment of tumor biological behavior (73). Finally, DLR is a "black box" technology, that lacks transparency and biological interpretability for algorithms (74). Therefore, how correlating DLR image features with biological information, and quantifying the key molecular information in the development of BC using tumor images, which are major challenges for future research. We believe this is important because radiomics plays a supporting role in the foreseeable future by providing physicians with more interpretative and understandable information.

Additionally, multi-omics studies have become a hot topic for characterizing the molecular biology of tumors, including genomics, transcriptomics, proteomics, and metabolomics (72, 75). Thus, multi-omics studies are accelerating BC research and making precision medicine possible. In the future, ultrasound radiomics should be combined with clinical data and microscopic genetic data to develop multi-omics studies, which may accelerate BC research in precision diagnosis, decision making and prediction. Although most DLR is still in the technology development stage, the development of genomics and deep learning technologies may facilitate the extraction of deep features and explore new possibilities in BC radiomics or radio-genomics.

Conclusion

In conclusion, radiomics has emerged rapidly as one of the most interesting research topics in breast ultrasonography, with promising results for the clinical management of BC. This article has outlined the application of ultrasound radiomics in the clinical practice for the management of BC patients, including the diagnosis of benign and malignant lesions, prediction of molecular staging, assessment of lymph node status, prediction of NAC response and prediction of survival. Ultrasound radiomics is a promising tool for personalized precision medicine by virtue of its noninvasive nature. We also identify the limitations of radiomics that currently hinder its translation into clinical practice and strategies to overcome these limitations. In the future, the establishment of multi-omics studies including radiomics will hopefully connect the information extracted from breast US images to the tumor microenvironment, and provide precise and personalized treatment decisions for BC patients.

Author contributions

JG and TJ, conception and design the study. JG and TJ, medical support and manuscript correction. JG, manuscript writing. TJ, expert guidance and manuscript review. All authors, final approval of the manuscript. All authors contributed to the article and approved the submitted version.

Funding

This study was supported by the Development Project of National Major Scientific Research Instrument (82027803); National Natural Science Foundation of China (81971623); Key Project of Natural Science Foundation of Zhejiang Province (LZ20H180001); Zhejiang Provincial Association Project for Mathematical Medicine (LSY19H180015).

Conflict of interest

The authors declare that the research was conducted in the absence of any commercial or financial relationships that could be construed as a potential conflict of interest.

Publisher's note

All claims expressed in this article are solely those of the authors and do not necessarily represent those of their affiliated organizations, or those of the publisher, the editors and the reviewers. Any product that may be evaluated in this article, or claim that may be made by its manufacturer, is not guaranteed or endorsed by the publisher.

References

1. Sung H, Ferlay J, Siegel RL, Laversanne M, Soerjomataram I, Jemal A, et al. Global cancer statistics 2020: GLOBOCAN estimates of incidence and mortality worldwide for 36 cancers in 185 countries. *CA Cancer J Clin* (2021) 71(3):209–49. doi: 10.3322/caac.21660

2. Goetz MP, Gradishar WJ, Anderson BO, Abraham J, Aft R, Allison KH, et al. NCCN guidelines insights: Breast cancer, version 3.2018. *J Natl Compr Canc Netw* (2019) 17(2):118–26. doi: 10.6004/jnccn.2019.0009

3. Yogananda CGB, Shah BR, Nalawade SS, Murugesan GK, Yu FF, Pinho MC, et al. MRI-Based deep-learning method for determining glioma MGMT promoter methylation status. *AJNR Am J Neuroradiol* (2021) 42(5):845–52. doi: 10.3174/ajnr.A7029

4. Galati F, Moffa G, Pediconi F. Breast imaging: Beyond the detection. *Eur J Radiol* (2022) 146:110051. doi: 10.1016/j.ejrad.2021.110051

5. Lee HJ, Kim EK, Kim MJ, Youk JH, Lee JY, Kang DR, et al. Observer variability of breast imaging reporting and data system (BI-RADS) for breast ultrasound. *Eur J Radiol* (2008) 65(2):293–8. doi: 10.1016/j.ejrad.2007.04.008

6. Abdullah N, Mesurolle B, El-Khoury M, Kao E. Breast imaging reporting and data system lexicon for US: interobserver agreement for assessment of breast masses. *Radiology* (2009) 252(3):665–72. doi: 10.1148/radiol.2523080670

7. Cui Q, Sun L, Zhang Y, Zhao Z, Li S, Liu Y, et al. Value of breast MRI omics features and clinical characteristics in breast imaging reporting and data system (BI-RADS) category 4 breast lesions: an analysis of radiomics-based diagnosis. *Ann Transl Med* (2021) 9(22):1677. doi: 10.21037/atm-21-5441

8. Chen Y, Wang Z, Yin G, Sui C, Liu Z, Li X, et al. Prediction of HER2 expression in breast cancer by combining PET/CT radiomic analysis and machine learning. *Ann Nucl Med* (2021) 36(2):172–82. doi: 10.1007/s12149-021-01688-3

9. Romeo V, Cuocolo R, Apolito R, Stanzione A, Ventimiglia A, Vitale A, et al. Clinical value of radiomics and machine learning in breast ultrasound: a multicenter study for differential diagnosis of benign and malignant lesions. *Eur Radiol* (2021) 31(12):9511–9. doi: 10.1007/s00330-021-08009-2

10. Zhang HX, Sun ZQ, Cheng YG, Mao GQ. A pilot study of radiomics technology based on X-ray mammography in patients with triple-negative breast cancer. *J Xray Sci Technol* (2019) 27(3):485–92. doi: 10.3233/XST-180488

11. Cao C, Liu F, Tan H, Song D, Shu W, Li W, et al. Deep learning and its applications in biomedicine. *Genomics Proteomics Bioinf* (2018) 16(1):17–32. doi: 10.1016/j.gpb.2017.07.003

12. Acs B, Rantalainen M, Hartman J. Artificial intelligence as the next step towards precision pathology. *J Intern Med* (2020) 288(1):62–81. doi: 10.1111/joim.13030

13. Lambin P, Rios-Velazquez E, Leijenaar R, Carvalho S, van Stiphout RG, Granton P, et al. Radiomics: extracting more information from medical images using advanced feature analysis. *Eur J Cancer* (2012) 48(4):441–6. doi: 10.1016/j.ejca.2011.11.036

14. Aerts HJ, Velazquez ER, Leijenaar RT, Parmar C, Grossmann P, Carvalho S, et al. Decoding tumour phenotype by noninvasive imaging using a quantitative radiomics approach. *Nat Commun* (2014) 5:4006. doi: 10.1038/ncomms5006

15. Deng JL, Xu YH, Wang G. Identification of potential crucial genes and key pathways in breast cancer using bioinformatic analysis. *Front Genet* (2019) 10:695. doi: 10.3389/fgene.2019.00695

16. LeCun Y, Bengio Y, Hinton G. Deep learning. *Nature* (2015) 521 (7553):436–44. doi: 10.1038/nature14539

17. Fleury EFC, Marcomini K. Impact of radiomics on the breast ultrasound radiologist's clinical practice: From lumpologist to data wrangler. *Eur J Radiol* (2020) 131:109197. doi: 10.1016/j.ejrad.2020.109197

18. Li J, Bu Y, Lu S, Pang H, Luo C, Liu Y, et al. Development of a deep learning-based model for diagnosing breast nodules with ultrasound. *J Ultrasound Med* (2021) 40(3):513–20. doi: 10.1002/jum.15427

19. Mango VL, Sun M, Wynn RT, Ha R. Should we ignore, follow, or biopsy? impact of artificial intelligence decision support on breast ultrasound lesion assessment. *AJR Am J Roentgenol* (2020) 214(6):1445–52. doi: 10.2214/AJR.19.21872

20. Ciritsis A, Rossi C, Eberhard M, Marcon M, Becker AS, Boss A. Automatic classification of ultrasound breast lesions using a deep convolutional neural network mimicking human decision-making. *Eur Radiol* (2019) 29(10):5458–68. doi: 10.1007/s00330-019-06118-7

21. Shen Y, Shamout FE, Oliver JR, Witowski J, Kannan K, Park J, et al. Artificial intelligence system reduces false-positive findings in the interpretation of breast ultrasound exams. *Nat Commun* (2021) 12(1):5645. doi: 10.1038/s41467-021-26023-2

22. Fujioka T, Katsuta L, Kubota K, Mori M, Kikuchi Y, Kato A, et al. Classification of breast masses on ultrasound shear wave elastography using convolutional neural networks. *Ultrason Imaging* (2020) 42(4-5):213–20. doi: 10.1177/0161734620932609

23. Moustafa AF, Cary TW, Sultan LR, Schultz SM, Conant EF, Venkatesh SS, et al. Color Doppler ultrasound improves machine learning diagnosis of breast cancer. *Diagn (Basel)* (2020) 10(9):631. doi: 10.3390/diagnostics10090631

24. Fujioka T, Kubota K, Mori M, Kikuchi Y, Katsuta L, Kasahara M, et al. Distinction between benign and malignant breast masses at breast ultrasound using deep learning method with convolutional neural network. *Jpn J Radiol* (2019) 37 (6):466–72. doi: 10.1007/s11604-019-00831-5

25. Dong F, She R, Cui C, Shi S, Hu X, Zeng J, et al. One step further into the blackbox: a pilot study of how to build more confidence around an AI-based decision system of breast nodule assessment in 2D ultrasound. *Eur Radiol* (2021) 31(7):4991–5000. doi: 10.1007/s00330-020-07561-7

26. Qian X, Pei J, Zheng H, Xie X, Yan L, Zhang H, et al. Prospective assessment of breast cancer risk from multimodal multiview ultrasound images *via* clinically applicable deep learning. *Nat BioMed Eng* (2021) 5(6):522–32. doi: 10.1038/s41551-021-00711-2

27. Zhang N, Li XT, Ma L, Fan ZQ, Sun YS. Application of deep learning to establish a diagnostic model of breast lesions using two-dimensional grayscale ultrasound imaging. *Clin Imaging* (2021) 79:56–63. doi: 10.1016/j.clinimag.2021.03.024

28. Chen C, Wang Y, Niu J, Liu X, Li Q, Gong X. Domain knowledge powered deep learning for breast cancer diagnosis based on contrast-enhanced ultrasound videos. *IEEE Trans Med Imaging* (2021) 40(9):2439–51. doi: 10.1109/TMI.2021.3078370

29. Jiang M, Li CL, Chen RX, Tang SC, Lv WZ, Luo XM, et al. Management of breast lesions seen on US images: dual-model radiomics including shear-wave elastography may match performance of expert radiologists. *Eur J Radiol* (2021) 141:109781. doi: 10.1016/j.ejrad.2021.109781

30. Zhang Q, Song S, Xiao Y, Chen S, Shi J, Zheng H. Dual-mode artificially-intelligent diagnosis of breast tumours in shear-wave elastography and b-mode ultrasound using deep polynomial networks. *Med Eng Phys* (2019) 64:1–6. doi: 10.1016/j.medengphy.2018.12.005

31. Misra S, Jeon S, Managuli R, Lee S, Kim G, Yoon C, et al. Bi-modal transfer learning for classifying breast cancers *via* combined b-mode and ultrasound strain imaging. *IEEE Trans Ultrason Ferroelectr Freq Control* (2022) 69(1):222–32. doi: 10.1109/TUFFC.2021.3119251

32. Zhang X, Liang M, Yang Z, Zheng C, Wu J, Ou B, et al. Deep learning-based radiomics of b-mode ultrasonography and shear-wave elastography: Improved performance in breast mass classification. *Front Oncol* (2020) 10:1621. doi: 10.3389/fonc.2020.01621

33. Wang XY, Cui LG, Feng J, Chen W. Artificial intelligence for breast ultrasound: An adjunct tool to reduce excessive lesion biopsy. *Eur J Radiol* (2021) 138:109624. doi: 10.1016/j.ejrad.2021.109624

34. Heller SL, Wegener M, Babb JS, Gao Y. Can an artificial intelligence decision aid decrease false-positive breast biopsies? *Ultrasound Q* (2020) 37(1):10–5. doi: 10.1097/RUQ.0000000000000550

35. Niu S, Huang J, Li J, Liu X, Wang D, Zhang R, et al. Application of ultrasound artificial intelligence in the differential diagnosis between benign and malignant breast lesions of BI-RADS 4A. *BMC Cancer* (2020) 20(1):959. doi: 10.1186/s12885-020-07413-z

36. Misra S, Jeon S, Managuli R, Lee S, Kim G, Yoon C, et al. Bi-modal transfer learning for classifying breast cancers *via* combined b-mode and ultrasound strain imaging. *IEEE Trans Ultrason Ferroelectr Freq Control* (2021) 69(1):222–32. doi: 10.1109/TUFFC.2021.3119251

37. Li C, Li J, Tan T, Chen K, Xu Y, Wu R. Application of ultrasonic dual-mode artificially intelligent architecture in assisting radiologists with different diagnostic levels on breast masses classification. *Diagn Interv Radiol* (2021) 27(3):315–22. doi: 10.5152/dir.2021.20018

38. Jiang M, Zhang D, Tang SC, Luo XM, Chuan ZR, Lv WZ, et al. Deep learning with convolutional neural network in the assessment of breast cancer molecular subtypes based on US images: a multicenter retrospective study. *Eur Radiol* (2021) 31(6):3673–82. doi: 10.1007/s00330-020-07544-8

39. Guo Y, Hu Y, Qiao M, Wang Y, Yu J, Li J, et al. Radiomics analysis on ultrasound for prediction of biologic behavior in breast invasive ductal carcinoma. *Clin Breast Cancer* (2018) 18(3):e335–44. doi: 10.1016/j.clbc.2017.08.002

40. Wu L, Zhao Y, Lin P, Qin H, Liu Y, Wan D, et al. Preoperative ultrasound radiomics analysis for expression of multiple molecular biomarkers in mass type of breast ductal carcinoma in situ. *BMC Med Imaging* (2021) 21(1):84–4. doi: 10.1186/s12880-021-00610-7

41. Cui H, Zhang D, Peng F, Kong H, Guo Q, Wu T, et al. Identifying ultrasound features of positive expression of Ki67 and P53 in breast cancer using radiomics. *Asia Pac J Clin Oncol* (2021) 17(5):e176–84. doi: 10.1111/ajco.13397

42. Li JW, Cao YC, Zhao ZJ, Shi ZT, Duan XQ, Chang C, et al. Prediction for pathological and immunohistochemical characteristics of triple-negative invasive breast carcinomas: the performance comparison between quantitative and qualitative sonographic feature analysis. *Eur Radiol* (2021) 32(3):1590–600. doi: 10.1007/s00330-021-08345-3

43. Xiong L, Chen H, Tang X, Chen B, Jiang X, Liu L, et al. Ultrasound-based radiomics analysis for predicting disease-free survival of invasive breast cancer. *Front Oncol* (2021) 11:621993. doi: 10.3389/fonc.2021.621993

44. Yu F, Hang J, Deng J, Yang B, Wang J, Ye X, et al. Radiomics features on ultrasound imaging for the prediction of disease-free survival in triple negative breast cancer: a multi-institutional study. *Br J Radiol* (2021) 94(1126):20210188. doi: 10.1259/bjr.20210188

45. Boughey JC, Moriarty JP, Degnim AC, Gregg MS, Egginton JS, Long KH. Cost modeling of preoperative axillary ultrasound and fine-needle aspiration to guide surgery for invasive breast cancer. *Ann Surg Oncol* (2010) 17(4):953–8. doi: 10.1245/s10434-010-0919-1

46. Langer I, Guller U, Berclaz G, Koechli OR, Schaer G, Fehr MK, et al. Morbidity of sentinel lymph node biopsy (SLN) alone versus SLN and completion axillary lymph node dissection after breast cancer surgery: a prospective Swiss multicenter study on 659 patients. *Ann Surg* (2007) 245(3):452–61. doi: 10.1097/01.sla.0000245472.47748.ec

47. Lee SE, Sim Y, Kim S, Kim E-K. Predictive performance of ultrasonography-based radiomics for axillary lymph node metastasis in the preoperative evaluation of breast cancer. *Ultrasonography* (2021) 40(1):93–102. doi: 10.14366/usg.20026

48. Qiu X, Jiang Y, Zhao Q, Yan C, Huang M, Jiang TA. Could ultrasound-based radiomics noninvasively predict axillary lymph node metastasis in breast cancer? *J ultrasound Med* (2020) 39(10):1897–905. doi: 10.1002/jum.15294

49. Zhou W-J, Zhang Y-D, Kong W-T, Zhang C-X, Zhang B. Preoperative prediction of axillary lymph node metastasis in patients with breast cancer based on radiomics of gray-scale ultrasonography. *Gland Surg* (2021) 10(6):1989–2001. doi: 10.21037/gs-21-315

50. Yu F-H, Wang J-X, Ye X-H, Deng J, Hang J, Yang B. Ultrasound-based radiomics nomogram: A potential biomarker to predict axillary lymph node metastasis in early-stage invasive breast cancer. *Eur J Radiol* (2019) 119:108658. doi: 10.1016/j.ejrad.2019.108658

51. Guo X, Liu Z, Sun C, Zhang L, Wang Y, Li Z, et al. Deep learning radiomics of ultrasonography: Identifying the risk of axillary non-sentinel lymph node involvement in primary breast cancer. *EBioMedicine* (2020) 60:103018–8. doi: 10.1016/j.ebiom.2020.103018

52. Lee Y-W, Huang C-S, Shih C-C, Chang R-F. Axillary lymph node metastasis status prediction of early-stage breast cancer using convolutional neural networks. *Comput Biol Med* (2021) 130:104206. doi: 10.1016/j.compbiomed.2020.104206

53. Sun Q, Lin X, Zhao Y, Li L, Yan K, Liang D, et al. Deep learning vs. radiomics for predicting axillary lymph node metastasis of breast cancer using ultrasound images: Don't forget the peritumoral region. *Front Oncol* (2020) 10:53–3. doi: 10.3389/fonc.2020.00053

54. Jiang M, Li CL, Luo XM, Chuan ZR, Chen RX, Tang SC, et al. Radiomics model based on shear-wave elastography in the assessment of axillary lymph node status in early-stage breast cancer. *Eur Radiol* (2021) 32(4):2313–25. doi: 10.21203/rs.3.rs-75554/v1

55. Zheng X, Yao Z, Huang Y, Yu Y, Wang Y, Liu Y, et al. Deep learning radiomics can predict axillary lymph node status in early-stage breast cancer. *Nat Commun* (2020) 11(1):1236–6. doi: 10.1038/s41467-020-15027-z

56. Gao Y, Luo Y, Zhao C, Xiao M, Ma L, Li W, et al. Nomogram based on radiomics analysis of primary breast cancer ultrasound images: prediction of axillary lymph node tumor burden in patients. *Eur Radiol* (2021) 31(2):928–37. doi: 10.1007/s00330-020-07181-1

57. Derks MGM, van de Velde CJH. Neoadjuvant chemotherapy in breast cancer: more than just downsizing. *Lancet Oncol* (2018) 19(1):2–3. doi: 10.1016/S1470-2045(17)30914-2

58. Houssami N, Macaskill P, von Minckwitz G, Marinovich ML, Mamounas E. Meta-analysis of the association of breast cancer subtype and pathologic complete response to neoadjuvant chemotherapy. *Eur J Cancer* (2012) 48(18):3342–54. doi: 10.1016/j.ejca.2012.05.023

59. Petrelli F, Borgonovo K, Cabiddu M, Ghilardi M, Barni S. Neoadjuvant chemotherapy and concomitant trastuzumab in breast cancer: a pooled analysis of two randomized trials. *Anticancer Drugs* (2011) 22(2):128–35. doi: 10.1097/CAD.0b013e32834120aa

60. Xiong Q, Zhou X, Liu Z, Lei C, Yang C, Yang M, et al. Multiparametric MRI-based radiomics analysis for prediction of breast cancers insensitive to neoadjuvant chemotherapy. *Clin Transl Oncol* (2020) 22(1):50–9. doi: 10.1007/s12094-019-02109-8

61. Dialani V, Chadashvili T, Slanetz PJ. Role of imaging in neoadjuvant therapy for breast cancer. *Ann Surg Oncol* (2015) 22(5):1416–24. doi: 10.1245/s10434-015-4403-9

62. Li H, Yao L, Jin P, Hu L, Li X, Guo T, et al. MRI And PET/CT for evaluation of the pathological response to neoadjuvant chemotherapy in breast cancer: A systematic review and meta-analysis. *Breast* (2018) 40:106–15. doi: 10.1016/j.breast.2018.04.018

63. Marinovich ML, Houssami N, Macaskill P, Sardanelli F, Irwig L, Mamounas EP, et al. Meta-analysis of magnetic resonance imaging in detecting residual breast cancer after neoadjuvant therapy. *J Natl Cancer Inst* (2013) 105(5):321–33. doi: 10.1093/jnci/djs528

64. Weber JJ, Jochelson MS, Eaton A, Zabor EC, Barrio AV, Gemignani ML, et al. MRI And prediction of pathologic complete response in the breast and axilla after neoadjuvant chemotherapy for breast cancer. *J Am Coll Surg* (2017) 225(6):740–6. doi: 10.1016/j.jamcollsurg.2017.08.027

65. Quiaoit K, DiCenzo D, Fatima K, Bhardwaj D, Sannachi L, Gangeh M, et al. Quantitative ultrasound radiomics for therapy response monitoring in patients with locally advanced breast cancer: Multi-institutional study results. *PloS One* (2020) 15(7):e0236182. doi: 10.1371/journal.pone.0236182

66. DiCenzo D, Quiaoit K, Fatima K, Bhardwaj D, Sannachi L, Gangeh M, et al. Quantitative ultrasound radiomics in predicting response to neoadjuvant chemotherapy in patients with locally advanced breast cancer: Results from multi-institutional study. *Cancer Med* (2020) 9(16):5798–806. doi: 10.1002/cam4.3255

67. Sannachi L, Gangeh M, Tadayyon H, Gandhi S, Wright FC, Slodkowska E, et al. Breast cancer treatment response monitoring using quantitative ultrasound and texture analysis: Comparative analysis of analytical models. *Transl Oncol* (2019) 12(10):1271–81. doi: 10.1016/j.tranon.2019.06.004

68. Jiang M, Li CL, Luo XM, Chuan ZR, Lv WZ, Li X, et al. Ultrasound-based deep learning radiomics in the assessment of pathological complete response to neoadjuvant chemotherapy in locally advanced breast cancer. *Eur J Cancer* (2021) 147:95–105. doi: 10.1016/j.ejca.2021.01.028

69. Byra M, Dobruch-Sobczak K, Klimonda Z, Piotrzkowska-Wroblewska H, Litniewski J. Early prediction of response to neoadjuvant chemotherapy in breast cancer sonography using Siamese convolutional neural networks. *IEEE J BioMed Health Inform* (2021) 25(3):797–805. doi: 10.1109/JBHI.2020.3008040

70. Gu J, Tong T, He C, Xu M, Yang X, Tian J, et al. Deep learning radiomics of ultrasonography can predict response to neoadjuvant chemotherapy in breast cancer at an early stage of treatment: a prospective study. *Eur Radiol* (2021) 32(3):2099–109. doi: 10.1007/s00330-021-08293-y

71. Sannachi L, Tadayyon H, Sadeghi-Naini A, Tran W, Gandhi S, Wright F, et al. Non-invasive evaluation of breast cancer response to chemotherapy using quantitative ultrasonic backscatter parameters. *Med Image Anal* (2015) 20(1):224–36. doi: 10.1016/j.media.2014.11.009

72. Saini G, Mittal K, Rida P, Janssen EAM, Gogineni K, Aneja R. Panoptic view of prognostic models for personalized breast cancer management. *Cancers (Basel)* (2019) 11(9):1325. doi: 10.3390/cancers11091325

73. Castiglioni I, Gallivanone F, Soda P, Avanzo M, Stancanello J, Aiello M, et al. AI-Based applications in hybrid imaging: how to build smart and truly multi-parametric decision models for radiomics. *Eur J Nucl Med Mol Imaging* (2019) 46(13):2673–99. doi: 10.1007/s00259-019-04414-4

74. Wang F, Kaushal R, Khullar D. Should health care demand interpretable artificial intelligence or accept "Black box" medicine? *Ann Intern Med* (2020) 172(1):59–60. doi: 10.7326/M19-2548

75. Ponzi E, Thoresen M, Haugdahl Nøst T, Møllersen K. Integrative, multi-omics, analysis of blood samples improves model predictions: applications to cancer. *BMC Bioinf* (2021) 22(1):395. doi: 10.1186/s12859-021-04296-0

frontiers | Frontiers in Oncology

TYPE Original Research
PUBLISHED 23 November 2022
DOI 10.3389/fonc.2022.949111

OPEN ACCESS

EDITED BY
Jiansong Ji,
Lishui Central Hospital, China

REVIEWED BY
Stephanie Tanadini-Lang,
University Hospital Zürich, Switzerland
Asli Suner,
Ege University, Turkey

*CORRESPONDENCE
Minjing Zuo
minjingzuo@163.com

†These authors have contributed equally to this work and share first authorship

SPECIALTY SECTION
This article was submitted to Cancer Imaging and Image-directed Interventions, a section of the journal Frontiers in Oncology

RECEIVED 20 May 2022
ACCEPTED 26 October 2022
PUBLISHED 23 November 2022

CITATION
Chen Z, Yi L, Peng Z, Zhou J, Zhang Z, Tao Y, Lin Z, He A, Jin M and Zuo M (2022) Development and validation of a radiomic nomogram based on pretherapy dual-energy CT for distinguishing adenocarcinoma from squamous cell carcinoma of the lung. *Front. Oncol.* 12:949111. doi: 10.3389/fonc.2022.949111

Development and validation of a radiomic nomogram based on pretherapy dual-energy CT for distinguishing adenocarcinoma from squamous cell carcinoma of the lung

Zhiyong Chen[1†], Li Yi[1†], Zhiwei Peng[1], Jianzhong Zhou[2], Zhaotao Zhang[1], Yahong Tao[1], Ze Lin[1], Anjing He[1], Mengni Jin[1] and Minjing Zuo[1*]

[1]Department of Radiology, The Second Affiliated Hospital of Nanchang University, Nanchang, China, [2]Department of Radiology, The Quzhou City People's Hospital, Quzhou, Zhejiang, China

Objective: Based on pretherapy dual-energy computed tomography (DECT) images, we developed and validated a nomogram combined with clinical parameters and radiomic features to predict the pathologic subtypes of non-small cell lung cancer (NSCLC) — adenocarcinoma (ADC) and squamous cell carcinoma (SCC).

Methods: A total of 129 pathologically confirmed NSCLC patients treated at the Second Affiliated Hospital of Nanchang University from October 2017 to October 2021 were retrospectively analyzed. Patients were randomly divided in a ratio of 7:3 (n=90) into training and validation cohorts (n=39). Patients' pretherapy clinical parameters were recorded. Radiomics features of the primary lesion were extracted from two sets of monoenergetic images (40 keV and 100 keV) in arterial phases (AP) and venous phases (VP). Features were selected successively through the intra-class correlation coefficient (ICC) and the least absolute shrinkage and selection operator (LASSO). Multivariate logistic regression analysis was then performed to establish predictive models. The prediction performance between models was evaluated and compared using the receiver operating characteristic (ROC) curve, DeLong test, and Akaike information criterion (AIC). A nomogram was developed based on the model with the best predictive performance to evaluate its calibration and clinical utility.

Results: A total of 87 ADC and 42 SCC patients were enrolled in this study. Among the five constructed models, the integrative model (AUC: Model 4 = 0.92, Model 5 = 0.93) combining clinical parameters and radiomic features had a higher AUC than the individual clinical models or radiomic models (AUC: Model 1 = 0.84, Model 2 = 0.79, Model 3 = 0.84). The combined clinical-venous

phase radiomics model had the best predictive performance, goodness of fit, and parsimony; the area under the ROC curve (AUC) of the training and validation cohorts was 0.93 and 0.90, respectively, and the AIC value was 60.16. Then, this model was visualized as a nomogram. The calibration curves demonstrated it's good calibration, and decision curve analysis (DCA) proved its clinical utility.

Conclusion: The combined clinical-radiomics model based on pretherapy DECT showed good performance in distinguishing ADC and SCC of the lung. The nomogram constructed based on the best-performing combined clinical-venous phase radiomics model provides a relatively accurate, convenient and noninvasive method for predicting the pathological subtypes of ADC and SCC in NSCLC.

KEYWORDS

dual-energy CT, dual-energy CT quantitative parameters, radiomics, lung adenocarcinoma, lung squamous cell carcinoma

1 Introduction

Lung cancer is the second most common cancer worldwide and the leading cause of cancer death (1). Non-small cell lung cancer (NSCLC) accounts for approximately 85% of lung cancers, with adenocarcinoma (ADC) and squamous cell carcinoma (SCC) being the most common subtypes (2, 3). In recent years, the prognosis of some lung cancer patients has improved thanks to the rapid development of individualized medicine and precise therapy, such as targeted therapies and immunotherapy (4–6). However, different pathological subtypes have distinct phenotypic and biological characteristics, which directly affect clinical treatment and outcomes (6–8). For example, bevacizumab has good effects in the treatment of lung adenocarcinoma, but it may lead to a lung squamous cell carcinoma patient bleeding profusely (9). Therefore, it is important to accurately predict pathological subtypes before treatment to establish better therapeutic strategies for NSCLC.

Currently, invasive biopsy for histological confirmation is usually performed before the treatment of NSCLC (9, 10). However, it is difficult to obtain a biopsy for several reasons. First, lung cancer is a heterogeneous tumor, and the tissue obtained from the biopsy of the lung tumor may contain only a few tumor cells and may not reflect the complete biological information (5, 9). Then, tumor samples are difficult to obtain in some patients, ang biopsy is contraindicated, and so on. In addition, biopsy may also increase the potential risk of cancer transmission (11). Therefore, it is necessary to develop a reliable, non-invasive, safe and economical approach to help pretherapy predict the pathological subtypes in NSCLC for treatment decision-making and prognosis estimation in NSCLC patients.

Dual-energy computed tomography (DECT) is a new technology in the field of CT imaging in recent years. It not only shows the morphological features of tumors, but also provides extensive quantitative information (12). Many studies have used DECT for tumor diagnosis and prediction. Zhang et al. (13) found that quantitative parameters based on venous phase DECT, including iodine concentration (IC), normalized iodine concentration (NIC), and slope of the curve (λHU), can effectively distinguish ADC and SCC of the lung. Radiomics analyzes medical images in an automated high-throughput manner and aims to extract quantitative and reproducible tumor information that the human eye cannot distinguish, quantify tumor heterogeneity, and monitor tumor development, progression, and even prognosis (14–17). Many studies have explored the role of radiomics in the pathological classification of NSCLC. Zhu et al. (18) enrolled 129 NSCLC patients for retrospective studies, and the LASSO regression model was constructed by screening 5 radiomic features. The result was that the radiomic features could be used as a diagnostic factor to distinguish the histological subtypes of NSCLC.

To further explore the additional value of the DECT image, some studies combine DECT with radiomics. Liu et al. (19) built and evaluated a pretherapy dual-energy CT-based clinical-radiomics model that can effectively predict the clinical response to systemic chemotherapy in patients with advanced gastric cancer (AGC). However, to our knowledge, the application and potential advantages of DECT-based radiomics in predicting the pathological subtypes of NSCLC have not been explored. Theoretically, DECT contains more information than single-energy CT. Radiomic analysis of DECT

images may extract more features relevant to tumor heterogeneity and biology.

Therefore, the aim of this study was to establish an independent predictive model for predicting the pathological subtypes of NSCLC by combining clinical parameters and DECT-based radiomic features. In addition, we provide a visually quantitative nomogram in clinical practice, as an additional predictive method for patients who cannot obtain pathological subtypes before treatment.

2 Materials and methods

2.1 Patients

Eligible patients with NSCLC treated at the Second Affiliated Hospital of Nanchang University between October 2017 and October 2021 were retrospectively analyzed. This single-center retrospective study was approved by the Ethics Committee of Second Affiliated Hospital of Nanchang University (Ethics Number: 2017061), and the requirement of informed consent was exempted due to the retrospective study design. The inclusion criteria were as follows: 1) all patients had standard DECT plain scan and enhanced scan images; 2) all lesions were examined by DECT within two weeks, and pathological results were confirmed by puncture biopsy, fiberoptic bronchoscopy or surgical resection; 3) lesion diameter >10 mm, and the boundary was clear; and 4) all patients had detailed clinical data, including age, sex, smoking history, etc. Exclusion criteria included the following: 1) patients who have been or are being treated for oncological disease; 2) dense metal or implants interference in the scanning area; and 3) patients who cannot cooperate during scanning and who experience respiratory motion artifacts.

The patient recruitment process is presented in Figure 1. A total of 129 patients were randomly divided at a ratio of 7:3 into training and validation cohorts. The training cohort consisted of 90 patients (ADC 61, SCC 29), whereas the validation cohort consisted of 39 patients (ADC 26, SCC 13).

2.2 Clinical features

The following pretherapy clinical features of each patient were recorded from the medical system: age, sex, smoking status (never, ever/always), carcinoembryonic antigen (CEA) level, and distant metastasis (with/without).

2.3 Dual-energy CT image acquisition

The patient was in the supine position. After breath holding at the end of inhalation, the dual-energy plain scan and dual-

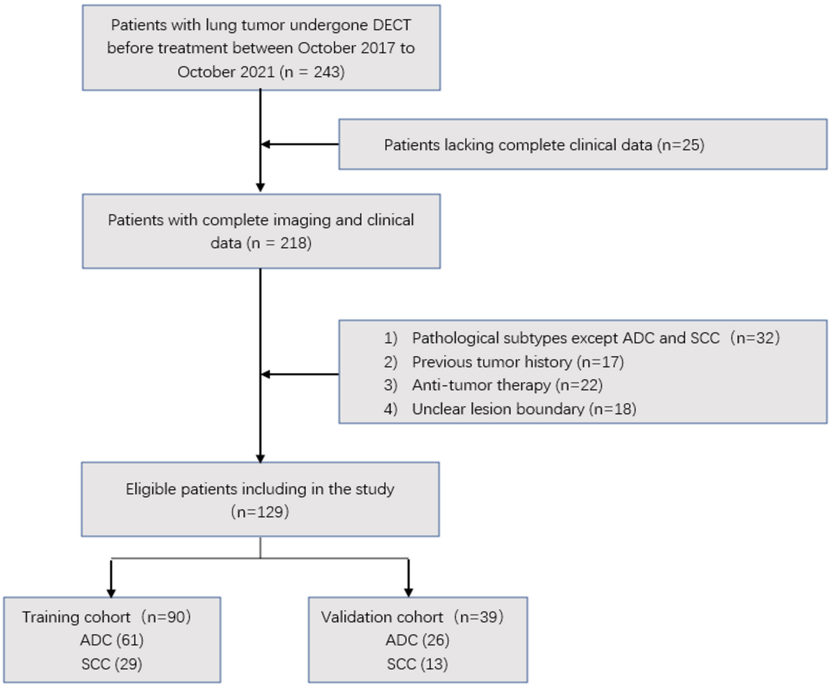

FIGURE 1
Flow chart showing the patient selection and exclusion.

energy enhanced scan in AP and VP were performed from the thoracic inlet to the bottom of the lung.

CT scans were performed in DE mode on a second-generation dual-source CT scanner (SOMATOM Definition FLASH, Siemens Healthcare, Germany). After unenhanced CT was performed, 350 mg I/mL of nonionic iodinated contrast agent (Ioversol) at a dose of 1.2 mL/kg weight was injected into an antecubital vein together with 20 mL of saline at rates of 3 mL/s and 4 mL/s, respectively. AP and VP dual-energy contrast-enhanced CT images were obtained after post-injection delays of 30 and 60 s, respectively. The scan parameters for the DECT mode were summarized as follows. The tube voltages of A and B were set at 100 kVp and 140 kVp, respectively, with a real-time adjustable variable tube current. Collimation was 128 × 0.6 mm; rotation speed was 0.28 s/r; gantry rotation was 330 ms; slice thickness was 5 mm. Finally, 100 kVp and 140 kVp images were acquired in the arterial and venous phases, respectively, and 120 kVp equivalent mixed images were generated (linear fusion coefficient, 0.4). These images were reconstructed with a slice thickness of 1 mm and an interval of 1 mm using iterative reconstruction software (SAFIRE, Siemens Healthcare, Germany).

2.4 Dual energy-CT image analysis

CT Semantic Feature Acquisition: Two radiologists (with five and fifteen years of experience in diagnostic thoracic imaging), blinded to the patient's pathologic data, viewed and analyzed the 120 kVp equivalent hybrid images and obtained CT semantic features of each lesion. Six CT semantic features for each mass were included (1): spiculation sign (2), lobulation sign (3), null vacuole sign (4), tumor location (central/peripheral type) (5), pleural effusion on the tumor side (yes/no), and (6) pericardial effusion (yes/no). If any disagreements arose, final consensus was reached through group discussions.

DECT Quantitative Parameter Acquisition: Data from AP and VP DECT were loaded and postprocessed using specific software (Siemens Healthcare, Germany). The iodine diagram was obtained by the Liver VNC program. Manually, the region of interest (ROI) was drawn as large as possible on the solid part of the primary lesion, avoiding tumor margins, necrosis, cavities, calcifications and large vessels. Then, the iodine concentration (IC, mean value, units of 100 μg/ml) of the lesion was recorded in the ROI. Simultaneously, ROIs were placed in the same slice to obtain the ICs of the aorta. Finally, the normalized iodine concentration (NIC) was calculated according to the following formula: NIC = IC (lesion)/IC (artery). Then, through the Monogenetic program, the CT values of 40 keV and 100 keV single energy images of the solid part of the lesion were recorded. The slope of the spectrum attenuation curves (λHU) was calculated using the following formula: λHU=((CT40KeV-CT100keV)/60). All data were measured three times and averaged.

2.5 Radiomic analysis

2.5.1 Tumor segmentation

The 40-keV and 100-keV monoenergetic images (NIFTI format) reconstructed in AP and VP were imported into the open source software ITK-snap (version 3.8.0, University of Pennsylvania, USA, http://www.itksnap.org). A radiologist (with five years of experience in diagnostic thoracic imaging) performed semi-automatic or manual combined semi-automatic layer-by-layer segmentation of the lung window.

2.5.2 Feature extraction

Artificial Intelligence Kit software (A.K. Software; GE Healthcare, China) was used to extract the radiomics features from each ROI. A total of 107 features were extracted including first-order statistical features, shape features, and texture features. In addition, the software provides a variety of options to standardize image preprocessing before feature extraction. The extracted features were reproducible and based on the benchmarks of the image biomarker standardization initiative (IBSI).

2.5.3 Feature selection

To assess segmentation variability, 20 patients were randomly selected and re-segmented after one month by the same two radiologists. The inter- and intra-observer reproducibility of tumor segmentation was assessed by intraclass correlation coefficients (ICCs). The features with an ICC greater than 0.75 are defined as having good repeatability. After selecting the repeatable features based on ICC, the LASSO algorithm was applied to select the most useful predictive features in the training cohort.

2.5.4 Radiomics model establishment

Radiomics models were established by multivariable logistic regression analysis of radiomic features selected in the images from AP and VP DECT. Radiomic signatures, also called the radiomic score (Rad-score), were calculated separately for the training and validation cohorts in the AP and VP *via* a linear combination of selected features weighted by their respective coefficients in the model.

2.6 Clinical model and nomogram establishment

Clinical features, CT semantic features, and DECT quantification parameters are collectively referred to as clinical parameters in this study.

Univariate analysis was performed for candidate clinical parameters. The significant variables (p value < 0.05) in the univariable analysis were then introduced into stepwise logistic

regression analyses. The independent clinical predictors were determined and the clinical model was established. Then, the selected clinical predictors were combined with the radiomic signatures of the arterial and venous phases to establish two combination models. To visualize the prediction results of the model for ADC and SCC, the nomogram was developed based on the model with the best performance.

2.7 Evaluation and comparison of model performance

Evaluation of the model included discrimination, calibration, and clinical utility. Receiver operating characteristic (ROC) curve analysis was used to evaluate the predictive performance of each model. The Delong test was used to compare the difference in the area under the curve (AUC) between different models. The Akaike information criterion (AIC) is used to compare the goodness of fit and parsimony between models. Calibration curves were constructed to describe calibration performance based on the agreement between predicted and actual response probabilities. Decision curve analysis (DCA) was used to determine the value of the predictive model for clinical application and to determine the net benefit to patients at each threshold probability.

2.8 Statistical analysis

IBM SPSS 25.0 (IBM, Armonk, NY, USA) software was used for statistical analysis of clinical parameters: Normality of distribution of continuous variables was tested using a Kolmogorov–Smirnov test; independent samples t-test (or Mann-Whitney U-test) for continuous variables and chi-square test for categorical variables.

Other statistical analyses were conducted with R (version 4.1.2, http://www.r-project.org) software. The "MASS" package was used for stepwise logistic regression to further filter clinical features. The "glmnet" package was used for lasso logistic regression to filter radiomic features and multiple logistic regression to build models. The "pROC" package was used for plotting ROC curves and calculating AUC values and related indicators. And the "rms" package was used for drawing nomograms and calibration curves. The Delong test was used for comparison between models, and the Akaike information criterion (AIC) was used for model ranking and selection. Two-sided p values < 0.05 indicate statistical significance.

3 Results

3.1 Clinical parameters

A total of 129 NSCLC patients, including 87 ADC patients and 42 SCC patients, were enrolled in this study. After univariate analysis, eight clinical parameters, including age, sex, smoking status, spiculation sign, tumor location (central/peripheral type), distant metastasis (with/without), NIC and λ HU in the VP, were significantly associated with the pathological subtypes of NSCLC ($p < 0.05$; the results of univariate analysis of patients' clinical parameters are shown in Table 1). Subsequently, three of these parameters (sex, distant metastasis, and NIC in the VP) were selected using stepwise logistic analysis to form the clinical model (related data in eTable 1 in the Supplementary Materials).

3.2 Radiomic features selection and radiomic signature building

The workflow of tumor segmentation, feature extraction and selection, model establishment and evaluation is illustrated in Figure 2. A total of 107 features were extracted from the reconstructed 40 keV and 100 keV monoenergetic images from AP and VP DECT for each patient, respectively. Excluding features with low reproducibility according to ICC (intra- and inter-observer ICC <0.75, ICC results are shown in eTable 2 in the Supplementary Materials). Thus, the numbers of 40 keV and 100 keV in the AP (AP40 keV, AP100 keV), and 40 keV and 100 keV in the VP (VP40 keV, VP100 keV) features were reduced to 76, 78, 86 and 84 respectively. Then, the LASSO algorithm was used to exclude redundant features. This left 2, 3, 5, and 5 features at AP 40 keV, AP 100 keV, VP 40 keV, and VP 100 keV respectively (eTable 3 in the Supplementary Materials). Finally, the five features selected from 40-keV and 100-keV DECT images in AP were combined, and the radiomic signature based on AP (rad-score AP) was established by multivariate logistic regression analysis in the training cohort. The same method was used to establish the radiomic signature based on VP (rad-scoreVP). The radiomic score calculation formula is presented in eTable 1 in the Supplementary Materials.

3.3 Prediction model establishment and evaluation of model performance

All models were established by multivariate logistic regression analysis.

TABLE 1 Clinical parameters of patients.

Variables	Training cohort (n =90)		P	Validation cohort (n = 39)		P
	ADC (n=61)	SCC (n=29)		ADC (n=26)	SCC (n=13)	
Age (year)	62.03 ± 9.06	66.27 ± 8.97	0.040	60.08 ± 9.96	63.62 ± 9.81	0.300
Gender			<0.001*			0.022*
Male	30	28		11	12	
Female	31	1		15	1	
Smoking			<0.001*			0.029*
Never	15	15		7	9	
Ever/Always	46	10		19	4	
Spiculation			0.004*			0.307
Yes	48	13		16	5	
No	13	14		10	8	
lobulation			0.930			0.397
Yes	53	25		24	10	
No	8	4		2	3	
null Vacuole			0.628			0.687
Yes	12	7		7	2	
No	49	22		19	11	
tumor location			0.030*			0.687
Peripheral	53	25		24	10	
Central	8	4		2	3	
pleural effusion on the tumor side			0.738			0.852
Yes	5	3		2	2	
No	56	26		24	11	
pericardial effusion			0.274			0.608
Yes	5	0		1	1	
No	56	29		25	12	
distant metastasis			0.016*			0.420
Yes	21	3		7	2	
No	40	26		19	11	
CEA(ug/L)	3.18 (1.76,9.90)	2.60 (2.02,5.20)	0.610	2.33 (1.63,5.50)	3.28 (1.37,4.37)	0.532
NIC_{AP}	0.09 (0.04,0.18)	0.08 (0.01,0.14)	0.223	0.12 (0.05,0.20)	0.05 (0.03,0.12)	0.136
λHU_{AP}	1.39 ± 1.03	1.14 ± 1.02	0.267	1.86 ± 1.40	1.01 ± 0.65	0.044*
NIC_{VP}	0.28 (0.16,0.46)	0.19 (0.08,0.33)	0.019*	0.37 (0.21,0.47)	0.17 (0.03,0.23)	0.003*
λHU_{VP}	1.88 ± 1.07	1.21 ± 0.82	0.004*	2.17 ± 1.13	0.96 ± 0.69	0.001*

Data are the proportion of sample size, mean value ± SD or median (interquartile range). P values were the results of univariate analysis of each parameter, *p < 0.05.
AP, arterial phase; VP, venous phase.

Clinical model: The clinical model (Model 1) consisted of three clinical parameters (sex, distant metastasis, and NIC in the VP). The AUCs of the training and validation cohorts were 0.84 (95% CI 0.75-0.93) and 0.87 (95% CI 0.77-0.98) respectively.

Radiomics model: The AUCs for the radiomics model in AP (Model 2) and the radiomics model in VP (Model 3) in the training cohort were 0.79 (95% CI 0.69-0.89) and 0.84 (95% CI 0.75-0.93), respectively; in the validation cohort, they were 0.78 (95% CI 0.63-0.93) and 0.80 (95% CI 0.64-0.95), respectively. Compared with AP, the AUC of the VP radiomics model was higher, but there was no significant difference between the 2 AUCs (Delong test, P = 0.067).

Combined model: The combined clinical-arterial phase radiomics model (Model 4) and the combined clinical-venous phase radiomics model (Model 5) were established by combining the clinical parameters with the radiomic features

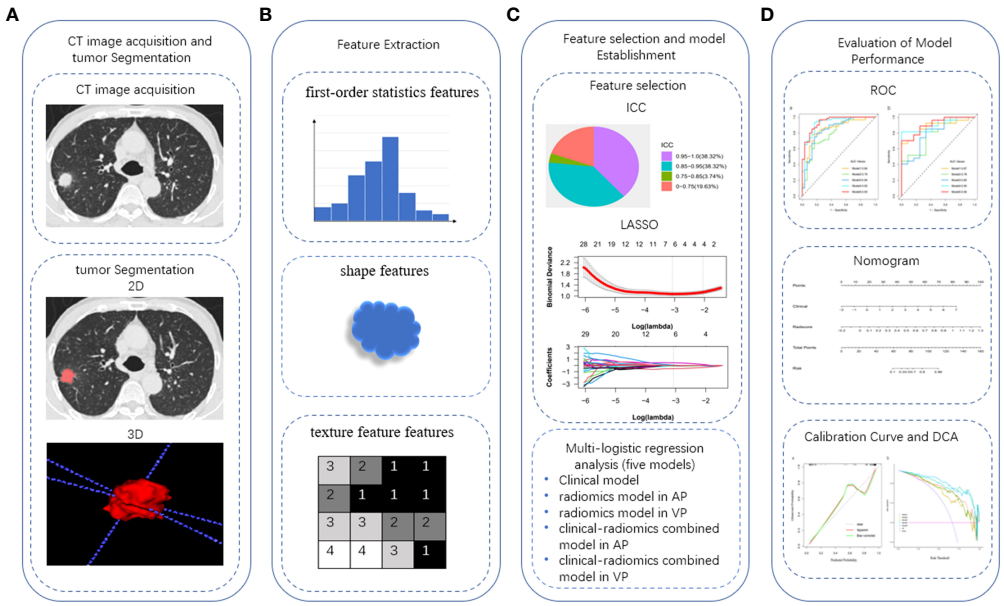

FIGURE 2
Work flow of tumor segmentation, feature extraction and signature building. ICC, intra-class correlation coefficient; LASSO, the least absolute shrinkage and selection operator; ROC, receiver operating characteristic; DCA, decision curve analysis.

of AP and VP, respectively. The AUC values were 0.92 (0.86-0.98) and 0.93 (0.88-0.98) in the training cohort and 0.90 (0.81-0.99) and 0.90 (0.81-0.99) in the validation cohort.

The results showed that the predictive performance of the combined model was significantly higher than that of the single radiomic or clinical model (DeLong test, $p > 0.05$ for each comparison). The combined clinical-venous phase radiomics model (Model 5) had the best predictive performance (AUC: training cohort 0.93, validation cohort 0.90), but there was no significant difference in AUC between Model 5 and Model 4 (DeLong test, p=0.384). In addition, the Akaike information criterion (AIC) was introduced to evaluate the goodness and parsimony of fit of the model, and Model 5 achieved the lowest AIC value at 60.16 among all prediction models. Based on the overall consideration of ROC curves and AIC, Model 5 was proven to have the best predictive performance, good goodness of fit and parsimony. The ROC curves, detailed performance and AIC values of the five models are illustrated in Figure 3 and Table 2. The result of the DeLong test is given in Table 3.

3.4 Development and performance evaluation of the nomogram

Based on the above results, Model 5 with the best prediction efficiency was selected and visualized as a nomogram for individualized patient prediction. Multivariate logistic regression analysis showed that the clinical signature (odds ratio (OR) = 1.11; 95% CI, 1.07 to 1.16; $p < 0.001$) and radiomic signature (odds ratio (OR) = 2.21; 95% CI, 1.68 to 2.90; $p < 0.001$) represented independent predictors in the nomogram (eTable 4 in the Supplementary Materials).

As shown in the nomogram (Figure 4), the radiological signature accounted for the largest proportion compared with the clinical signature, making it the most important biomarker for distinguishing ADC from SCC. In clinical practice, based on the obtained features, the clinical signature and radiomic signature can be calculated using the formula. Then, the probability of the predictive variable was converted into a fraction corresponding to the first scale "point" at the top of the nomogram. After adding up the corresponding prediction probability, the risk of ADC was at the bottom of the nomogram.

The calibration curves (Figure 5A) of the nomogram demonstrated good agreement between the nomogram prediction and the actual observation. A nonsignificant difference in the accompanied Hosmer–Lemeshow test (p=0.384) indicated that the nomogram was adequately calibrated without departure from the ideal fit. DCAs (Figure 5B) were used to evaluate the clinical utility of the five predictive models by calculating the net benefit at various probability thresholds. According to the decision curves, Model 5 was the most reliable clinical treatment tool for

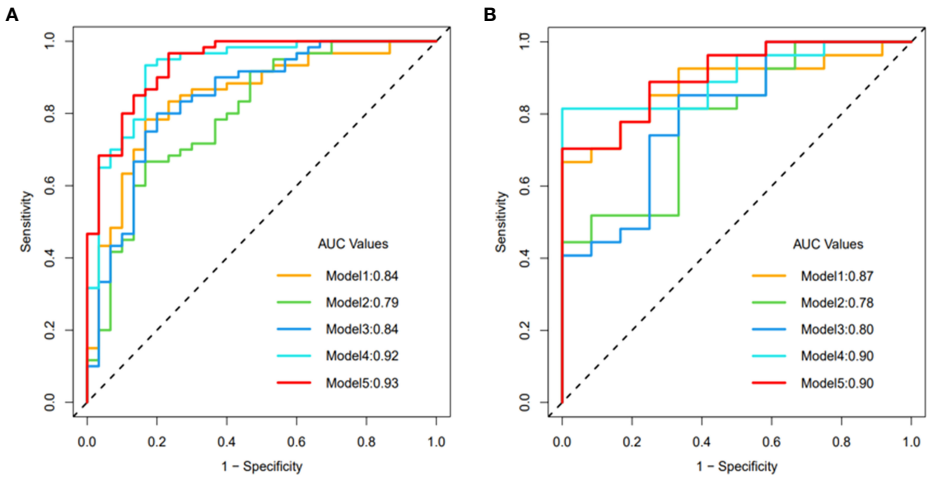

FIGURE 3
ROC curve of model 1-5: **(A)** training cohort, **(B)** validation cohort.

predicting pathologic subtypes in NSCLC when the probability threshold was above 0.25 in a patient's or physician's clinical decision.

4 Discussion

In this study, we successfully developed and validated a combined clinical-radiomics model based on DECT, which has excellent performance in noninvasively stratifying the pathological subtypes of NSCLC patients. Furthermore, we visualized this model as a nomogram and demonstrated the excellent performance of the nomogram by high AUC and low AIC. DCAs indicated that the nomogram is a reliable clinical treatment decision support tool for personalized prediction of the pathological subtypes of NSCLC patients.

Different pathological subtypes lead to different clinical treatment strategies and prognoses for NSCLC patients (20–22). Dual-energy imaging improves image quality to some degree, expands the capabilities of traditional CT, and has the potential to improve lesion detection and characterization (23–25).Several previous studies have combined DECT with radiomics or texture analysis (26–29). However, most feature extractions are based on virtual monoenergetic, 120 kV equivalent hybrid images or iodine images. Recently, some researchers have demonstrated in their studies that radiomic models based on multi-energy images can more effectively support the diagnosis and prediction of tumors compared with clinical and monoenergetic models As demonstrated by Liu et al. (19), the radiomics model based on multi-energy images can better predict the clinical response of systemic chemotherapy in advanced gastric cancer (AGC) compared to clinical and

TABLE 2 Prediction performance of model 1-5.

Cohort	Model	AUC (95%CI)	SEN	SPE	ACC	PPV	NPV	AIC
Training cohort	Model 1	0.84(0.75-0.93)	0.78	0.83	0.80	0.93	0.66	88.87
	Model 2	0.79(0.69-0.89)	0.66	0.83	0.72	0.88	0.65	90.81
	Model 3	0.84(0.75-0.93)	0.80	0.80	0.79	0.88	0.66	83.36
	Model 4	0.92(0.86-0.98)	0.93	0.83	0.90	0.91	0.86	64.06
	Model 5	0.93(0.88-0.98)	0.96	0.76	0.90	0.89	0.92	60.14
Validation cohort	Model 1	0.87 (0.77-0.98)	0.66	1.00	0.82	1.00	0.63	—
	Model 2	0.78 (0.63-0.93)	0.81	0.66	0.76	0.84	0.61	—
	Model 3	0.80(0.64-0.95)	0.85	0.66	0.79	0.85	0.66	—
	Model 4	0.90(0.81-0.99)	0.81	1.00	0.87	1.00	0.70	—
	Model 5	0.91(0.81-0.99)	0.70	1.00	0.79	1.00	0.60	—

AUC, area under the curve; CI, confidence interval; SEN, sensitivity; SPE, specificity; ACC, accuracy; PPV, positive predictive value; NPV, negative predictive value; AIC, Akaike information criterion.

10.3389/fonc.2022.949111

TABLE 3 Delong test between models 1-5.

Model 1	1				
Model 2	0.500	1			
Model 3	0.945	0.067	1		
Model 4	0.035*	0.003*	0.036*	1	
Model 5	0.016*	0.001*	0.009*	0.348	1
	Model 1	Model 2	Model 3	Model 4	Model 5

*P<0.05.

monoenergetic models. This study extracts the radiomics features from DECT multi-energy images and jointly constructs the model, which proves that the image radiomics features extracted from DECT multi-energy images can reflect the heterogeneity of NSCLC. Radiomics may serve as a promising technique to predict the pathological subtypes of NSCLC.

Among the clinical features selected in the combined model, SCC is more common in males, and this sex difference among NSCLC patients has been widely reported (30, 31). Distant metastasis is more common in patients with ADC than in those with SCC, which is also consistent with the biological characteristics that lung adenocarcinoma is prone to early hematogenous metastasis. In addition, the results of univariate and multivariate analyses in this study showed that NICVP was also an important clinical predictor. In enhanced DECT, IC represents iodine deposition in tissue. The quantification of IC can reflect the microvessel density (MVD) and perfusion of the tumor (32–34). In this study, the NIC of adenocarcinoma was higher than that of squamous cell carcinoma, indicating that the MVD of adenocarcinoma was greater, which is consistent with the results of previous pathological studies (35, 36). Moreover, this result was significantly different in the venous phase but not in the arterial phase. This may be due to the different microvessel densities and vascular permeabilities of different subtypes of tumors, resulting in different times of iodine contrast agent penetration into the intercellular space. This is consistent with the results of a previous study by Zhang et al (13).

In terms of image selection, in DECT scanning, due to the high X-ray attenuation at lower energy levels, when the photon energy gradually decreases from 100 keV to 40 keV, the contrast of the iodized structure gradually increases, but it is also accompanied by an increase in image noise at lower energy levels (37). Therefore, we selected 120 kV equivalent hybrid images with both high contrast and low background noise in evaluating the semantic features of CT lesions (38). In terms of monoenergetic selection for radiomics model establishment, we chose a 100 KeV image with fine detail but low contrast, and a 40 KeV image with higher contrast but more noise. As a result, the AUC of the multi-energy image-based radiomics model was 0.79 and 0.84 in the AP and VP, respectively. This shows that the combination of different energy images can deeply mine tumor information and effectively distinguish ADC from SCC.

In terms of radiomic features, three types of radiomic features were extracted: 1) “First-order statistics: Energy”, describing the overall density of the tumor volume; 2) “Shape: Compactness”, quantifying the compactness of the tumor volume relative to that of a sphere (i.e., the most compact shape); and 3) “texture features: spatial arrangement relationship between voxel gray levels”, describing intra-tumor heterogeneity (39, 40). Among the features we selected, compared with the AP, the VP increased the first-order statistics features (original first-order kurtosis, original first-order skewness), and the first-order statistics features reflected the overall density of the tumor. We believe that this is also related to the different MVD and vascular permeability of

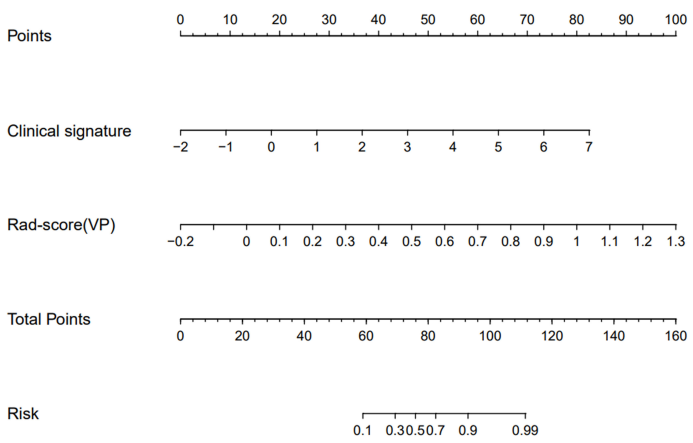

FIGURE 4
Nomogram based on the clinical signature and radiomic signature in venous phase to predict the pathological subtypes of NSCLC patients.

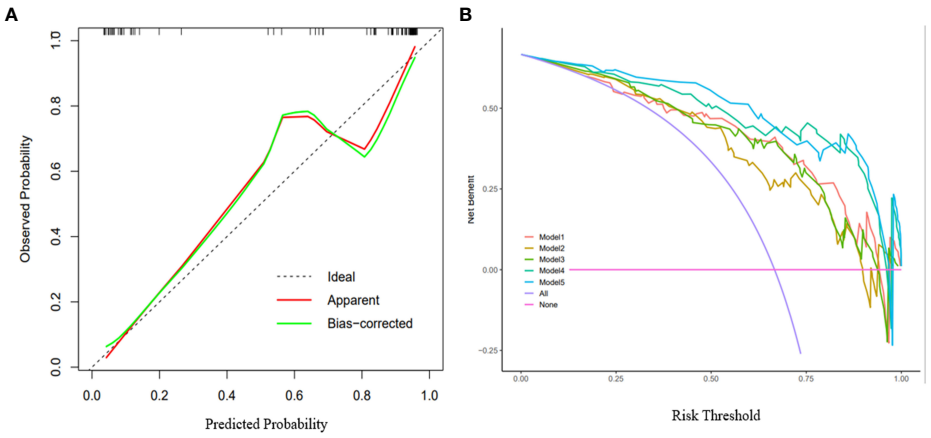

FIGURE 5
Calibration curves and decision curve analysis of the nomogram. **(A)** Calibration curves of the nomogram: The X-axis represented the predicted probability estimated by nomogram, whereas the Y-axis represented the actual observed rates. the red line represented the apparent prediction of nomogram, the green line represented the fitting line after bias-corrected. the dashed line represented the ideal estimation. Calibration curves showed the actual probability is relatively close to the prediction of nomogram. **(B)** Decision curve analysis for the models 1-5: The X-axis represented the threshold probability that was where the expected benefit of treatment was equal to the expected benefit of avoiding treatment. The Y-axis represented the net benefit. The purple line represents the hypothesis that all patients are ADC, and the red line represents the hypothesis that all patients are SCC. Other curves are shown in the figure, representing models 1-5 in turn.

different subtypes of tumors, which may also lead to the slightly lower AUC in the AP-based model than VP.

Our study had some limitations. First, it is a retrospective study at a single center, which may lead to patient selection bias, and the number of samples is limited. Future plans include collaboration with other dual-energy CT centers to reduce bias and expand the sample size. Second, the previous radiomics model developed by He et al. (41) for the differential diagnosis of solitary pulmonary nodules showed better differential diagnosis performance based on the radiomics features of plain CT images than those of contrast-enhanced CT images. This study lacks a radiomics model based on plain CT. In the future, it is expected to build a radiomics model based on DECT plain scans to mine tumor features more comprehensively and improve the performance of the model. Finally, semi-automatic or semiautomatic and manual combined segmentation of lesions is time-consuming and variable. In the future, it is expected to combine radiomics with machine learning or deep learning to create better models.

5 Conclusion

In this study, we developed and validated a combined clinical-radiomics model based on pretherapy DECT to reliably predict ADC and SCC. Compared with the traditional single clinical model, the combined model significantly improved the prediction performance of ADC and SCC. The combined clinical-venous phase radiomics model was visualized as a nomogram, which could provide a relatively accurate, convenient, and noninvasive method for the individualized discrimination of ADC from SCC in NSCLC patients and assist in clinical decision-making.

Data availability statement

The raw data supporting the conclusions of this article will be made available by the authors, without undue reservation.

Ethics statement

The studies involving human participants were reviewed and approved by The Second Affiliated Hospital of Nanchang University Medical Research Ethics Committee. Written informed consent for participation was not required for this

study in accordance with the national legislation and the institutional requirements.

Author contributions

MZ and ZC designed the study. ZC and JZ collected and classified the data. ZC, LY, ZZ, and ZP did the statistical analysis. YT, AH, ZL, and MJ made substantial revisions to the manuscript. All authors contributed to the article and approved the submitted version.

Funding

This study was supported by Jiangxi Provincial Education Department Key Projects (grant number GJJ200106).

Acknowledgments

We thank the Patient for his kind cooperation.

Conflict of interest

The authors declare that the research was conducted in the absence of any commercial or financial relationships that could be construed as a potential conflict of interest.

Publisher's note

Supplementary material

The Supplementary Material for this article can be found online at: https://www.frontiersin.org/articles/10.3389/fonc.2022.949111/full#supplementary-material

References

1. Sung H, Ferlay J, Siegel RL, Laversanne M, Soerjomataram I, Jemal A, et al. Global cancer statistics 2020: GLOBOCAN estimates of incidence and mortality worldwide for 36 cancers in 185 countries. *CA Cancer J Clin* (2021) 71(3):209–49. doi: 10.3322/caac.21660

2. Schabath MB, Cote ML. Cancer progress and priorities: Lung cancer. *Cancer Epidemiol Biomarkers Prev* (2019) 28(10):1563–79. doi: 10.1158/1055-9965.EPI-19-0221

3. Ren C, Zhang J, Qi M, Zhang J, Zhang Y, Song S, et al. Machine learning based on clinico-biological features integrated (18)F-FDG PET/CT radiomics for distinguishing squamous cell carcinoma from adenocarcinoma of lung. *Eur J Nucl Med Mol Imaging.* (2021) 48(5):1538–49. doi: 10.1007/s00259-020-05065-6

4. Hirsch FR, Scagliotti GV, Mulshine JL, Kwon R, Curran WJ Jr, Wu YL, et al. Lung cancer: Current therapies and new targeted treatments. *Lancet* (2017) 389 (10066):299–311. doi: 10.1016/S0140-6736(16)30958-8

5. Osmani L, Askin F, Gabrielson E, Li QK. Current WHO guidelines and the critical role of immunohistochemical markers in the subclassification of non-small cell lung carcinoma (NSCLC): Moving from targeted therapy to immunotherapy. *Semin Cancer Biol* (2018) 52(Pt 1):103–9. doi: 10.1016/j.semcancer.2017.11.019

6. Thomas A, Liu SV, Subramaniam DS, Giaccone G. Refining the treatment of NSCLC according to histological and molecular subtypes. *Nat Rev Clin Oncol* (2015) 12(9):511–26. doi: 10.1038/nrclinonc.2015.90

7. Detterbeck FC, Boffa DJ, Kim AW, Tanoue LT. The eighth edition lung cancer stage classification. *Chest* (2017) 151(1):193–203. doi: 10.1016/j.chest.2016.10.010

8. Jotte RM, Spigel DR. Advances in molecular-based personalized non-small-cell lung cancer therapy: Targeting epidermal growth factor receptor and mechanisms of resistance. *Cancer Med* (2015) 4(11):1621–32. doi: 10.1002/cam4.506

9. Cadioli A, Rossi G, Costantini M, Cavazza A, Migaldi M, Colby TV. Lung cancer histologic and immunohistochemical heterogeneity in the era of molecular therapies: Analysis of 172 consecutive surgically resected, entirely sampled pulmonary carcinomas. *Am J Surg Pathol* (2014) 38(4):502–9. doi: 10.1097/PAS.0000000000000154

10. Beslic S, Zukic F, Milisic S. Percutaneous transthoracic CT guided biopsies of lung lesions; fine needle aspiration biopsy versus core biopsy. *Radiol Oncol* (2012) 46(1):19–22. doi: 10.2478/v10019-012-0004-4

11. Kong YC, Bhoo-Pathy N, O'Rorke M, Subramaniam S, Bhoo-Pathy NT, See MH, et al. The association between methods of biopsy and survival following breast cancer: A hospital registry based cohort study. *Med (Baltimore).* (2020) 99(6): e19093. doi: 10.1097/MD.0000000000019093

12. Goo HW, Goo JM. Dual-energy CT: New horizon in medical imaging. *Korean J Radiol* (2017) 18(4):555–69. doi: 10.3348/kjr.2017.18.4.555

13. Zhang Z, Zou H, Yuan A, Jiang F, Zhao B, Liu Y, et al. A single enhanced dual-energy CT scan may distinguish lung squamous cell carcinoma from adenocarcinoma during the venous phase. *Acad Radiol* (2020) 27(5):624–9. doi: 10.1016/j.acra.2019.07.018

14. Dong D, Fang MJ, Tang L, Shan XH, Gao JB, Giganti F, et al. Deep learning radiomic nomogram can predict the number of lymph node metastasis in locally advanced gastric cancer: An international multicenter study. *Ann Oncol* (2020) 31 (7):912–20. doi: 10.1016/j.annonc.2020.04.003

15. Dong D, Tang L, Li ZY, Fang MJ, Gao JB, Shan XH, et al. Development and validation of an individualized nomogram to identify occult peritoneal metastasis in patients with advanced gastric cancer. *Ann Oncol* (2019) 30(3):431–8. doi: 10.1093/annonc/mdz001

16. Ligero M, Garcia-Ruiz A, Viaplana C, Villacampa G, Raciti MV, Landa J, et al. A CT-based radiomics signature is associated with response to immune checkpoint inhibitors in advanced solid tumors. *Radiology* (2021) 299(1):109–19. doi: 10.1148/radiol.2021200928

17. Mayerhoefer ME, Materka A, Langs G, Häggström I, Szczypiński P, Gibbs P, et al. Introduction to radiomics. *J Nucl Med* (2020) 61(4):488–95. doi: 10.2967/jnumed.118.222893

18. Zhu X, Dong D, Chen Z, Fang M, Zhang L, Song J, et al. Radiomic signature as a diagnostic factor for histologic subtype classification of non-small cell lung cancer. *Eur Radiol* (2018) 28(7):2772–8. doi: 10.1007/s00330-017-5221-1

19. Liu YY, Zhang H, Wang L, Lin SS, Lu H, Liang HJ, et al. Predicting response to systemic chemotherapy for advanced gastric cancer using pre-treatment dual-energy CT radiomics: A pilot study. *Front Oncol* (2021) 11:740732. doi: 10.3389/fonc.2021.740732

20. McAleese J, Taylor A, Walls GM, Hanna GG. Differential relapse patterns for non-small cell lung cancer subtypes adenocarcinoma and squamous cell carcinoma: Implications for radiation oncology. *Clin Oncol (R Coll Radiol).* (2019) 31(10):711–9. doi: 10.1016/j.clon.2019.07.008

21. Yuan C, Tao X, Zheng D, Pan Y, Ye T, Hu H, et al. The lymph node status and histologic subtypes influenced the effect of postoperative radiotherapy on patients with N2 positive IIIA non-small cell lung cancer. *J Surg Oncol* (2019) 119 (3):379–87. doi: 10.1002/jso.25308

22. Abel S, Hasan S, White R, Schumacher L, Finley G, Colonias A, et al. Stereotactic ablative radiotherapy (SABR) in early stage non-small cell lung cancer: Comparing survival outcomes in adenocarcinoma and squamous cell carcinoma. *Lung Cancer.* (2019) 128:127–33. doi: 10.1016/j.lungcan.2018.12.022

23. Rassouli N, Chalian H, Rajiah P, Dhanantwari A, Landeras L. Assessment of 70-keV virtual monoenergetic spectral images in abdominal CT imaging: A comparison study to conventional polychromatic 120-kVp images. *Abdom Radiol (NY).* (2017) 42(10):2579–86. doi: 10.1007/s00261-017-1151-2

24. Silva AC, Morse BG, Hara AK, Paden RG, Hongo N, Pavlicek W. Dual-energy (spectral) CT: Applications in abdominal imaging. *Radiographics* (2011) 31 (4):1031–46. doi: 10.1148/rg.314105159

25. Stiller W, Schwarzwaelder CB, Sommer CM, Veloza S, Radeleff BA, Kauczor HU. Dual-energy, standard and low-kVp contrast-enhanced CT-cholangiography: A comparative analysis of image quality and radiation exposure. *Eur J Radiol* (2012) 81(7):1405–12. doi: 10.1016/j.ejrad.2011.03.030

26. Reinert CP, Krieg EM, Bösmüller H, Horger M. Mid-term response assessment in multiple myeloma using a texture analysis approach on dual energy-CT-derived bone marrow images - a proof of principle study. *Eur J Radiol* (2020) 131:109214. doi: 10.1016/j.ejrad.2020.109214

27. Zhou Y, Su GY, Hu H, Tao XW, Ge YQ, Si Y, et al. Radiomics from primary tumor on dual-energy CT derived iodine maps can predict cervical lymph node metastasis in papillary thyroid cancer. *Acad Radiol* (2022) 29 Suppl 3:S222–s31. doi: 10.1016/j.acra.2021.06.014

28. Wang L, Zhang Y, Chen Y, Tan J, Wang L, Zhang J, et al. The performance of a dual-energy CT derived radiomics model in differentiating serosal invasion for advanced gastric cancer patients after neoadjuvant chemotherapy: Iodine map combined with 120-kV equivalent mixed images. *Front Oncol* (2020) 10:562945. doi: 10.3389/fonc.2020.562945

29. Zhou Y, Su GY, Hu H, Ge YQ, Si Y, Shen MP, et al. Radiomics analysis of dual-energy CT-derived iodine maps for diagnosing metastatic cervical lymph nodes in patients with papillary thyroid cancer. *Eur Radiol* (2020) 30(11):6251–62. doi: 10.1007/s00330-020-06866-x

30. Harichand-Herdt S, Ramalingam SS. Gender-associated differences in lung cancer: Clinical characteristics and treatment outcomes in women. *Semin Oncol* (2009) 36(6):572–80. doi: 10.1053/j.seminoncol.2009.10.007

31. Caldarella A, Crocetti E, Comin CE, Janni A, Pegna AL, Paci E. Gender differences in non-small cell lung cancer: A population-based study. *Eur J Surg Oncol* (2007) 33(6):763–8. doi: 10.1016/j.ejso.2007.01.001

32. Deniffel D, Sauter A, Fingerle A, Rummeny EJ, Makowski MR, Pfeiffer D. Improved differentiation between primary lung cancer and pulmonary metastasis by combining dual-energy CT-derived biomarkers with conventional CT attenuation. *Eur Radiol* (2021) 31(2):1002–10. doi: 10.1007/s00330-020-07195-9

33. Ren Y, Jiao Y, Ge W, Zhang L, Hua Y, Li C, et al. Dual-energy computed tomography-based iodine quantitation for response evaluation of lung cancers to Chemoradiotherapy/Radiotherapy: A comparison with fluorine-18 fluorodeoxyglucose positron emission Tomography/Computed tomography-based positron emission Tomography/Computed tomography response evaluation criterion in solid tumors. *J Comput Assist Tomogr* (2018) 42(4):614–22. doi: 10.1097/RCT.0000000000000734

34. Muenzel D, Lo GC, Yu HS, Parakh A, Patino M, Kambadakone A, et al. Material density iodine images in dual-energy CT: Detection and characterization of hypervascular liver lesions compared to magnetic resonance imaging. *Eur J Radiol* (2017) 95:300–6. doi: 10.1016/j.ejrad.2017.08.035

35. Zieliński KW, Kulig A. Morphology of the microvascular bed in primary human carcinomas of lung. part I: Three–dimensional pattern of microvascular network. *Pathol Res Pract* (1984) 178(3):243–50. doi: 10.1016/S0344-0338(84)80106-5

36. Yuan A, Yu CJ, Kuo SH, Chen WJ, Lin FY, Luh KT, et al. Vascular endothelial growth factor 189 mRNA isoform expression specifically correlates with tumor angiogenesis, patient survival, and postoperative relapse in non-small-cell lung cancer. *J Clin Oncol* (2001) 19(2):432–41. doi: 10.1200/JCO.2001.19.2.432

37. Kaza RK, Caoili EM, Cohan RH, Platt JF. Distinguishing enhancing from nonenhancing renal lesions with fast kilovoltage-switching dual-energy CT. *AJR Am J Roentgenol.* (2011) 197(6):1375–81. doi: 10.2214/AJR.11.6812

38. Li Q, Tan H, Lv F. Molecular characterization of solitary pulmonary nodules in dual-energy CT nonlinear image fusion technology. *J Recept Signal Transduct Res* (2022) 42(1):95–9. doi: 10.1080/10799893.2020.1853158

39. Leijenaar RT, Carvalho S, Hoebers FJ, Aerts HJ, van Elmpt WJ, Huang SH, et al. External validation of a prognostic CT-based radiomic signature in oropharyngeal squamous cell carcinoma. *Acta Oncol* (2015) 54(9):1423–9. doi: 10.3109/0284186X.2015.1061214

40. de Jong EEC, van Elmpt W, Rizzo S, Colarieti A, Spitaleri G, Leijenaar RTH, et al. Applicability of a prognostic CT-based radiomic signature model trained on stage I-III non-small cell lung cancer in stage IV non-small cell lung cancer. *Lung Cancer.* (2018) 124:6–11. doi: 10.1016/j.lungcan.2018.07.023

41. He L, Huang Y, Ma Z, Liang C, Liang C, Liu Z. Effects of contrast-enhancement, reconstruction slice thickness and convolution kernel on the diagnostic performance of radiomics signature in solitary pulmonary nodule. *Sci Rep* (2016) 6:34921. doi: 10.1038/srep34921

frontiers | Frontiers in Oncology

TYPE Original Research
PUBLISHED 07 December 2022
DOI 10.3389/fonc.2022.991948

OPEN ACCESS

EDITED BY
Jiansong Ji,
Lishui Central Hospital, China

REVIEWED BY
Ming Xu,
The First Affiliated Hospital of Sun Yat-sen University, China
Lian-Ming Wu,
Shanghai Jiao Tong University, China

*CORRESPONDENCE
Xinhua Ye
ultrasoundye@163.com
Pingyang Zhang
zhpy28@126.com

†These authors have contributed equally to this work and share first authorship

SPECIALTY SECTION
This article was submitted to Cancer Imaging and Image-directed Interventions, a section of the journal Frontiers in Oncology

RECEIVED 12 July 2022
ACCEPTED 14 November 2022
PUBLISHED 07 December 2022

CITATION
Deng H, Zhou Y, Lu W, Chen W, Yuan Y, Li L, Shu H, Zhang P and Ye X (2022) Development and validation of nomograms by radiomic features on ultrasound imaging for predicting overall survival in patients with primary nodal diffuse large B-cell lymphoma. *Front. Oncol.* 12:991948. doi: 10.3389/fonc.2022.991948

Development and validation of nomograms by radiomic features on ultrasound imaging for predicting overall survival in patients with primary nodal diffuse large B-cell lymphoma

Hongyan Deng[1†], Yasu Zhou[1†], Wenjuan Lu[1], Wenqin Chen[1], Ya Yuan[1], Lu Li[1], Hua Shu[1], Pingyang Zhang[2*] and Xinhua Ye[1*]

[1]Department of Ultrasound, The First Affiliated Hospital of Nanjing Medical University, Nanjing, Jiangsu, China, [2]Department of Cardiovascular Ultrasound, Nanjing First Hospital, Nanjing Medical University, Nanjing, Jiangsu, China

Objectives: To develop and validate a nomogram to predict the overall survival (OS) of patients with primary nodal diffuse large B-cell lymphoma(N-DLBCL) based on radiomic features and clinical features.

Materials and methods: A retrospective analysis was performed on 145 patients confirmed with N-DLBCL and they were randomly assigned to training set(n=78), internal validation set(n=33), external validation set(n=34). First, a clinical model (model 1) was established according to clinical features and ultrasound (US) results. Then, based on the radiomics features extracted from conventional ultrasound images, a radiomic signature was constructed (model 2), and the radiomics score (Rad-Score) was calculated. Finally, a comprehensive model was established (model 3) combined with Rad-score and clinical features. Receiver operating characteristic (ROC) curves were employed to evaluate the performance of model 1, model 2 and model 3. Based on model 3, we plotted a nomogram. Calibration curves were used to test the effectiveness of the nomogram, and decision curve analysis (DCA) was used to asset the nomogram in clinical use.

Results: According to multivariate analysis, 3 clinical features and Rad-score were finally selected to construct the model 3, which showed better predictive value for OS in patients with N-DLBCL than mode 1 and model 2 in training (AUC,0. 891 vs. 0.779 vs.0.756), internal validation (AUC, 0.868 vs. 0.713, vs.0.756) and external validation (AUC, 914 vs. 0.866, vs.0.789) sets. Decision curve analysis demonstrated that the nomogram based on model 3 was more clinically useful than the other two models.

10.3389/fonc.2022.991948

Conclusion: The developed nomogram is a useful tool for precisely analyzing the prognosis of N-DLBCL patients, which could help clinicians in making personalized survival predictions and assessing individualized clinical options.

KEYWORDS

diffuse large B-cell lymphoma, overall survival, radiomic, nomograms, predict

Introduction

Diffuse large B-cell lymphoma (DLBCL) is the most common subtype of lymphoma, accounting for about 30% to 40% of the total incidence of all non-Hodgkin's lymphomas (NHL) (1, 2). According to the site of origin, DLBCL can be divided into primary nodal diffuse large B-cell lymphoma (N-DLBCL) and primary extranodal diffuse large B-cell lymphoma (EN-DLBCL) (3). DLBCL has obvious heterogeneity in morphology, immunophenotype, genetics and clinical manifestations (4). Nowadays, the treatment of DLBCL has made great progress, immunochemical therapy of rituximab, cyclophosphamide, doxorubicin, vincristine and prednisone (R-CHOP) is the preferred treatment regimen for DLBCL (5). The application of rituximab increased the 5-year survival rate of DLBCL by at least 15% and the cure rate significantly, but there were still more than 30% of patients with primary drug resistance or relapse (6). These recurrent or refractory patients had a poor prognosis and high mortality (7). How to identify these patients as early as possible, accurately predict their efficacy and prognosis, and carry out individualized treatment? It has been an urgent clinical problem to be solved.

At present, 18F-deoxyglucose (FDG) positron emission tomography/computed tomography (PET/CT) has been widely used in evaluating the prognosis of DLBCL (8). Several studies (9, 10) have tested the use of metabolic intensity to predict Progression-Free Survival (PFS) and overall survival (OS) in patients with lymphoma. The most used parameter is the maximum standard uptake value (SUVmax) because it provides a method of measurement independent of the observer (11). However, the reliability of SUVmax may be affected by many factors, such as the attenuation of injection dose, the time between injection and imaging acquisition, partial volume effect and technical characteristics and parameters (12). Recently, new indicators for estimating the overall tumor load based on PET/CT staging, such as metabolic tumor volume (MTV) or total lesion glycolysis (TLG), have been used to predict PFS and OS in patients with lymphoma (13). In addition, international prognostic index (IPI) is currently used for estimating pretreatment risk, while IPI only comes from the clinicopathological features before treatment, which lacks the information to reflect the functional and metabolic characteristics of the tumor. Hence, the IPI often does not reliably predict the individual patient outcome (14).Therefore, the above evaluation indicators fail to capture the heterogeneity of tumors, which is a key prognostic factor for the progression, recurrence, and drug resistance of DLBCL, and closely related to tumor invasiveness, metastasis, and molecular characteristics. This limitation is a major challenge in DLBCL treatment. Therefore, we need to find a new imaging method, which can not only evaluate the treatment effect of patients in real time and dynamically, but capture the heterogeneity of metabolism in the tumor, to help clinicians modify the treatment plan in time and accurately predict the clinical outcome of DLBCL.

Ultrasound (US) can evaluate the shape, size, echo texture and blood flow pattern of lymph nodes in real time and dynamically (15). Radiomic is a method that uses complex computer algorithms to extract a large amount of data from images routinely obtained in the clinical environment, revealing hidden features of tumor from various imaging modes (16, 17), which can assist doctors to make the most accurate diagnosis by means of deeper mining and analysis of massive image data (18, 19). Hence, heterogeneity-related parameters provided by images could contribute to more personalized treatment and reduce the occurrence of toxicity. In this way, the possibility of favorable outcomes is increased, and intensive treatment programs can be provided for high-risk patients (20). Radiomic of 18F-FDG PET/CT have been demonstrated to be useful in predicting the outcomes of DLBCL and Hodgkin's lymphoma (21, 22). Radiomic based on ultrasound has a good application prospect in the evaluation of curative effect and prognosis of other malignant tumors such as breast and gastrointestinal tumors (23–25). In lymphoma, radiomic shows hope in the differential diagnosis of lymphoma from other Lymph node diseases (26). To our knowledge, no previous study has associated radiomic signatures based on ultrasound with the outcome of patients with N-DLBCL.

This study was aimed at developing and validating the nomogram by radiomic features on ultrasound imaging to predict OS of patients with N-DLBCL more accurately and provide new ideas for personalized clinical treatment and visual evaluation of N-DLBCL.

Patients

Patients newly confirmed with DLBCL and treated in our medical central from August 2009 to October 2021 were retrospectively analyzed. Exclusion criteria: ①Patients with other malignant tumors; ②Patients with Ann arbor IE staging; ③Patients treated in other hospitals or relapsed patients; ④Patients without complete US and clinical data. Inclusion criteria: ①Patients who underwent PET-CT; ②Lymph nodes with a maximum SUV value; ③Lymph nodes with core needle biopsy or resection biopsy. Finally, 111 patients with a total of 111 lymph nodes were included in this study. They were randomly assigned to training set(n=78) and internal validation set(n=33) (7:3 ratio). Besides, the independent external validation set consists of 34 patients from the other two institutions who meet the above exclusion and inclusion criteria. Histopathological diagnosis was based on the result of core needle biopsy or lymph node excision (excision biopsy is required only if the ultrasound-guided biopsy results are uncertain). Clinical variables of each patient were recorded, including gender, age at diagnosis, Bulky disease, B symptoms, Ann Arbor stage, Eastern Cooperative Oncology Group (ECOG), lactate dehydrogenase (LDH) level, serum β2-microglobulin (β2-MG) level, serum hemoglobin (HB) level, extra-nodal involvement, international prognostic index (IPI), state after first-line standardized chemotherapy, POD24, BCL6, BCL2 and treatment regimens. Disease staging was conducted in accordance with the Ann Arbor system. Bulky disease was defined as a nodal mass larger than 10 cm in diameter. State after first-line standardized chemotherapy were separated into two response categories as complete response(CR) and incomplete response (ICR, including partial response, stable and progression) (27).

The study was approved by the Institutional Ethics Committee of our hospital [Ethical number 2022-SR-058], and because it is a retrospective analysis, the requirement of written informed consent was waived.

US image acquisition

The LogiqE9 ultrasound machine (GE Healthcare), with a 15–4 MHz linear probe (Super Linear^{TM} SL15-4) was employed in ultrasonic examination. Two experienced radiologists used standardized institutional protocols to independently record and review all preoperative US features. If the radiologist had a different opinion on the conclusion, the final decision was made between them after a discussion. The patient was taken in a comfortable posture to fully expose the site of examination. The lymph node that underwent biopsy at the site of onset was selected as the target lymph node. The following parameters of lymph nodes were observed and measured, including size (cross-section, longitudinal-section), the ratio of the longitudinal diameter to the short axis (Solbiati index, SI>2, SI<2), sharp (regular, irregular), visibility of the hilum (present, absent), border (clear, unclear), Adler grade of blood flow (grades 0-3) (28).

ROI segmentation and radiomics features extraction

The US images of all DLBCL patients were export from the Ultrasonic instrument. The maximum longitudinal-section area of images was manually segmented by two ultrasound experts (more than 5 years of experience) using open-source software (ITK-SNAP 3.8.0; http://www.itksnap.org) to generate a region of interest (ROI) containing all the segmented lesions. A total of 464 radiomics features were extracted from the US images, including 90 first-order features and 374 texture features. The first-order features include shape, size, and strength features and texture feature extraction is based on four texture matrices, including grey level cooccurrence matrix (GLCM), grey level run-length matrix (GLRLM), grey level size zone matrix (GLSZM) and gray level dependence matrix (GLDM). All radiomics features were analyzed and mined by PyRadiomic open-source software package.

Radiomics features selection and signature calculation

One radiologist randomly selected 20 lesions from the training cohort to draw ROI again, and the other radiologist repeated it independently within three weeks. The stability of the feature is determined by calculating the inter-observe correlation coefficient (ICC). Radiomics features with ICC lower than 0.75 were excluded from the final feature data set (18).

To obtain the optimal subset of radiomics features, minimal redundancy maximum relevancy (mRMR) and the least absolute shrinkage selection operator (LASSO) with 10-fold cross-validation (the criteria as maximum area under the ROC curve) was further used to select most candidate radiomic features. Finally, 10 radiomics features were screened out. Therefore, the radiomics "Radcore" is calculated according to formula (1) (29).

$$\text{Radscore} = \beta 0 + \beta 1\chi 1 + \beta 2\chi 2 + \ldots + \beta n\,\chi n \qquad (1)$$

where β_0 is the constant term in the regression, β_i is logistic regression coefficient, and χ_i the value of selected features.

Construction of clinical model, radiomics model, and combined model

Univariate and multivariate COX regression analysis were used to analyze the influence of clinical variables, US characteristics. Then the characteristics of $p< 0.05$ in multivariate analysis were used to establish the model 1 (clinical and US characteristics) of the training set. The optimal radiomics feature subset obtained by LASSO Logistic

regression method was used to construct model 2 (radiomics features) in the training set. ROC curves were used to determine the cut-off value of each group feature, and the continuous variables were transformed into classified variables. The radiological signals constructed were mixed with clinical factors, and the univariate analysis and minimum Akaike information criterion (AIC) criterion COX regression analysis were obtained in turn. Model 3 (combined features) was constructed based on COX regression coefficient.

Model performance assessment

Three established models were validated using independent internal and external datasets. The discriminant ability of each model was analyzed by receiver operating characteristic curve (ROC), and area under curve (AUC), sensitivity, specificity of them were obtained.

Development and validation of the nomogram

According to the model 3, a nomogram, convenient for clinical application, was plotted. The model correction was evaluated by correction curve analysis and Hosmer-Lemeshow test. Decision curve analysis (DCA) was used to evaluate the clinical usefulness and net benefit of the predictive model in validation set. Delong test was used to compare the AUC of each pair of models.

Patients' treatment and follow-up

Patients diagnosed with N-DLBCL received standardized R-CHOP chemotherapy (n=105) or approved clinical drug verification(n=40). The follow-up data were obtained by electronic medical records and telephone interviews. Overall survival (OS) refers to the time from diagnosis until death due to any cause.

Statistical analysis

The classification variables were expressed by the number of cases, using chi-square test (χ^2) or Fisher exact test. A SPSS software (version 25.0) was used for univariate analysis and multivariate analysis. R software (version 3.6.1, R Project for Statistical Computing, www.r-project.org) was used for radiomic features analysis. The LASSO logistic regression method was implemented using the glmnet package in R software. Two-sided p value less than 0.05 was assumed to indicate statistical significance.

Result

Patient characteristics

One hundred and forty-five patients with 145 lymph nodes were enrolled in this study, including 78 males and 67 females, ranging from the age of 21 to 85 (mean age, 58 ± 12). The research flowchart is shown in Figure 1. The median follow-up time was 36 months (range, 3–137 months). By the date of the last follow-up, a total of 41 patients had died, with a total survival rate of 71.7%. 1-year survival rate, 3-year survival rate and 5-year survival rate were 88.3%, 80.6% and 73.8% respectively. The clinical and ultrasonic features of the training set and verification set were summarized in Table 1. All the characteristics were not statistically significant between the two sets.

Model 1: Clinical features and US features

In the training set, univariate analysis in Table 2 showed that five variables were related to OS. Multivariate analysis showed that hilus, extra-nodal involvement, state after first-line standardized chemotherapy were independent predictors of OS ($p<0.05$) (Table 3). The diagnostic performance of this model was moderate with an AUC of 0.779 (95% CI, 0.660-0.897). The sensitivity and specificity were 73.6% and 81.4%, respectively.

Model 2: Radiomics signature

After intra-observer and inter-observer reliability analysis, 340 stable features with ICC score larger than 0.75 were retained for follow-up analysis, and finally 10 radiomics features were selected into the LASSO Logistic regression model (Figures 2, 3). ICC values are provided in the supplementary information. Table 4 displays that variables A to J represent 10 selected radiomic features, Rad-score=−1.317+0.403×A+0.094×B+(−0.349) ×C+(−0.081) ×D+ 0.005×E+(−0.0.310) ×F+0.682×G+0.036×H+(−0.161) ×I+0.005×J. The discriminative ability of radiomics model was low with an AUC of 0.756 (95% CI, 0.622-0.889). The sensitivity and specificity are 93.2%, 52.6% respectively.

Model 3: Comprehensive model

A comprehensive model was constructed based on multivariate Cox analysis of significant risk factors. The risk factors included Rad-score(p=0.012) and hilus (p=0.020), Extra-nodal involvement (p=0.027), state after first-line (p=0.023). The diagnostic efficiency of combined model is significantly improved, with an AUC of 0.891 (95% CI, 0.807-0.975). The sensitivity and specificity were 89.8% and 73.7% respectively.

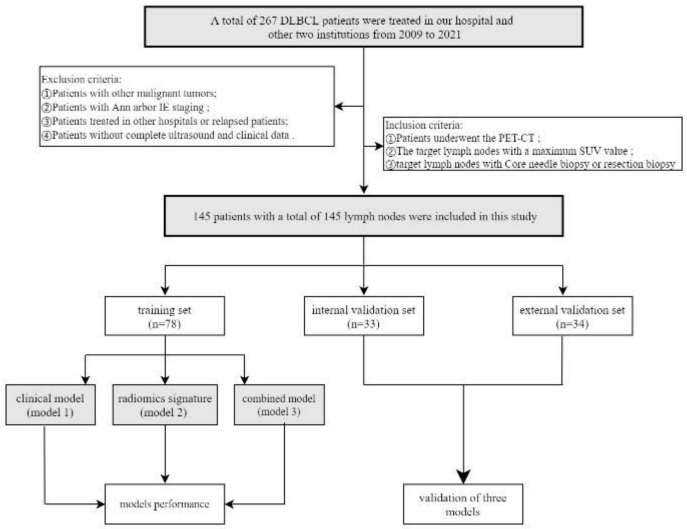

FIGURE 1
Flow chart of patients'recruitment pathway. DLBCL, Diffuse large B-cell lymphoma; PET-CT, Positron emission tomography/computed tomography. According to the inclusion and exclusion criteria, 145 patients with a total of 145 lymph nodes were included in this study. The patients of our institutions were randomly assigned to training set(n=78) and internal validation set(n=33) (7:3 ratio). The independent external validation set(n=34) from the other two institutions.

TABLE 1 Clinic and ultrasound features of training and validation sets.

Univariate analysis	Features	Training set (n=78)	Internal validation set (n=33)	p value	External validation set (n=33)	p value
	Gender			0.946		0.509
	Male	42(53.8)	18(54.5)		18(52.9)	
	Female	36(46.2)	15(45.5)		16(47.1)	
	age			0.982		0.681
	<60	41(52.5)	17(51.5)		16(47.1)	
	≥60	37(47.4)	16(48.5)		18(52.9)	
	Bulky			0.546		0.927
	<7.5cm	12(15.4)	3(9.1)		5(14.7)	
	≥7.6cm	66(84.6)	30(90.9)		29(85.3)	
	Extra-nodal involvement			0.285		0.235
	Yes	48(61.5)	18(54.5)		11(32.3)	
	No	30(38.5)	15(45.5)		23(67.6)	
	IPI			0.729		0.805
	0	37(47.4)	17(51.5)		15(44.1)	
	1-2	1(1.3)	1(3.0)		1(2.9)	
	3-5	40(51.3)	15(45.5)		18(52.9)	
	ECOG			0.946		0.235
	0-1	61(70.1)	25(75.8)		23(67.6)	
	≥2	16(29.9)	8(24.2)		11(32.4)	
	Stage			0.423		0.958
	I-II	18(23.1)	10(30.3)		8(23.5)	

(Continued)

TABLE 1 Continued

Univariate analysis	Features	Training set (n=78)	Internal validation set (n=33)	p value	External validation set (n=33)	p value
	III-IV	60(76.9)	23(69.7)		26(76.5)	
	State of first			0.053		0.285
	CR	54(69.2)	16(48.5)		20(58.8)	
	ICR	24(30.8)	17(51.5)		14(41.2)	
	POD24			0.436		0.726
	No	62(79.5)	24(72.7)		28(82.4)	
	Yes	16(20.5)	9(27.3)		6(17/6)	
	LDH			0.577		0.656
	<271	31(39.7)	9(27.3)		6(18.2)	
	≥271	47(60.3)	24(72.7)		28(84.8)	
	b2mg			0.329		0.411
	<2.53	41(52.6)	14(42.4)		15(44.1)	
	≥2.53	37(47.4)	19(57.6)		19(55.9)	
	HB			0.628		0.592
	<120	37(47.4)	14(42.4)		12(35.3)	
	≥120	41(52.6)	19(57.6)		22(64.7)	
	BCL6			0.442		0.590
	–	17(21.8)	5(15.2)		9(26.5)	
	+	61(78.2)	28(84.8)		25(73.5)	
	BCL2			0.113		0.520
	–	18(23.1)	3(9.1)		6(17.6)	
	+	60(76.9)	30(90.9)		28(82.4)	
	SI			0.713		0.637
	SI≥2	51(65.4)	9(27.3)		12(35.3)	
	SI<2	27(34.6)	24(72.7)		22(64.7)	
	Hilus			0.215		0.745
	Absence	55(70.5)	25(75.8)		21(61.8)	
	Presence	23(29.5)	8(24.2)		13(38.2)	
	Border			0.886		0.631
	Clear	67(85.9)	24(72.7)		28(82.4)	
	Unclear	11(14.1)	9(27.3)		6(17.6)	
	Sharp			0.436		0.713
	Regular	51(65.4)	19(57.6)		21(61.8)	
	Irregular	27(34.6)	14(42.4)		13(38.2)	
	Alder			0.996		0.982
	0	20(25.6)	9(27.3)		8(23.5)	
	1	29(37.2)	13(39.4)		14(41.2)	
	2	15(19.2)	5(15.2)		6(17.6)	
	3	14(17.9)	6(18.2)		6(17.6)	

IPI, International Prognostic Index; ECOG, Eastern Cooperative Oncology Group; CR, Complete response; ICR, Incomplete response; LDH, Lactate dehydrogenase; HB, Hemoglobin; SI, Solbiati index, the ratio of the longitudinal diameter to the short axis.

Validation and diagnostic performance comparison of three models

Three established models were validated using independent datasets. In the internal validation set, the AUC, sensitivity, and specificity of model 1 were 0.713(95%CI,0.532-0.894), 59.1%, 81.8%. The AUC, sensitivity, specificity of model 2 were 0.756 (95%CI,0.593-0.919), 54.5%, 73.2%; The AUC, sensitivity, specificity of model 3 were 0.868(95%CI,0.746-0.990), 81.8%, 81.8%. In the external validation set, the AUC, sensitivity, and specificity of model 1 were 0.866(95%CI,0.808-0.925), 87.7%, 80.8%. The AUC, sensitivity, specificity of model 2 were 0.789 (95%CI,0.714-0.863), 92.7%, 60.6%; The AUC, sensitivity, specificity of model 3 were 0.914(95%CI,0.868-0.960), 95.1%,

TABLE 2 Clinic and ultrasound features between survival group and death group.

Univariate analysis	Features	Training set (59/19)	p	Internal validation set (22/11)	p	External validation set (23/11)	p
	Gender		0.684		0.266		0.180
	Male	31(52.5)/11 (57.9)		10(45.5)/8(72.7)		14(60.9)/4(36.4)	
	Female	28(47.5)/8(42.1)		12(54.5)/3(27.3)		9(39.1)/7(63.6)	
	age		0.695		0.325		0.897
	<60	31(52.5)/10 (52.6)		10(45.5)/7(63.6)		11(47.8)/5(45.5)	
	≥60	28(47.5)/9(47.4)		12(54.5)/4(36.4)		12(52.2)/6(54.5)	
	Bulky		0.720		1.000		0.692
	<10cm	10(16.9)/2(10.5)		2(9.1)/1(9.1)		3(13.0)/2(18.2)	
	≥10cm	49(83.1)/17 (89.5)		20(90.9)/10(90.9)		20(87.0)/9(81.8)	
	Extra-nodal involvement		0.006		0.034		0.016
	Yes	31(52.5)/17 (89.5)		9(40.9)/9(81.8)		12(52.2)/1(9.1)	
	No	28(47.5)/2(10.5)		13(59.1)/2(18.2)		11(47.8)/10(90.9)	
	IPI		0.076		0.338		0.256
	0	32(54.2)/5(26.3)		15(68.1)/2(18.2)		12(52.2)/3(27.3)	
	1-2	1(1.7)/0(0.0)		1(4.5)/0(0.0)		1(4.3)/0(0.0)	
	3-5	26(44.1)/14 (73.7)		6(27.2)/9(81.8)		10(43.5)/8(72.7)	
	ECOG		0.583		0.774		0.222
	0-1	47(79.7)/14 (73.7)		17(77.3)/8(72.7)		14(60.9)/9(81.8)	
	≥2	12(20.3)/5(26.3)		5(22.7)/3(27.3)		9(39.1)/2(18.2)	
	Stage		0.211		0.430		0.611
	I-II	16(27.1)/2(10.5)		8(36.4)/2(18.2)		6(26.1)/2(18.2)	
	III-IV	43(72.9)/17 (89.5)		14(63.6)/9(81.8)		17(73.9)/9(81.8)	
	State of first		0.001		0.002		0.023
	CR	47(79.7)/7(36.8)		15(68.2)/1(9.1)		17(73.9)/3(27.3)	
	ICR	12(20.3)/12 (63.2)		7(31.8)/10(90.9)		6(26.1)/8(72.7)	
	POD24		0.043		0.002		0.048
	No	50(84.7)/12 (63.2)		20(90.9)/4(36.4)		21(91.3)/7(63.6)	
	Yes	9(15.3)/7(36.8)		2(9.1)/7(63.6)		2(8.7)/4(36.4)	
	LDH		0.065		0.681		0.053
	<271	27(45.8)/4(21.1)		7(31.8)/2(18.2)		21(91.3)/7(63.6)	
	≥271	32(54.2)/15 (78.9)		15(68.2)/9 (81.8)		2(8.7)/4(36.4)	
	b2mg		0.429		0.719		0.387
	<2.53	33(55.9)/8(42.1)		10(45.5)/4(36.4)		9(39.1)/6(54.5)	
	≥2.53	26(44.1)/11 (57.9)		12(54.5)/7(63.6)		14(60.9)/5(45.5)	
	HB		0.186		0.136		0.245
	<120	25(42.4)/12 (63.2)		7(31.8)/7(63.6)		6(26.0)/6(54.5)	
	≥120	34(57.6)/7(36.8)		15(68.2)/4(36.4)		17(73.9)/5(45.5)	
	BCL6		0.750		0.304		1.000

(Continued)

TABLE 2 Continued

Univariate analysis	Features	Training set (59/19)	p	Internal validation set (22/11)	p	External validation set (23/11)	p
	–	12(20.3)/5(26.3)		2(9.1)/3(27.3)		6(26.1)/3(27.3)	
	+	47(79.7)/14 (73.7)		20(90.9)/8(72.7)		17(73.9)/8(72.7)	
	BCL2		0.536		0.252		1.000
	–	15(25.4)/3(15.8)		1(4.5)/2(18.2)		4(17.4)/2(18.2)	
	+	44(74.6)/16 (84.2)		21(95.5)/9(81.8)		19(82.6)/9(81.8)	
	SI		0.179		0.681		0.705
	SI≥2	41(69.5)/10 (52.6)		7(31.8)/2(18.2)		9(39.1)/3(27.3)	
	SI<2	18(30.5)/9(47.4)		15(68.2)/9(81.8)		14(60.9)/8(72.7)	
	Hilus		0.045		0.012		0.016
	Absence	38(64.4)/17 (89.5)		16(72.7)/9(81.8)		11(47.8)/10(90.9)	
	Presence	21(35.6)/2(10.5)		6(27.3)/2(18.2)		12(52.2)/1(9.1)	
	Border		0.012		0.033		0.048
	Clear	54(91.5)/13 (68.4)		19(86.4)/5(45.5)		21(91.3)/7(63.6)	
	Unclear	5(8.5)/6(31.6)		3(13.6)/6(54.5)		2(8.7)/4(36.4)	
	Sharp		0.179		0.618		0.176
	Regular	41(69.5)/10 (52.6)		12(54.5)/7(63.6)		15(69.6)/5(45.5)	
	Irregular	18(30.5)/9(47.4)		10(45.5)/4(36.4)		7(30.4)/6(54.5)	
	Alder		0.154		0.391		0.542
	0	13(22.0)/7(36.8)		7(31.8)/2(18.2)		5(21.7)/3(27.3)	
	1	20(33.9)/9(47.4)		8(36.4)/5(45.5)		8(34.8)/6(54.5)	
	2	14(23.7)/1(5.3)		2(9.1)/3(27.3)		5(21.7)/1(9.1)	
	3	12(20.3)/2(10.5)		5(22.7)/1(9.1)		5(21.7)/1(9.1)	

IPI, International Prognostic Index; ECOG, Eastern Cooperative Oncology Group; CR, Complete response; ICR, Incomplete response; LDH, Lactate dehydrogenase; HB, Hemoglobin; SI, Solbiati index, the ratio of the longitudinal diameter to the short axis.

81.7%. Figure 4 shows the ROC curves of each model for both the training and validation sets, Table 5 shows the cut-off value, sensitivity, specificity, and AUC of each mode. The AUC of the comprehensive model was significantly higher than that of model 1 or model 2 in both the training and validation sets.

Development and performance of the nomogram

A nomogram (Figure 5A) was conducted based on the comprehensive model, and favorable calibrations of the

TABLE 3 Multivariate analysis of clinical and ultrasonic features.

Multivariate analysis	Features	Estimate	Std.Error	Z value	p
Training set	Hilus	-2.369	1.161	-2.039	0.041
	Extra-nodal involvement	2.712	1.078	2.516	0.012
	State of first	0.986	0.482	2.045	0.041
Internal validation set	Hilus	-1.975	0.926	-2.132	<0.000
	Extra-nodal involvement	2.317	0.867	2.671	0.007
	State of first	1.201	0.404	2.973	0.003
External validation set	Hilus	-1.211	0.646	0.298	0.042
	Extra-nodal involvement	1.759	0.620	5.890	0.005
	State of first	1.454	0.491	4.28	0.003

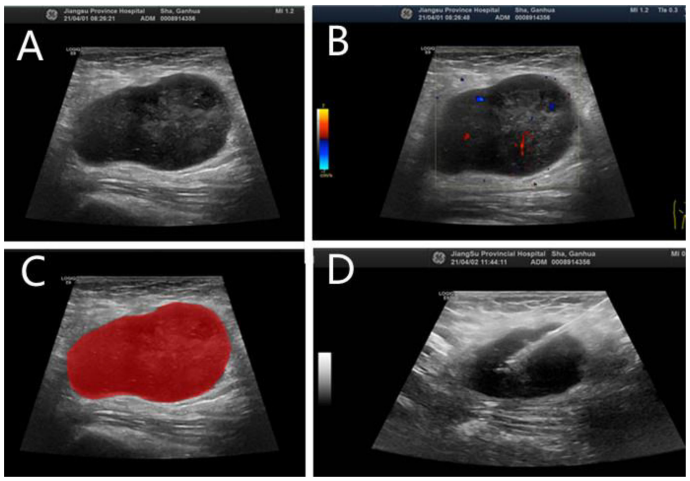

FIGURE 2
N-DLBCL in a 58-year-old man. **(A)** Gray-scale ultrasonic image. **(B)** CDFI image. **(C)** Radiomic ROI segmentation segmentation of the mass. **(D)** Ultrasound-guided core needle biopsy.

nomogram were confirmed both in the training (Figure 5B), the internal validation set (Figure 5C), the internal validation set (Figure 5D). Hosmer–Lemeshow test possessed a p value of 0.334, 0.738 and 0.679, respectively. The DCA (Figures 6A, B) indicated that the nomogram had a higher diagnostic efficiency than model 1 or model 2.

Discussion

This study established three models for predicting the prognosis of patients with N-DLBCL, and it was found that the model with the combination of radiomic and clinical features had good predictive value. On this basis, we developed a nomogram based on the combined model, and verified the nomogram. The results showed that the nomogram could well predict the OS of patients with N-DLBCL. Thus, nomograms can be used by clinicians to make precise and individualized medical decisions.

All N-DLBCL patients in our study were adults, which was in line with that reported in the literature for Chinese studies, Sun et al. (30)showed that the mean age of DLBCL patients was 51.6 years. Besides, consistent with the previous study (30, 31), most of the DLBCL cohort in this study was male patients, who accounted for 53.7% (78/145). The 5-year survival rate of 145patients in this study was 73.8% (107/145), which was almost the same as the report (74.8%) of Xia et al. (32), but higher than previous reports (43%-52%) (33). The reason is that the subjects in this study and Xia et al. are all primary intranodal DLBCL. Moo-Kon Song et al. (34) reported EN- DLBCL, such as originating from the gastric, intestinal tract and so on are even worse, especially in the non-GCB type. Some studies (3, 35) also have demonstrated that the involvement of the extranodal tissue may lead to a worse prognosis for patients with nodal lesions. The results of univariate and multivariate analysis showed state after the 6 cycles standardized treatment was the prediction factors of OS. After 6 cycles of standardized treatment, according to the results of PET-CT assessment, the CR rate of patients was 62.1% (90/145) in our study, which was lower than that reported by Ivan et al (36). At present, the effect of BCL-6 gene translocation on the prognosis of DLBCL patients is still controversial. Most scholars believe that the prognosis of BCL-6 positive expression is better, but some scholars hold the opposite view. Akyurek et al. (37) found that BCL-6 gene translocation can affect the OS of DLBCL patients(p=0.04), but there is no significant effect on PFS. This phenomenon is more significant in non-GCB DLBCL patients. In addition, foreign studies (38, 39) conclude that MYC/BCL2 co-expression in DLBCL is associated with an aggressive clinical course, which is more common in the ABC subtype, and contributes to the overall inferior prognosis of patients with ABC-DLBCL. However, in this study, probably due to the small sample size, BCL2 and BCL6 were not predictors of OS. For the same reason, the results of multivariate analysis showed that the other clinical features reported in the literature, including IPI score, LDH level, HB level, β2-MG level, Bulky disease, ECOG, Arbor stage, POD 24, were not associated with OS in the training group and the verification group.

US is also a commonly used diagnostic imaging technique, which possess a higher sensitivity in the detection of superficial

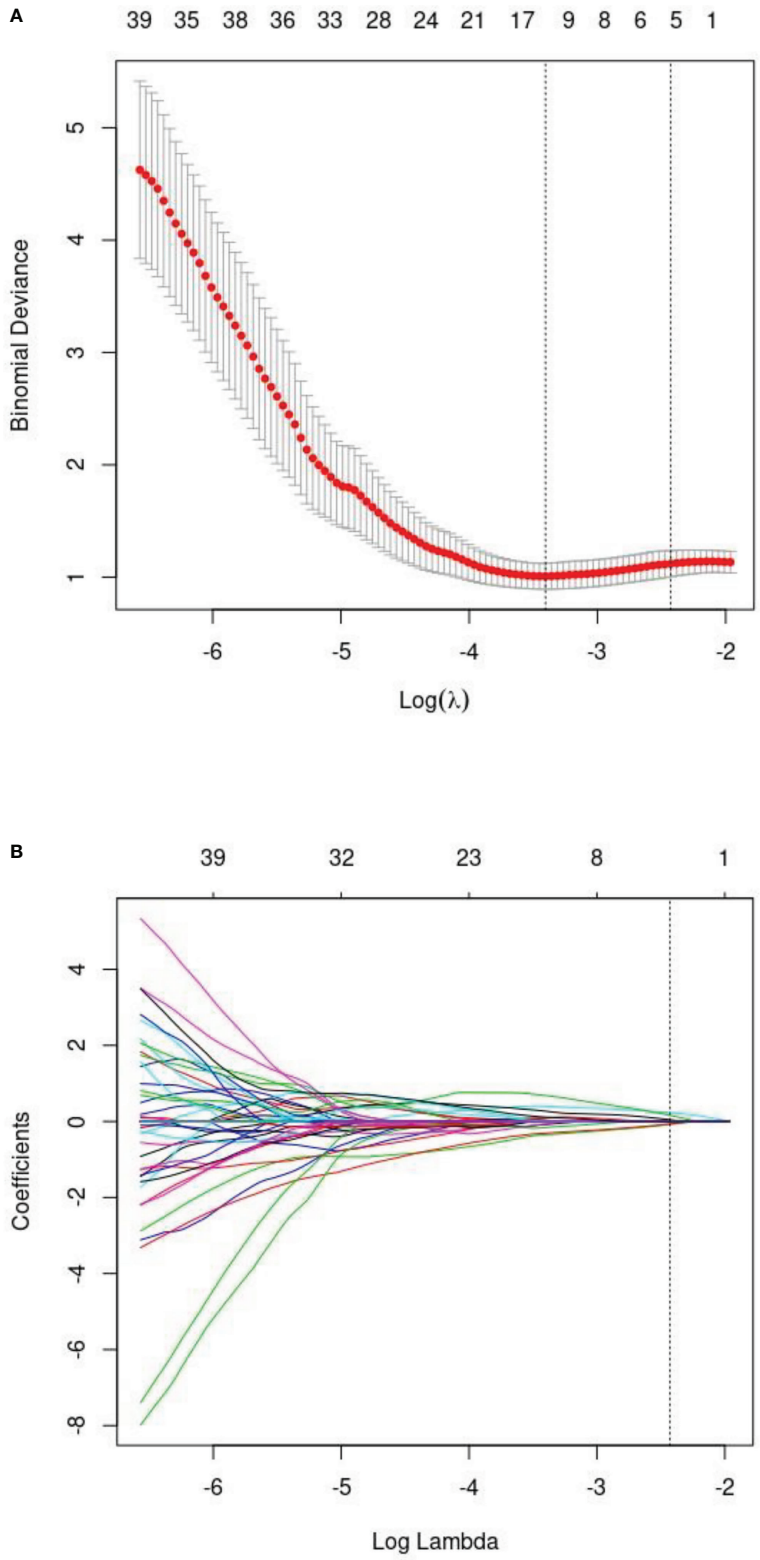

FIGURE 3
(A) The least absolute shrinkage andselection operator (LASSO) logistic regression for radiomics features selection and signature construction. **(B)** On the basis of minimum criteria for the least cross-validation binominal deviance, a tuning parameter (l) was selected via 10-fold cross validation.according to 10-fold cross-validation, 10 radiomic features were obtained.

TABLE 4 Radiomics feature selection results.

Variables	Radiomics features name	Coef
A	original_glrlm_LowGrayLevelRunEmphasis	0.403277408
B	wavelet.LH_firstorder_Median	0.094560940
C	wavelet.LH_firstorder_Skewness	-0.349875709
D	wavelet.LH_glszm_LargeAreaHighGrayLevelEmphasis	-0.081542829
E	wavelet.LH_glszm_LargeAreaLowGrayLevelEmphasis	0.005653936
F	wavelet.HL_glcm_ClusterShad	-0.310516391
G	wavelet.HL_glszm_ZoneVariance	0.682458423
H	wavelet.HH_glcm_Idmn	0.035780343
I	wavelet.HH_glszm_GrayLevelNonUniformity	-0.161635402
J	wavelet.LL_ngtdm_Busyness	0.004573644

enlarged lymph nodes. The feature of lymph nodes can be evaluated according to the hilum, shape, border, size, echo texture and blood flow pattern of lymph nodes (40). In this study, univariate analysis found that the lymphatic hilum structure and boundary is related to OS, while multivariate study found that the absence of lymphatic hilum is an independent predictor of OS. B lymphocytes mainly settle in the superficial cortex of the lymph nodes, some studies demonstrated that the abnormal lymphocytes of DLBLC in the early stage grew locally and did not invade the whole lymph node, but in the late stage, the abnormal lymphocytes infiltrated into the whole lymph node, resulting in the disappearance of the lymphatic hilum or eccentric and thin stripe under pressure (41). At the same time, studies have shown that patients with stage III-IV have a poor prognosis (3, 34). Therefore, in model 1, the absence of lymphatic hilum is a predictor of OS (training set, p=0.045; internal validation set, p=0.012; external validation set, p=0.016). From the previous literatures, in lymphoma, the disease frequently arises inside the lymph node, and (depending on the aggressiveness and natural history of the tumor) it may never reach the subcapsular area, or it may progress in a centrifugal fashion to invade the whole lymph node; in high-grade aggressive lymphomas, the neoplastic cells may even reach the lymph node from outside (as with metastasis) when the disease originates in another lymph node of the group and subsequently infiltrates the remaining nodes, the lesions fused with each other and the boundary was not clear (42), which may explain why in univariate analysis, the boundary is related to OS (training set, p=0.012; internal validation set, p=0.033; external validation set, p=0.048). The univariate and multivariate analysis showed that other ultrasonic features were not related to OS (p≥0.05).

18F-FDG PET/CT has been widely used for diagnosis, staging and response assessment in DLBCL (43). In recent years, there are also many literatures (12, 14, 44) to predict the prognosis of DLBCL based on 18F-FDG PET/CT baseline radiomic features. However, we have not seen a specific explanation about which target lymph nodes should be selected as the object of study, nor the criteria for selection. In this study, the target lymph nodes with the highest SUV value on PET-CT and ultrasound-guided pathological biopsy (Figure 2) were selected as the objects of study to reduce false

TABLE 5 Diagnostic performance of three models.

Model	Cut-off value	AUC (95%CI)	Sensitivity %	Specificity %
Training set(n=78)				
Model 1	0.908	0.779(0.660-0.897)	73.6	81.4
Model 2	0.598	0.756(0.662-0.889)	93.2	52.6
Model 3	0.729	0.891(0.807-0.975)	89.8	73.3
Internal validation set (n=33)				
Model 1	0.891	0.713(0.532-0.894)	59.1	81.8
Model 2	0.932	0.756(0.593-0.919)	54.5	73.2
Model 3	0.843	0.868(0.746-0.990)	81.8	81.8
External validation set (n=34)				
Model 1	0.775	0.866(0.808-0.925)	87.7	80.8
Model 2	0.757	0.789(0.714-0.863)	92.7	60.6
Model 3	0.770	0.914(0.868-0.960)	95.1	81.7

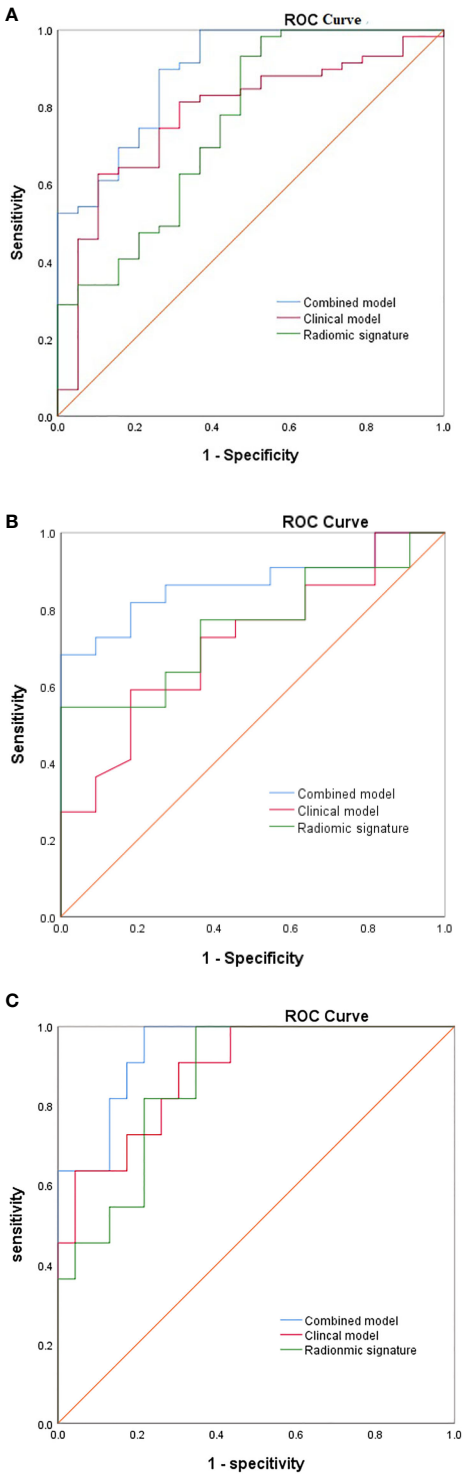

FIGURE 4
The ROC of the three model from **(A)** the training cohorts, **(B)** the internal validation cohort, **(C)** the external validation cohort.

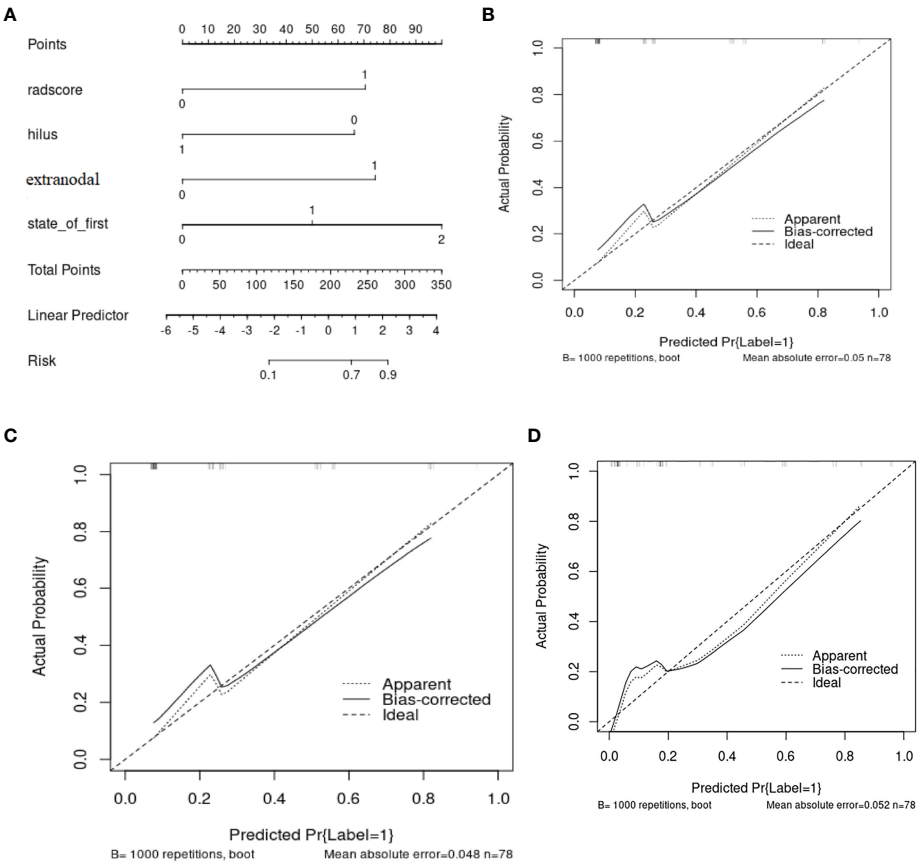

FIGURE 5
(A) The nomogram base on the model 3 and the calibration curve from **(B)** the training cohorts, **(C)** the internal validation cohort, **(D)** the internal validation cohort.

positive and false negative and improve accuracy. As far as we know, there have been no radiomics based on ultrasound images to predict the prognosis of DLBCL, and the literatures on molecular imaging radiomics of DLBCL are also very limited. Parvez et al. (45) found that GLNGLSZM correlated with disease free survival, and that kurtosis correlated with OS. Aide et al. (4, 46) found that skewness of skeletal heterogeneity was a prognostic factor for PFS, and long-zone high gray level emphasis from GLSZM was a prognostic parameter for 2-year event-free survival. Meanwhile, Cottereau et al. (47) reported that the radiomic feature characterizing lesion dissemination was associated with PFS and OS. Our study found that radiomic features related to OS included two first-order features, two GLCM, four GLSZM, a GLSZM and a GLRLM, which is consistent with the above literature reports. In addition, Wang et al. (39) reported that radiomics are not superior to traditional imaging parameters. In our study, the diagnostic efficacy of radiomic signature (training set, AUC=0.756; internal validation set, AUC=0.756; external validation set, AUC=0.789) is lower than that of clinical model (training set, AUC=0.779; internal validation set, AUC=0.713; external validation set, AUC=0.866), but it can be used as a supplementary index of clinical model, and the diagnostic efficacy of combined model (training set, AUC=0.891; internal validation set, AUC=0.868; external validation set, AUC=0.914) is higher than radiomic signature or clinical model.

Still, there are some limitations in our study. First, this was a retrospective study, and the sample size was relatively small. But we have been collecting more cases and collaborating with other medical centers to expand the sample size, using external verification sets to further validate the nomogram. Second, the radiomic features were only extracted from gray-scale ultrasound images, and hopefully in the future, we can extract them from multimode ultrasound images such as elastography and contrast-enhanced ultrasound.

In conclusion, based on clinic and radiomic features, we have developed and validated a nomogram to predict OS of

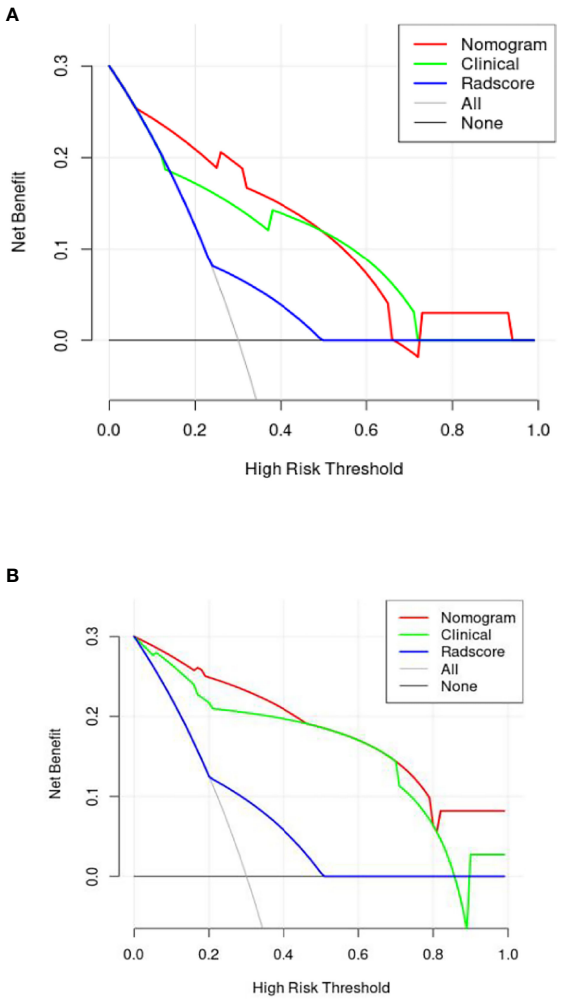

FIGURE 6
The decision curve [**(A)** is internal verification, **(B)** is external verification] analysis of the combined nomogram for prediction overall survival in patients with primary nodal Diffuse large B-cell lymphoma. The DCA indicated that the nomogram had a higher diagnostic efficiency than the clinical model and radiomics signature.

patients with N-DLBCL. The established nomograms can provide a visualized estimation of risk for each prognostic factor, to assist clinicians take personalized treatment for N-DLBCL patients and improve their prognosis.

Data availability statement

The original contributions presented in the study are included in the article/Supplementary Material. Further inquiries can be directed to the corresponding authors.

Ethics statement

The studies involving human participants were reviewed and approved by The study was approved by the Institutional Ethics Committee of the First Affiliated Hospital of Nanjing Medical University [Ethical number 2022-SR-058], and the requirement of written informed consent was waived. Written informed consent for participation was not required for this study in accordance with the national legislation and the institutional requirements.

Author contributions

HD designed the study and wrote the manuscript. YY, WL, YZ and WC collected the data. LL and HS analyzed the data. HD, PZ, and XY evaluated US images and segmented lesions. All authors contributed to the article and approved the submitted version.

Acknowledgments

Thanks to all the authors for their contributions to this article.

Conflict of interest

The authors declare that the research was conducted in the absence of any commercial or financial relationships that could be construed as a potential conflict of interest.

Publisher's note

All claims expressed in this article are solely those of the authors and do not necessarily represent those of their affiliated organizations, or those of the publisher, the editors and the reviewers. Any product that may be evaluated in this article, or claim that may be made by its manufacturer, is not guaranteed or endorsed by the publisher.

Supplementary material

The Supplementary Material for this article can be found online at: https://www.frontiersin.org/articles/10.3389/fonc.2022.991948/full#supplementary-material

References

1. Bray F, Ferlay J, Soerjomataram I, Siegel RL, Torre LA, Jemal A. Global cancer statistics 2018: GLOBOCAN estimates of incidence and mortality worldwide for 36 cancers in 185 countries. *CA: Cancer J Clin* (2018) 68:394–424. doi: 10.3322/caac.21492

2. Liu W, Liu J, Song Y, Zeng X, Wang X, Mi L, et al. Burden of lymphoma in China, 2006-2016: an analysis of the global burden of disease study 2016. *J Hematol Oncol* (2019) 12:115. doi: 10.1186/s13045-019-0785-7

3. Shi Y, Han Y, Yang J, Liu P, He X, Zhang C, et al. Clinical features and outcomes of diffuse large b-cell lymphoma based on nodal or extranodal primary sites of origin: Analysis of 1,085 WHO classified cases in a single institution in China. *Chin J Cancer Res* (2019) 31:152–61. doi: 10.21147/j.issn.1000-9604.2019.01.10

4. Aide N, Fruchart C, Nganoa C, Gac AC, Lasnon C. Baseline (18)F-FDG PET radiomic features as predictors of 2-year event-free survival in diffuse large b cell lymphomas treated with immunochemotherapy. *Eur radiology.* (2020) 30:4623–32. doi: 10.1007/s00330-020-06815-8

5. Nowakowski GS, Blum KA, Kahl BS, Friedberg JW, Baizer L, Little RF, et al. Beyond RCHOP: A blueprint for diffuse Large b cell lymphoma research. *J Natl Cancer Institute* (2016) 108–16. doi: 10.1093/jnci/djw257

6. Gleeson M, Counsell N, Cunningham D, Lawrie A, Clifton-Hadley L, Hawkes E, et al. Prognostic indices in diffuse large b-cell lymphoma in the rituximab era: an analysis of the UK national cancer research institute r-CHOP 14 versus 21 phase 3 trial. *Br J Haematol* (2021) 192:1015–9. doi: 10.1111/bjh.16691

7. Sehn LH, Berry B, Chhanabhai M, Fitzgerald C, Gill K, Hoskins P, et al. The revised international prognostic index (R-IPI) is a better predictor of outcome than the standard IPI for patients with diffuse large b-cell lymphoma treated with r-CHOP. *Blood* (2007) 109:1857–61. doi: 10.1182/blood-2006-08-038257

8. Lue KH, Wu YF, Lin HH, Hsieh TC, Liu SH, Chan SC, et al. Prognostic value of baseline radiomic features of (18)F-FDG PET in patients with diffuse Large b-cell lymphoma. *Diagnostics (Basel Switzerland)* (2020) 11-23. doi: 10.3390/diagnostics11010036

9. Chen Y, Zhou M, Liu J, Huang G. Prognostic value of bone marrow FDG uptake pattern of PET/CT in newly diagnosed diffuse Large b-cell lymphoma. *J Cancer.* (2018) 9:1231–8. doi: 10.7150/jca.23714

10. Ollila TA, Olszewski AJ. Extranodal diffuse Large b cell lymphoma: Molecular features, prognosis, and risk of central nervous system recurrence. *Curr Treat options Oncol* (2018) 19:38. doi: 10.1007/s11864-018-0555-8

11. Takeda K, Takanami K, Shirata Y, Yamamoto T, Takahashi N, Ito K, et al. Clinical utility of texture analysis of 18F-FDG PET/CT in patients with stage I lung cancer treated with stereotactic body radiotherapy. *J Radiat Res* (2017) 58:862–9. doi: 10.1093/jrr/rrx050

12. Zhou Y, Ma XL, Pu LT, Zhou RF, Ou XJ, Tian R, et al. Prediction of overall survival and progression-free survival by the (18)F-FDG PET/CT radiomic features in patients with primary gastric diffuse Large b-cell lymphoma. *Contrast media Mol imaging.* (2019) 2019:5963607. doi: 10.1155/2019/5963607

13. Xie M, Wu K, Liu Y, Jiang Q, Xie Y. Predictive value of f-18 FDG PET/CT quantization parameters in diffuse large b cell lymphoma: A meta-analysis with 702 participants. *Med Oncol (Northwood London England).* (2015) 32:446. doi: 10.1007/s12032-014-0446-1

14. Zhang X, Chen L, Jiang H, He X, Feng L, Ni M, et al. A novel analytic approach for outcome prediction in diffuse large b-cell lymphoma by [(18)F]FDG PET/CT. *Eur J Nucl Med Mol imaging.* (2022) 49:1298–310. doi: 10.1007/s00259-021-05572-0

15. Cui XW, Hocke M, Jenssen C, Ignee A, Klein S, Schreiber-Dietrich D, et al. Conventional ultrasound for lymph node evaluation, update 2013. *Z Gastroenterol* (2014) 52:212–21. doi: 10.1055/s-0033-1356153

16. Dissaux G, Visvikis D, Da-Ano R, Pradier O, Chajon E, Barillot I, et al. Pretreatment (18)F-FDG PET/CT radiomics predict local recurrence in patients treated with stereotactic body radiotherapy for early-stage non-small cell lung cancer: A multicentric study. *J Nucl Med* (2020) 61:814–20. doi: 10.2967/jnumed.119.228106

17. Jiang Y, Yuan Q, Lv W, Xi S, Huang W, Sun Z, et al. Radiomic signature of (18)F fluorodeoxyglucose PET/CT for prediction of gastric cancer survival and chemotherapeutic benefits. *Theranostics* (2018) 8:5915–28. doi: 10.7150/thno.28018

18. Zhou Y, Su GY, Hu H, Ge YQ, Si Y, Shen MP, et al. Radiomics analysis of dual-energy CT-derived iodine maps for diagnosing metastatic cervical lymph nodes in patients with papillary thyroid cancer. *Eur radiology.* (2020) 30:6251–62. doi: 10.1007/s00330-020-06866-x

19. Peng H, Dong D, Fang MJ, Li L, Tang LL, Chen L, et al. Prognostic value of deep learning PET/CT-based radiomics: Potential role for future individual induction chemotherapy in advanced nasopharyngeal carcinoma. *Clin Cancer Res* (2019) 25:4271–9. doi: 10.1158/1078-0432.Ccr-18-3065

20. Forgacs A, Pall Jonsson H, Dahlbom M, Daver F, DiFranco MD, Opposits G, et al. A study on the basic criteria for selecting heterogeneity parameters of F18-FDG PET images. *PloS One* (2016) 11:e0164113. doi: 10.1371/journal.pone.0164113

21. Zhou Y, Zhu Y, Chen Z, Li J, Sang S, Deng S, et al. Radiomic features of (18) F-FDG PET in Hodgkin lymphoma are predictive of outcomes. *Contrast media Mol imaging.* (2021) 2021:6347404. doi: 10.1155/2021/6347404

22. de Jesus FM, Yin Y, Mantzorou-Kyriaki E, Kahle XU, de Haas RJ, Yakar D, et al. Machine learning in the differentiation of follicular lymphoma from diffuse large b-cell lymphoma with radiomic [(18)F]FDG PET/CT features. *Eur J Nucl Med Mol imaging.* (2022) 49:1535–43. doi: 10.1007/s00259-021-05626-3

23. Lu W, Zhong L, Dong D, Fang M, Dai Q, Leng S, et al. Radiomic analysis for preoperative prediction of cervical lymph node metastasis in patients with papillary thyroid carcinoma. *Eur J Radiol* (2019) 118:231–8. doi: 10.1016/j.ejrad.2019.07.018

24. Jiang M, Li C, Tang S, Lv W, Yi A, Wang B, et al. Nomogram based on shear-wave elastography radiomics can improve preoperative cervical lymph node staging for papillary thyroid carcinoma. *Thyroid* (2020) 30:885–97. doi: 10.1089/thy.2019.0780

25. Conti A, Duggento A, Indovina I, Guerrisi M, Toschi N. Radiomics in breast cancer classification and prediction. *Semin Cancer Biol* (2021) 72:238–50. doi: 10.1016/j.semcancer.2020.04.002

26. Liu Y, Chen J, Zhang C, Li Q, Zhou H, Zeng Y, et al. Ultrasound-based radiomics can classify the etiology of cervical lymphadenopathy: A multi-center retrospective study. *Front Oncol* (2022) 12:856605. doi: 10.3389/fonc.2022.856605

27. Coskun N, Okudan B, Uncu D, Kitapci MT. Baseline 18F-FDG PET textural features as predictors of response to chemotherapy in diffuse large b-cell lymphoma. *Nucl Med Commun* (2021) 42:1227–32. doi: 10.1097/mnm.0000000000001447

28. Giovagnorio F, Galluzzo M, Andreoli C, De CM, David V. Color Doppler sonography in the evaluation of superficial lymphomatous lymph nodes. *J Ultrasound Med* (2002) 21:403–8. doi: 10.7863/jum.2002.21.4.403

29. Yu Y, Tan Y, Xie C, Hu Q, Ouyang J, Chen Y, et al. Development and validation of a preoperative magnetic resonance imaging radiomics-based signature to predict axillary lymph node metastasis and disease-free survival in patients with early-stage breast cancer. *JAMA Netw Open* (2020) 3:e2028086. doi: 10.1001/jamanetworkopen.2020.28086

30. Sun J, Yang Q, Lu Z, He M, Gao L, Zhu M, et al. Distribution of lymphoid neoplasms in China: analysis of 4,638 cases according to the world health organization classification. *Am J Clin Pathol* (2012) 138:429–34. doi: 10.1309/ajcp7yltqpusdq5c

31. Aoki R, Karube K, Sugita Y, Nomura Y, Shimizu K, Kimura Y, et al. Distribution of malignant lymphoma in Japan: analysis of 2260 cases, 2001-2006. *Pathol Int* (2008) 58:174–82. doi: 10.1111/j.1440-1827.2007.02207.x

32. Xia Y, Huang S, Wang Y, Lei D, Wang Y, Yang H, et al. Prognostication of primary tumor location in early-stage nodal diffuse Large b-cell lymphoma: An analysis of the SEER database. *Cancers (Basel)* (2021) 13(2):3954. doi: 10.3390/cancers13163954

33. Colomo L, López-Guillermo A, Perales M, Rives S, Martínez A, Bosch F, et al. Clinical impact of the differentiation profile assessed by immunophenotyping in patients with diffuse large b-cell lymphoma. *Blood* (2003) 101:78–84. doi: 10.1182/blood-2002-04-1286

34. Song MK, Chung JS, Sung-Yong O, Lee GW, Kim SG, Seol YM, et al. Clinical impact of bulky mass in the patient with primary extranodal diffuse large b cell lymphoma treated with r-CHOP therapy. *Ann Hematol* (2010) 89:985–91. doi: 10.1007/s00277-010-0964-7

35. Castillo JJ, Winer ES, Olszewski AJ. Sites of extranodal involvement are prognostic in patients with diffuse large b-cell lymphoma in the rituximab era: an analysis of the surveillance, epidemiology and end results database. *Am J Hematol* (2014) 89:310–4. doi: 10.1002/ajh.23638

36. Dlouhy I, Karube K, Enjuanes A, Salaverria I, Nadeu F, Ramis-Zaldivar JE, et al. Revised international prognostic index and genetic alterations are associated with early failure to r-CHOP in patients with diffuse large b-cell lymphoma. *Br J Haematol* (2022) 196:589–98. doi: 10.1111/bjh.17858

37. Akyurek N, Uner A, Benekli M, Barista I. Prognostic significance of MYC, BCL2, and BCL6 rearrangements in patients with diffuse large b-cell lymphoma treated with cyclophosphamide, doxorubicin, vincristine, and prednisone plus rituximab. *Cancer* (2012) 118:4173–83. doi: 10.1002/cncr.27396

38. Hu S, Xu-Monette ZY, Tzankov A, Green T, Wu L, Balasubramanyam A, et al. MYC/BCL2 protein coexpression contributes to the inferior survival of activated b-cell subtype of diffuse large b-cell lymphoma and demonstrates high-risk gene expression signatures: a report from the international DLBCL rituximab-CHOP consortium program. *Blood* (2013) 121:4021–4031; quiz 4250. doi: 10.1182/blood-2012-10-460063

39. Li M, Zhang QL, Zhao W, Huang X, Gong LP, Shi Q, et al. [The incidence of high-grade b-cell lymphoma with MYC and BCL2 and/or BCL6 rearrangements in diffuse large b-cell lymphoma]. *Zhonghua Xue Ye Xue Za Zhi.* (2021) 42:124–8. doi: 10.3760/cma.j.issn.0253-2727.2021.02.006

40. Youk JH, Kwak JY, Lee E , Son EJ, Kim JA. Grayscale ultrasound radiomic features and shear-wave elastography radiomic features in benign and malignant breast masses. *Ultraschall der Med (Stuttgart Germany 1980).* (2020) 41:390–6. doi: 10.1055/a-0917-6825

41. Trenker C, Neesse A, Görg C. Sonographic patterns of renal lymphoma in b-mode imaging and in contrast-enhanced ultrasound (CEUS)–a retrospective evaluation. *Eur J Radiol* (2015) 84:807–10. doi: 10.1016/j.ejrad.2014.12.027

42. Rettenbacher T. Sonography of peripheral lymph nodes part 2: Doppler criteria and typical findings of distinct entities. *Ultraschall der Med (Stuttgart Germany 1980).* (2014) 35:10–27; quiz 28-32. doi: 10.1055/s-0033-1355593

43. McKay MJ, Taubman KL, Lee S, Scott AM. Radiotherapy planning of lymphomas: role of metabolic imaging with PET/CT. *Ann Nucl Med* (2022) 36:162–71. doi: 10.1007/s12149-021-01703-7

44. Eertink JJ, van de Brug T, Wiegers SE, Zwezerijnen GJC, Pfaehler EAG, Lugtenburg PJ, et al. (18)F-FDG PET baseline radiomics features improve the prediction of treatment outcome in diffuse large b-cell lymphoma. *Eur J Nucl Med Mol imaging.* (2022) 49:932–42. doi: 10.1007/s00259-021-05480-3

45. Parvez A, Tau N, Hussey D , Maganti M, Metser U. (18)F-FDG PET/CT metabolic tumor parameters and radiomics features in aggressive non-hodgkin's lymphoma as predictors of treatment outcome and survival. *Ann Nucl Med* (2018) 32:410–6. doi: 10.1007/s12149-018-1260-1

46. Aide N, Talbot M, Fruchart C, Damaj G, Lasnon C. Diagnostic and prognostic value of baseline FDG PET/CT skeletal textural features in diffuse large b cell lymphoma. *Eur J Nucl Med Mol imaging.* (2018) 45:699–711. doi: 10.1007/s00259-017-3899-6

47. Cottereau AS, Nioche C, Dirand AS, Clerc J, Morschhauser F, Casasnovas O, et al. (18)F-FDG PET dissemination features in diffuse Large b-cell lymphoma are predictive of outcome. *J Nucl Med* (2020) 61:40–5. doi: 10.2967/jnumed.119.229450

frontiers | Frontiers in Oncology

TYPE Original Research
PUBLISHED 06 February 2023
DOI 10.3389/fonc.2023.992096

OPEN ACCESS

EDITED BY
Jiansong Ji,
Lishui Central Hospital, China

REVIEWED BY
Marta Zerunian,
Sapienza University of Rome, Italy
Alessandro Stefano,
National Research Council (CNR), Italy

*CORRESPONDENCE
Xiaoyu Cui
cuixy@bmie.neu.edu.cn
Hongshan Zhong
hszhong@cmu.edu.cn

†These authors have contributed equally to this work and share first authorship

SPECIALTY SECTION
This article was submitted to Cancer Imaging and Image-directed Interventions, a section of the journal Frontiers in Oncology

RECEIVED 12 July 2022
ACCEPTED 12 January 2023
PUBLISHED 06 February 2023

CITATION
Qu H, Zhai H, Zhang S, Chen W, Zhong H and Cui X (2023) Dynamic radiomics for predicting the efficacy of antiangiogenic therapy in colorectal liver metastases. *Front. Oncol.* 13:992096. doi: 10.3389/fonc.2023.992096

Dynamic radiomics for predicting the efficacy of antiangiogenic therapy in colorectal liver metastases

Hui Qu[1†], Huan Zhai[2,3†], Shuairan Zhang[4], Wenjuan Chen[5], Hongshan Zhong[2,3*] and Xiaoyu Cui[1,6*]

[1]College of Medicine and Biological Information Engineering, Northeastern University, Shenyang, Liaoning, P.R, China, [2]Department of Interventional Radiology, First Affiliated Hospital of China Medical University, Shenyang, Liaoning, China, [3]Key Laboratory of Diagnostic Imaging and Interventional Radiology of Liaoning Province, First Affiliated Hospital of China Medical University, Shenyang, Liaoning, China, [4]Department of Gastroenterology, First Affiliated Hospital of China Medical University, Shenyang, China, [5]Department of Medical Oncology, The First Affiliated Hospital of China Medical University, Shenyang, Liaoning, China, [6]Key Laboratory of Intelligent Computing in Medical Image, Ministry of Education, Shenyang, China

Background and objective: For patients with advanced colorectal liver metastases (CRLMs) receiving first-line anti-angiogenic therapy, an accurate, rapid and noninvasive indicator is urgently needed to predict its efficacy. In previous studies, dynamic radiomics predicted more accurately than conventional radiomics. Therefore, it is necessary to establish a dynamic radiomics efficacy prediction model for antiangiogenic therapy to provide more accurate guidance for clinical diagnosis and treatment decisions.

Methods: In this study, we use dynamic radiomics feature extraction method that extracts static features using tomographic images of different sequences of the same patient and then quantifies them into new dynamic features for the prediction of treatmentefficacy. In this retrospective study, we collected 76 patients who were diagnosed with unresectable CRLM between June 2016 and June 2021 in the First Hospital of China Medical University. All patients received standard treatment regimen of bevacizumab combined with chemotherapy in the first-line treatment, and contrast-enhanced abdominal CT (CECT) scans were performed before treatment. Patients with multiple primary lesions as well as missing clinical or imaging information were excluded. Area Under Curve (AUC) and accuracy were used to evaluate model performance. Regions of interest (ROIs) were independently delineated by two radiologists to extract radiomics features. Three machine learning algorithms were used to construct two scores based on the best response and progression-free survival (PFS).

Results: For the task that predict the best response patients will achieve after treatment, by using ROC curve analysis, it can be seen that the relative change rate (RCR) feature performed best among all features and best in linear discriminantanalysis (AUC: 0.945 and accuracy: 0.855). In terms of predicting PFS, the Kaplan–Meier plots suggested that the score constructed using the RCR features could significantly distinguish patients with good response from those with poor response (Two-sided P<0.0001 for survival analysis).

Conclusions: This study demonstrates that the application of dynamic radiomics features can better predict the efficacy of CRLM patients receiving antiangiogenic therapy compared with conventional radiomics features. It allows patients to have a more accurate assessment of the effect of medical treatment before receiving treatment, and this assessment method is noninvasive, rapid, and less expensive. Dynamic radiomics model provides stronger guidance for the selection of treatment options and precision medicine.

KEYWORDS

colorectal cancer liver metastases, radiomics, dynamic radiomics, antiangiogenic therapy, efficacy prediction

1 Introduction

Colorectal cancer (CRC) is the fourth most common malignancy worldwide, with approximately 800,000 newly diagnosed cases each year (1). CRC accounts for approximately 10% of all tumors (2). The liver is the most common metastatic site for CRC, and approximately a quarter of all patients with CRC have liver metastases (3, 4). Surgery is the best treatment for colorectal cancer liver metastases (CRLMs). At present, judging whether CRLM patients can undergo surgery is mainly based on two aspects: "technical" and "oncological". For the "technical" definition of resectable CRLM, the current consensus is that complete macroscopic resection is feasible while maintaining at least 30% of future liver remnants (FLRs) or a residual liver to body weight ratio >0.5. The "oncological" criteria for resectable CRLM mainly consider that patients can achieve higher disease-free survival and cure rate, and based on the number of this lesion ≥ 5, concomitant unresectable extrahepatic lesions and tumor progression are contraindications for surgery in patients with CRLM (5). Under these criteria surgical resection can only be applied to a limited number of cases, and the probability of postoperative recurrence of the liver is extremely high (6). Inhibition of angiogenesis during tumor growth is the standard treatment for unresectable CRLM. Antiangiogenic drugs (e.g., bevacizumab) are currently used in combination with chemotherapy in patients with CRLM (7). However, the patient response to this treatment varies, and there are currently no good indicators for predicting the efficacy of treatment (8). Therefore, it is important to accurately and noninvasively predict the response of CRLM patients to the initial treatment.

Radiomics is a promising and noninvasive method that analyzes traditional medical images to extract quantifiable data, which show the biological characteristics of pathological processes at the microscopic level (9, 10). These data can be converted into image-based signatures to improve the accuracy of diagnosis, prognosis and prediction of cancer patients. Computed tomography (CT) has the advantages of repeatability, standardization, and extraction of quantitative data. It is indispensable in diagnosis and follow-up (11). Although some PET and MRI based radiomics studies have achieved remarkable results in the field of metastatic colorectal cancer (12, 13), CT based imaging criteria are still the preferred criteria for evaluation of tumor drug response in clinical trials so far. CT-based radiomics has been shown to help predict therapy response and outcome in multiple cancers, including CRC (14–16). Ligero et al. verified that their established CT-based radiomics signature is associated with the response of a variety of advanced solid tumors to immune checkpoint inhibitors (17). Jain et al. predicted the overall survival (OS) and response to chemotherapy of small cell lung cancer (SCLC) patients based on the radiomic features within and around lung tumors extracted from CT images (18). In predicting the efficacy and prognosis of CRLM after treatment, Wei et al. constructed a deep learning-based radiomics model using CT images to predict the response of CRLM to advanced first-line chemotherapy, with an AUC of 0.935 in the validation cohort (19); Liu et al. constructed a CT-based radiomics model to predict the survival of unresectable colorectal liver metastases treated with hepatic arterial infusion chemotherapy, and the c-index of the test group reached 0.743 (20).

On the other hand, although various imaging modalities such as ultrasound (US), computed tomography (CT), magnetic resonance imaging (MRI), and positron emission tomography/computed tomography (PET/CT) can be used for the diagnosis and evaluation of CRLM, CT is still the current method of choice for the diagnosis and treatment of CRLM (21, 22). Previous studies have shown that the sensitivity and specificity of CT for the diagnosis of CRLM are 82.1% and 73.5%, respectively (23).

Existing radiomics features were mainly analyzed based on static medical images at one time point. However, the occurrence and development of tumors is a dynamic process, and static image features cannot contain more dynamic information. For this reason, Carvalho et al. proposed "delta radiomics", which can represent the change in radiomics characteristics over time (24). This approach can provide additional information to identify, quantify, and potentially predict treatment-induced changes during treatment and has been shown to have potential for predicting treatment efficacy and prognosis in colorectal (25) esophageal (26), pancreatic (27), and lung (28) cancers. To improve the workflow and specific techniques of radiomics related to time series, Qu et al. proposed a feature extraction method called dynamic radiomics (29, 30). This method can use multiple series of images from the same type of imaging examination to jointly extract features to delineate the changes in features over time.

For antiangiogenic therapy, the number of blood vessels in the tumor is a common indicator used to evaluate its efficacy (31). In the process of contrast-enhanced CT (CECT), after intravenous injection of contrast medium, tumor vascularity can be effectively observed by comparing the images acquired at different vascular phases (32), while dynamic radiomics features can reflect the changes in the scanned images at different periods and then indirectly evaluate the vascularity of tumors. Therefore, this method is suitable for assessing the efficacy of antiangiogenic therapy. In this retrospective study, dynamic radiomics was applied to predict the efficacy of antiangiogenic therapy for the first time. Compared with conventional radiomics, the model constructed by this method can more accurately predict patient response to treatment and progression-free survival (PFS). Achieve more efficient and precise assessment of patients before they receive treatment. It is helpful for clinicians to make clinical decisions and stratify patients' prognosis.

2 Materials and methods

2.1 Patients

The entire cohort was enrolled from June 2016 to June 2021 by reviewing records of the institutional Picture Archiving and Communication System (PACS, Philips) for the identification of patients with histologically confirmed CRLM. A total of 76 patients were confirmed to meet the criteria and all included patients were from single center. The inclusion criteria for this study were as follows: (1) patients were older than 18 years; (2) colorectal adenocarcinoma with liver metastasis was confirmed by histopathological examination; (3) no surgery or other therapy prior to first-line treatment; (4) advanced first-line treatment with bevacizumab combined with a standard chemotherapy regimen (FOLFOX/XELOX/FOLFIRI) was used; (5) first-line treatment evaluation information based on Response Evaluation Criteria in Solid Tumors (RECIST) was available; (6) baseline images of abdominal CECT before first-line treatment were available, which needed to include images in the precontrast phase (PP), arterial phase (AP), portal venous phase (PVP) and delay phase (DP); and (7) the interval between abdominal CT examination and histopathological diagnosis was less than 31 days (range 4–30 days). The exclusion criteria were as follows: (1) the patient had more than one primary tumor site; (2) the CT image quality was poor due to patient respiration or motion artifacts; (3) the patient's margin was too blurred to delineate; (4) the patient's clinical data were missing; and (5) the patient's advanced first-linetreatment had not been completed or the best efficacy had not been reached. Clinical information included age, sex, primary tumor location (left-sided, right-sided and rectum), primary tumor size, and serum carcinoembryonic antigen (CEA) and alpha-fetoprotein (AFP) results at baseline.

This retrospective study was conducted in accordance with the principles of the Declaration of Helsinki and approved by the Ethics Committee of the First Affiliated Hospital of China Medical University, with a waiver of the requirement for informed consent based on its retrospective design.

2.2 CT protocol

The contrast administration of abdomen CT scans are patient specific and based on clinical guidelines (33). Sixty-four-slice spiral CT scanners were used to collect the image data of the patients according to a standardized scanning protocol (34). The CT manufacturers used included GE, Phillips, Siemens and Toshiba. The acquisition methods of each CT phase are as follows: Routine plain scan was performed to obtain PP, then 1.2-1.5 mL/kg body weight iohexol was injected intravenously with a high-pressure syringe at a flow rate of 2.5 mL/s, followed by a 20-30 mL saline flush. Patients were imaged in the supine position at full inspiration. AP was obtained 30-35 s after intravenous injection of contrast, PVP was obtained 60-75 s after intravenous injection of contrast, and DP was obtained 100-120 s after intravenous injection of contrast. As shown in Table 1, the scanning parameters were as follows: tube voltage 120 kVp (range 100-140 kVp), layer thickness 2 mm, matrix 512 × 512, tube current 333 mA (range 100-752 mA), exposure time 751 ms (range 500-1782 ms), and standardreconstruction algorithm.

All steps were in accordance with the Image Biomarker Standardization Initiative (IBSI) standards. The CT images were stored in DICOM format. Prior to radiographic analysis, each image was examined to ensure that the images collected were suitable for analysis (35).

2.3 Lesion segmentation

The CT images were anonymized for all personal and institutional data and labeled with random numbers. For each patient, metastatic liver lesion with the largest cross-sectional area and well-defined margin was selected as target lesion for segmentation, and lesions were segmented separately at different phases. The specific process wasas follows: First, all CT images (PP, AP, PVP and DP) of 76 lesions were contoured slice by slice using a soft tissue window (window width: 350 HU, window level: 40 HU) for selected liver lesions using a semiautomatic fast marching segmentation algorithm. Then, the images were manually modified and segmented using open-source 3D-Slicer software (www.slicer.org) by two radiologists with 10 years of work experience to remove adjacent normal tissues or surrounding bile ducts. In case of contradiction, othersenior radiologists (over 20 years of work experience) would assess the tumor mask again for agreement. CT images in DICOM format were imported into 3D-Slicer software, and regions of interest (ROIs) were subsequently exported into Nearly Raw Raster Data (NRRD) and Medical Reality Markup Language (MRML) formats for storage and further analysis.

TABLE 1 Equipment parameters of this study.

Manufacturers: Toshiba, GE, Phillips and Siemen
Tube voltage: 120 kVp (range 100–140*kVp*)
Slice thickness: 2.0 mm
Matrix: 512×512
Tube current: 333 mA (range 100–752 mA)
Exposure time: 751 ms (range 500–1782 ms)

2.4 Feature extraction

The radiomics features of the ROIs were extracted using the "PyRadiomics" package in the Python environment. The extracted radiomics features could be divided into the following categories: first-order features, shape-based features, texture features and wavelet features. First-order features describe the distribution of the ROI's endogenous intensities (36). Shape-based features capture the intuitive features of the ROI into two-dimensional and three-dimensional sizes and shapes. These features are independent of the grayscale intensity distribution in the ROI. Texture features were extracted based on five texture matrices: (1) gray level co-occurrence matrix (GLCM), (2) gray level size zone matrix (GLSZM), (3) gray level running length matrix (GLRLM), (4) neighboring gray level difference matrix (NGTDM) and (5) gray level dependence matrix (GLDM) (37). Wavelet features refer to the characteristics of different frequency bands extracted from the wavelet decomposition of the image (38). Based on the suggestions of Pyradiomics developers, we used the following initial settings for feature extraction: 'binWidth' = 25; 'Interpolator' = sitk.sitkBSpline; 'resampledPixelSpacing' = [1, 1, 1]; 'voxelArrayShift' = 1000; 'normalize'= True; 'normalizeScale' = 100.

2.5 Dynamic feature construction

Dynamic radiomics features use the static feature changes of different series of the same imaging examination or different imaging examinations to construct new features that can describe the change rule, which can be expressed as:

$$\phi(\psi(x(t_1)), \psi(x(t_2)), \cdots, \psi(x(t_k))) \tag{1}$$

where $\phi(\cdot)$ represents the conversion from static radiomic features to dynamic radiomic features, $\psi(\cdot)$ represents the process of extracting static features from images, and $x(t_k)$ represents a series of medical images.

According to the number of series collected and the feature extraction method, 5 construction methods of dynamic features are proposed:

(1) Standard discrete (SD) feature:

$$SD(\psi(x(t))) = \frac{1}{k}\sum_{i=1}^{k}|\psi(x(t_i)) - \psi(x(\bar{t}))| \tag{2}$$

(2) Discrete change (DC) feature:

$$DC(\psi(x(t))) = (\frac{1}{k}\sum_{i=1}^{k}|\psi(x(t_i)) - \psi(x(\bar{t}))|)/\psi(x(\bar{t})) \tag{3}$$

(3) Relative change rate (RCR):

$$RCR(\psi(x(t))) = \frac{|\psi(x(t_j)) - \psi(x(t_i))|}{\psi(x(t_i))}, 1 \le j \le i \le k \tag{4}$$

(4) Relative average change rate (RACR):

$$RACR(\psi(x(t))) = \frac{|\psi(x(t_j)) - \psi(x(t_i))|}{\psi(x(\bar{t}))}, 1 \le j \le i \le k \tag{5}$$

(5) Ploy (P) feature:

$$\begin{cases} \hat{\theta} = \arg\min \sum_{i=1}^{k}(\psi(x(t_i)) - m(t_i, \theta)) \\ m(t_i, \theta) = \sum_{i=1}^{k} a_i \cdot t_i, \theta = (a_1, a_2 \cdots a_7)^T \end{cases} \tag{6}$$

where the set θ of P features is calculated based on the least-squares estimation model.

2.6 Evaluation

The patients were divided into two groups according to the best response to first-line treatment: those who achieved objective response (OR) and those who did not achieve objective response (NOR). Objective response was defined as achievement of complete response (CR) or partial response (PR) according to Response Evaluation Criteria in Solid Tumors (RECIST) criteria version 1.1 (39). Due to the small number of samples included, we employed leave-one-out cross-validation to measure the prediction performance of different features in different algorithms. We used the t test to screen the features that differed between the OR and NOR groups and then used the least absolute shrinkage and selection operator (Lasso) to reduce the dimensionality of the training set to obtain the required features for the training model. For comparison with traditional radiomics, in addition to the five constructed dynamic features, we included the static features of different series and the collection of static features for modeling. In the training cohort, three machine learning methods were used to construct the scores for the prediction of the efficacy of chemotherapy + bevacizumab, including support vector machine (SVM), linear discriminant analysis (LDA) and random forest (RF). Among all kinds of features, the one with the best predictive performance was selected.

The features with the best performance in the classification task were used for univariate Cox regression analysis to select the features related to Progression-free survival (PFS) ($P < 0.05$), and a PFS-based efficacy prediction score was constructed using a random survival forest model. PFS was defined as the time from randomization to the first occurrence of disease progression or death from any cause.

2.7 Statistical analysis

The area under the receiver operating characteristic (ROC) curve (AUC) in the validation dataset was analyzed using the "pROC" package in R, and the performance of different prediction scores was compared using the AUC and accuracy. Time-dependent ROC curves were plotted using the ßurvivalROC" package in R, and the predictive performance of the model at 90, 180, 270 and 360 days was evaluated using AUCs. We used the "rms" package to draw nomograms, and calibration curves were used to assess the discriminability of the nomograms. Kaplan–Meier plots were constructed to analyze potential differences in PFS between the high-risk and low-risk groups. All statistical analyses were performed using R (version 4.1.1). Fisher's exact test was used to determine whether there were significant differences in clinical variables between the OR and NOR groups. Two-sided p values<0.05 were considered statistically significant.

3 Results

3.1 Patient characteristics

A total of 76 patients (40 males and 36 females, median age of 60 years, age range between 36 and 76 years) diagnosed with CRLM at the First Affiliated Hospital of China Medical University were enrolled in this study. Figure 1 shows the patient recruitment process. Based on the best response, the patients were divided into an OR group (33 patients) and an NOR group (43 patients). As shown in Table 2, no significant differences in other clinical variables were found between these two groups. Our work flow diagram is shown in Figure 2.

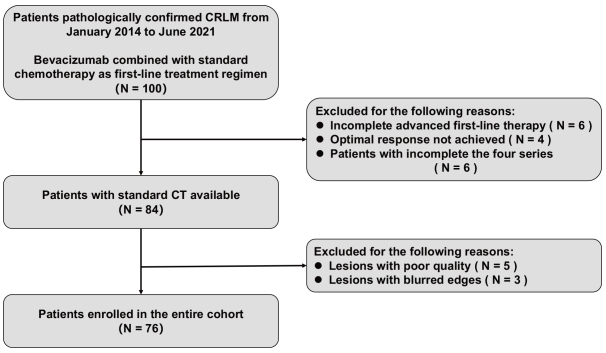

FIGURE 1
Flow chart of the enrolled patients in the study.

3.2 Construction and validation of classification prediction scores

After excluding features with the same values in all patients (40), we obtained 1329 radiomic features and constructed dynamic features using static features from four different vascular phases. After performing a t test (P s 0.05), we further screened features on the training set using Lasso. Table 3 and Table 4 show the performance of different features in test samples after cross-validation based on the leave-one-out method.

Of the three machine learning methods, all five dynamic features showed their best predictive performance in LDA (Figures 3A–C). Compared with other dynamic features, RCR features showed the best classification performance in all three machinelearning methods. As shown in Table 5, after lasso processing, the RCR features constructed from each of the 16 radiomics features were selected for constructing machine learning models. In the LDA model, the RCR AUC and accuracy in the validation data reached 0.945 and 0.855, respectively. It also had the best performance compared to all static features (Figures 3D-F).

Previous studies have shown that age, sex, and CEA and AFP levels are also factors predicting the efficacy of bevacizumab (41, 42), so we used these variables and our best predictive score (the result of RCR features in the LDA model) to construct a nomogram (Figure 4A). The calibration curves of the nomogram showed good agreement between the classification results predicted by the nomogram and the actual observations (Figure 4C).

3.3 Efficacy prediction model based on PFS

We selected the RCR features with the best performance in the classification task, constructed a PFS-based efficacy prediction model using leave-one-out cross-validation + random survival forest, and divided the patients into high- and low-risk groups according to the median risk score. Kaplan–Meier plots demonstrated a significant difference (P <0.0001) in PFS between the two groups (Figure 5A). The time-dependent ROC curve indicated that the PFS-based prediction score had good predictive power at different time points (Figure 5B). We also constructed a nomogram (Figure 4B), and survival calibration plots showed that the survival probabilities predicted by the nomogram also had good agreement with the actual observations (Figure 4D).

4 Discussion

In this study, we use a new dynamic radiomics feature extraction method and workflow based on multiple series. The extraction of all dynamic features is based on static feature extraction, which describes the variation of static features at different times. In the study by Qu et al., it had been confirmed that dynamic radiomics had better predictive performance compared with traditional radiomics in the

TABLE 2 Baseline clinical characteristics of the patients.

	NOR,n(%)	OR,n(%)	P value
Total	43	33	
Sex			
male	20 (46.5)	20 (60.6)	0.323
female	23 (53.5)	13 (39.4)	
Tumor site			
left	11 (25.6)	12 (36.4)	0.597
rectum	17 (39.5)	11 (33.3)	
right	15 (34.9)	10 (30.3)	
Tumor size (mean (SD))	4.28 (2.55)	3.50 (2.15)	0.165
CEA			
normal	4 (9.3)	5 (15.2)	0.671
high	39 (90.7)	(84.8)	
AFP			
normal	41 (95.3)	31 (93.9)	1
high	2 (4.7)	2 (6.1)	
Age			
≤55	11 (25.6)	11 (33.3)	0.629
>55	32 (74.4)	22 (66.7)	

P values were derived from Fisher's exact test.

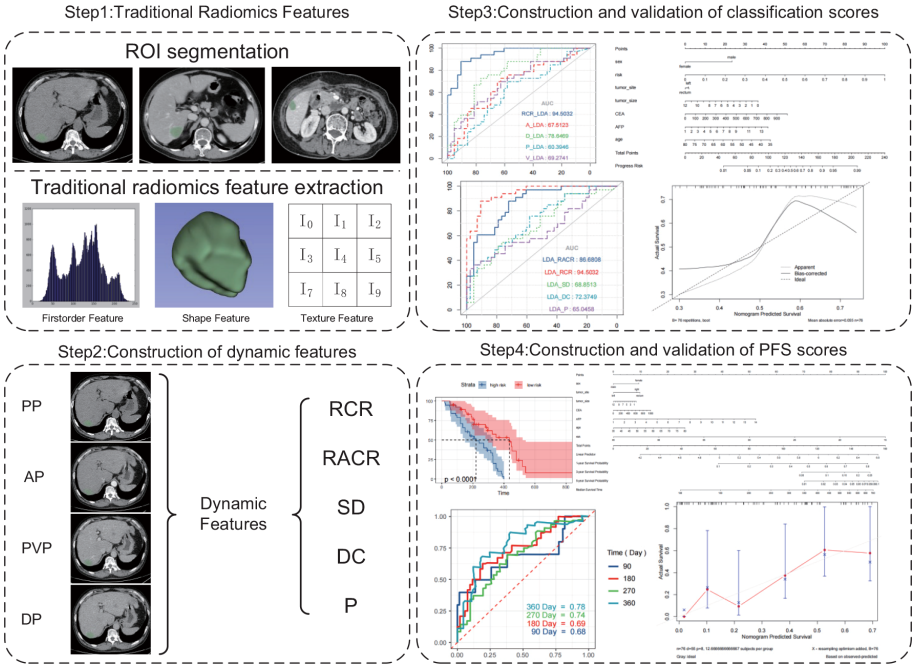

FIGURE 2
Workflow of the necessary steps in this study.

tasks of tumor diagnosis prediction, tumor patient gene mutation status prediction and patient prognosis prediction (29). We used this method to predict both the response to antiangiogenic therapy and PFS in patients with CRLM. Compared with traditional radiomics, the prediction performance of dynamic features is greatly improved and superior to that of clinical predictors (36, 37) (Figure S1, Figure S2).

In the field of CRC, radiomics has been widely used for diagnosis and predicting prognosis and the efficacy of drugs (43–45). In recent years, the analysis of CRLM using image features extracted by deep learning has also been common in radiology. Shi et al. used an artificial neural network (ANN) model to predict the mutation status of RAS and BRAF genes in CRLM patients (35). Zhu et al. used deep learning-assisted magnetic resonance imaging to predict tumor response to chemotherapy in CRLM patients (46). Starmans et al. used deep learning to differentiate the pure histopathological growth patterns of CRLM on CT (47). Compared with deep learning and traditional radiomic features, dynamic features have the following advantages. (1) Compared with traditional radiomic features, dynamic features can reflect changes in the static features of all sequences, so this method can extract more features and information for model construction. (2) Dynamic features calculate the relative changes in static features. Therefore, dynamic features are less affected by image quality differences between different series of the same patient or between different patients. (3) Compared with deep learning features, dynamic features are easier to interpret and

TABLE 3 Prediction AUCs based on various dimensions of LDA, RF and SVM.

	LDA	RF	SVM
RACR	0.867	0.780	0.822
RCR	0.945	0.841	0.908
SD	0.689	0.623	0.662
DC	0.724	0.615	0.716
P	0.651	0.631	0.671
AP	0.675	0.574	0.618
DP	0.787	0.666	0.749
PP	0.604	0.635	0.548
PVP	0.693	0.768	0.591
Multi_static	0.853	0.642	0.817

Multi_static refers to the feature set analysis of multiple series.

TABLE 4 Prediction accuracies based on various dimensions of LDA, RF and SVM.

	LDA	RF	SVM
RACR	0.737	0.684	0.737
RCR	0.855	0.803	0.803
SD	0.658	0.605	0.632
DC	0.645	0.592	0.618
P	0.605	0.645	0.618
AP	0.605	0.540	0.553
DP	0.737	0.658	0.645
PP	0.592	0.526	0.526
PVP	0.618	0.763	0.526
Multi_static	0.763	0.592	0.724

Where Multi_static refers to the feature set analysis of multiple series.

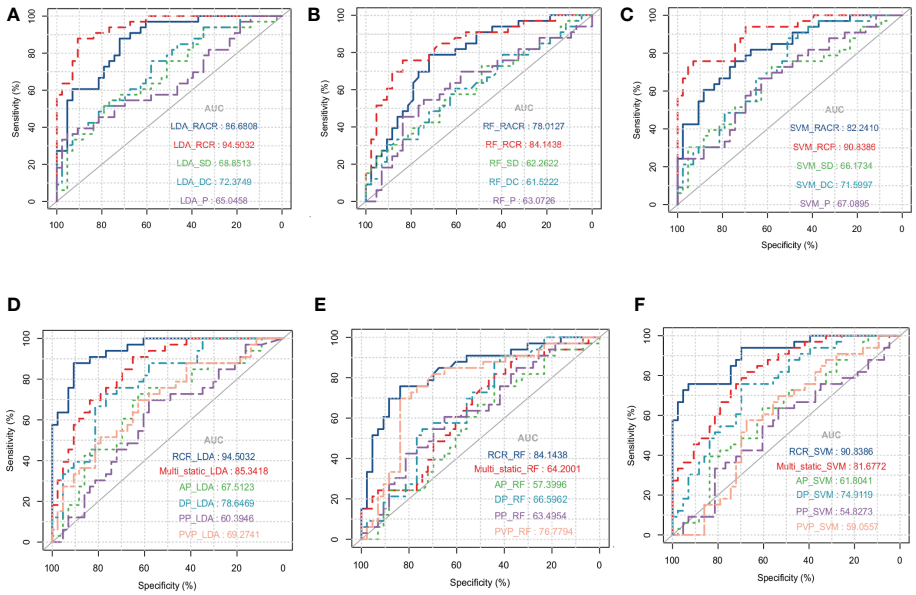

FIGURE 3
ROC curves for LDA **(A)**, RF **(B)** and SVM **(C)** models with different dynamic features when using leave-one-out cross-validation. ROC curves for LDA **(D)**, RF **(E)**, and SVM **(F)** models with static features of different series and RCR features when using leave-one-out cross-validation, where Multi_static refers to the feature set analysis of multiple series.

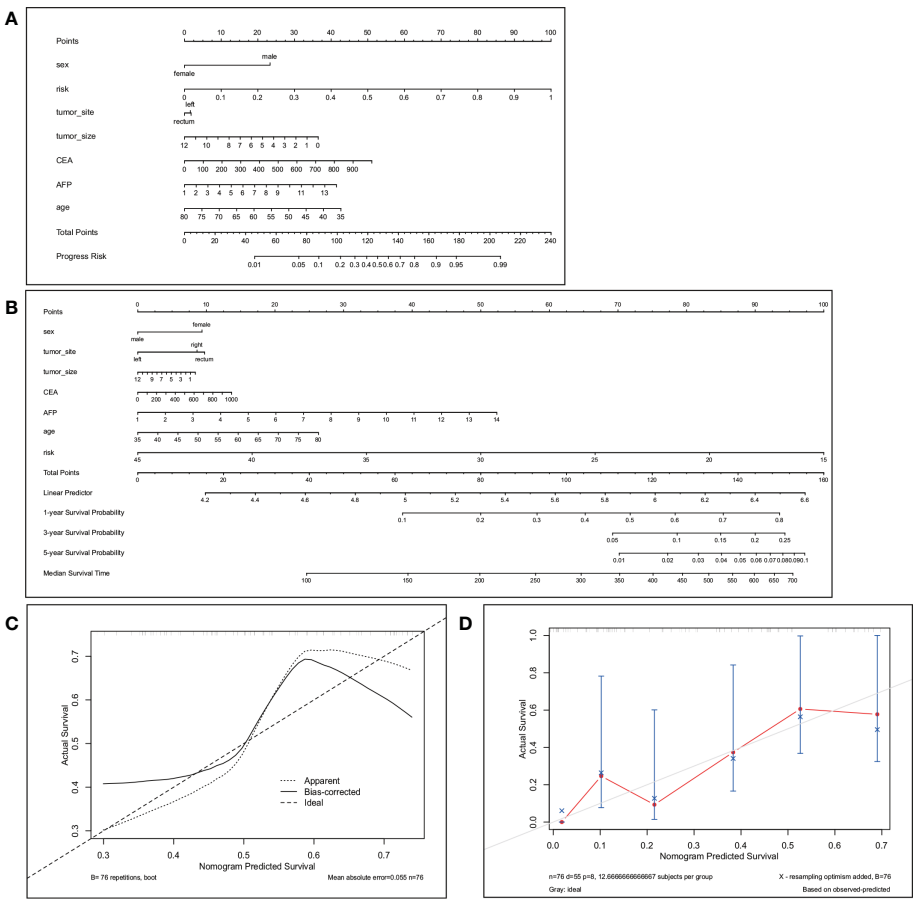

FIGURE 4
The nomogram **(A)** predicts the best response in patients with CRLM. The total score is calculated by summing the points for each factor. The total score corresponds to the patient's best response prediction. **(C)** is the calibration curve corresponding to the nomogram. The nomogram **(B)** predicts 1-year, 3-year and 5-year PFS in patients with CRLM. Total points are calculated by summing the points for each factor. The total score corresponds to the 1-, 3-, and 5-year PFS probabilities of the patients. **(D)** Calibration plots to predict 1-year progression-free survival (PFS).

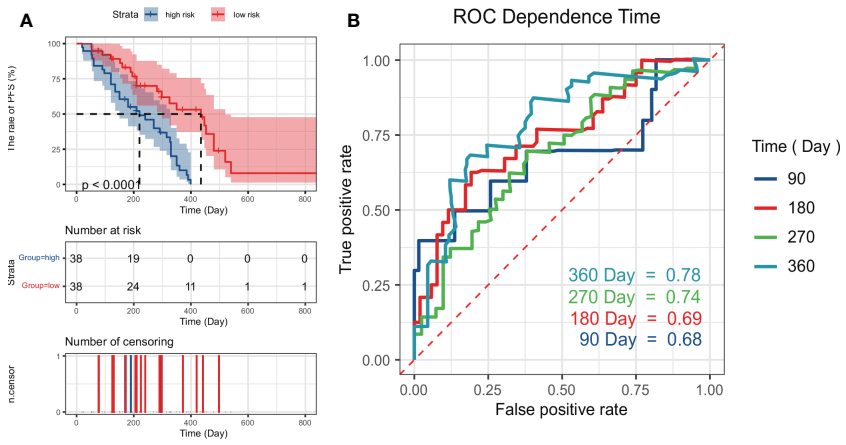

FIGURE 5
Kaplan–Meier plots **(A)** obtained by dividing patients into high-risk and low-risk groups using the median predictive score of the random survival forest model; **(B)** shows ROC curves estimated at 90, 180, 270, and 360 days using the predictive scores.

TABLE 5 Radiomics features used to construct RCR features obtained after lasso selecting.

Radiomics feature
wavelet.HHH_glszm_LowGrayLevelZoneEmphasis
wavelet.HHL_glrlm_RunEntropy
wavelet.HLH_glcm_Imc2
wavelet.LHH_firstorder_Median
wavelet.HLL_glcm_MCC
original_shape_Elongation
wavelet.HHH_glszm_SizeZoneNonUniformityNormalized
wavelet.LHH_firstorder_Skewness
wavelet.LLL_glcm_Idn
wavelet.LLH_glszm_SizeZoneNonUniformityNormalized
exponential_glrlm_RunVariance
squareroot_glcm_DifferenceEntropy
wavelet.HLH_glszm_HighGrayLevelZoneEmphasis
wavelet.HLH_ngtdm_Contrast
wavelet.HLL_glszm_LowGrayLevelZoneEmphasis
wavelet.LHL_firstorder_Mean

therefore more acceptable to doctors (48). (4) Compared with deep learning, it is suitable for small sample research and more suitable for medical (49). (5) Different sequences of medical images are considered, which is more consistent with the actual image diagnostic process of doctors (21).

In this study, the RCR feature had the best prediction performance among all models, which may be because it contains the relationship between any two sequences, contains the most features and has less information about the whole population. Further research is needed on how to optimize other dynamic features and explore how to select features for different tasks.

Lesion segmentation is a critical task for both radiomics and dynamic radiomics. Stefano et al. discussed the impact of manual segmentation and semi-automated segmentation on radiomics studies in their study (50), and the authors concluded that manual flexible delineation of targets allows highly accurate segmentation. However, manual segmentation is labor-intensive and time-consuming and is less feasible due to tasks with large data. Moreover, manual segmentation results are easily influenced by observer subjectivity. Therefore, many semi-automatic delineation algorithms are applied in practice, such as region growing or thresholding. But the result of semi-automatic segmentation is not as precise as manual segmentation. In this paper, we used manual segmentation to delineate ROIs for the following reasons: (1) the data volume in this study was small, which requires us to minimize bias as much as possible in the operation, while the results of manual segmentation are more accurate; (2) the additional workload due to the use of manual segmentation in this study is acceptable; (3) in order to reduce the influence of subjective factors on the segmentation results, each lesion was segmented independently by two radiologists. Once their segmentedresults were quite different, a senior physician would adjudicate the results to ensure the accuracy of the results.

As Pasini et al. reported in their study (51), due to the use of four different CT scanners, some analysis is necessary to assess whether there is a batch effect. For this reason, we performed principal component analysis (PCA) on the RCR features finally adopted in this paper, and the results are shown in Figure S3. No significant batch effects was observed among the data collected by different scanners. Therefore, we did not use any statistical harmonization methods such as ComBat to calibrate the data.

Despite the good results achieved by dynamic features, our study still has some limitations. First, the data in this study were collected retrospectively. Secondly, although omitted leave-one-out cross-validation was used to test the performance of models, the insufficient sample size may still lead to the bias of the results, requiring very large datasets and multicenter data for prospective investigation to further verify the robustness and reproducibility of our conclusions. Despite these limitations, we believe that the results obtained in this study are credible and can be extended to a larger patient population.

5 Conclusion

In this study, dynamic radiomic feature extraction and workflow were used to predict the efficacy of advanced first-line chemotherapy combined with antiangiogenic therapy in patients with CRLM. While retaining the advantages of traditional radiomics, such as non-invasive, rapid and inexpensive, the dynamic radiomics model achieved higher accuracy than radiomics in predicting both optimal efficacy and PFS. The application of dynamic radiomics to predict the efficacy of antiangiogenic therapy has strong clinical significance and broad development prospect.

Data availability statement

Due to privacy restrictions, the datasets presented in this article are not publicly available. Requests to access the datasets should be directed to Xiaoyu Cui, cuixy@bmie.neu.edu.cn.

Ethics statement

The studies involving human participants were reviewed and approved by the First Affiliated Hospital of China Medical University. Written informed consent for participation was not required for this study in accordance with the national legislation and the institutional requirements.

Author contributions

Conceptualization, XC and HSZ; methodology, HQ; validation, HQ, SZ and HZ; formal analysis, HQ and SZ; resources, HZ; data curation, WC; writing—original draft preparation, HQ; writing—review and editing, HZ; supervision, XC; project administration, HSZ; funding acquisition, HSZ and XC. All authors contributed to reviewing and revising the manuscript.

Funding

This study was supported by The National Hi-Technology Research and Development Program (863 Program, No.2012 AA022701); The Fundamental Research Funds for the Central Universities N2219001; Ningbo Science and Technology Bureau (Grant No. 2021Z027) and Natural Science Foundation of Liaoning Province (Grant No.2022-MS-105).

Acknowledgments

We thank Professor Haibo Shao, Department of Interventional Therapy, First Affiliated Hospital of China Medical University, for his comments and suggestions to improve the quality of this paper.

Conflict of interest

The authors declare that the research was conducted in the absence of any commercial or financial relationships that could be construed as a potential conflict of interest.

Publisher's note

All claims expressed in this article are solely those of the authors and do not necessarily represent those of their affiliated organizations, or those of the publisher, the editors and the reviewers. Any product that may be evaluated in this article, or claim that may be made by its manufacturer, is not guaranteed or endorsed by the publisher.

Supplementary material

The Supplementary Material for this article can be found online at: https://www.frontiersin.org/articles/10.3389/fonc.2023.992096/full#supplementary-material

References

1. Siegel RL, Miller KD, Miller KD. Ca: a cancer journal for clinician. *Cancer Stat* (2020) 70:7–30. doi: 10.3322/caac.21590

2. Song JH, Jeong JU, Lee JH. Korean Clinical practice guideline for, c. rectal cancer, preoperative chemoradiotherapy versus postoperative chemoradiotherapy for stage ii-iii resectable rectal cancer: a meta-analysis of randomized controlled trials. *Radiat Oncol J* (2017) 35:198–207. doi: 10.3857/roj.2017.00059

3. Lentz RW, Messersmith WA. Transarterial radioembolization in patients with unresectable colorectal cancer liver metastases. *J Clin Oncol* (2021) 39:3887–9. doi: 10.1200/JCO.21.01993

4. Fiorentini G, Sarti D, Nardella M. Transarterial chemoembolization alone or followed by bevacizumab for treatment of colorectal liver metastases. *Hepatic Oncol* (2022) 9:Hep40. doi: 10.2217/hep-2020-0031

5. Van Cutsem E, Cervantes A, Adam R. Esmo consensus guidelines for the management of patients with metastatic colorectal cancer. *Ann Oncol* (2016) 27:1386–422. doi: 10.1093/annonc/mdw235

6. Jones RP, Kokudo N, Folprecht G. Colorectal liver metastases: A critical review of state of the art. *Liver Cancer* (2016) 6:66–71. doi: 10.1159/000449348

7. Romero-Lorca A, Novillo A, Gaibar M. Mir-7, mir-10a and mir-143 expression may predict response to bevacizumab plus chemotherapy in patients with metastatic colorectal cancer. *Pharmacogenomics personalized Med* (2021) 14:1263–73. doi: 10.2147/PGPM.S313594

8. Azam F, Mehta S, Harris AL. Mechanisms of resistance to antiangiogenesis therapy. *Eur J Cancer* (2010) 46:1323–32. doi: 10.1016/j.ejca.2010.02.020

9. Alahmari SS, Cherezov D, Goldgof D. Delta radiomics improves pulmonary nodule malignancy prediction in lung cancer screening. *IEEE Access* (2018) 6:77796–806. doi: 10.1109/ACCESS.2018.2884126

10. de la Pinta C, Castillo ME, Collado M. Radiogenomics: Hunting down liver metastasis in colorectal cancer patients. *Front Neurosci* (2021) 13:5547. doi: 10.3390/cancers13215547

11. Freeman M, Laks S. Surveillance imaging for metastasis in high-risk melanoma: importance in individualized patient care and survivorship. *Front Neurosci* (2019) 6: MMT12. doi: 10.2217/mmt-2019-0003

12. Alongi P, Stefano A, Comelli A. Artificial intelligence applications on restaging [18f]fdg pet/ct in metastatic colorectal cancer: A preliminary report of morpho-functional

radiomics classification for prediction of disease outcome. *Appl Sci* (2022) 12:2941. doi: 10.3390/app12062941

13. Granata V, Fusco R, De Muzio F. Radiomics and machine learning analysis based on magnetic resonance imaging in the assessment of colorectal liver metastases growth pattern. *Diagnostics* (2022) 12:1115. doi: 10.3390/diagnostics12051115

14. Sun R, Limkin EJ, Vakalopoulou M. A radiomics approach to assess tumour-infiltrating cd8 cells and response to anti-pd-1 or anti-pd-l1 immunotherapy: an imaging biomarker, retrospective multicohort study. *Lancet Oncol* (2018) 19:1180–91. doi: 10.1016/S1470-2045(18)30413-3

15. Trebeschi S, Drago SG, Birkbak NJ. Predicting response to cancer immunotherapy using noninvasive radiomic biomarkers. *Ann Oncol* (2019) 30:998–1004. doi: 10.1093/annonc/mdz108

16. Peng J, Huang J, Huang G. Predicting the initial treatment response to transarterial chemoembolization in intermediate-stage hepatocellular carcinoma by the integration of radiomics and deep learning. *Front Oncol* (2021) 11:730282. doi: 10.3389/fonc.2021.730282

17. Ligero M, Garcia-Ruiz A, Viaplana C. A ct-based radiomics signature is associated with response to immune checkpoint inhibitors in advanced solid tumors. *Radiology* (2021) 299:109–19. doi: 10.1148/radiol.2021200928

18. Jain P, Khorrami M, Gupta A. Novel non-invasive radiomic signature on ct scans predicts response to platinum-based chemotherapy and is prognostic of overall survival in small cell lung cancer. *Front Oncol* (2021) 11:744724. doi: 10.3389/fonc.2021.744724

19. Wei J, Cheng J, Gu D. Deep learning-based radiomics predicts response to chemotherapy in colorectal liver metastases. *Med Phys* (2020) 48:513–22. doi: 10.1002/mp.14563

20. Liu P, Zhu H, Zhu H. Predicting survival for hepatic arterial infusion chemotherapy of unresectable colorectal liver metastases: Radiomics analysis of pretreatment computed tomography. *J Trans Internal Med* (2022) 10:56–64. doi: 10.2478/jtim-2022-0004

21. Xu LH, Cai SJ, Cai GX. Imaging diagnosis of colorectal liver metastases. *World J Gastroenterol* (2011) 17:4654–9. doi: 10.3748/wjg.v17.i42.4654

22. Baghdadi A, Mirpour S, Ghadimi M. Imaging of colorectal liver metastasis. *J Gastrointestinal Surg* (2022) 26:245–57. doi: 10.1007/s11605-021-05164-

23. Choi SH, Kim SY, Park SH. Diagnostic performance of ct, gadoxetate disodium-enhanced mri, and pet/ct for the diagnosis of colorectal liver metastasis: Systematic review and meta-analysis. *J Magnetic Resonance Imaging* (2018) 47:1237–50. doi: 10.1002/jmri.25852

24. Carvalho S, Leijenaar RTH, Troost EGC. 42 - Early variation of FDG-PET radiomics features in NSCLC is related to overall survival - the 'delta radiomics' concept. *Radiother Oncol* (2016) 118(2016):S20–S21. doi: 10.1016/S0167-8140(16)30042-1

25. Chiloiro G, Rodriguez-Carnero P, Lenkowicz J. Delta radiomics can predict distant metastasis in locally advanced rectal cancer: The challenge to personalize the cure. *Front Oncol* (2020) 10:595012. doi: 10.3389/fonc.2020.595012

26. Wang L, Gao Z, Li C. Computed tomography-based delta-radiomics analysis for discriminating radiation pneumonitis in patients with esophageal cancer after radiation therapy. *Int J Radiat oncology biology Phys* (2021) 111:443–55. doi: 10.1016/j.ijrobp.2021.04.047

27. Nasief H, Hall W, Zheng C. Improving treatment response prediction for chemoradiation therapy of pancreatic cancer using a combination of delta-radiomics and the clinical biomarker ca19-9. *Front Oncol* (2019) 9:1464. doi: 10.3389/fonc.2019.01464

28. Khorrami M, Prasanna P, Gupta A. Changes in ct radiomic features associated with lymphocyte distribution predict overall survival and response to immunotherapy in non-small cell lung cancer. *Cancer Immunol Res* (2020) 8:108–19. doi: 10.1158/2326-6066.CIR-19-0476

29. Qu H, Shi R, Li S. Dynamic radiomics: A new methodology to extract quantitative time-related features from tomographic images. *Appl Intell* (2022) 52:11827–45. doi: 10.1007/s10489-021-03053-3

30. Chen X, Ma K. Neoadjuvant therapy in lung cancer: What is most important: Objective response rate or major pathological response? *Curr Oncol* (2021) 28:4129–38. doi: 10.3390/curroncol28050350

31. Zhang Q, Wu J, Bai X. Evaluation of intra-tumoral vascularization in hepatocellular carcinomas. *Front Med* (2020) 7:584250. doi: 10.3389/fmed.2020.584250

32. Van Camp L, Deak P, Haspeslagh M. A prospective clinical study using a dynamic contrast-enhanced ct-protocol for detection of colorectal liver metastases. *Eur J Radiol* (2018) 107:143–8. doi: 10.1016/j.ejrad.2018.08.022

33. Xu Y, Hosny A, Zeleznik R. Deep learning predicts lung cancer treatment response from serial medical imaging. *Clin Cancer Res* (2019) 25:3266–75. doi: 10.1158/1078-0432.CCR-18-2495

34. Rios Velazquez E, Parmar C, Liu Y. Somatic mutations drive distinct imaging phenotypes in lung cancer. *Cancer Res* (2017) 77:3922–30. doi: 10.1158/0008-5472.CAN-17-0122

35. Shi R, Chen W, Yang B. Prediction of kras, nras and braf status in colorectal cancer patients with liver metastasis using a deep artificial neural network based on radiomics and semantic features. *Am J Cancer Res* (2020) 10:4513–26.

36. Larue RT, Defraene G, De Ruysscher D. Quantitative radiomics studies for tissue characterization: a review of technology and methodological procedures. *Br J Radiol* (2017) 90:20160665. doi: 10.1259/bjr.20160665

37. Mayerhoefer ME, Materka A, Langs G. Introduction to radiomics. *J Nucl Med* (2020) 61:488–95. doi: 10.2967/jnumed.118.222893

38. Aerts HJ, Velazquez ER, Leijenaar RTH. Decoding tumour phenotype by noninvasive imaging using a quantitative radiomics approach. *Nat Commun* (2014) 5:4006. doi: 10.1038/ncomms5006

39. Li S, Zheng T, Fan Z, Qu H, Wang J, Bi J. A dynamic-static combination model based on radiomics features for prostate cancer using multiparametric MRI. *Phys Med Biol* (2022) 68:(1). doi: 10.1088/1361-6560/aca954

40. Zhang YC, Li M, Jin YM. Radiomics for differentiating tumor deposits from lymph node metastasis in rectal cancer. *World J Gastroenterol* (2022) 28:3960–70. doi: 10.3748/wjg.v28.i29.3960

41. Rehman AH, Jones RP, Poston G. Prognostic and predictive markers in liver limited stage iv colorectal cancer. *Eur J Surg Oncol* (2019) 45:2251–6. doi: 10.1016/j.ejso.2019.06.038

42. Jones RP, Brudvik KW, Franklin JM. Precision surgery for colorectal liver metastases: Opportunities and challenges of omics-based decision making. *Eur J Surg Oncol* (2017) 43:875–83. doi: 10.1016/j.ejso.2017.02.014

43. Huang YQ, Liang CH, He L. Development and validation of a radiomics nomogram for preoperative prediction of lymph node metastasis in colorectal cancer. *J Clin Oncol* (2016) 34:2157–64. doi: 10.1200/JCO.2015.65.9128

44. Han Y, Chai F, Wei J. Identification of predominant histopathological growth patterns of colorectal liver metastasis by multi-habitat and multi-sequence based radiomics analysis. *Front Oncol* (2020) 10:1363. doi: 10.3389/fonc.2020.01363

45. Li M, Li X, Guo Y. Development and assessment of an individualized nomogram to predict colorectal cancer liver metastases. *Quantitative Imaging Med Surg* (2020) 10:397–414. doi: 10.21037/qims.2019.12.16

46. Zhu HB, Xu D, Ye M. Deep learning-assisted magnetic resonance imaging prediction of tumor response to chemotherapy in patients with colorectal liver metastases. *Int J Cancer* (2021) 148:1717–30. doi: 10.1002/ijc.33427

47. Starmans MPA, Buisman FE, Renckens M, Willemssen FEJA, van der Voort SR, Groot Koerkamp B. Distinguishing pure histopathological growth patterns of colorectal liver metastases on ct using deep learning and radiomics: a pilot study. *Clin Exp Metastasis* (2021) 38(5):483–94. doi: 10.1007/s10585-021-10119-6

48. Miller T. Explanation in artificial intelligence: Insights from the social sciences. *Artif Intell* (2019) 267:1–38. doi: 10.1016/j.artint.2018.07.007

49. Suk H. An introduction to neural networks and deep learning. *Deep Learn Med Image Anal* (2017), 3–24.

50. Stefano A, Leal A, Richiusa S. Robustness of pet radiomics features: Impact of co-registration with mri. *Appl Sci* (2021) 11:10170. doi: 10.3390/app112110170

51. Pasini G, Bini F, Russo G. Matradiomics: A novel and complete radiomics framework, from image visualization to predictive model. *J Imaging* (2022) 8:221. doi: 10.3390/jimaging8080221

frontiers | Frontiers in Oncology

TYPE Original Research
PUBLISHED 16 March 2023
DOI 10.3389/fonc.2023.1006172

OPEN ACCESS

EDITED BY
Kaustav Bera,
Maimonides Medical Center, United States

REVIEWED BY
Zhongxiang Ding,
Zhejiang University, China
Bilgin Kadri Aribas,
Bülent Ecevit University, Türkiye
Wenjie Liang,
Zhejiang University, China
Zhenzhou Yang,
Chongqing Medical University, China

*CORRESPONDENCE
Meihao Wang
wzwmh@wmu.edu.cn
Jiansong Ji
jijiansong@zju.edu.cn

†These authors have contributed equally to this work

SPECIALTY SECTION
This article was submitted to Cancer Imaging and Image-directed Interventions, a section of the journal Frontiers in Oncology

RECEIVED 29 July 2022
ACCEPTED 06 March 2023
PUBLISHED 16 March 2023

CITATION
Su Y, Lu C, Zheng S, Zou H, Shen L, Yu J, Weng Q, Wang Z, Chen M, Zhang R, Ji J and Wang M (2023) Precise prediction of the sensitivity of platinum chemotherapy in SCLC: Establishing and verifying the feasibility of a CT-based radiomics nomogram.
Front. Oncol. 13:1006172.
doi: 10.3389/fonc.2023.1006172

Precise prediction of the sensitivity of platinum chemotherapy in SCLC: Establishing and verifying the feasibility of a CT-based radiomics nomogram

Yanping Su[1,2,3,4†], Chenying Lu[1,4†], Shenfei Zheng[1,4], Hao Zou[1,4], Lin Shen[1,4], Junchao Yu[1,4], Qiaoyou Weng[1,4], Zufei Wang[1,4], Minjiang Chen[1,4], Ran Zhang[5], Jiansong Ji[1,4*] and Meihao Wang[2,3*]

[1]Key Laboratory of Imaging Diagnosis and Minimally Invasive Intervention Research, Institute of Imaging Diagnosis and Minimally Invasive Intervention Research, The Fifth Affiliated Hospital of Wenzhou Medical University, Lishui, Zhejiang, China, [2]Department of Radiology, Key Laboratory of Intelligent Medical Imaging of Wenzhou, Institute of Aging, The First Affiliated Hospital of Wenzhou Medical University, Wenzhou Medical University, Wenzhou, Zhejiang, China, [3]Key Laboratory of Alzheimer's Disease of Zhejiang, Wenzhou, Zhejiang, China, [4]Clinical College of The Affiliated Central Hospital, School of Medicine, Lishui University, Lishui, Zhejiang, China, [5]AI Research Department, Huiying Medical Technology Co., Ltd, Beijing, China

Objectives: To develop and validate a CT-based radiomics nomogram that can provide individualized pretreatment prediction of the response to platinum treatment in small cell lung cancer (SCLC).

Materials: A total of 134 SCLC patients who were treated with platinum as a first-line therapy were eligible for this study, including 51 patients with platinum resistance (PR) and 83 patients with platinum sensitivity (PS). The variance threshold, SelectKBest, and least absolute shrinkage and selection operator (LASSO) were applied for feature selection and model construction. The selected texture features were calculated to obtain the radiomics score (Rad-score), and the predictive nomogram model was composed of the Rad-score and the clinical features selected by multivariate analysis. Receiver operating characteristic (ROC) curves, calibration curves, and decision curves were used to assess the performance of the nomogram.

Results: The Rad-score was calculated using 10 radiomic features, and the resulting radiomics signature demonstrated good discrimination in both the training set (area under the curve [AUC], 0.727; 95% confidence interval [CI], 0.627–0.809) and the validation set (AUC, 0.723; 95% CI, 0.562–0.799). To improve diagnostic effectiveness, the Rad-score created a novel prediction nomogram by combining CA125 and CA72-4. The radiomics nomogram showed good calibration and discrimination in the training set (AUC, 0.900; 95% CI, 0.844-0.947) and the validation set (AUC, 0.838; 95% CI, 0.534-0.735). The radiomics nomogram proved to be clinically beneficial based on decision curve analysis.

Conclusion: We developed and validated a radiomics nomogram model for predicting the response to platinum in SCLC patients. The outcomes of this model can provide useful suggestions for the development of tailored and customized second-line chemotherapy regimens.

KEYWORDS

radiomics, computed tomography, small cell lung cancer, chemotherapy, platinum

1 Introduction

Small cell lung cancer (SCLC), the most aggressive kind of lung cancer, accounts for approximately 14% of all lung cancer types and has a 5-year overall survival (OS) rate of just 6.7%. Due to its strong invasiveness, medication resistance, and the fact that no new, effective treatments have been developed in recent years (1, 2). Etoposide and platinum (EP) chemotherapy are the standard first-line therapies for SCLC, with initial response rates of 70–80% and high chemotherapeutic sensitivity. However, almost all patients will experience progression (3, 4). According to current studies, platinum-sensitive (PS) patients have a 15% to 20% better response rate to conventional second-line platinum chemotherapy than platinum-resistant (PR) patients, and their OS can be increased by 2-3 months (2, 5–7). For PS patients, the median PFS from the time of EP rechallenge as second-line treatment was 5.5 months, but PR patients had limited efficacy. Therefore, platinum reactivation is recommended for PS patients as second-line treatment, while PR patients are recommended to undergo topotecan treatment and other clinical trials. Thus, individualized second-line therapy based on an evaluation of platinum sensitivity is essential for improving the overall survival of SCLC patients (8–12).

Several studies have sought to use serum indicators and genetic tissue features to predict the responses to platinum in SCLC. SCLC is composed of four distinct subtypes, each of which reacts differently to platinum-based chemotherapy. The percentage of each subtype in the tumor influences how sensitive it is to platinum-based chemotherapy as a whole. However, the majority of SCLC tissue test samples are collected using needle biopsy, which unavoidably results in test variance and instability of prediction results (13). Other studies have attempted to use peripheral blood indices such as LDH and the systemic immune-inflammation index to predict the OS and PFS of SCLC (14, 15). However, the basic peripheral blood information is unconvincing, and these studies do not account for the tumor's size, shape, location, or other relevant factors. Compared with the above methods, radiomics nomograms can be combined with radiomic and clinical features for noninvasive diagnosis, prognosis evaluation, and treatment response prediction. Previous studies have demonstrated that features based on radiomics are inextricably linked to underlying genomic patterns across a range of cancer types (16–18). Several studies using radiomics to predict platinum resistance in non-small cell lung cancer have been reported, and their radiomics models have shown excellent diagnostic efficacy (19–23). Nonetheless, there is no radiomics model for predicting platinum resistance in SCLC.

In this study, we aimed to develop and validate a CT-based radiomics nomogram that can provide individualized pretreatment prediction of the response to platinum treatment in SCLC, while effectively integrating image texture features and clinical factors. Using this nomogram, clinicians can enhance the treatment plan before initiating platinum-based chemotherapy and direct second-line therapy, optimize existing treatment combinations, and increase patient survival.

2 Materials and methods

2.1 Patients

The study was approved by the Institutional Review Board and Human Ethics Committee of the Fifth Affiliated Hospital of Wenzhou Medical University, and the requirement for informed consent was waived. Patients who were diagnosed with pathologically confirmed SCLC from February 2014 to November 2021 were enrolled. A total of 134 patients were included according to the following inclusion criteria: (1) they underwent a CT examination before treatment; (2) they used platinum derivatives on a regular basis in first-line chemotherapy and had never received any other treatment before; (3) dynamic CT follow-up was performed during treatment; and (4) endpoint events occurred. A total of 133 patients were excluded due to the following factors: (1) they were not treated in our hospital (n = 74); (2) they underwent other chemotherapy regimens or treatments (n = 30); (3) they underwent surgical resection (n = 16); (4) there was no follow-up after treatment (n = 9); and (5) no endpoint events occurred during follow-up (n = 4). Finally, 134 patients were selected for the present study. The flow of the case identification process is shown in Figure 1.

2.2 Endpoints

We evaluated the tumor response of SCLC patients who received CT examinations during platinum chemotherapy based

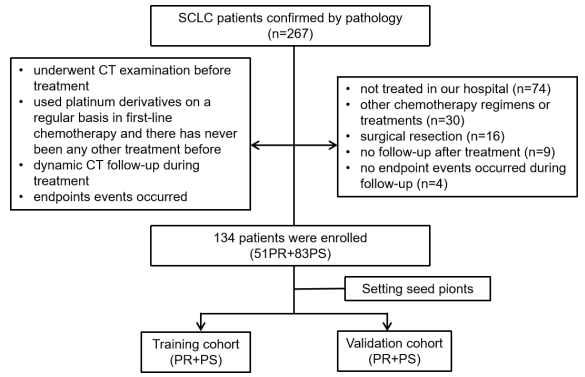

FIGURE 1
Flowchart of study enrollment.

on the modified Response Evaluation Criteria in Solid Tumors (mRECIST). The corresponding mRECIST responses were as follows: (1) complete response (CR): complete tumor disappearance; (2) partial response (PR): a minimum of 30% decrease in the sum of target lesion diameters; (3) progressive disease (PD): a minimum of 20% increase in the sum of target lesion diameters; and (4) stable disease (SD): neither PR nor PD. In this study, all patients underwent CT before and after platinum treatment, and the endpoint event was defined as the occurrence of PD. The patients were divided into PR and PS groups according to whether the time from platinum chemotherapy to the first PD was within 6 months. Representative CT images for PR and PS patients are shown in Figure 2.

2.3 CT image acquisition and interpretation

The patients underwent nonenhanced CT scans with a 256-slice Philips Brilliance iCT system prior to treatment (Philips Medical Systems). The following are the detailed acquisition parameter settings: tube voltage 120 kV, reference tube current 113 mAs, automatic millisecond technology, scanning field of view (SFOV) 15-20 cm, tube rotation time 0.75 s/circle, collimation width 80 mm (128×0.625 mm), reconstruction thickness 0.9 mm, reconstruction interval 0.45 mm, reconstruction matrix 1024× 1024, using the iDose3 iterative reconstruction algorithm.

Two thoracic radiologists with 5 and 15 years of experience (Y.S. and C.L.) independently conducted retrospective reviews. Disagreements were settled by a third radiologist who had 25 years of experience (J.J.). The image features included the following: (1) number of lesions and (2) volume, measured using the Extended Brilliance Workspace and Lung Nodule Assessment software (Philips); (3) location: central or peripheral; (4) morphology: regular or irregular; (5) shape: regular or irregular; (6) lobulation (present/absent); (7) necrosis (present/absent); (8) hydrothorax (present/absent); (9) intratumoral calcification (present/absent); (10) staging (limited-stage/extensive-stage); and (11) metastasis (lymph den/bone/parenchyma organ/cardiovascular/pleural and pericardium).

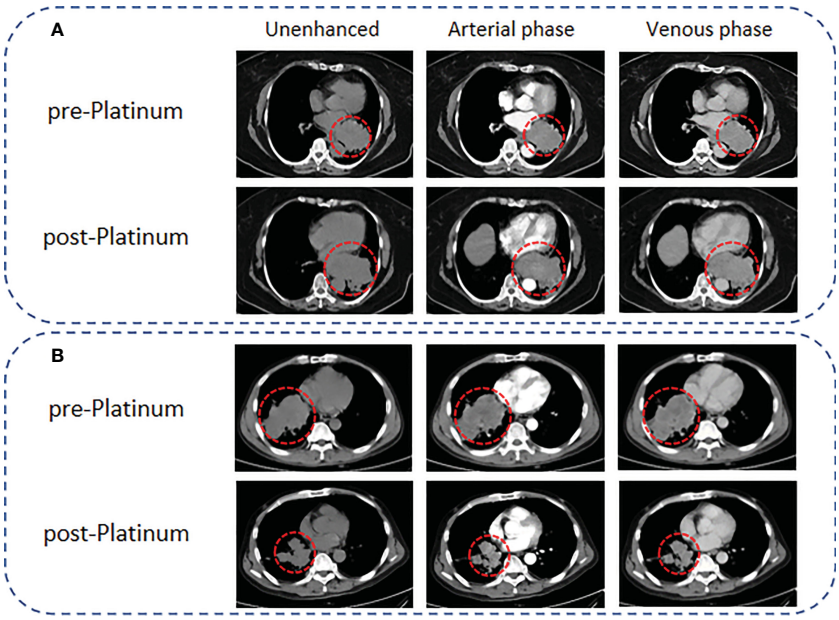

FIGURE 2
Representative CT images for PR and PS of SCLC patients according to the mRECIST criteria. **(A)** A 65-year-old female SCLC patient with a lesion diameter of 71 mm underwent CT scanning 1 week before EP chemotherapy, followed by CT scanning 2 months later. The lesion diameter increased to 97 mm, and the results showed that the patient presented with PR. **(B)** A 54-year-old male SCLC patient with a lesion diameter of 95 mm. CT scanning was performed 1 week before EP chemotherapy, and follow-up CT examinations were performed regularly after EP chemotherapy. Ten months later, the lesion diameter decreased to 56 mm, and the results showed that the patient presented with PS.

2.4 Tumor segmentation of volumes of interest and extraction of radiomic features

The radiomics workflow is shown in Figure 3. Tumors and mediastinal lymph nodes fused with tumors in the mediastinal window were included in the volume of interest (VOI). First, a radiologist (reader 1, Y. S, a radiologist with five years of chest imaging experience) manually annotated 3D tumor VOIs around the largest lesion using the Radcloud platform (Huiying Medical Technology Co., Ltd, http://mics.radcloud.cn). To evaluate the reproducibility of the extracted features, reader 2 (C. L, a radiologist with 15 years of chest imaging experience) independently segmented 10% of lesions randomly selected from both the PR and PS groups.

For each VOI on our CT images, 1,409 radiomic features were extracted using a tool from the Radcloud platform, which extracted radiomic features from medical image data with a large panel of engineered hard-coded feature algorithms (https://pyradiomics.readthedocs.io/en/latest/features.html). The 1,409 features obtained were divided into four main categories: first-order statistics, shape, texture [gray-level cooccurrence (GLCM), gray-level run length (GLRLM), gray-level size zone (GLSZM), neighboring gray tone difference (NGTDM), gray-level dependence (GLDM), Matrices], and higher-order statistics (Laplacian of Gaussian, wavelet, square, square root, logarithm, exponential, gradient, and local binary pattern filters) features.

The intraclass correlation coefficient (ICC) was used to validate the reproducibility of extracted features from the two radiologists. Radiomic features with intra-ICCs >0.75 were selected for the subsequent statistical analysis.

2.5 Construction of a radiomics signature and assessment of performance

In the imaging and storage of medical images, to make the intensity information consistent, the following formula was used to normalize all the radiomic features of CT images.

$$f(x) = \frac{s(x - u_x)}{\sigma_x}$$

Where $f(x)$ is the normalized intensity, x is the original intensity, μ and σ are the mean value and variance, respectively, and s represents an optional scaling whose default is 1.

The samples were randomly divided into a training cohort (n=58, 70%) and a validation cohort (n=25, 30%). To reduce the redundant features, the feature selection methods included the variance threshold, SelectKBest, and the least absolute shrinkage and selection operator (LASSO). For the variance threshold method, the threshold is 0.8, so that the eigenvalues of the variance smaller than 0.8 are removed. The SelectKBest method, which is a single-variable feature selection method, uses the p value to analyze the relationship between the features and the classification results; all the features with a p value smaller than 0.05 are used. For the LASSO model, L1 regularization is used as the cost function, the error value of cross-validation is 10, and the maximum number of iterations is 1,000. Subsequently, the radiomic parameters with nonzero coefficients in the LASSO model generated by the entire training cohort with the optimal a were selected. The radiomics signature (i.e., Rad-score) was computed for each lesion by a linear combination of the selected features as weighted by their respective quotient.

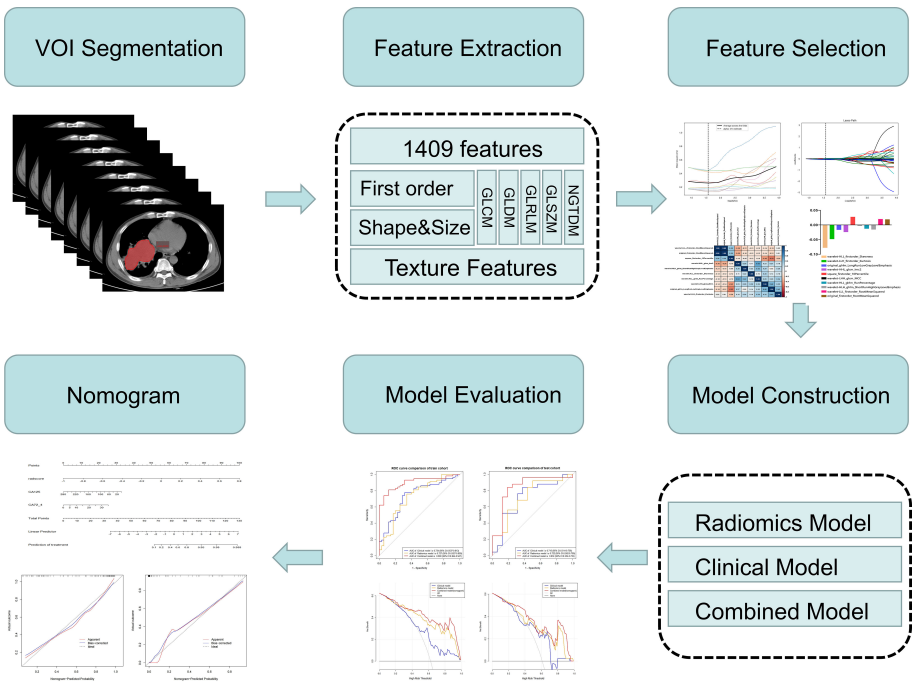

FIGURE 3
Flowchart of the study.

2.6 Construction and internal validation of the nomogram model

The variables, including clinical factors, conventional CT findings, and Rad-scores between the samples of platinum-resistant groups and platinum-sensitive groups with significant differences, were analyzed *via* multivariate logistic regression to build the radiomics nomogram. The performance of the nomogram was evaluated by plotting receiver operating characteristic curves.

The Hosmer–Lemeshow test was used to evaluate the goodness-of-fit of the nomogram. The classification accuracy between the predicted probability and the observed results was evaluated using calibration curves. The diagnostic performance of the nomogram was assessed by evaluating the AUC, sensitivity, specificity, and accuracy. The AUC between the optimized signature and the nomogram was evaluated by using the DeLong test. Decision curve analysis (DCA) was performed to evaluate the clinical utility of the nomogram.

2.7 Statistical analysis

All quantitative features were analyzed with SPSS 25. $P<0.05$ was considered as statistically significant.

Categorical variables are shown as frequencies, and continuous variables are presented as the mean and standard deviation or median and interquartile range. The $\chi 2$ test was used to analyze the categorical variables, the t test was applied to analyze the continuous variables with a normal distribution, and the Mann–Whitney U test was used for variables with an abnormal or unknown distribution. Multivariable logistic regression analysis was used to select the independent prognostic factors. The performance of the model was assessed in the primary and validation cohorts. The discrimination of the signature was measured by the area under the curve (AUC).

The ICC was graded as follows: poor (<0.20), moderate (0.20–0.40), fair (0.40–0.60), good (0.60–0.80), or very good (0.80–1.00).

Statistical analyses were performed using SPSS software (Ver. 25, IBM, Armonk, New York), SigmaPlot (Ver. 14.0), R software package (Ver. 3.5.2, R Development Core Team: https://www.r-project.org/), and the Python scikit-learn package (Ver. 3.7, scikit-learn Ver. 0.21, http://scikit-learn.org/).

3 Results

3.1 Clinical factors of the patients and construction of the clinical factor model

The baseline clinical characteristics of the patients are summarized in Table 1. A total of 134 patients were enrolled in this study: 51 patients with PR and 83 patients with PS. The mean

TABLE 1 Baseline characteristics of the patients in the PR and PS groups.

Variables	PR (51)	PS (83)	$t/\chi^2/U$	*P*
Sex			0.063	0.802
Male	45 (88%)	72 (87%)		
Female	6 (12%)	11 (13%)		
Age	62.71 ± 9.38	61.28 ± 7.33	0.983	0.327
BMI/kg·m-2	22.06 (20.20, 25.00)	22.53 (20.57, 24.61)	0.472	0.637
Smoking	38 (75%)	62 (75%)	<0.001	0.981
Superior vena cava syndrome	3 (6%)	5 (6%)	<0.001	1.000
Spinal cord compression	3 (6%)	5 (6%)	<0.001	1.000
Ki67	80% (70%, 85%)	80% (70%, 85%)	0.576	0.565
Tumor number			0.737	0.692
1	41 (80%)	69 (83%)		
2	1 (2%)	3 (4%)		
≥3	9 (18%)	11 (13%)		
Tumor volume	115.06 (14.50, 247.30)	65.99 (18.72, 160.40)	1.191	0.233
Intratumoral calcification	3 (6%)	2 (2%)	0.314	0.575
Tumor location			<0.001	0.987
Central	40 (78%)	65 (78%)		
Peripheral	11 (22%)	18 (22%)		

(Continued)

TABLE 1 Continued

Variables	PR (51)	PS (83)	$t/\chi^2/U$	*P*
Tumor morphology			1.615	0.532
Regular	16 (31%)	25 (30%)		
Irregular	35 (69%)	58 (70%)		
Lobulated			<0.001	1.000
Absent	2 (4%)	4 (5%)		
Present	49 (96%)	79 (95%)		
Necrosis			0.285	0.594
Absent	27 (53%)	41 (48%)		
Present	24 (47%)	43 (52%)		
Hydrothorax			1.941	0.164
Absent	27 (53%)	55 (65%)		
Present	24 (47%)	29 (35%)		
Staging			0.202	0.653
LS	25 (49%)	45 (53%)		
ES	26 (51%)	39 (47%)		
Metastasis				
Lymph den	49 (96%)	73 (88%)	1.659	0.198
Bone	9 (18%)	6 (7%)	3.449	0.063
Parenchyma organ	12 (24%)	14 (17%)	0.897	0.344
Cardiovascular	12 (24%)	16 (19%)	0.346	0.557
Pleural and pericardium	7 (14%)	8 (10%)	0.531	0.466
NSE	37.30 (22.20, 103.60)	31.80 (18.20, 55.90)	1.991	**0.046**
CEA	7.30 (2.90, 18.60)	3.80 (2.20, 6.50)	2.390	**0.017**
Pro-GRP	714.9 (129.90, 3212.20)	597.80 (156.90, 1953.10)	0.660	0.509
CYFRA-211	3.20 (2.30, 5.20)	2.90 (2.00, 4.40)	1.407	0.159
CA125	33.40 (18.20, 66.60)	17.30 (13.10, 31.10)	4.443	**<0.001**
CA72-4	1.60 (1.00, 2.60)	2.50 (1.20, 5.60)	2.726	**0.006**
CA199	23.40 (5.60, 48.80)	12.10 (4.80, 23.20)	2.809	**0.005**
FER	249.70 (156.00, 491.80)	280.50 (188.30, 387.90)	0.332	0.740
SCC	0.90 (0.50, 1.10)	0.70 (0.60, 1.00)	0.600	0.549
ApoB/ApoA	0.76 (0.63, 0.82)	0.67 (0.60, 0.80)	1.241	0.215
HDL	1.12 (0.90, 1.32)	1.12 (0.97, 1.27)	0.133	0.894
LDL	2.47 (2.12, 3.10)	2.37 (2.12, 3.10)	0.500	0.617
TG	0.98 (0.77, 1.43)	1.40 (1.12, 2.01)	4.015	**<0.001**

NSE, neuron-specific enolase; CEA, carcinoembryonic antigen; pro-GRP, progastrin-releasing peptide; CA125, carbohydrate antigen 125; CA72-4, carbohydrate antigen 72-4; CA199, carbohydrate antigen 199; FER, ferroprotein; SCC, squamous cell carcinoma; ApoB, apolipoprotein B; ApoA, apolipoprotein A; HDL, high-density lipoprotein; LDL, low-density lipoprotein; TG, triglyceride.

ages were 62.71 ± 9.38 and 61.28 ± 7.33, respectively. Univariate analysis showed that NSE, CEA, CA125, CA72-4, CA199, and TG were significantly different between the two groups. Subsequently, multivariate analysis suggested that CA125 (OR: 0.98, 95% CI: 0.977-0.998, P =0.022) and CA72-4 (OR: 1.172, 95% CI: 1.023-1.341, P =0.022) were independent predictors of SCLC with PS (Table 2). The ROC curves of CA125, CA72-4 and the clinical model are shown in Figure S1.

TABLE 2 Univariate and multivariate analyses of clinical factors.

Characteristic	Univariate			Multivariate		
	OR	95% CI	*P*	OR	95% CI	*P*
NSE	0.994	0.988-0.999	0.024	0.994	0.987-1.000	0.063
CEA	0.982	0.962-1.002	0.078			
CA125	0.986	0.975-0.997	0.014	0.987	0.977-0.998	0.022
CA72-4	1.187	1.037-1.359	0.013	1.172	1.023-1.341	0.022
CA199	0.995	0.987-1.003	0.212			
TG	1.043	0.913-1.190	0.538			

3.2 Feature extraction, selection, and radiomic signature building

Of the 1409 radiomic features extracted from CT images, 1186 were demonstrated to have good interobserver agreement, with intra-ICCs >0.75. A total of 1107 radiomic features by variance threshold were enrolled in SelectKBest to select the most valuable 60 features. Finally, 10 features were screened out by LASSO to build the radiomic signature model. The optimal parameter λ of each fold and the selected features of the corresponding fold are shown in Figure 4. The ROC curves of the 10 radiomic features and radiomics model are shown in Figure 5.

Based on these 10 features and their regression coefficients, the radiomics score (Rad-score) formula was constructed as follows: Rad-score = feature * coefficient (Table 3).

3.3 Radiomics nomogram building and assessment of the performance of different models

The ROC and decision curves of the nomogram model are shown in Figures 6A–D. The CA125, CA72-4, and Rad-score were incorporated into the construction of the radiomics nomogram (Figure 6E). Figures 6F, G shows the calibration curve of the nomogram. The Nomo-scores for each patient are shown in Figure S2. The AUC of the clinical model was higher than that of the radiomics model in the training cohort, whereas the AUC value of the radiomics model was higher than that of the clinical model in the validation cohort. The AUC value of the nomogram model was significantly higher than that of the clinical and radiomics models in the training cohort and verification cohort. The calibration curve

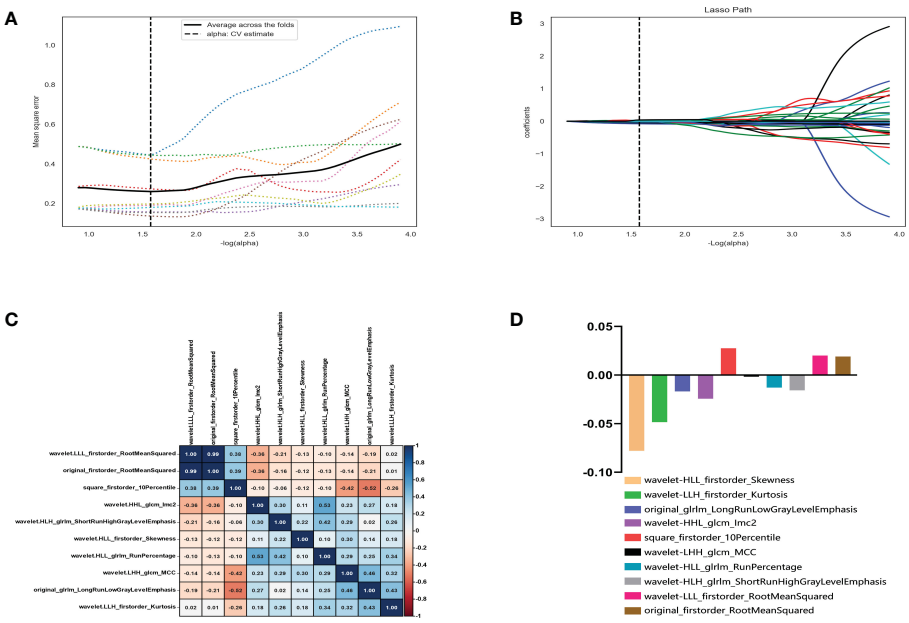

FIGURE 4
Radiomic feature selection using the variance threshold, SelectKBest and selection operator (LASSO) regression model. LASSO regression model on CT images. The mean square error on each fold in the tenfold cross-validation method and the optimal value of the lasso tuning parameter (-log (α) =1.574,α= 2.978) were found **(A)**. The vertical line was plotted with 10 selected radiomic features **(B)**. The 10 radiomic features were selected after dimension reduction **(C, D)**.

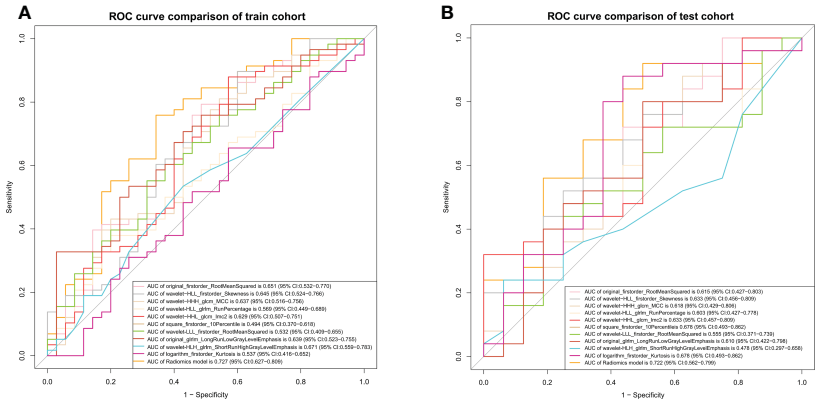

FIGURE 5
ROC curves of the radiomics model. The ROC curves of the radiomics model in the training **(A)** and validation **(B)** cohorts.

showed good calibration in the training cohort and validation cohort (Figure S3). The radiomics nomogram showed the highest net benefit of the three models.

The radiomics signatures based on the nomogram model showed high performance in differentiating between platinum-resistant groups and platinum-sensitive groups, with an AUC of 0.900 (95% CI, 0.844-0.947; sensitivity, 83.61%; specificity, 78.13%; accuracy, 81.72%) in the training cohort and 0.838 (95% CI, 0.534-0.735; sensitivity, 68.57%; specificity, 83.33%; accuracy, 70.73%) in the validation cohort. The AUC of the CT image model was 0.727 (95% CI, 0.627-0.809; sensitivity, 73.85%; specificity, 64.29%; accuracy, 70.97%) in the training cohort and 0.723 (95% CI, 0.562-0.799; sensitivity, 71.88%; specificity, 77.78%; accuracy, 73.17%) in the validation dataset. The AUC of the clinical model was 0.734 (95% CI, 0.637–0.814; sensitivity, 65.82%; specificity, 57.14%; accuracy, 64.52%) in the training cohort and 0.715 (95% CI, 0.514–0.756; sensitivity, 70.00%; specificity, 63.64%; accuracy, 68.29%) in the test dataset. For the combined radiomics signature, the Hosmer–Lemeshow test yielded P values of 0.219 and 0.308 in the training and validation cohorts, respectively, indicating no departure from a good fit.

4 Discussion

The standard first-line therapy for SCLC is platinum-based chemotherapy, which has a 70–80% success rate and often a very pronounced early effect (3, 4). However, the disease will progress quickly, on average, six months after the first treatment has been administered (2). Current management advice is that PR patients should try clinical trial medication such as topotecan or lurbinectedin because they would gain little from an EP regimen, whereas PS patients should be restimulated with an EP regimen (6). To increase the overall survival rate, it is crucial to evaluate the tumor's response to platinum chemotherapy and choose a suitable second-line treatment prior to first-line therapy (24, 25). In this study, we established a CT-based, noninvasive radiomics nomogram model that incorporates the radiomics signature and clinical factors to predict a customized platinum response in SCLC patients. Overall, our study serves as an example of precision medicine and can influence treatment options.

In our study, mediastinal window texture characteristics in patients with SCLC were extracted using radiological methods, and 1409 potential radiological features were chosen for further

TABLE 3 Description of the selected radiomic features with their associated feature group and filter.

Radiomic feature	Radiomic class	Filter	Coefficient
Skewness	firstorder	wavelet-HLL	-0.0778821372989
Kurtosis	firstorder	wavelet-LLH	-0.048467472885
LongRunLowGrayLevelEmphasis	glrlm	original	-0.0168388737795
Imc2	glcm	wavelet-HHL	-0.0243113156389
10Percentile	firstorder	square	0.0276043499311
MCC	glcm	wavelet-LHH	-0.00170586466044
RunPercentage	glrlm	wavelet-HLL	-0.0129710574977
ShortRunHighGrayLevelEmphasis	glrlm	wavelet-HLH	-0.0156495283052
RootMeanSquared	firstorder	wavelet-LLL	0.0201114297855
RootMeanSquared	firstorder	original	0.0190099678839

Imc2, Informational Measure of Correlation 2; MCC, Maximal Correlation Coefficient; glrlm, gray level tun length matrix; glcm, gray-level cooccurrence matrix.

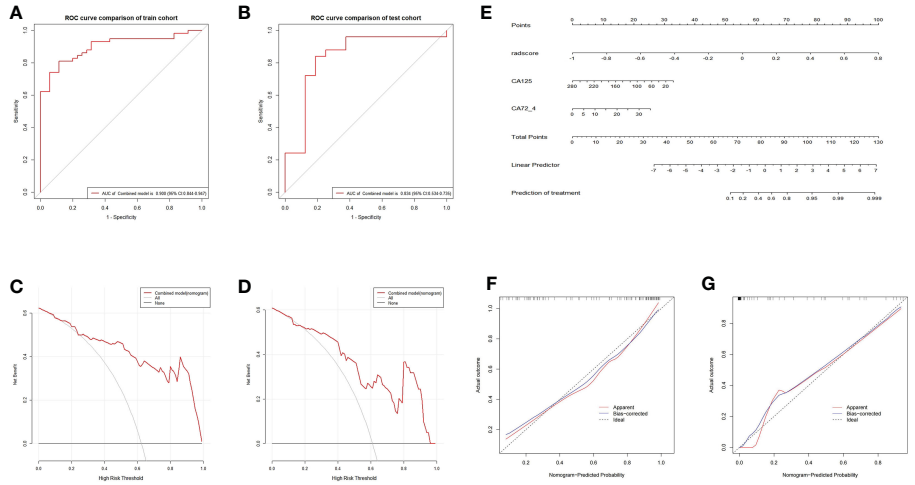

FIGURE 6
ROC and curve decision curve analysis of the nomogram model. The radiomics nomogram and calibration curves for the radiomics nomogram. The ROC curves of the nomogram model in the training **(A)** and validation **(B)** sets and the decision curve analysis for the nomogram model in the training **(C)** and validation **(D)** sets. The radiomics nomogram, combining CA125, CA72-4, and Rad-score, was developed in the training cohort **(E)**. Calibration curves for the radiomics nomogram in the training **(F)** and validation **(G)** cohorts. Calibration curves indicate the goodness-of-fit of the nomogram. The 45° gray line represents the ideal prediction, and the blue lines and red lines represent the performance of the corrected and apparent bias, respectively. The closer the line approaches the ideal prediction line, the better the predictive efficacy of the nomogram.

investigation. We were able to greatly enhance the number of texture characteristics by utilizing 3D annotation, which allowed us to avoid missing any crucial aspects altogether. Wavelet-based characteristics have been proposed as a tool for illness diagnosis and predicting therapy response (26, 27). GLCM and GLRLM are both matrix-based features: GLCM describes the pairwise arrangement of voxels with the same gray value and is used to highlight local heterogeneity information; GLRLM is used to measure the distribution of high gray values, and the GrayLevelEmphasis value is expected to be larger for images with higher gray values. Our Rad-score includes two GLSZM features, MCC and GLCM. The MCC represents the complexity of the texture, and the lower the value, the more complex the texture. In this study, the MCC value of the sensitive group was lower, indicating that the lesion heterogeneity in the sensitive group was higher, and thus, the probability of a response to the treatment outcome was higher.

Meanwhile, the potential 1409 candidate radiomic features were finally reduced to 10 potential predictors by shrinking the regression coefficients with the LASSO method for further integration to form the Rad-score, which contains effective biological information and could reflect the heterogeneity of the tumor. The radiomics signature demonstrated good discrimination in both the training set (AUC, 0.727; 95% CI, 0.627-0.809) and the validation set (AUC, 0.723; 95% CI, 0.562-0.799). Several previous studies have demonstrated that the Rad-score can effectively predict the prognosis of patients due to its high correlation with tumor biological characteristics (28). Several radiomic model prediction algorithms have been developed in the past to predict tumor response to medications, including platinum-based chemotherapeutics, in a variety of cancers (16, 17, 19, 20). A recent study showed that the computed tomography-based radiomics signature was closely associated with the PFS of SCLC; however, this study primarily concentrated on PFS prediction and made no recommendations to enhance PFS, which only offered minimal clinical support (23). These preliminary studies have further confirmed that the texture feature-based radiomics method of SCLC is feasible for predicting platinum responsiveness. Additionally, our study expands on these findings to achieve more significant outcomes with regard to clinical requirements and increased patient survival.

To improve the prediction efficacy, predictors beyond radiomics should also be incorporated with the radiomics signature to further increase the power of the decision support model. In previous studies, patient prognosis was influenced by characteristics such as patient sex, smoking history, tumor stage, and other variables; however, in our study, these variables had no impact on the tumor's sensitivity to platinum-based chemotherapy. NSE, Pro-GRP, and CYFRA 21-1 are all linked to the prognosis of SCLC; however, they also cannot predict platinum resistance. As a result, CA125 and CA72-4 with corresponding odds ratios of 0.987 and 1.172 were selected by multivariable logistic regression analysis. The ORs suggest that the higher the CA125 and CA72-4 levels are, the greater the probability of a favorable response to platinum treatment in SCLC. The clinical phases of SCLC were linked to CA125 (29). According to the literature, a higher level of CA125 can indicate a better impact of first-line treatment (30). Although Ca72-4 can predict the degree of differentiation in gastric cancer (31–33), no studies have found a link between it and small cell lung cancer. The baseline expression of CA 125 and CA72-4 in SCLC can predict platinum resistance, according to our findings.

After selecting candidate predictors using multivariate logistic regression analysis, a nomogram model was built that included radiomics signatures, CA125, and CA72-4. Of note, our radiomics nomogram showed favorable discrimination (AUC 0.900) in the training cohort, which was further validated in the internal validation cohorts (AUC 0.834). Furthermore, DCA showed a higher overall net

benefit of the radiomics model, thus highlighting its value as a better tool for assisting in clinical decision-making. Using the radiomics nomogram model, if a patient is predicted to have a favorable response to platinum, second-line platinum chemotherapy should be recommended; if not, immune checkpoint inhibitors are a good alternative (11, 34, 35). This is particularly important for those with PR, since doctors can choose other treatment options at an earlier stage to prevent tumor progression due to drug resistance and improve recurrence-free survival. However, our study has several limitations. First, given the retrospective nature of this study, selection bias may exist. Second, the training/testing cohort is tiny. Due to morbidity, the sample size is smaller than other tumor type radiomics research samples but similar to those in SCLC radiomics studies. Larger datasets are needed to verify and improve our results, and external validation of our model's performance with an independent cohort from other institutions is necessary.

In summary, we developed and validated a radiomics model that incorporates the pretreatment CT-based radiomics signature and clinical variables for the prediction of the response to platinum treatment in patients with SCLC. This study can assist patients in customizing second-line chemotherapy, improve clinical decision-making, and increase patient survival. Additionally, this research could be utilized to forecast second-line therapy responsiveness and support the development of third-line treatment approaches. It offers a wide range of potential applications and is also applicable to different tumor types.

Data availability statement

The raw data supporting the conclusions of this article will be made available by the authors, without undue reservation.

Ethics statement

The studies involving human participants were reviewed and approved by Institutional Review Board and Human Ethics Committee of Lishui Central Hospital. Written informed consent for participation was not required for this study in accordance with the national legislation and the institutional requirements.

Author contributions

MW and JJ designed the study. SZ, HZ, LS and JY collected the data and drafted the paper. RZ, YS, QW, CL and ZW analyzed the data and made the figures. YS, MC, CL, JJ and MW revised the paper. All authors contributed to the article and approved the submitted version.

Funding

This study was supported by Zhejiang Medical and Health Science Project (2023KY418, 2020KY1085, 2020KY1080), Natural Science Foundation of Zhejiang (LGF21H180002).

Conflict of interest

Author RZ is/was employed by Huiying Medical Technology Co., Ltd.

The remaining authors declare that the research was conducted in the absence of any commercial or financial relationships that could be construed as a potential conflict of interest.

Publisher's note

Supplementary material

The Supplementary Material for this article can be found online at: https://www.frontiersin.org/articles/10.3389/fonc.2023.1006172/full#supplementary-material

References

1. Das M, Padda SK, Weiss J, Owonikoko TK. Advances in treatment of recurrent small cell lung cancer (Sclc): Insights for optimizing patient outcomes from an expert roundtable discussion. *Adv Ther* (2021) 38(11):5431–51. doi: 10.1007/s12325-021-01909-1

2. Tariq S, Kim SY, Monteiro de Oliveira Novaes J, Cheng H. Update 2021: Management of small cell lung cancer. *Lung* (2021) 199(6):579–87. doi: 10.1007/s00408-021-00486-y

3. Schild SE, Sio TT, Daniels TB, Chun SG, Rades D. Prophylactic cranial irradiation for extensive small-cell lung cancer. *J Oncol Pract* (2017) 13(11):732–8. doi: 10.1200/JOP.2017.026765

4. Gazdar AF, Bunn PA, Minna JD. Small-cell lung cancer: What we know, what we need to know and the path forward. *Nat Rev Cancer* (2017) 17(12):765. doi: 10.1038/nrc.2017.106

5. Mao MM, Li HM, Shi J, Qiu QS, Feng F. Prediction of platinum-based chemotherapy sensitivity for epithelial ovarian cancer by multi-sequence mri-based radiomic nomogram. *Zhonghua Yi Xue Za Zhi* (2022) 102(3):201–8. doi: 10.3760/cma.j.cn112137-20210816-01844

6. Ettinger DS, Wood DE, Akerley W, Bazhenova LA, Borghaei H, Camidge DR, et al. Nccn guidelines insights: Non-small cell lung cancer, version 4.2016. *J Natl Compr Canc Netw* (2016) 14(3):255–64. doi: 10.6004/jnccn.2016.0031

7. Wilson MK, Pujade-Lauraine E, Aoki D, Mirza MR, Lorusso D, Oza AM, et al. Fifth ovarian cancer consensus conference of the gynecologic cancer intergroup: Recurrent disease. *Ann Oncol* (2017) 28(4):727–32. doi: 10.1093/annonc/mdw663

8. Alvarado-Luna G, Morales-Espinosa D. Treatment for small cell lung cancer, where are we now?-a review. *Transl Lung Cancer Res* (2016) 5(1):26–38. doi: 10.3978/j.issn.2218-6751.2016.01.13

9. von Pawel J, Jotte R, Spigel DR, O'Brien ME, Socinski MA, Mezger J, et al. Randomized phase iii trial of amrubicin versus topotecan as second-line treatment for patients with small-cell lung cancer. *J Clin Oncol* (2014) 32(35):4012–9. doi: 10.1200/JCO.2013.54.5392

10. O'Brien ME, Ciuleanu TE, Tsekov H, Shparyk Y, Cucevia B, Juhasz G, et al. Phase iii trial comparing supportive care alone with supportive care with oral topotecan in patients with relapsed small-cell lung cancer. *J Clin Oncol* (2006) 24(34):5441–7. doi: 10.1200/JCO.2006.06.5821

11. Trigo J, Subbiah V, Besse B, Moreno V, Lopez R, Sala MA, et al. Lurbinectedin as second-line treatment for patients with small-cell lung cancer: A single-arm, open-label, phase 2 basket trial. *Lancet Oncol* (2020) 21(5):645–54. doi: 10.1016/S1470-2045(20)30068-1

12. Genestreti G, Tiseo M, Kenmotsu H, Kazushige W, Di Battista M, Cavallo G, et al. Outcomes of platinum-sensitive small-cell lung cancer patients treated with Platinum/Etoposide rechallenge: A multi-institutional retrospective analysis. *Clin Lung Cancer* (2015) 16(6):e223–8. doi: 10.1016/j.cllc.2015.04.006

13. Plaja A, Moran T, Carcereny E, Saigi M, Hernandez A, Cucurull M, et al. Small-cell lung cancer long-term survivor patients: How to find a needle in a haystack? *Int J Mol Sci* (2021) 22(24):13508. doi: 10.3390/ijms222413508

14. He M, Chi X, Shi X, Sun Y, Yang X, Wang L, et al. Value of pretreatment serum lactate dehydrogenase as a prognostic and predictive factor for small-cell lung cancer patients treated with first-line platinum-containing chemotherapy. *Thorac Cancer* (2021) 12(23):3101–9. doi: 10.1111/1759-7714.13581

15. Wang C, Jin S, Xu S, Cao S. High systemic immune-inflammation index (Sii) represents an unfavorable prognostic factor for small cell lung cancer treated with etoposide and platinum-based chemotherapy. *Lung* (2020) 198(2):405–14. doi: 10.1007/s00408-020-00333-6

16. Yi X, Liu Y, Zhou B, Xiang W, Deng A, Fu Y, et al. Incorporating Sulf1 polymorphisms in a pretreatment ct-based radiomic model for predicting platinum resistance in ovarian cancer treatment. *BioMed Pharmacother* (2021) 133:111013. doi: 10.1016/j.biopha.2020.111013

17. Khorrami M, Khunger M, Zagouras A, Patil P, Thawani R, Bera K, et al. Combination of peri- and intratumoral radiomic features on baseline ct scans predicts response to chemotherapy in lung adenocarcinoma. *Radiol Artif Intell* (2019) 1(2):e180012. doi: 10.1148/ryai.2019180012

18. Chen Y, Fang Z, Tang Y, Jin Y, Guo C, Hu L, et al. Integrative analysis of multi-omics data reveals the heterogeneity and signatures of immune therapy for small cell lung cancer. *Clin Transl Med* (2021) 11(12):e620. doi: 10.1002/ctm2.620

19. Rekhtman N. Lung neuroendocrine neoplasms: Recent progress and persistent challenges. *Mod Pathol* (2022) 35(Suppl 1):36–50. doi: 10.1038/s41379-021-00943-2

20. He L, Li Z, Chen X, Huang Y, Yan L, Liang C, et al. A radiomics prognostic scoring system for predicting progression-free survival in patients with stage iv non-small cell lung cancer treated with platinum-based chemotherapy. *Chin J Cancer Res* (2021) 33(5):592–605. doi: 10.21147/j.issn.1000-9604.2021.05.06

21. Fave X, Zhang L, Yang J, Mackin D, Balter P, Gomez D, et al. Delta-radiomics features for the prediction of patient outcomes in non-small cell lung cancer. *Sci Rep* (2017) 7(1):588. doi: 10.1038/s41598-017-00665-z

22. Wei H, Yang F, Liu Z, Sun S, Xu F, Liu P, et al. Application of computed tomography-based radiomics signature analysis in the prediction of the response of small cell lung cancer patients to first-line chemotherapy. *Exp Ther Med* (2019) 17(5):3621–9. doi: 10.3892/etm.2019.7357

23. Jain P, Khorrami M, Gupta A, Rajiah P, Bera K, Viswanathan VS, et al. Novel non-invasive radiomic signature on ct scans predicts response to platinum-based chemotherapy and is prognostic of overall survival in small cell lung cancer. *Front Oncol* (2021) 11:744724. doi: 10.3389/fonc.2021.744724

24. Wheeler HE, Maitland ML, Dolan ME, Cox NJ, Ratain MJ. Cancer pharmacogenomics: Strategies and challenges. *Nat Rev Genet* (2013) 14(1):23–34. doi: 10.1038/nrg3352

25. Weinshilboum RM, Wang L. Pharmacogenomics: Precision medicine and drug response. *Mayo Clin Proc* (2017) 92(11):1711–22. doi: 10.1016/j.mayocp.2017.09.001

26. Zhou J, Lu J, Gao C, Zeng J, Zhou C, Lai X, et al. Predicting the response to neoadjuvant chemotherapy for breast cancer: Wavelet transforming radiomics in mri. *BMC Cancer* (2020) 20(1):100. doi: 10.1186/s12885-020-6523-2

27. Chun SH, Suh YJ, Han K, Park SJ, Shim CY, Hong GR, et al. Differentiation of left atrial appendage thrombus from circulatory stasis using cardiac ct radiomics in patients with valvular heart disease. *Eur Radiol* (2021) 31(2):1130–9. doi: 10.1007/s00330-020-07173-1

28. Sala E, Mema E, Himoto Y, Veeraraghavan H, Brenton JD, Snyder A, et al. Unravelling tumour heterogeneity using next-generation imaging: Radiomics, radiogenomics, and habitat imaging. *Clin Radiol* (2017) 72(1):3–10. doi: 10.1016/j.crad.2016.09.013

29. Wang L, Wang D, Zheng G, Yang Y, Du L, Dong Z, et al. Clinical evaluation and therapeutic monitoring value of serum tumor markers in lung cancer. *Int J Biol Markers* (2016) 31(1):e80–7. doi: 10.5301/jbm.5000177

30. Fu J, Fang S, Wen Y, Wang Y, Yin X, Wang D. The efficacy and safety of irinotecan combined with nedaplatin in the treatment of small cell lung cancer. *J BUON* (2020) 25(4):1707–13.

31. Wu T, Wang CH, Wang W, Liu LL, Yun JP, Zhou ZW. Association of preoperative and postoperative Ca72-4 with gastric cancer outcome. *J Surg Oncol* (2021) 123(8):1699–707. doi: 10.1002/jso.26446

32. Tong Y, Zhao Y, Shan Z, Zhang J. Ca724 predicts overall survival in locally advanced gastric cancer patients with neoadjuvant chemotherapy. *BMC Cancer* (2021) 21(1):4. doi: 10.1186/s12885-020-07666-8

33. Liu S, Xu M, Qiao X, Ji C, Li L, Zhou Z. Prediction of serosal invasion in gastric cancer: Development and validation of multivariate models integrating preoperative clinicopathological features and radiographic findings based on late arterial phase ct images. *BMC Cancer* (2021) 21(1):1038. doi: 10.1186/s12885-021-08672-0

34. Mak MP, Tong P, Diao L, Cardnell RJ, Gibbons DL, William WN, et al. A patient-derived, pan-cancer emt signature identifies global molecular alterations and immune target enrichment following epithelial-to-Mesenchymal transition. *Clin Cancer Res* (2016) 22(3):609–20. doi: 10.1158/1078-0432.CCR-15-0876

35. Gay CM, Stewart CA, Park EM, Diao L, Groves SM, Heeke S, et al. Patterns of transcription factor programs and immune pathway activation define four major subtypes of sclc with distinct therapeutic vulnerabilities. *Cancer Cell* (2021) 39(3):346–60.e7. doi: 10.1016/j.ccell.2020.12.014

Frontiers in Oncology

Advances knowledge of carcinogenesis and tumor progression for better treatment and management

The third most-cited oncology journal, which highlights research in carcinogenesis and tumor progression, bridging the gap between basic research and applications to imrpove diagnosis, therapeutics and management strategies.

Discover the latest Research Topics

See more →

Frontiers

Avenue du Tribunal-Fédéral 34
1005 Lausanne, Switzerland
frontiersin.org

Contact us

+41 (0)21 510 17 00
frontiersin.org/about/contact